Visualization and quantification of autophagy in primary gastrointestinal epithelia cell cultures.

Matthew Carl Whelband

A Thesis submitted for the degree of Doctor of Philosophy.

School of Medicine, Health Policy and Practice
University of East Anglia

2013

Abstract

Autophagy is an intracellular bulk degradation pathway which can be used during cellular maintenance to encapsulate and target intracellular content such as organelles and proteins to be degraded by the lysosome. The autophagosome is a double membrane vesicle which is used to encapsulate this cellular content. During the cellular response to starvation, autophagy can degrade cytoplasmic organelles and long-lived proteins in lysosomes, to recover amino acids within the cell and form new proteins. Stimulation of autophagy during infection can enhance immune responses by degrading pathogens and increasing presentation of microbial components to the immune system. Genome wide association studies (GWAS) have identified mutations in the autophagy related (Atg) protein Atg16L1, and NOD2 as risk alleles for Crohn's disease. Atg16L1 is essential for the formation of autophagosomes and autophagosome formation is stimulated following recognition of bacterial cell wall peptide muramyl dipeptide (MDP) by NOD2. Crohn's disease results from an autoimmune reaction to gut epithelial cells, and this raises the possibility that the risk alleles alter autophagy and/or NOD2-mediated microbial sensing in gut epithelial cells. The aim of this thesis has been to develop methods to quantifying autophagy in primary epithelial cells cultured from human intestinal biopsy material. Atg8/LC3 is the major structural protein of the autophagosome. Images of GFP-Atg8/LC3 puncta generated in response to starvation, or NOD2 signalling, were taken by fluorescence microscopy, and pixel densities were rendered to generate digital datasets that were amenable to statistical analysis. Rendered puncta were displayed graphically to indicate autophagosome diameters, spatial location within the cell, lifetime, expansion and movement. The methods were validated in tissue culture cell lines and then extended to study human colon crypts cultures transduced by adenoviral vectors expressing GFP-LC3. In comparison to cell lines after starvation, there were less GFP LC3 puncta in the smaller epithelial cells from colon crypt tissue (20-30 compared to 5.8+/-2.2). MDP generated significantly more LC3 puncta (9.5+/-4) in colon crypt epithelial cells compared to starvation (5.8+/-2.2). This work provides a method to quantify autophagy in colon crypt cultures, and if applied to biopsies taken from patients will be able to determine if autophagy and NOD2 sensing are altered in patients carrying with Crohn's disease risk alleles.
Keywords: Autophagy, in vitro culture, adenoviral transduction, Imaris quantification.

Contents

Abstract.....2

Contents.....3

List of Figures.....7

List of Tables.....8

Abbreviations.....9

Chapter 1 - Introduction.....11

1.1) Genome wide association studies (GWAS) link mutations in Autophagy protein Atg16L1, and NOD2, with bacterial handling and Crohn's disease.....12

1.1-a) Origins of inflammatory bowel disease. 12

1.1-b) Genetic links between Crohn's disease and autophagy. 14

1.2) Autophagy 15

1.3) Autophagy Induction. 18

1.3-a) Control of autophagy by the mechanistic target of rapamycin (mTOR). 18

1.3-b) Regulation of mTOR by protein degradation in lysosomes. 20

1.4) Formation of the autophagosome after autophagy induction. 22

1.4-a) Canonical autophagy and the formation of autophagosomes following starvation of mammalian cells. 22

1.4-b) Early stages in autophagosome formation. 26

1.4-c) Association of Atg5-12, 16 complexes to the autophagosome.....27

1.4-d) Processing of LC3 for incorporation into autophagosome membranes. 28

1.4-e) Autophagosome membrane donors. 33

1.4-f) Quantification of autophagosome puncta. 35

1.5) Selective autophagy by LIR proteins. 38

1.6) Recycling and renewal of lysosomes. 39

1.7) Autophagy and bacterial degradation; Xenophagy. 41

1.7-a) Autophagy, Xenophagy and bacterial handling within cells. 41

1.7-b) Targeting of bacteria to the autophagosome by LIR proteins. 41

1.7-c) Anti-inflammatory role for autophagy.....42

1.7-d) Autophagy induced by NOD2 signalling. 44

1.8) Bacterial handling and Autophagy. 44

1.8-a) Links between NOD2 Crohn's disease mutations, bacterial handling and Autophagy. 44

1.8-b) Atg16L1 Crohn's disease mutant, bacterial handling, and autophagy.. 45

1.8-c) Mouse models of inflammation by Atg16L1 deficiency. 47

1.9) Summary.....48

1.10) Aims of the study. 49

Chapter 2 - Materials and Methods. **51**

2.1) Cell line cell culture **52**
2.1-a) Cells and media. **52**
2.1-b) Cell seeding for microscopy. **53**
2.1-c) Jetprime Transfection **53**
2.1-d) Adenovirus production. **53**
2.1-e) Viral infection of Vero Cells. **54**
2.1-f) Immunocytochemistry. **54**
2.2) Culturing of intestinal crypts **55**
2.2-a) Tissue samples and crypt isolation. **55**
2.2-a-i) Mouse crypt isolation **55**
2.2-a-ii) Isolation of crypts from human colon biopsy **56**
2.2-b) Induction of autophagy in crypt tissue. **57**
2.2-c) Immunostaining of crypt tissue. **58**
2.3 Microscopy **58**
2.3-a) Wide field fluorescent microscopy. **59**
2.3-b) Confocal live cell imaging for cell culture. **59**
2.3-c) Microscopy of crypt samples. **60**
2.3-d) Live cell imaging of crypt cultures. **60**
2.4) Imaris Software **61**
2.4-a) Puncta number analysis **61**
2.4-c) Colocalisation **62**
2.4-b) Tracking of puncta **62**
2.4-d) Surfaces **63**
2.4-e) Statistics **63**

Chapter 3 - Development of methods to quantify autophagy using fixed cell and live cell microscopy. **65**

3.1) Aim **66**
3.2) Analysis of LC3 puncta **67**
3.3) Pixel density measurements of LC3 puncta provide a quantitative analysis of autophagosome formation **67**
3.3-a) Spot selection using 'Spot Function' **69**
3.3-b) Vesicle rendering using the 'surface border function' to generate different spot sizes **71**
3.4) Tracking fluorescent puncta during live cell imaging. **74**
3.5) Analysis of protein colocalisation using Imaris software. **77**
3.6) Summary **81**

Chapter 4 - Quantitative analysis of autophagosomes formed during starvation.....82

4.1) Aims.....**83**
4.2) Use of LC3B as a marker for autophagosomes. **83**
4.3)Live cell analysis of autophagy and autophagosome lifetime.....**83**
4.4) Monitoring lysosomes for autophagy research. **83**
4.5) Pixel density analysis of Autophagosome puncta in fixed cells using Imaris. **84**
4.5-a) Pixel density analysis of LC3b puncta within cell lines.....**84**
4.5-b) Pixel density analysis of puncta containing early autophagosome marker WIPI2.....**88**
4.5-c) A comparison of LC3 puncta detected through immunostaining of endogenous LC3 in fixed cells with GFP-LC3 puncta generated in living cells. **90**
4.6) Analysis of autophagosomes at different time points during starvation.....**91**
4.6-a) Analysis of numbers and diameters of LC3 puncta at different time points during starvation. **91**
4.6-b) Analysis of numbers and diameters of WIPI and SQSTM1/p62 puncta at different time points during starvation.....**96**
4.6-c) Analysis of the lifetime of LC3 puncta formed at increasing times following starvation...**99**
4.7) Summary **105**

Chapter 5 – Analysis of autophagy in human biopsy samples and mouse organoid cultures.....107

5.1)Aims. **108**
5.2) Development of gut organoid cultures. **108**
5.3)Growing 3D cultures of gut organoids.....**111**
5.3-a)Organoid culture from mouse intestine. **113**
5.3-b)Organoid culture from human biopsy.....**115**
5.4) Analysis of autophagosomes within primary intestinal tissues **115**
5.4-a) Adenoviral transduction of organoids.....**116**
5.4-b) Adenoviral transduction of crypts cultured from human biopsy. **120**
5.5) Summary. **122**

Chapter 6 – Quantifying autophagy in primary human colon crypt cultures obtained from biopsy.....123

6.1) Aims.....**124**
6.2) Detection of endogenous autophagy proteins in fixed tissue. **124**
6.3) Detection of GFP-LC3 puncta in crypts transduced with adenovirus. **125**
6.4) Quantitative analysis of autophagosomes in colon crypt cells. **125**
6.4-a) Analysis of GFP-LC3 puncta in tissue fixed at increasing times after starvation.....**125**
6.4-b) Analysis of LC3 puncta in cells at different positions along the crypt axis. **134**
6.5) Quantitative analysis of autophagosome dynamics in response to starvation in live crypt cultures**136**
6.5-a) Movement and diameters of GFP-LC3 puncta. **136**
6.5-b) Lifetimes of GFP-LC3 puncta **139**
6.6) Quantitative analysis of autophagosome induced by Muramyl Dipeptide.....**141**
6.6-a) Caco2 cells.....**141**
6.6-b) Human colon crypt cells. **141**
6.7) Summary.....**146**

Chapter 7) Discussion.....150

7.1) Quantifying autophagosomes within cells. **151**
7.1-a) Use of Imaris software to obtain digital data sets.....**151**
7.1-b) Quantitative analysis of LC3 puncta produced in response to starvation. **152**
7.1-c) Quantitative analysis of LC3 puncta observed by live cell imaging.....**153**
7.2) Possible role for TFEB in autophagosome expansion.....**154**
7.3) Quantifying SQSTM1 puncta during starvation. **155**
7.4) Analysis of autophagy in colon crypt cells. **156**
7.4-a) Adenovirus transduction of organoid and crypt cultures. **157**
7.4-b) Analysis of GFP-LC3 puncta in crypt cells following starvation. **159**
7.4-c) Quantitative estimation of autophagic capacity. **160**
7.5) Future work. **160**

Appendix.....161

Acknowledgements.....169

References.....170

List of Figures

- Figure 1.1 - The architecture of the small intestine crypt-villus and the Colon crypt.
- Figure 1.2 -Autophagosome formation.
- Figure 1.3- Formation of autophagosomes and delivery to lysosomes
- Figure 1.4 -The recruitment of mTORC1 to the lysosome membrane via the Ragulator complex.
- Figure 1.5 - ULK1 complex association by inhibition of the mTORC1 complex.
- Figure 1.6 - The canonical pathway of autophagy.
- Figure 1.7 - Ubiquitin-like protein conjugations in autophagosome formation.
- Figure 1.8 - Timeline of requirement of LC3 and GABARAP/GATE16 in autophagosome formation.
- Figure 1.9- Homotypic and heterotypic fusion of Atg16 and Atg9 bound endosomes.
- Figure 1.10 - Movement of TFEB to the nucleus.
- Figure 1.11 - The targeting of intracellular bacteria to autophagosomes .
- Figure 1.12 - The arrangement of the yeast and mammalian homologues of *Atg16* gene.
- Figure 1.13 - The known effects on bacterial handling and inflammation linked to autophagy protein Atg16L1 and bacterial sensing protein NOD2.
- Figure 3.1 - Immunostaining of autophagy protein LC3 in tissue culture cell lines.
- Figure 3.2 - Live cell imaging of Autophagy using Adenoviral transduction of GFP-LC3.
- Figure 3.3 - Use of the 'spot selection' function in Imaris to analyse LC3 puncta.
- Figure 3.4 - Refining the use of the 'spot selection' function in Imaris to analyse LC3 puncta.
- Figure 3.5 - Rendering LC3 puncta by generating appropriate spot borders.
- Figure 3.6 - Tracking GFP-puncta during live cell imaging.
- Figure 3.7 - Editing tracks by changing the maximum distances and times tolerated between images in a timelapse video.
- Figure 3.8 - Assessing colocalisation between two fluorescent signals using Imaris.
- Figure 4.1 - Quantitative analysis of LC3 puncta formed in response to starvation in CHO cells expressing GFP-LC3.
- Figure 4.2 - Quantitative analysis of LC3 puncta formed in CaCo2 cells in response to starvation.
- Figure 4.3 - Quantitative analysis of LC3 puncta formed in Vero cells in response to starvation.
- Figure 4.4 - Quantitative analysis of WIPI puncta formed in Vero cells in response to starvation.
- Figure 4.5 - A comparison of LC3 puncta in Vero cells generated by immunostaining for LC3B or Live cell imaging of GFP-LC3.
- Figure 4.6 - Comparison of LC3 puncta diameters and numbers in CHO cells and CaCo2 cells.
- Figure 4.7 - Analysis of LC3 puncta in Vero cells at increasing times after starvation.
- Figure 4.8 - Analysis of WIPI2 puncta in Vero cells at increasing times after starvation.
- Figure 4.9- Colocalisation of LC3 with SQSTM1 within puncta formed at increasing times of starvation.
- Figure 4.10 - Colocalisation of LC3 and LAMP-1 within puncta formed at increasing times of starvation.
- Figure 4.11 - Time lapse imaging of LC3 puncta formed at different times following onset of starvation.
- Figure 4.12- Live cell imaging of the interacation of GFP-LC3 puncta with lysosomes labelled with Lysotracker.
- Figure 4.13- Average diameter of autophagosomes across cell lines from nutrient media, to 4 hours of HBSS.
- Figure 5.1 - The organisation of the small intestine and colon epithelia.
- Figure 5.2 - 'In vitro' culture of organoids from mouse small intestine
- Figure 5.3 - 'In vitro' culture of organoids from mouse colon.

- Figure 5.4 - 'In vitro' culture of crypt/organoids from human biopsy.
- Figure 5.5 - Attempted transduction of mouse crypt cultures with adenovirus expressing GFP-LC3.
- Figure 5.6 -Transduction of human crypt cultures with GFP-LC3 Adenovirus.
- Figure 5.7 - Generation of GFP-LC3 puncta following starvation of human colon crypt cultures transduced with GFP-LC3 Adenovirus.
- Figure 6.1- Immunofluorescence analysis of endogenous LC3 and other autophagy marker proteins in human colon crypts.
- Figure 6.2- Immunofluorescence analysis of autophagy marker proteins in human colon crypts transduced with adenovirus expressing GFP-LC3.
- Figure 6.3 - Comparison of Vero cell and Colon crypt cell Imaris quantified endogenous and GFP-LC3 positive autophagosomes.
- Figure 6.4 - Numbers of GFP-LC3 positive autophagosomes across the crypt axis.
- Figure 6.5 - Imaris-tracked movement of autophagosomes in Vero cells and colon crypt cells.
- Figure 6.6 - Single cell early vs late HBSS analysis of GFP-LC3 expressed in Vero and Colon crypt cells.
- Figure 6.7 - Autophagosome number increases in MDP incubations and starvation in Caco2 cells.
- Figure 6.8 - Analysis of MDP Incubated tissue compared to nutrient media using fixed and live cell GFP-LC3 transduced colon crypts.
- Figure 6.9 - Comparison of GFP-LC3 positive autophagosomes formed during starvation, with those formed after > 2 hours of HBSS.
- Supplementary Figure 1- Colocalisation of anti LC3B , anti GFP and GFP-LC3.
- Supplementary Figure 2- Staining of LC3B antibodies in human colon crypt cells.
- Supplementary Figure 3- Isotype control staining compared to LC3B staining in human colon crypt cells.
- Supplementary Figure 4- Expression of GFP-LC3 within differentiated cells in human colon crypts.
- Supplementary Figure 5- distance moved of autophagosomes within different crypt cells.
- Supplementary Figure 6- Secondary control staining of human colon crypt cells.
- Supplementary Figure 7- Ranges of lifetimes of autophagosomes.

List of Tables

- Table 1) Media Additives.
- Table 2) Primary antibody table.
- Table 3) Secondary antibody table.
- Table 4) Mouse Small Intestine growth media.
- Table 5) Human colon/small intestine growth media
- Table 6) Excitation and emission of fluorescent probes.

Abbreviations

- API- aminopeptidase 1
- Atg- Autophagy-Related Protein
- BMM- Bone Marrow Macrophage
- BMP-Bone Morphogenic Protein
- BSA- Bovine Serum Albumin
- Caco- Human Colorectal Adenocarcinoma
- CHO- Chinese Hamster Ovary
- CroA- Cromogrannin A
- CvT- Cytoplasmic to Vacuole targeting
- DAPI- 4'-6'-diamidino-2-phenylindole
- DIC- Differential interference contrast]
- DFCP1- Double-FYVE containing protein 1
- DMV- Double membrane vesicles
- DMEM- Dulbecco's modified Eagles media
- EDTA- Ethylenediaminetetraacetic acid
- EGF- Epidermal Growth Factor
- eIF4E - Eukaryotic translation initiation factor 4E
- eIF4E-BP1- Eukaryotic translation initiation factor 4E binding protein 1
- FIP200- Focal adhesion kinase family interacting protein of 200 kD
- GABARAP- γ-aminobutyric acid receptor-associated protein
- GATE-16- Golgi-associated ATPase enhancer of 16 kDa
- GEF- GTP exchange factor
- GFP- Green Fluorescent Protein
- GI- Gastrointestinal
- GWAS- Genome wide association screen
- HBSS- Hanks balanced salt solution
- HM- Hypomorphic
- IBD- Inflammatory bowel disease
- LAMP- lysosome associated membrane protein
- LAP- LC3 associated phagocytosis

- LC3- Microtubule-associated protein light chain 3
- LIR- LC3 Interacting Region
- MEF- Mouse embryonic fibroblast
- MDP-Muramyl Dipeptide
- MHC-Major histocompatability complex
- MSCV- Mouse Stem Cell Virus
- mTOR- Mechanistic Target of rapamycin
- mTORC1/2- mTOR complex 1/2
- NDP52 - Nuclear dot protein 52kDa
- NOD- Nucleotide-binding oligomerization domain containing proteins
- PAMP- Pathogen associated molecular pattern
- PE-Phosphatidylehtanolamine
- PFA- Paraformaldehyde
- PI(3)K- Phosphatidylinositol-3-kinase
- PI(3)P- Phosphatidylinositol-2-phosphate
- Raptor- Regulatory associated protein of mTOR
- RFP- Red Fluorescent Protein
- Rictor- Rapamycin- insensitive companion of mTOR
- S6K- S6 kinase
- SCV- Salmonella containing vacuole
- SNARE- Soluble NSF attachment protein receptor
- SNP- Single nucleotide polymorphism
- SQSTM1- Sequestersome1 protein (p62)
- TFEB- Transcription factor EB
- TLR- Toll-Like Receptor
- TTSS- Type three secretion systems
- UBD- Ubiquitin binding domain
- Ubl- Ubiquitin-like
- ULK1- Unc-51 like kinase 1
- VMP1- Vacuole membrane protein 1
- WIPI2- WD repeat domain, phosphoinositide interacting 2

Chapter 1:

Introduction

1.1) Genome wide association studies (GWAS) link mutations in Autophagy protein Atg16L1, and NOD2, with bacterial handling and Crohn's disease.

There is increasing evidence for an association between autophagy and an organized inflammatory response, which will be discussed here. The link between autophagy and inflammation is apparent in Crohn's disease, a type of inflammatory bowel disease (IBD). Crohn's disease is an inflammatory condition affecting the entire gastrointestinal (GI) tract and is acknowledged as causing altered mucosal barrier function, disordered cytokine production and inflammation within the GI tract (Loftus *et al*, 1998).

1.1-a) Origins of inflammatory bowel disease.

The gastrointestinal tract consists of the stomach, small intestine and large intestine (colon). The mucosa of the small and large intestine contain large populations of microbial flora, which are exposed to the immune system via the epithelial layers of the intestine. In the small intestine, bacterial numbers increase along the lumen away from the stomach, as the pH increases. In the small and large intestines, the epithelial layer is invaginated, consisting of crypts (small and large intestine) and villi (small intestine). The epithelium of the intestine regenerates every 4 to 5 days, with cells at the top of villi being shed into the lumen. The epithelial layer is maintained by intestinal stem cells which produce all the cells within the epithelial wall. The stem cells are located at the

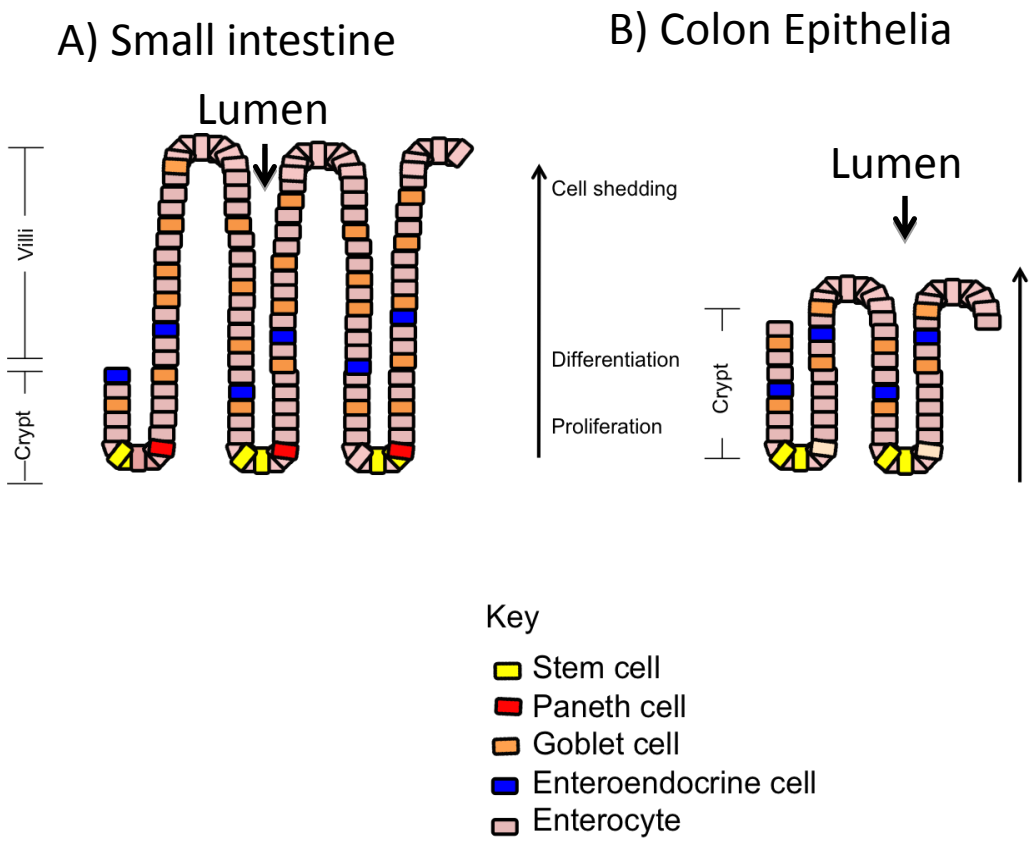

Figure 1.1 - The architecture of the small intestine crypt-villus and the Colon crypt. The small intestine (A) contains a crypt, and a villus in its epithelial layer, whereas the colon contains crypts (B), but no villus, with differentiated cell types contained shown in the key. Arrow indicates the movement of the cells from the stem cell containing crypt base, to the top of the crypt or villus, with the lumen of each crypt shown for both A and B.

base of the crypt in the colon, or at the +4 position above the Paneth cells in the small intestine, and differentiate into enterocytes (absorptive), enteroendocrine (hormone releasing) and goblet (mucous secreting) cells (fig 1.11), (Reya *et al*, 2005).

The intestinal immune system is a large and complex and has to discriminate between beneficial and harmful antigens. The usual response to harmless gut bacteria is the induction of local and systemic tolerance, known as oral tolerance (Mowat, 2003). At the same time, the intestinal immune system has to combat pathogenic microorganisms and maintain the microbiota. Alterations in the intestinal immune system are thought to lead to hypersensitivity responses against components of the microbiota or dietary antigens that can lead to the inflammatory disorders such as Crohn's disease and

Coeliac disease, respectively (Baumgart and Carding, 2006). Autophagy can remove microorganisms from cells and present microbial components to the immune system through a pathway called xenophagy (Levine, 2005, chapter 1.6). This raises the possibility that alterations autophagy/xenophagy in gut epithelial cell may contribute to Crohn's disease.

The intestinal immune system is large and complex and has to discriminate between beneficial and harmful antigens. The usual response to harmless gut bacteria is the induction of local and systemic tolerance, known as oral tolerance (Mowat, 2003). At the same time, the intestinal immune system has to combat pathogenic microorganisms and maintain the microbiota. Alterations in the intestinal immune system are thought to lead to hypersensitivity responses against components of the microbiota or dietary antigens that can lead to the inflammatory disorders such as Crohn's disease and Coeliac disease, respectively (Baumgart and Carding, 2006). Autophagy can remove microorganisms from cells and present microbial components to the immune system through a pathway called xenophagy (Levine, 2005, chapter 1.7). This raises the possibility that alterations autophagy/xenophagy in gut epithelial cell may contribute to Crohn's disease.

1.1-b) Genetic links between Crohn's disease and autophagy.

Studies identify that as a whole, risk between family members is higher if the patient has Crohn's disease instead of ulcerative colitis (another IBD affecting the mucosa of the gut). Twin studies of Crohn's disease (Halme *et al*, 2006) identify monozygotic twins exhibiting a 800-fold increase in Crohn's disease susceptibility compared to the general population. However, IBD is a Western phenomenon. The risk of having IBD is much greater in Europe (100–150 per 100,000 people) compared to Japan, where the risk of

Crohn's disease is as low as 0.5 per 100, 000 people. This suggests the role of environmental factors for the incidence of Crohn's disease along with genetic influences, due to geographical differences in its incidence (Loftus *et al*, 2004).

The precise causes of Crohn's disease remain unknown but current disease models suggest that poorly regulated immune responses to the commensal bacteria of the intestine may lead to chronic inflammation. This has stimulated a search for genetic polymorphisms associated with Crohn's disease that may provide a link between innate recognition of the commensal bacteria of the gut flora and the control of immune responses. The success of this approach is illustrated by genome wide association studies (GWAS) that have linked susceptibility to Crohn's disease to single nucleotide polymorphisms (snps) in the autophagy gene *ATG16L1*, and the intracellular pathogen recognition gene for Nucleotide-binding oligomerization domain 2 *(NOD2)*. As described below (section 1.7), autophagy can deliver bacteria to lysosomes to limit microbial growth and increase exposure of antigens to innate and acquired immune defences. Recent studies show that NOD2 binds Atg16L1 to activate autophagy during bacterial infection. This has led to the hypothesis that the chronic inflammation associated with Crohn's disease may result from defects in NOD2 signalling and autophagy following recognition of commensal gut flora.

Clinically, the inhibitor of the mechanistic target of rapamycin (mTOR), rapamycin, has been attributed to positive outcomes in the treatment of Crohn's disease. Typical treatment for this disease ranges from therapeutic diets to immune suppressive drugs such as methotrexate or anti-tumor necrosis factor (TNF) antibody treatments such as infliximab. These treatments are used to induce remission in patients with Crohn's disease, but in some patients this desired effect does not occur. Due to the links between autophagy gene *ATG16L1* and susceptibility to Crohn's disease, Massey *et al*

(2008) used rapamycin at 4mg/ml a day for a patient with severe refractory colonic and perianal Crohn's disease. Following this treatment, the patient's symptoms of increased bowel movements, recto-vaginal fistula and perianal pain were decreased. However, there are risks to using rapamycin as a Crohn's disease treatment, as it is an immunosuppressant, so opportunistic infection is a risk due to defective T-cell development. This may bypass the improvement of increased autophagy, aiding clearance of invading bacteria and decrease inflammation if used as a treatment. (Massey *et al*, 2008).

The next sections of the introduction will describe the autophagy pathway in detail, from key steps in its activation, and the formation of the full autophagosome. It will then describe links of autophagy with innate immunity and bacterial clearance, which could cause autophagy protein Atg16L1 to be a susceptibility gene for Crohn's disease.

1.2) Autophagy.

Autophagy is one of the main intracellular processes for bulk degradation of organelles and long-lived proteins. This occurs when cells are under stress, most notably during amino acid starvation. Autophagy begins with the formation of double-membrane autophagosome from a phagophore membrane, allowing capture of portions of the cytoplasm within vesicles that then fuse with late endosomes (amphisome) or lysosomes (autophagolysosome) (Figure 1.2). Proteases within the lysosome break down the contents of the autophagosome and amino acids obtained from degradation of proteins are then recycled into the cell for use in protein synthesis (Klionsky, 2005)

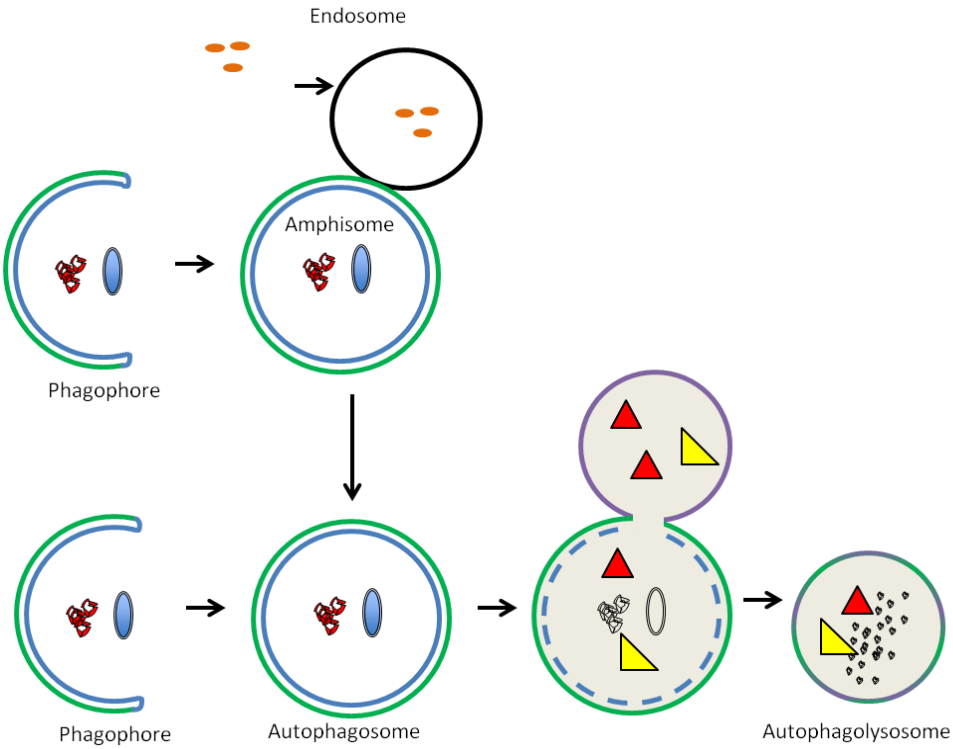

Figure 1.2 -Autophagosome formation. The formation of autophagosomes from a phagophore, and fusion with endosomes and lysosomes for autophagosome content breakdown at the lysosome.

Autophagosomes are formed after mechanistic target of rapamycin (mTOR) inhibition, which brings autophagy-related (Atg) protein complexes together at a region of the cell called the isolation membrane. Genetic screens in yeast first discovered Atg proteins in yeast, where there are 17 gene products essential for autophagy (Thumm *et al*, 1994). Atg genes were characterised in yeast, using the cytoplasm to vacuole (CvT) pathway (Klionsky *et al*, 1992). By tracking movement of a hydrolase API (aminopeptidase 1) by SDS-PAGE, to analyse processing from pr-API, present at the CvT vesicle, to API at the vacuole (yeast lysosome), they determined mutants to pathway (Klionsky *et al*, 1992). Mutants which did not allow for API processing in yeast were also found to affect autophagy in mammalian systems (Thumm *et al*, 1994).

The developing autophagosome vesicle is docked with the Atg5-12-16 complex, which then allows for the autophagosome to be coated with lipidated LC3 (LC3-II). LC3-II stays

with the autophagosome until fusion with the lysosome, where the intracellular contents of the autophagosome and autophagosome lipid membranes are degraded by proteases and lipases contained within the lysosome (Figure 1.3). The degradation of proteins and organelles to amino acids can allow recycled amino acids to be used for protein production when there is a lack of amino acids during starvation.

1.3) Autophagy Induction.

1.3-a) Control of autophagy by the mechanistic target of rapamycin (mTOR).

The mechanistic target of rapamycin (mTOR) is a serine/threonine protein kinase, which acts as a nutrient sensor and controls autophagy in mammalian cells. When amino acid levels are high, mTOR inhibits autophagy and promotes mRNA translation and protein synthesis by ribosomes (Tokunaga *et al*, 2004). When amino acids are low, mTOR is inhibited. This slows protein synthesis, and activates autophagy (Jung *et al*, 2010) (Figure 1.3). The mTOR protein kinase acts as the catalytic subunit in two protein complexes called mTORC1 and mTORC2 (Figure 1.3). The mTORC1 complex is important in the context of autophagy and contains regulatory associated protein of mTOR (Raptor).

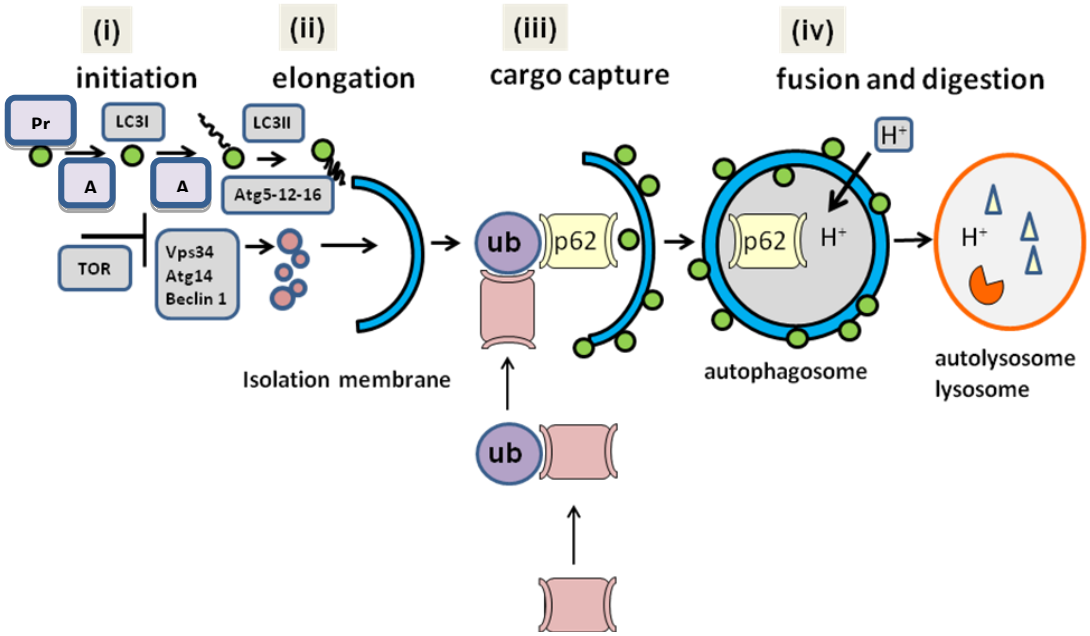

Figure 1.3- Formation of autophagosomes and delivery to lysosomes. Upon autophagy activation by TOR inhibition (i), the isolation membrane is formed after targeting of protein complexes to the developing membrane, and LC3 processing from pro-LC3 to LC3-I, and then to LC3-II to join to the autophagosome membrane (ii). Ubiquitinated protein cargo can be targeted for destruction by joining to LC3 binding proteins such as p62 (iii). Autophagosome fusion to lysosomes occurs for degradation of intracellular content (iv).

The mTORC2 complex contains mTOR and aids assembly of the cytoskeleton. The mTORC2 complex contains a protein called rapamycin- insensitive companion of mTOR (Rictor), which causes mTORC2 to be insensitive to rapamycin (Sarbassov *et al*, 2004, Jung *et al*, 2010). The mTORC1 complex incorporates signals from nutrients and hormones and promotes protein translation through the phosphorylation of downstream effectors such as S6 kinase (S6K) and eIF4E-BP1 (eukaryotic translation initiation factor 4E binding protein 1). The mTORC1 complex inhibits autophagy through phosphorylation of Atg13, which prevents the formation of a complex containing Atg13, Atg1/ULK1 (unc-51 like autophagy activating kinase 1), and its interacting partner FIP200 (focal adhesion kinase family interacting protein of 200 kD) (Jung *et al*, 2010), which is important for the formation of the autophagosome membrane, as described later (1.3a).

Rapamycin is a pharmacological inhibitor of the mTOR protein and can induce autophagy in the absence of nutritional deprivation in both yeast (Heitman *et al*, 1991, Noda, 1998), and mammalian (Shigemitsu *et al*, 1999) systems. Rapamycin inhibits mTOR by binding to the FKBP12 protein associated with mTORC1 (Yip *et al*, 2010), destabilising the complex. New inhibitors of mTOR called Torins have been introduced recently. Torins block ATP binding to the kinase region of mTOR, and have greater specificity for inhibiting mTOR across both mTORC1 and mTORC2 than rapamycin (Thoreen *et al*, 2009). Torin1 was also shown to induce autophagy more rapidly than rapamycin in mammalian cells, which was measured with a larger number of autophagosomes visible in Torin1 treated cells compared to rapamycin treated cells, alongside increased dephosphorylation of mTORC1 target proteins such as 4E-BP1 (Thoreen *et al*, 2009). By phosphorylating 4E-BP1, mTORC1 complex activates translation by releasing it from its complex with eIF4E (eukaryotic translation initiation factor 4E), which can then bind to the 5'cap of mRNA, alongside other translation initiation factors to form an initiation complex that can allow for synthesis of protein to begin (Gingras *et al*, 1998). Active mTORC1also moves to S6K, a protein which needs phosphorylation to allow for activation of translation, by phosphorylating ribosomal protein S6, allowing for the formation of an initiation complex at the ribosome (Peterson *et al*, 1998).

1.3-b) Regulation of mTOR by protein degradation in lysosomes.

Autophagy results in delivery of long-lived proteins to lysosomes (Figure 1.2, 1.3), and recent work shows that transport of amino acids from lysosomes into the cytoplasm can affect subcellular distribution and activity of mTOR. The mTOR protein within the mTORC1 complex localises to the cytoplasmic face of the lysosomes during starvation. During this process mTOR binds to Rheb, which is essential for amino acid sensing by

mTOR (Roccio *et al*, 2006). Rheb has GTPase activity that can activate mTOR and mutations in Rheb designed to increase GTP bound to the protein from 60% to 90%, increased mTOR kinase activity within the mTORC1 complex (Roccio *et al*, 2006). Korolchuck *et al* (2011) show that mTORC1 moves to the lysosomes only when amino acids are plentiful in the cytosol, and suggest that activation of the mTORC1 complex is dependent on localisation with Rheb. A second pathway for sensing amino acids functions in parallel with Rheb and involves small G proteins called Rag GTPases. The four Rag GTPases (RagA, B, C and D) form Rag A/B and Rag C/D heterodimers and bind GTP in response to amino acids and bind to raptor within mTORC1 in an amino acid dependent manner (Sancak *et al*, 2008). The recruitment of Rag proteins, which lack membrane docking motifs, to the lysosome surface requires the Ragulator complex and recent work suggests that Ragulator acts as a GTP exchange factor (GEF) for Rag proteins allowing them to be loaded with GTP and therefore bind mTORC1 (Sancak *et al*, 2010, Bar-Peled *et al* 2012) (Figure 1.4)).

The function of the lysosome within this complex is still to be fully understood, but lysosome positioning close to the nucleus during starvation has been associated with mTORC1 activity, and treatment with microtubule depolymerising drug Nocodazole, dispersed lysosomes evenly throughout the cytoplasm (Korolchuck *et al*, 2011). This correlated with suppression of mTORC1 signalling in nutrient media, and prevented any recovery of mTORC1 signalling after recovery from starvation (Korolchuck *et al*, 2011). The lysosomal H+ ATPase used to acidify the lysosome, which allows for activity of the enzymes within, may play a role in amino acid sensing. Zoncu *et al* (2011) inhibited the lysosome H+ ATPase, and saw that mTORC1 localisation to lysosomes was inhibited.

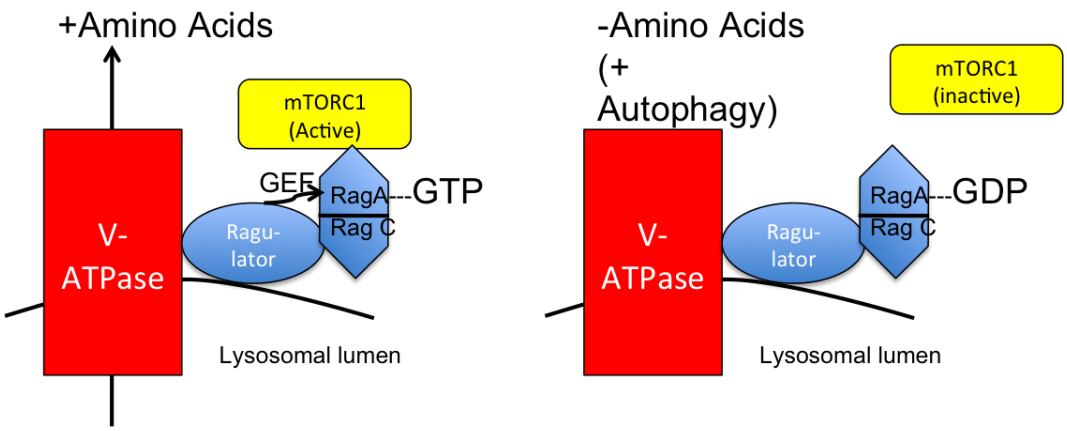

Figure 1.4 -The recruitment of mTORC1 to the lysosome membrane via the Ragulator complex. Ragulator, bound to the vacuolar ATPase on the lysosome membrane, activates RAG GTPases in the presence of amino acids in the lysosomal lumen to bring active mTORC1 to the lysosome membrane (adapted from Bar-Peled et al, 2012).

Direct binding of the Ragulator on the lysosome and the H+ ATPase has been demonstrated and the strength of interactions was dependent on starvation. Raptor within the mTORC1 complex was also shown to interact with RagB on the lysosome membrane, only when amino acids were within the lysosome (Zoncu *et al*. 2011). This indicates that amino acid content within the lysosome has a key role in determining the activity of mTORC1, and explains the localisation of mTORC1 at the lysosome membrane when active.

1.4) Formation of the autophagosome after autophagy induction.

1.4-a) Canonical autophagy and the formation of autophagosomes following starvation of mammalian cells.

The first stages in autophagy after mTOR inhibition involve formation of a protein complex containing ULK1 (Atg1) -Atg13-FIP200. When the mTOR protein is active, it localises to and phosphorylates ULK1 and Atg13 at multiple residues, disrupting the downstream activity of the ULK1 containing early-stage autophagy protein complex

(Jung *et al*, 2010). Under starvation conditions, inactive mTOR cannot localize to this complex, thus cannot phosphorylate ULK1, allowing ULK1 to phosphorylate Atg13 using its own kinase activity (Congcong *et al*, 2009), (Figure 1.5)).

Kim *et al* (2011) showed that mTOR directly phosphorylates ULK1 and prevented it from interaction with another kinase, AMPK. Phosphorylation of ULK1 by AMPK is at different serine residues to phosphorylation by mTOR, and causes activation of ULK1. This identifies the need for the ULK1 complex with Atg13 and FIP200 for autophagy induction (Kim *et al* 2011, Hsu *et al* 2011).

Under nutrient rich conditions, autophagy is inhibited due to Beclin 1 (mammalian Atg6) binding to Bcl-2 family members. However, during starvation, Bcl-2 proteins become phosphorylated by kinases such as JNK, and no longer bind Beclin 1, allowing autophagy to occur (Wei *el al* 2008). Once Beclin 1 is free from Bcl-2 interactions it can bind to other proteins such as UVRAG, Ambra-1, Atg14L or Rubicon. Amino acid starvation results in Atg14 localisation to the endoplasmic reticulum (ER), and recruitment of a class III phosphatidylinositol-3-kinase (PI(3)K) called Vps34 into a complex, (Matsunaga *et al* 2010 Koyama-Honda *et al*, 2013). Atg14 is an essential protein within this complex as part of the PI(3)K complex interacting with Beclin 1, with knockdown of Atg14L causing loss in PI(3)P coating of the endoplasmic reticulum (ER) membrane by the Vps34 complex (Matsunaga *et al* 2010). ULK1 has been shown to directly phosphorylate Beclin-1 in response to amino acid starvation, and induce autophagy within in mammalian cells (Russell *et al*, 2013), linking the ULK1 complex to activation of Beclin1 in a complex further downstream of mTORC1 inhibition (Russell *et al*, 2013).

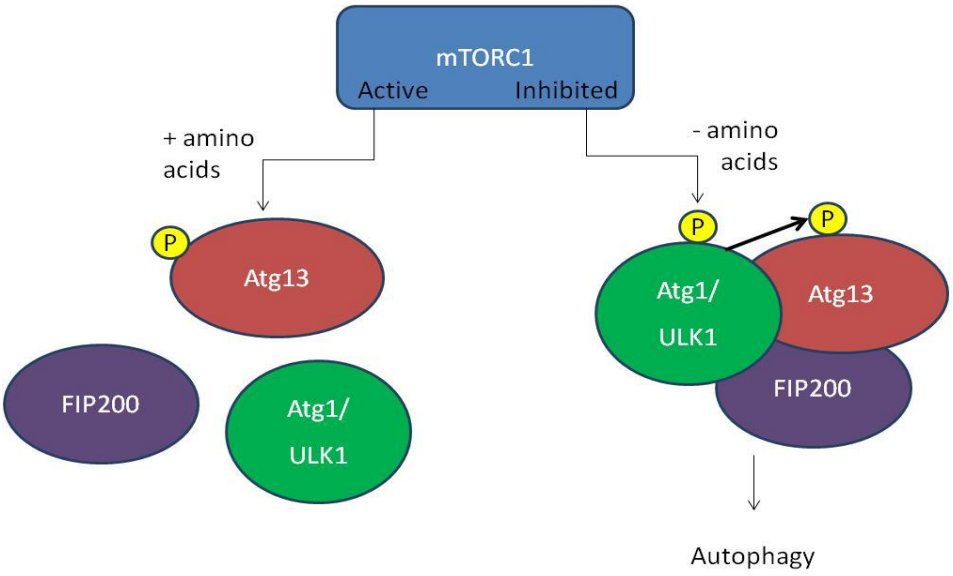

Figure 1.5 - ULK1 complex association by inhibition of the mTORC1 complex. Mtorc1 activation causes phosphorylation of Atg13, so no association with ULK1 occurs. mTORC1 inhibition allows ULK1 to frm a complex with Atg13 and FIP200 for activation of the autophagy pathway (adapted from Zheng et al, 2011).

Beclin1 interaction with Vacuole membrane protein 1 (VMP1), has also been shown to have importance in autophagy activation. Itakura *et al*, (2010) saw that VMP1 localised to autophagosome forming regions of ER membranes, alongside autophagy proteins already described, and Ropolo *et al* (2007), saw that expression of VMP1 induced autophagosome formation. Molejon *et al* (2013), show that localisation of VMP1 to the autophagosome forming regions of the ER is due to VMP1 containing an autophagy related domain, which can bind the BH3 domain of Beclin-1 (Figure 1.6). This in turn could bind Vps34 and promote PI(3)P coating of ER membranes (Molejon *et al*, 2013). Activation of Vps34 results in phosphorylation of phosphatidylinositol lipids PI(3)P, and recruitment of proteins involved in autophagosome formation which contain phosphatidylinositol binding domains. The precise sites of lipid phosphorylation remain controversial, and include the ER, mitochondria and plasma membrane. One of the best-characterised pathways involves formation of omegasomes from the ER (Figure

1.6). The omegasome is named because generation of PI(3)P occurs at a fold within the ER membrane that appears as an 'omega ' in electron micrographs (Hayashi-Nishino, 2009, Matsunaga, 2010). The use of an omegasome for autophagosome formation was proposed by Axe *et al*, (2008), who found that during amino acid starvation, PI(3)P binding protein double FYVE domain-containing protein 1 (DFCP1) localised to punctate structures at the ER which were enriched with PI(3)P. They saw that this region localised with LC3 protein also. The omegasome supports the formation of the isolation membrane, and budding of the mature autophagosome from the ER (Figure 1.6). The use of ER as a potential membrane source for formation of autophagosomes was confirmed by Hayashi-Nishino *et al* (2009). They saw direct links between the omegasome, and the isolation membrane of a forming autophagosome by using electron microscopy. The source of membrane for the formation of the autophagosome is contested, and may come from the ER membrane, or by other intracellular compartments, such as Atg9 and Atg16 containing vesicles from the plasma membrane, as discussed later (chapter 1.4-e).

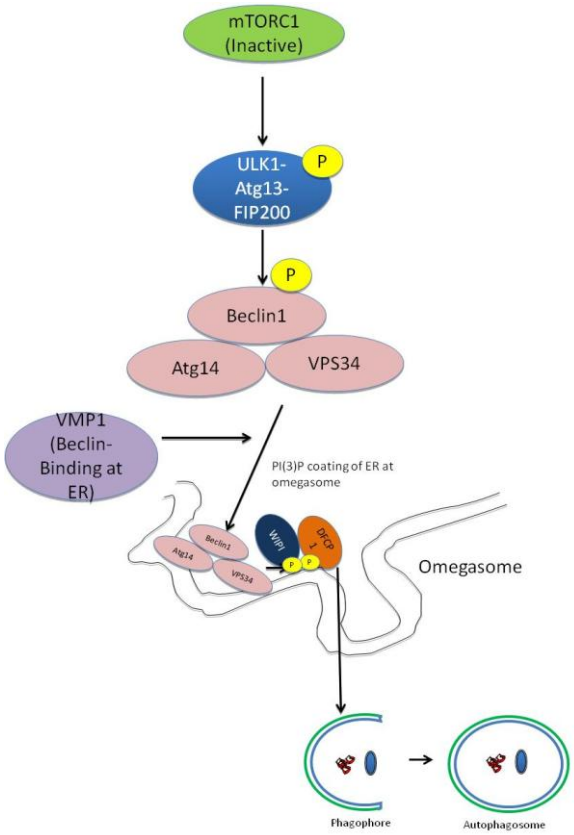

Figure 1.6 - The canonical pathway of autophagy. Atg14L recruits the Beclin1/Vps34 complex to the ER membrane after ULK1 Phosphorylation of At13, allowing for generation of PI(3)P of the ER membrane at the omegasome. This is recognised by the effectors DFCP1 & WIPI2 (Atg18) . Isolation membrane production and phagophore elongation allows for autophagosome production.

1.4-b) Early stages in autophagosome formation.

The isolation membrane is distinguishable by two proteins; WIPI2 (WD-40 repeat containing protein that interacts with PtdIns) and DFCP1. These proteins have PI(3)P binding sites and both bind to the isolation membrane after it is phosphorylated by Vps34 and therefore coated with PI(3)P. Axe *et al* (2008) showed that when WIPI2 was depleted in cells, many more DFCP1 puncta were seen, but no autophagosomes, indicating that these both locate to autophagosome precursors (omegasomes), and also shows that WIPI2 is important in the switch from omegasomes to full autophagosomes at the ER membrane. Polson *et al* (2010) found a functional role of WIPI2 in aiding

docking of LC3-II to the developing autophagosome (described in 1.4-d), as siRNA against the *WIPI2* gene, caused decreased GFP-LC3 puncta. Atg14L, part of the Beclin1-Vps34 complex, is required for this process, as these proteins do not localise together in regions along the ER with *Atg14L* gene knockdown. This caused inhibition of the formation of autophagosomes (Matsunaga *et al*, 2010).

1.4-c) Association of Atg5-12, 16 complexes to the autophagosome.

Docking of DFCP1 and WIPI at the omegasome facilitates recruitment of core autophagy protein complexes necessary for the formation of the autophagosome. The Atg5-12-16L1 complex containing Atg16L! shown to have implications in Crohn's disease susceptibility (chapter 1.1-b), associates with the developing autophagosome and is released when the mature autophagosome is formed. Due to its similarities to the ubiquitination pathway, the autophagy pathway has also been described as containing two ubiquitination-like (Ubl) pathways. For Atg5-12 complex formation, the E1-like enzyme of this pathway is the Atg7 protein, homologous to the E1 ubiquitin-activating enzyme. Atg7, an enzyme which hydrolyses ATP, activates Atg12 by forming a thioester bond between an active cysteine residue within itself, and a glycine residue within Atg12. Activated Atg12 can be transferred to E2 Ubl protein Atg10, and form an Atg12-10 thioester. The Atg12-5 complex is formed by linking a glycine of Atg12 to a lysine of Atg5 catalysed by the Atg10 conjugating enzyme, (Mizushima *et al*, 1998, 2008) (Figure 1.7). The Atg5-12 complex appears to be the major form of these proteins in cells, as indicated by Muzishima *et al* (2008). It is believed that the Atg5-12 complex has E3-like activity, where this complex promotes the conjugation of Atg8 to the membrane of the autophagosome, by enhancing the movement of Atg8 from Atg3, its E2-like protein, to phosphatidylethanolamine (PE), for incorporation of Atg8 to the membrane (described

in 1.4-d), (Hanada *et al*, 2007). There is a noncovalent-bound partner to this complex, Atg16, which homo-oligomerizes to form the Atg12-5-16 multimer. The mammalian Atg16 protein is Atg16L1, and this forms an 800 kDa complex with Atg5-12 proteins, and a coiled-coiled domain of Atg16L1 has been shown to allow for dimerisation of the Atg16L1 protein in mammals, shown with size-exclusion chromatography (Fujita *et al*, 2009), giving the protein the ability to form its complex with Atg5-12. Atg16L1 can form a tetramer within this complex with Atg5 -12, and mainly resides on the outer side of the developing autophagosome membrane (Mizushima *et al*, 1998, Xie *et al*, 2007).

1.4-d) Processing of LC3 for incorporation into autophagosome membranes.

As already stated Atg8 (LC3) is the main component of autophagosome membranes and stays within the membranes of the vesicle throughout its lifetime. Humans express seven isoforms of Atg8 within three families, compared to the yeast's singular Atg8 gene. These are the microtubule-associated protein 1 light chain 3 (MAP1LC3, or LC3) family (LC3A, LC3B, LC3B2 and LC3C), Gate16 (Golgi-associated ATPase enhancer of 16 kDa) family, and GABARAP (γ-aminobutyric-acid-type-A (GABA A) receptor-associated protein) family (GABARAP and GABARAPL1) (Shpilka *et al*., 2011). All mammalian Atg8 proteins are cleaved by Atg4 and lipidated by PE, but LC3 will be used in explanations of Atg8 processing to allow for incorporation into the autophagosome. Atg4 is a cysteine protease that, like LC3, has one version within yeast systems. It is required to cleave the cytoplasmic pro-LC3 to form LC3-I, which can be further modified by lipidation with PE to be incorporated within autophagosome membranes. In mammalian systems there are 4 Atg4 proteins, Atg4A-D, (Li *et al*, 2011). The affinities of Atg4 subtypes for the different Atg8 subtypes have been analysed by Li *et al* (2011), who saw that Atg4B had

the greatest activity across all LC3 subtypes. Also, Kabeya *et al* (2004), and Scherz-Shouval *et al* (2003) saw that Atg4A had greater protease activity against GABARAP and GATE-16 than LC3, with Li *et al* (2011) also suggesting Atg4C and D had relatively low protease activity across all subgroups. However, Mariño *et al* (2007), suggest that Atg4C is required for starvation-induced autophagy in mice diaphragm tissue, indicating its activity may be tissue specific and reliant on starvation occurring within cells. Atg4 cleavage of LC3, exposes a glycine residue, which binds to an E1-like Atg7 within this first Ubl step of LC3 processing requiring E1-like Atg7, which transfers LC3 to E2-like Atg3 for conjugation of PE to the LC3 protein (Figure 1.7). The conjugation to PE allows LC3-II to bind membranes and this is indicated by the formation of 'LC3 puncta' in cells. Conjugation to PE requires Atg3 which in turn binds directly to the Atg12 protein in the Atg5-12,16 complex. Atg7 is also required for PE binding to LC3, binding to Atg3 in a complex that can interact with all Atg8 proteins (Tanida *et al*, 2000). The binding of Atg3 to Atg12 is believed to be important for allowing the Atg5-12,16 complex to facilitate LC3 processing, (Hanada *et al*, 2007). Mizushima *et al* (2001) show that Atg5 is essential for canonical autophagy and that cells lacking Atg5 protein (*Atg5*-/-) cannot form LC3 positive autophagosomes.

The conjugation of LC3 to PE is a reversible reaction, where Atg4 can also cleave LC3 bound to the autophagosome on its outer membrane. This cleavage allows for the lipid region of LC3-II to be removed, so LC3 can be recycled after the autophagosome has fused with a lysosome. The now-cytoplasmic LC3-I can then be re-lipidated, and incorporated into new autophagosomes. (Noda *et al*, 2009).

By over expressing an inactive Atg4b, which cannot cleave LC3, Fujita *et al* (2009) saw that autophagosomes appeared unclosed by electron microscopy, indicating LC3 proteins' role in producing a fully closed, functional autophagosome. Staining for

mammalian LC3 subfamily protein LC3B, has previously been shown to deliver the best correlation between LC3-II processing as seen by western blot, and autophagosome number increases by immunostaining, compared to LC3A (Klionsky *et al*, 2008). However, all mammalian Atg8 forms localise to autophagosomes as identified by Kabeya *et al* (2004).

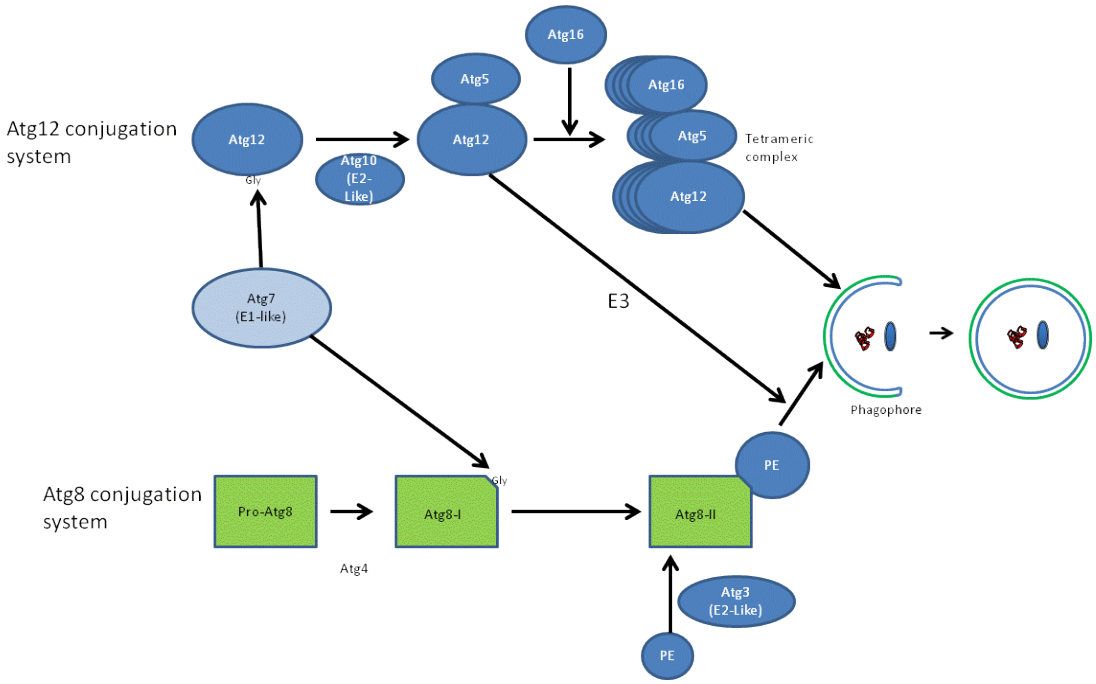

Figure 1.7 - Ubiquitin-like protein conjugations in autophagosome formation. The Atg5-12 conjugation involves Atg7 (E1-like) activation of Atg12 by joining at a Gly residue. Atg12 is then transferred to Atg10 (E2-like), and attached to Atg5, which then forms a complex with Atg16. The Atg8 conjugation system involves Joining of E1-like Atg7 (E1-like) to an exposed Glycine of Atg8 after Atg4 cleavage. Atg3 (E2-like) then aids PE conjugation. The E3-like function of Atg5-12 in fusion of Atg8 to the autophagosome is also proposed.

The structure of Atg8 is comparable to the post translational protein modification protein, Ubiquitin, involved in flagging proteins for degradation via the proteasome, or autophagy as described later (chapter 1.5). Thus, all mammalian Atg8 proteins contain amino-terminal α-helices in carboxy-terminal ubiquitin-like cores, (Paz *et al*, 2000).

The functional significance of Atg8 within the assembly of autophagosome has been described. Computational modelling of Atg8 assembly within autophagosome formation

in yeast indicates that enough Atg8 coats the autophagosome for it to be comparable to a COPII membrane coat. COPII coating aids in the stability of vesicles used for the movement of proteins from the endoplasmic reticulum to the Golgi apparatus. Thus, autophagosome stability is a main theory of the use of Atg8 when localised to the autophagosome (Xie *et al*, 2009).

Unlike COPII coated vesicles, autophagosomes are double membrane vesicles, whose membranes appear smooth, thus do not require proteins similar to COPII to stabilise the formation of a curved double membrane (Knorr *et al*, 2012). Knorr *et al*, (2012) propose that autophagosomes are formed from membrane sheets, containing different densities of protein to allow for curvature. A critical size of curvature is believed to cause the formation of the organelle. This is believed to require minimal energy to occur, thus would be advantageous in growing autophagosomes when they are needed quickly, such as during starvation. Knorr *et al*, (2012) also state that the ER has the ability to form flat sheets that could be used for this process.

Proper localisation of Atg16, within the Atg5-12-16 complex, is needed for the incorporation of lipidated LC3 protein to autophagosomes. In a system where Atg16 was directed to the plasma membrane, Fujita *et al* (2008) also saw lipidated LC3, Atg5 and 12 localisation to the plasma membrane, without the formation of autophagosomes. This indicated that the Atg16 protein, within the Atg5-12,15 complex is needed for the final step in autophagosome formation, LC3 incorporation into to the membrane, with mutations affecting this protein causing possible effects in autophagy within cells.

As previously mentioned, the mammalian Atg8 family is divided into LC3, Gate16 and GABARAP subfamilies. To determine whether these are all required in the same way for autophagosome formation, a liposome-based cell free system has been used (Weidberg *et al*, 2011). The LC3b and GATE-16 used were modified to induce PE binding without

the autophagy machinery. When the first α-helix of both proteins was used alone, it promoted both PE binding to the Atg8 proteins, and liposome membrane localisation, indicating the importance of this region within the structure of these Atg8 proteins. The N-terminus of each Atg8 protein was shown to be important in allowing for membrane interaction after PE conjugation, with ionic interactions of LC3B and hydrophobic interactions of GATE-16, allowing for the successful membrane localisation of LC3. A separate study by Weidberg *et al* (2010), found that these two mammalian Atg8 proteins act differently in the formation of autophagosomes. Knockdown of LC3 still allowed for PE lipidation of GATE-16, and vice-versa, but autophagy was inhibited without the other subfamily present within the cell, thus did not compensate for the loss of the other subfamilies. It was found that LC3 bound vesicles within a GABARAP/ GATE-16 knockdown experiment, saw much greater Atg5-12-16 complex localisation to autophagosomes within cells, whereas GATE-16 overexpression in an LC3 knockdown cell system, saw greater dissociation of Atg5-12-16. This indicates their different roles in the joining, and removal of the Atg5-12-16 complex. GABARAP, inhibited by knockdown of ATG4A, its specific Atg4 partner for lipidation of the GABARAP protein, had unclosed membranes, indicating that ATG5-12-16 removal is needed, alongside GABARAP localisation to the autophagosome, for sealing events needed to form the mature autophagosome, largely lacking ATG5-12-16 (Figure 1.8) (Weidberg *et al* (2010)).

Specific phosphorylation events of LC3 have also been shown to regulate the autophagy process. Cherra *et al* (2010), show that cells contain a pool of phosphorylated LC3, that can, when dephosphorylated, rapidly aid in formation of autophagosomes when needed, such as during rapamycin treatment. Expression of a non-phosphorylatable LC3 protein

induced formation of more autophagosomes. This was due to losing the regulation occurring at the autophagosome formation step (Cherra *et al*, 2010).

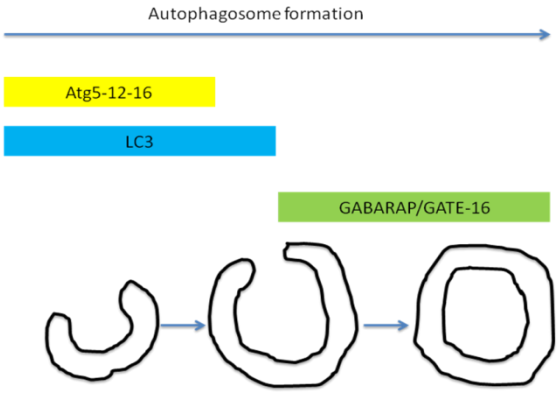

Figure 1.8 - Timeline of requirement of LC3 and GABARAP/GATE16 in autophagosome formation. LC3 is required for Atg5-12-16 localisation to the developing autophagosome, GABARAP/GATE16 are required to close the autophagosome to for a double membrane vesicle.

1.4-e) Autophagosome membrane donors.

The Endoplasmic reticulum as a site for autophagosome formation is well described (Axe *et al*, 2008, Hayashi-Nishino *et al*, 2009, chapter 1.4-b). However, Atg9 and Atg16-membrane compartments have both been suggested as autophagosome membrane donors. Yeast Atg9 positive vesicles have been shown to provide membrane sources for autophagosomes, and localise to the autophagosome outer membrane (Yamamoto *et al*, 2012), moving from an Atg9 pool within the cytoplasm, to the pre-autophagosome structure (PAS) where formation of autophagosomes occurs. (Mari *et al*, 2010). Mammalian Atg9 localises to the Golgi membrane and endosomes, and partially localises with autophagy protein complexes during starvation (Young *et al*, 2006). The role of Atg9 as a membrane source in mammalian autophagy is not fully understood. Young *et al* (2006) identified that mammalian Atg9 relocalises to endosomes with starvation, and this can be inhibited by the presence of an active ULK1. However, when assessing Atg9 localisation to autophagosomes in mammalian cells, Orsi *et al* (2012),

only found transient interactions between Atg9 and autophagosome membrane, so any membrane recruitment from Atg9 membrane sources does not require integration of this Atg9 containing complex. However, Atg9 is essential early in mammalian autophagy, as knockdown inhibited formation of puncta containing WIPI2 and DFCP1 (Orsi *et al*, 2012).

Atg16 containing vesicles were proposed as a site for autophagosome membrane donation by Ravikumar *et al* (2010). Atg16L1 interacted with Clathrin heavy chain, which coats vesicles in the endocytic pathway, seen with mass spectroscopy and immuno precipitation. Knock down of Clathrin heavy chain decreased autophagosome formation in this study. The plasma membrane as a pool of autophagosome membrane was shown by Atg16L1 close localisation to the plasma membrane by fluorescent microscopy, and immuno-EM of GFP-Atg16L1 (Ravikumar *et al*, 2010). Again, this indicates that the function of Atg16L1 is important within the formation of autophagosomes, by generating phospholipid membrane for autophagosome formation.

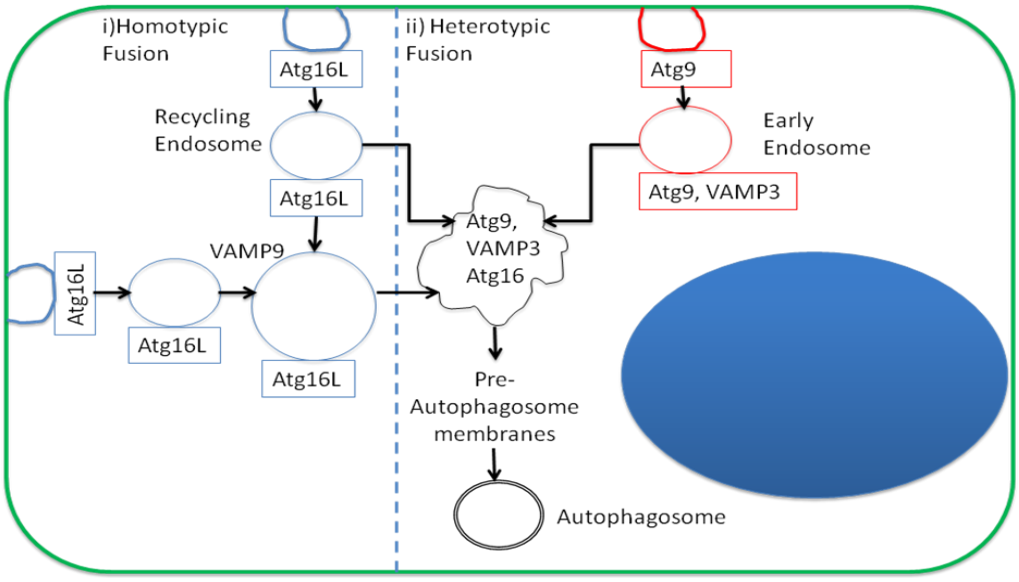

Figure 1.9- Homotypic and heterotypic fusion of Atg16 and Atg9 bound endosomes. i) Homotypic fusion of Atg16L1 bound recycling endosomes to form larger structures. ii) Formation of early endosomes containing Atg9, and heterotypic fusion of Atg16L1 containing recycling endosomes in a VAMP3 dependent manner to form pre- autophagosome membranes (adapted from Puri et al, 2014, Moreau et al, 2011)

Moreau *et al* (2011) saw that Atg16L1 vesicles increased in number, dependent upon knockdown of specific Soluble NSF attachment protein receptor (SNARE) proteins VAMP7, syntaxin 7, syntaxin 8 and Vti1b. SNARE proteins are mostly used for vesicle fusion within both yeast and mammalian cells (Ungar *et al*, 2003). The Atg16 vesicles formed after SNARE knockdown had decreased localisation with LC3. Live cell imaging of Atg16L1 vesicles saw many fusion events occurring between puncta not positive for LC3, with this lost during VAMP7, syntaxin 7, syntaxin 8, or Vti1b knockdown. By expressing tandem fluorescently labelled red (RFP) and green (GFP) Atg16L1 proteins within cells, they could show that Atg16L1 vesicles increased in size, to make yellow vesicles, termed homotypic fusion. Atg16L1 vesicles decreased in size after *VAMP7* knockdown, as did mature autophagosome sizes, indicating that fusion of these vesicles allows for the formation of fully formed autophagosomes (Moreau *et al*, 2011).
It has been noted that Atg9, and Atg16, both localise to the plasma membrane, and are endocytosed within separate clathirin coated endosomes. Atg9 in contained within the early endosome, whereas Atg16L1 is contained within recycling endosomes. Colocalisation of both of these endosomes has been shown by Puri *et al* (2014), displaying heterotypic fusion of autophagy protein containing vesicles prior to full autophagosome formation, dependent on expression of SNARE protein VAMP3. By blocking endosome recycling, homotypic fusion of these endosomes, and formation of autophagosomes, was inhibited (Puri *et al*, 2014) (Figure 1.9).

1.4-f) Quantification of autophagosome puncta.

As LC3-II is bound to the autophagosome membranes at all points in the pathway after the vesicle is created (Figure 1.3), it can be used as a tool to monitor autophagy. Immunofluorescence of LC3 indicates the location and quantity of autophagosomes,

whereas western blot analysis of LC3 can identify induction of autophagy by analysing the ratio of LC3-I (cytosolic) and LC3-II (membrane-bound). LC3 is 18 kDa when cytoplasmic protein, but when mTOR is inhibited, the LC3's proteolytic cleavage and lipidation forms a 16 kDa protein (Klionsky *et al*, 2005, Mizushima *et al*, 2004).

Using GFP-LC3 transgenic mice, where GFP-LC3 is expressed within all cells of the mouse, Yamamoto *et al* (2004) observed starvation induced autophagy within cells from the liver, muscles and pancreas. Interestingly, pancreas autophagosomes increased in size and number during 24 hours of the mouse starving. The work also served to indicate that overexpression of GFP-LC3 did not affect the autophagy signal within cells. Over-expressing GFP-LC3 within F9 teratocarcinoma cells still caused the development of autophagosome rings after 2 hours of starvation, even with 10x greater LC3 expression compared to control cells. Thus, even if the expression of GFP-LC3 within cells was normally higher than LC3 in control mice, it did not affect the autophagy output visualised in this study. Quantification of autophagy up regulation was performed here by manually counting autophagosome puncta number in a field of view in each mouse organ, with sizes and shapes of autophagosomes described but not quantified (Yamamoto *et al*, 2004).

Primary human embryonic fibroblasts transduced with GFP-LC3 lentivirus have been used by Tra *et al* (2011), to study the autophagy output of cells which can be differentiated from these pluripotent cells during differentiation. Puncta per cell were assayed using Volocity software. The lentiviral expression did not affect the autophagy output visualised in this study similarly to the transgenic GFP-LC3 mice study by Yamamoto *et al* (2004).

Rubenstein *et al* (2012) used Atg16L1-GFP and LC3-CFP to study the relationship of early autophagy protein Atg16L1 in the formation of autophagosomes, where only the

largest Atg16 puncta interacted with LC3 puncta during live cell experimentation, exacerbated by starvation of the cells. Puncta size was analysed using Image J software which could detect puncta at a resolution of around 150nm from confocal live cell imaging (Rubenstein *et al* 2012).

Kochl *et al* used GFP-LC3 expressing adenovirus to assess starvation induced autophagy within primary rat hepatocytes. The autophagosome number increase observed with 2 hours of starvation was quantified using an automated microscopy imaging system (the METAMORPH 6.2 software package, Molecular Devices). This again indicates induction of autophagy responses that are visualised using fluorescent microscopy can be quantified, even when using an automated system such as METAMORPH 6.2.

Quantification of autophagosomes from immunofluorescent images of autophagosomes can give more specific details about the autophagy induction present. Imaris software can be used to produce a 3D rendered spot where LC3 puncta are present within a cell. This spot can be then used to give measurements on the autophagosomes present within the cells, such as number, diameter and relative levels of colocalisation using filters against other fluorescence within the image (Bitplane). This software has been used to study autophagy induction during FMDV infection. Using Imaris, Berryman *et al* (2012) found that LC3 puncta present during FMDV infection were bona fide autophagosomes that displayed the same size characteristics as autophagosomes formed within starvation in the same cell lines used for FMDV infection. Maier *et al* (2013), used Imaris software to count the numbers of autophagosome puncta induced by Infectious Bronchitis Virus within primary chicken CK and DF1 cells, compared to Vero cells, using a GFP-LC3 expressing adenovirus for expression of the GFP-LC3 transgene. Activation of autophagy within the Vero cells, compared to CK and DF1 cells

after virus infection, was shown by using Imaris software to count the numbers of autophagosomes per cell (Maier *et al*, 2013).

1.5) Selective autophagy by LIR proteins.

LC3-interacting region (LIR) proteins are able to bind both LC3 via their LIR, and ubiquitin via their ubiquitin binding domain (UBD), to selectively degrade content within cells. Ubiquitin is a small, regulatory protein, which can bind to proteins within cells that may have mis-folded and carry no use within the cell, (Wilkinson, 2005). Much like the UBl processes described earlier (1.4 -c, 1.4-d), it requires E1(ubiquitin-activating), E2(ubiquitin-conjugating) and E3 (ubiqutin ligase) enzymes to allow for its conjugation to proteins it is targeting upon lysine residues (Pickart *et al*, 2004). The proteasome is designed to target ubiquitinated proteins to the proteases active at this complex and aid in their fast break down into small peptides. However, with the discovery of LIR proteins, the use of autophagy to degrade these specific proteins carrying ubiquitin chains, and not just to carry out bulk degradation, has also been demonstrated. SQSTM1/p62 is one of the most widely studied LIR proteins, and is carried with autophagy cargo to lysosomes and degraded (Figure 1.3). This means that degradation of SQSTM1/p62 can be used to measure activation of autophagy where an increase in autophagy is indicated by increased degradation of SQSTM1 analysed by western blot (Bjørkøy *et al*, 2009). NBR1 is another LIR protein. NBR1 can still be degraded by autophagy within cells deficient in SQSTM1, indicating its separate role in performing clearance of ubiquitinated intracellular material (Kirkin *et al*, 2009). The role of LIR proteins in targeting pathogens to the autophagosome is described later (section 1.7-b).

1.6) Recycling and renewal of lysosomes.

Lysosomes are generally considered to represent the end point of the autophagy pathway, and recent work shows that lysosome membranes can be recycled after fusion with autophagosomes (Yu *et al* 2010). An analysis of lysosomes in starved cells showed LAMP-1 positive vesicles appeared tubular, and not their usual spherical shape. These vesicles were LC3 positive at 4 hours of starvation, but at 8 hours were only LAMP-1 positive suggesting removal of LC3 after lysosome fusion. The LAMP-1 positive structures are initially non-acidic, but acidify when maturing, suggesting recruitment of the H+ ATPases able to decrease pH and aid in activity of the proteases within the lysosome (Yu *et al* 2010). Rong *et al* (2011) saw that lysosome reformation was dependent on the lysosome membrane protein spin, a sugar transporter of the lysosome membrane. When knocked down, lack of spin caused the formation of large autophagolysosomes after starvation, not being reformed as seen during control starvation. The lysosomes in spin knockout cells also contained undigested material, and only reformed by producing tubules, which pinch off into new lysosomes during re-addition of amino acids, activating mTOR within the system. This indicates that correct lysosome reformation in relation to mTOR activity is needed during autophagy (Rong *et al*, 2011).

TFEB (Transcription factor EB) is a transcription factor that controls the expression of genes required for the formation of lysosomes. Sardiello *et al* (2009) saw that genes that encode lysosome proteins tend to be expressed together, and share a regulatory element with a sequence termed a CLEAR (Coordinated lysosomal Expression and Regulation), which TFEB binds to. They also showed increased expression of genes for lysosome proteins when TFEB was expressed in HeLa cells. A link with autophagy is

provided by Settembre *et al* (2011) who show that RNAi directed against TFEB, decreased levels of LC3B in cells in nutrient media and following starvation, while overexpression of TFEB increased SQSTM1, WIPI, and LC3B. This linked TFEB to induction of proteins needed for autophagy alongside proteins required for formation of new lysosomes. Interestingly, the movement of TFEB to the nucleus during starvation is regulated by the mTORC1 kinase located at the lysosome membrane (Roczniak-Ferguson *et al* 2012) (Figure 1.10). Blocking lysosome acidification inhibits movement of TFEB to the nucleus, and nuclear localisation is increased when mTOR is inhibited by Torin1. Current models suggest that the sensing of amino acid efflux across the lysosome membrane by mTOR (chapter 1.2) may regulate phosphorylation of TFEB by mTOR. An efflux of amino acids activates mTOR leading to phosphorylation of TFEB, which in turn inhibits nuclear localisation. When cells are starved the flow of amino acids is reduced and TFEB moves to the nucleus to increase expression of genes with CLEAR regulatory elements. This generates proteins required for autophagy and delivery of material to lysosomes (Roczniak-Ferguson *et al* 2012).

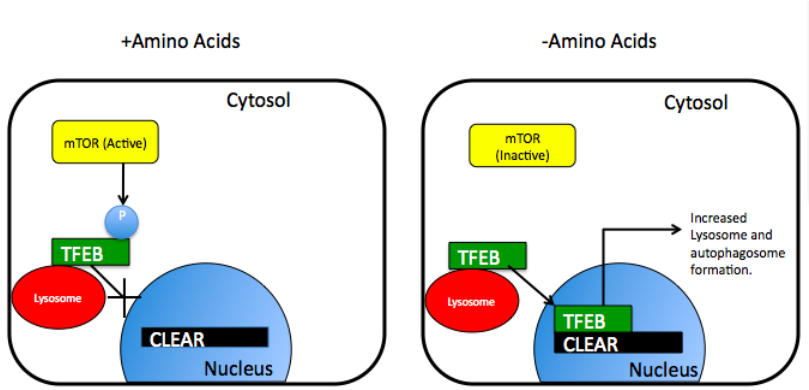

Figure 1.10 - Movement of TFEB to the nucleus. TFEB is phosphorylated and inactive at the lysosome membrane when mTOR is active in amino acid rich conditions. When mTOR is inactive, TFEB is active and moves to the nucleus to bind sequences containing CLEAR elements in the promoter region, which activates expression of genes required for making proteins for formation of lysosomes and autophagosomes (adapted from Martina et al, 2012).

1.7) Autophagy and bacterial degradation; Xenophagy.

1.7-a) Autophagy, Xenophagy and bacterial handling within cells.

Bacterial clearance by autophagy, xenophagy, is an adaptive function of the autophagy pathway. The innate immune response is the first line in defence of pathogenic entry into cells. As part of the innate immune response, autophagy has been shown to stop progression of infection in cells. Birmingham *et al* (2006) have studied autophagy in response to enteritis-causing Salmonella infection. During infection, *S. Typhimurium* localize to Salmonella containing vacuoles (SCV's) within cells. In their research, they identified that the damage that these vacuoles by pin-like type three secretion systems (TTSS) encoded by the bacterial genome, making pin-like projections across membranes, can induce autophagy, and that LC3 positive autophagosomes co localized with SCV's. Thus, autophagy could be used to overcome the initial infection of cells. The group also found that mouse embryonic fibroblasts (MEF's) from *Atg5* -/- mice, which inhibit the formation of the autophagosome, had a significant decrease in LAMP-1 compartments containing bacteria. This indicated there was a decreased bacterial clearance without autophagosome production machinery.

1.7-b) Targeting of bacteria to the autophagosome by LIR proteins.

The LIR protein SQSTM1 has been shown to be important in the clearance of intracellular bacteria by autophagy, alongside a role in selective degradation of polyubiquitinated proteins (Figure 1.11). Zheng *et al*, 2009, showed that in HeLa cells, 78% of the LC3 colocalise to intracellular Salmonella colocalised with SQSTM1, compared with only 5% of Salmonella for bacteria not coated in LC3. Thus, bacterial ubiquitination is a signal triggering the involvement of SQSTM1 in xenophagy, with

specific roles in bacterial targeting and degradation (Figure 1.10). Aside from SQSTM1, other methods for bacterial degradation by autophagy involve the LIR protein NDP52 (nuclear dot protein 52kDa). This protein binds ubiquitin and LC3 directly, similarly to SQSTM1, and has been shown by Thurston *et al* (2009), to degrade Salmonella by binding the ubiquitin surrounding the invading bacteria. The interactions of NDP52 and SQSTM1 with invading Salmonella have been shown to be independent of each other. Cemma *et al*, 2010, saw that NDP52 and SQSTM1 did not colocalise with each other, so could possibly work separately to target bacteria for clearance via autophagy (Cemma *et al*, 2010).

Pathogens can evade xenophagy, by avoiding ubiquitination. *L.monocytogenes* uses its own protein ActA, a protein which masks the bacteria by recruiting proteins to the bacterial surface, including actin (Yoshikawa *et al*, 2009). By generating protein complexes containing ActA within cells, bacteria were not degraded, compared to bacteria without the ability to express ActA.

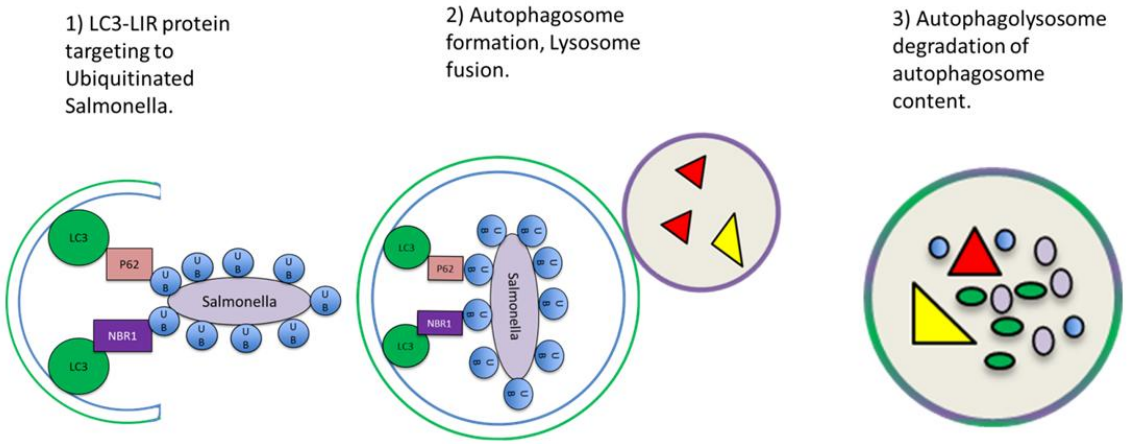

Figure 1.11 - The targeting of intracellular bacteria to autophagosomes . Upon pathogen entry to cells, its localisation to LC3 positive autophagosomes occurs after ubiquitination and SQSTM1 localisation.

It is possible that moving bacteria to the lysosomes for degradation can dampen immune responses by hiding potential PAMPS (pathogen-associated membrane patterns) within autophagosomes, and degrading them before an inflammatory response is activated. Without autophagy, this controlled response to bacteria may be lost, and could aid in the inflammation seen in patients with Crohn's disease who have the susceptibility mutation in *Atg16L1*, as described in chapter 1.1.

1.7-c) Anti-inflammatory role for autophagy.

The inflammasome and the interleukins IL-1β and IL-18 are induced in response to infection and are seen in myeloid cells. Autophagy is believed to inhibit the secretion of IL-1β in basal conditions containing amino acids after inflammasome formation using the drug nigericin. However, Dunpont *et al* (2011) show that when Bone Marrow Macrophage (BMM) cells were starved, IL-1β secretion is enhanced. The mTOR inhibitor PP242 also caused this effect. This effect is believed to be due to the autophagosome aiding in the secretion of this immune modulator. In cells not containing inflammasome components, the activity of autophagy induction to increase IL-1β was also suppressed, indicating the inflammasome was required for autophagy-induced secretion of IL-1β. Further links with autophagy aiding in IL-1β secretion came with using *Atg5* -/- BMM cells, which had a reduction in secretion of IL-1β with a reduced expression of Atg5 protein. Both LC3 and IL-1β colocalised visually within cells also. Linking autophagy and secretion came with investigation into Rab8a, a GTPase required for membrane trafficking to the plasma membrane. Using siRNA directed against *Rab8a*, diminished the autophagy dependent secretion of IL-1β (Dunpont, 2011). This is a novel link between the secretion of inflammatory modulators, and the autophagy pathway which deviates from the canonical autophagy pathway previously described.

1.7-d) Autophagy induced by NOD2 signalling.

NOD2 is an intracellular pathogen receptor found in monocytes, granulocytes and dendritic cells (Ogura *et al*, 2001), but is found in lower levels in epithelial cells such as the gut epithelium (Uehara *et al*, 2007). Bacterial MDP, a component of peptidoglycan walls of Gram positive and negative bacteria is a ligand for NOD2 (Girardin *et al*, 2003). NOD2 signalling induced by intracellular bacteria, leads to translocation of the transcription factor NF-kappaB to the nucleus and activation of genes involved in the innate immune response such as inflammatory mediators and further NF-kappaB expression, increasing immune responses to bacteria (Gutierrez *et al*, 2002). A link between NOD2 and autophagy was described by Cooney *et al* (2010) where MDP induced autophagy by a pathway requiring Atg5, Atg12 and Atg16L1. Parallel studies (Travassos *et al*, 2010) showed a direct interaction between Atg16L1 and NOD2 and both proteins co-localised at the plasma membrane at sites of bacterial entry, and will be described later (section 1.8b).

1.8) Bacterial handling and Autophagy.

1.8-a) Links between NOD2 Crohn's disease mutations, bacterial handling and Autophagy.

The snps identified in *NOD2* include snps 8, 12 and 13. Snp 13 causes a frame shift mutation (3020 ins C) where insertion of cytosine results in a protein lacking in the leucine rich-repeat domain of Nod2, which is believed to either make it unable to sense bacteria by binding to Muramyl dipeptide within the bacterial cell wall, or unable to dimerise and cause downstream signalling from NOD2 (Hugot *et al*, 2001). Patients carrying the frameshift mutation show reduced cytokine responses to MDP and mice

lacking *NOD2* (*NOD2*-/-) are more susceptible to microbial infections and do not respond to MDP (Noguchi *et al* 2009). Recent studies have implicated the *NOD2* frame shift mutation 3020insC to a decreased expression of anti-inflammatory interleukin IL-10 in human primary monocytes (Noguchi *et al* 2009*)*. IL10 is important in stopping a hyper-reactive innate response to microbes and hence dampening adaptive immune responses (Phillpot *et al*, 2009). This decrease in IL-10 with a Crohn's disease-associated *NOD2* frameshift mutation heightened immune response, similarly to the increase in IL-1beta caused by the *ATG16L1* knockouts. Travassos *et al* (2010), also identified that this *NOD2* mutation associated with Crohn's disease stops recruitment of the Atg16L1 protein to the plasma membrane. If this causes decreased bacterial clearance and autophagy induction, this could be the key contribution the susceptibility genes have to Crohn's disease. The functional link between bacterial sensing by NOD2 and autophagy relates these two processes directly, and gives reason for effects of mutants of both of these proteins in the inflammatory response in IBD's.

1.8-b) Atg16L1 Crohn's disease mutant, bacterial handling, and autophagy.

In spite of several GWAS studies, only one snp has been identified in *ATG16L1* resulting in conversion of threonine at position 300 to alanine (T300A). Mammalian Atg16L1 is a more complex protein than the yeast counterpart. In yeast, it binds with Atg5 and 12 similarly to the mammalian form of the protein, but only contains a coiled-coiled domain. In human GWAS, the susceptibility allele alanine at the 300 region of the *ATG16L1* gene is found in the linker region before the WD repeat domain (Figure 1.12) (Mizushima *et al*, 2003). The coiled-coiled domain allows for dimerisation of the Atg16L1 protein in mammals, shown with size-exclusion chromatography (Fujita *et al*, 2009), giving the protein the ability to form its complex with Atg5-12. Thus, the activity

of the rest of the protein found in the mammalian system, needs to be determined. WD-repeat domains within proteins are commonly used as platforms for protein interactions, so the Atg16L1 WD repeat domain is expected to do so also (Mizushima *et al*, 2003).

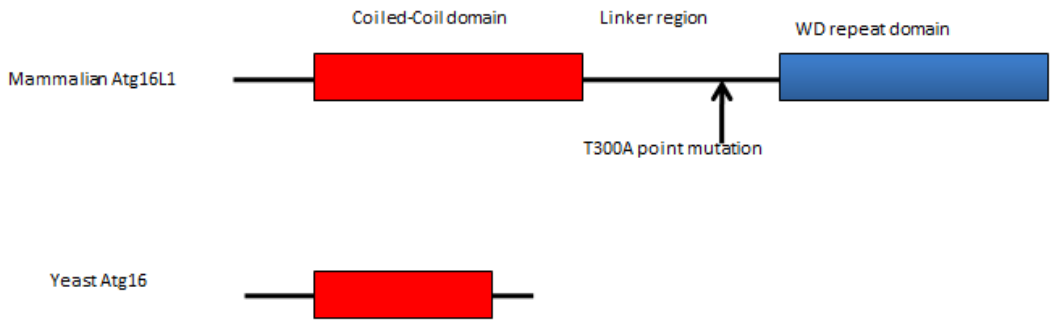

Figure 1.12 - The arrangement of the yeast and mammalian homologues of *Atg16L1*gene. The two proteins are homologous at the coiled-coil domain, with the mammalian protein containing an extra WD repeat region, with a linker between these two, which is where the T300A point mutation is found.

The T300A Atg16L1 mutant leads to a reduced capture of Salmonella by autophagosomes in human epithelial cells (Kuballa *et al*, 2008). Mice hypomorphic (HM) for *Atg16L1* have reduced expression of Atg16L1 and reduced autophagy in all tissues (Cadwell *et al*, 2009). These mice show defects in Paneth cell secretion and increased expression of leptin and adiponectin, which are mirrored in patients homozygous for the *ATG16L1* T300A snp. Furthermore, the development of chronic gut inflammation in Atg16L1 HM mice required the presence of commensal bacteria and persistent viral infection, recapitulating the relationship between genetic susceptibility and environment seen in humans (explained in more detail below).

Messer *et al* (2013) saw that when human HTC116 cells expressed the T300A version of Atg16L1, or had a complete knock out of Atg16L1, the complete Atg16 knock out cells, and the T300A mutant protein cells did not infect with as many intracellular bacteria as

control cells. This again indicates its role within uptake and processing of intracellular bacteria as a way of controlling bacterial invasion. Raju *et al* (2012), showed increased autophagosomes present after Helicobacter Pylori VacA incubation upon cells. However, the *ATG16L1* risk gene variant was shown to increase Helicobacter Pylori infection within human patients (Raju *et al*, 2012). Thus, more details in the specific effects of the Atg16L1 protein and its Crohn's disease associated mutant, in aiding homeostasis in the GI epithelia, will now be described.

1.8-c) Mouse models of inflammation by Atg16L1 deficiency.

Cadwell *et al* (2009) produced HM Atg16L1 mice, using Gene-trap technology, which results in decreased expression of the mRNA of the *Atg16L1* gene. Atg16L1 expression in these mice was decreased to around 23–37% of the normal Atg16L1 levels. Morphologically, the small and large intestines appeared normal. However, the effect of the HM mutation was at the cellular level, with a lack of granulated lysosyme (bacterial defence peptide) staining by immunohistochemical analysis of S.I crypt tissue compared to control S.I tissue. Granule secretion was affected in these HM mice, with the presence of intact granules in the lumen of the crypts. This cell-specific effect further indicates a role for autophagy in regulating the innate immune response at the intestinal epithelia, but now at the level of a differentiated cell in the GI epithelia. lysosome staining of Paneth cells within human Crohn's disease patients without the NOD2 risk allele, but with the *Atg16l1* T300A allele, also has a lack of granulated lysosyme staining. As the Atg16L1HM mice did not have this specific mutation, it is encouraging to see this Paneth cell phenotype in human patients also. In a following paper, Cadwell *et al* (2010) also found that Atg16L1 HM mice in a hyperclean environment, did not have such physiology, but did so when an environmental inducer, mouse norovirus (MNV) was

present within the gut of the mice. This indicates the important involvement of the gut lumen content to the physiological status of the epithelia where organisms have the ability to produce disordered immune response. The role of autophagy in maintaining this is shown below (Figure 1.13).

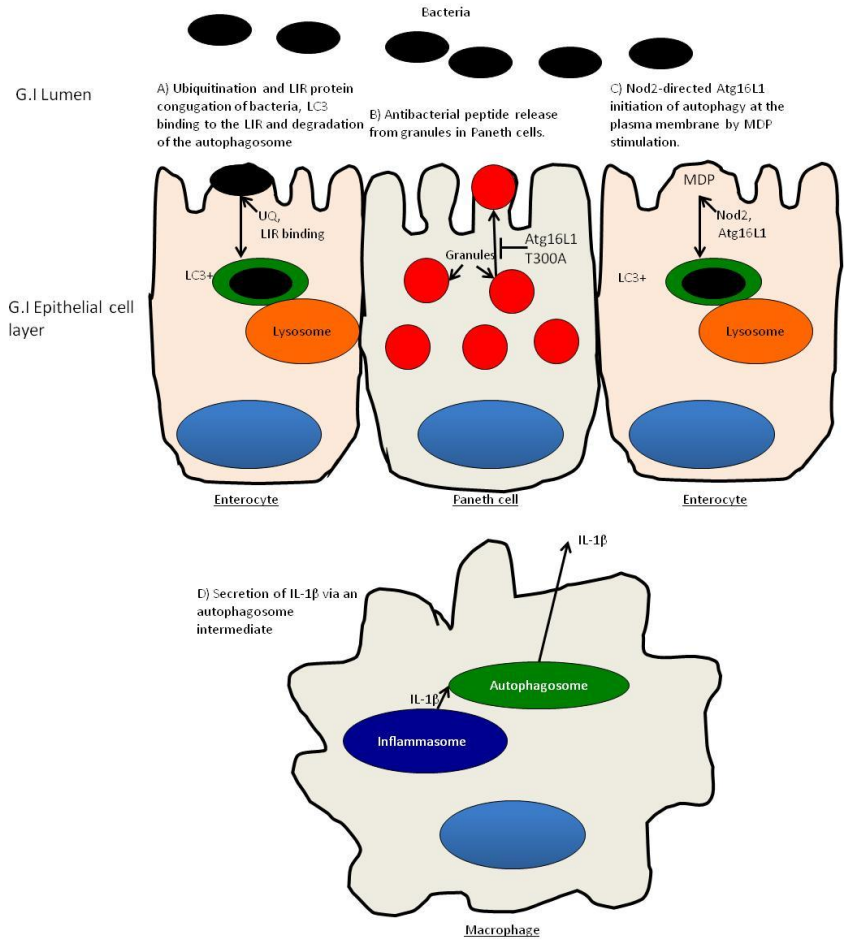

Figure 1.13 - The known effects on bacterial handling and inflammation linked to autophagy protein Atg16L1 and bacterial sensing protein NOD2. A) Targeting of bacteria with ubiquitin upon entry into the cell, and subsequent LIR protein attachment and autohagosome targeting to bacteria. B) Formation and release of granules within Paneth cells, affected by Atg16T300A expression. C) Localisation of Nod2 and Atg16L1 to the plasma membrane after stimulation of cells with bacterial peptide MDP. D) Secretion of IL-1β via an autophagosome intermediate.

1.9) Summary

Previous work shown in this introduction indicates a link between the T300A mutation in the essential autophagy protein Atg16L1, and a loss in gut homeostasis. Work by

Groulx *et al* (2012) used mucosa from healthy patients to assess the autophagy status of gut tissue. They used immunofluorescence of cryosectioned adult human biopsy specimens for staining of autophagy proteins SQSTM1 and Beclin1. Using this technique, they were able to indicate that colon crypt cells did produce autophagosomes in fixed tissue. This method does not allow for live cell incubations of tissue, to visualise autophagosomes after an autophagy triggering stimulus. To assess autophagy within living human epithelial tissue, we will use organoid cultures developed by Sato et al (2009). By culturing isolated human crypts from biopsy samples (described in Chapter 5) in autophagy-inducing conditions of starvation and MDP incubation, we will indicate if autophagy is visually active within living and fixed isolated crypt tissue using the autophagosome membrane marker protein LC3B. As quantification of fluorescent images is possible (Chapter 1.4-f), we will software to assess autophagosome puncta in cell lines, prior to visualising autophagosomes within crypt tissue.

1.10) Aims of the study.

Autophagy is an intracellular degradation pathway, which targets cytoplasmic content to lysosomes for degradation, and allows for amino acids to be recovered when cells are deprived of extracellular nutrients. Autophagosomes can also trap and degrade intracellular bacteria (xenophagy). Xenophagy can be used to hide pathogens from the immune system, and can also aid in processing of PAMPs to the immune system to aid in the clearance of a pathogenic attack. Mutations in the autophagy protein Atg16L1, have implicated autophagy in Crohn's disease, a form of IBD, which causes a disordered immune response to bacteria and other contents of the gastrointestinal lumen. We will assess autophagy within cell lines, and within isolated human epithelial crypt tissue, to address the activation of autophagy within the epithelial layer of the human GI tract .

Project Aims-

- Aim 1. To develop methods to quantify autophagy using fixed cell and live cell microscopy
- Aim 2. Validate The method through a quantitative analysis of autophagosomes formed during starvation in tissue culture cell lines.
- Aim 3. To develop methods to visualise autophagy in human biopsy samples and mouse organoid cultures.
- Aim 4. To quantify autophagy in primary human colon crypt cultures obtained from biopsy

Chapter 2:

Materials and Methods

2.1) Cell line cell culture

2.1-a) Cells and media.

African green monkey kidney epithelial cells or Vero cells (*ECACC* 84113001), (Caco2) cells (*EACC* 86010202), or Human embryonic kidney epithelial 293 (HEK 293) cells (*ECACC* 85120602) were obtained from European Collection of Cell Cultures (ECACC) (Porton Down, UK). Chinese Hamster Ovary (Cho) LC3 cells were previously used by Shvets *et al*, 2008. Vero cells, CHO cells expressing GFP-LC3, and HEK 293 cells were grown in DMEM + glutamax with 1% PenStrep (100 units/µl) and 10% FCS (Foetal Calf Serum) in a 37°C incubator with 5% CO_2. Caco2 cells were grown in DMEM + glutamax with 1% PenStrep and 10% FCS with additional 1% Non Essential Amino Acids (NEAA) and 1% Sodium Pyruvate in a 37°C incubator with 5% CO_2. Cells were grown in a T75 flask, and split twice a week using 1ml Trypsin (2.5%) (Invitrogen) to detach cells. Once detached, cells were then re-suspended in 9ml of fresh media and split in a 1 in 10 dilution into a new T75 flask. This was the case for all cell lines apart from HEK 293, which can be detached manually by resuspending in media using a 10ml stripette. For starvation experiments, cells were washed with, and then incubated in Hank's Balanced Salt Solution (HBSS, Sigma, Dorset) and left in the 37°C incubator before being fixed at the time points specified in each experiment. For Live cell imaging, HBSS + 1% HEPES buffer was used, to minimize the impact to the cells of being in an environment without the optimal cell culture incubator CO_2 conditions used during other incubations. Tissue culture additives used are shown in Table 1.

Table 1) Media treatments.

Compound name	Final concentration	Company
chloroquine	100μM	Invitrogen
Lysotracker	1μM	Sigma

2.1-b) Cell seeding for microscopy.

For immunocytochemistry, Vero cells were plated onto 13mm glass cover slips in 24 well plates at 40,000 cells per well. A haemocytometer was used to count cells/10μl, which was then used to count cells/ml used for plating. For live cell imaging of Vero cells, 40,000 cells were plated in a 5cm dish using a 45mm glass cover slip. This generated a 60-70% confluent slide within one day of plating.

2.1-c) Jetprime Transfection.

Vero cells were transfected with Jetprime according to the manufacturer's guidelines, with 1ug of DNA complexed to 2ul of Jetprime reagent for each well of a 24 well plate. Transfected plasmid used was LAMP-1-RFP (Addgene, plasmid 1817).

2.1-d) Adenovirus production.

GFP-LC3B adenovirus was originally made my Dr. Xiao-Ming Yin at the Univeristy of Florida and was a kind gift by Dr Helena Maier from the Institute of Animal health, Compton. Adenoviral particles were amplified using the standard Invitrogen methodology, using HEK 293A cells competent for Adenovirus production. Cells were grown in a T75 flask, counting $3x10^6$ cells per 10ml DMEM +10%FCS, 1%PenStrep. When the cells are at 80% confluency, 100μl of Adenoviral stock was added to the media and the plate was swirled to mix the virus. The cells were then grown at 37°C in a CO2 incubator, and checked for 2-3 days until the cells were rounded and lifting from

the base of the flask. The lifted cells were transferred to a 15ml tube. Cells were then frozen at -80°C for 30 minutes, then placed within a 37°C water bath for 15 minutes. This was repeated twice. The lysed cells were then centrifuged for 15 minutes at 3000rpm, to pellet debris from the lysed cells. 1ml aliquots of the supernantant containing virus were stored at -80°C.

2.1-e) Viral infection of Vero Cells.

Vero cells were grown to become 70% confluent on 40mm glass cover slips. 10ul of 293A cell lysates containing GFP-LC3 Adenovirus was left in new media overnight to allow for infection of Vero cells for 24 hours. Then, Vero cells were used for live cell imaging experiments.

2.1-f) Immunocytochemistry

Cells were fixed with 100% ice-cold methanol for 5 minutes, washed in PBS solution and blocked for 10 minutes in 2%BSA/1xPBS solution. Primary antibodies were resuspended in 2% BSA/1xPBS solution at the correct dilutions (Table 2) incubated either overnight at 4°C with shaking, or for 1 hour at room temperature. Cells were washed three time with 2% BSA for 5 minutes. 2% BSA washing was repeated three times before addition of appropriate secondary antibodies at 1:500 dilutions in 1xPBS (Table 3). Secondary antibodies were incubated with slide between 40-60 minutes at room temperature on a rocker, shielded from light before being washed 3 times for 5 minutes in PBS. Nuclei were stained with 4',6-diamidino-2-phenylindole (DAPI) , obtained from Sigma (Dorset, UK). DAPI was diluted 1 in 1000 in 1xPBS to make a final concentration of 10μg/ml. All coverslips were mounted onto glass slides using Fluoromount G (Cambridge Biosciences, Cambridge, UK) and stored at 4°C.

Table 2) Primary antibody table.

Antibody	Species	Company	Product code	Formulation	Dilution
LC3B	Mouse monoclonal	MBL	4E12	Affinity Purified	1 in 200
LC3B	Rabbit polyclonal	Sigma	L7543	Affinity Purified	1 in 1000
LC3B	Rabbit polyclonal	Abcam	AB48394	Affinity Purified	1 in 200
LC3B	Rabbit polyclonal	Cell Signalling	#2775	Affinity Purified	1 in 200
SQSTM1	Goat polyclonal	Santa Cruz	P-15	Affinity Purified	1 in 200
SQSTM1	Guinea Pig polyclonal	Progen	GP62-C	Stabilized antiserum	1 in 200
LAMP-1	Rabbit polyclonal	Abcam	ab24170	Affinity Purified	1 in 200
LAMP-2	Mouse monoclonal	Abcam	ab25631	Affinity Purified	1 in 200
Atg16L1	Rabbit polyclonal	Abgent	AP1817b	Purified polyclonal	1 in 200
IgG1 Isotype control	Mouse monoclonal	R&D	MAB002	Affinity Purified	1 in 200
WIPI2	Mouse monoclonal	Abcam	ab101985	Affinity Purified	1 in 500
Muc2	Rabbit polyclonal	Abcam	ab76774	Affinity Purified	1 in 200
Chromogranin A	Rabbit polyclonal	Santa Cruz	sc13090	Affinity Purified	1 in 200

2.2) Culturing of intestinal crypts

2.2-a) Tissue samples and crypt isolation.

2.2-a-i) Mouse crypt isolation

Mouse small intestines and colon were dissected, flushed with PBS and cut open londitudinally to expose the lumen. Tissue was then cut into small sections (around

0.5cm) and incubated in 2mM EDTA in 1x PBS for 30 minutes prior to shaking and crypt release. In the case of small intestine crypt suspensions were filtered through a 0.75mm filter to remove large villi. Crypts were pelleted by centrifugation at 100G and then resuspended in Matrigel in media as described in Table 4.

Table 3) Secondary antibody table.

Antibody	Species	Company	Dilution
Alexa Fluor 488-AP	Donkey Polyclonal	Stratech (112-545-143)	1:500
Alexa Fluor 594-AP	Donkey Polyclonal	Stratech (115-585-166)	1:500
Alexa Fluor 647=AP	Donkey Polyclonal	Stratech (112-605-144)	1:500

2.2-a-ii) Isolation of crypts from human colon biopsy

Human tissue for this study was acquired from the Norfolk and Norwich University Hospital in accordance to the Norwich District Ethics Committee, Norfolk and Norwich University Hospital, UK. Biopsy material was maintained in media (Table 5) before experimentation in a humidified 95% air, 5% CO_2 incubator at 37°C. Crypt isolation was performed using protocols adapted from the Clevers lab, and have been described previously (Koo *et al*, 2011). Colon biopsies were first washed in PBS and then incubated in 4mM EDTA solution in 1x PBS for 30 to 45 minutes followed by vigorous shaking in 1X PBS to release crypts from the biopsy. Crypts were pelleted at 300G for 5 minutes. Isolated crypts were then resuspended in 200µl of Matrigel. Crypts were transduced by adding 10ul of the GFP-LC3 adenovirus stock prior to suspension in Matrigel. The Matrigel-crypt suspension was then plated onto 18mm glass cover slips in

a 12 well plate and left in 5% CO_2 incubator at 37° for 20 minutes to harden the Matrigel prior to addition of media (Table 5) and overnight incubation at 37^0C.

Table 4) Mouse Small Intestine growth media.

Component	Volume	Stock Concentration	Final Concentration	Differentiation medium (wnt free)
GFP-LC3 Adenovirus	10µl/200µl Matrigel	-	-	+
F-12 Glutamax	1ml	-	-	+
N2	10µl	100x	1x	+
B27	20ul	50x	1x	+
R-Spondin	10µl	5mg/ml	500µg	+
EGF	10µl	2.5mg/ml	25µg	+
Noggin	10µl	5µg/ml	50ng	+
PenStrep	10µl	-	-	+
N Acetyl-Cysteine	20µl	50mM	1mM	+
Wnt3A	0.5µl	-	-	-

2.2-b) Induction of autophagy in crypt tissue.

Autophagy activated by NOD signalling was achieved by incubating crypt-Matrigel cultures with 1ug/ml MDP and analysed after 16 hours at 37^oC, in 5% CO_2. Autophagy activated by starvation was achieved by incubating crypt-Matrigel cultures in Hank's buffered salt solution (HBSS). HBSS provides osmotic and pH buffering but lacks organic salts and amino acids. Samples were washed two times in HBSS to remove amino acids from the Matrigel. Where stated, tissue was incubated in 100µM chloroquine for the duration of experiments prior to fixing in 4% Paraformaldehyde (PFA) or live cell imaging.

Table 5) Human colon/small intestine growth media

Component	Volume	Stock Concentration	Final Concentration (per ml media)	Differentiation medium (wnt free)
GFP-LC3 Adenovirus	10µl/200µl Matrigel	-	-	+
F-12 Glutamax	1ml	-	-	+
N2	10µl	100x	1x	+
B27	20ul	50x	1x	+
R-Spondin	10µl	5mg/ml	500µg	+
EGF	10µl	2.5mg/ml	25µg	+
Noggin	10µl	5µg/ml	50ng	+
PenStrep	10µl	-	-	+
N Acetyl-Cysteine	20µl	50mM/ml	1mM	+
Wnt3A	0.5µl	-	-	-
SB202190	0.1µl	100mM/ml	10µM	-
A-83-01	1µl	0.5mM/ml	500nM	+
Nicotinamide	200µl	50mM/ml	10mM	-
Gastrin	1µl	0.1mg/ml	10µg	+

2.2-c) Immunostaining of crypt tissue.

Crypt tissue was fixed in 4% PFA (pH 7.5) on ice for 1 hour, washed with PBS, and quenched with ammonium chloride (10mM) for 10minutes. Samples were washed again in PBS and incubated in sodium dodecyl sulphate (SDS, 1%) for 5minutes, washed in PBS 6 times before a second permeablisation in Triton-X100 (0.5%) for 30minutes. Crypts were then left for 2 hrs in blocking buffer (10% goat serum, 1% BSA in 1xPBS). Crypts were then placed in 1° antibody overnight at 4°C and subsequently fluorescently tagged with a conjugated 2° antibody for 2 hours at room temperature. Crypts were incubated in PBS for 1 hr prior to mounting up on poly-L-lysine coated slides (BDH)

with Hoechst (Sigma) diluted in Vectashield (1 in 1000).

2.3 Microscopy

2.3-a) Wide field fluorescent microscopy.

The fixed cell lines were imaged on a Zeiss Axioplan microscope with a 63x, 1.4NA oil-immersion objective using 350 ± 40 nm excitation and 445 ± 25 nm emission for DAPI, 470 ± 20 nm excitation and 525 ± 25 nm emission for GFP, and 560 ± 20 nm excitation and 630 ± 37.5 nm emission for AlexaFluor 594. Z stacks were kept the same thickness throughout the imaging, with 12 slices at 250nm per slice. This enables the cytoplasmic portion of the cell to be fully scanned for further analysis with Imaris software (Bitplane).

2.3-b) Confocal live cell imaging for cell culture.

For live-cell imaging, cells grown on 40mm diameter glass cover slips were placed in a Perfusion Open-Closed (POC) chamber (PeCon GmbH, Erbach, Germany) before mounting on the microscope in a heated stage at 37 ºC. Confocal-fluorescence imaging was carried out on a Zeiss LSM 510 META confocal microscope, using a 63x, 1.4 NA oil-immersion objective, with GFP excited at 488 nm and emission collected between 495 and 535 nm, and Cy3 excited at 543 nm and emission collected between 555 and 650 nm. Using the LSM image browser software provided with the microscope, cells and regions of interest were cropped from the x63 image, and the timeframe option was used to select the times between each image taken. Images were taken using the pinhole set at 1, an arbitrary unit that allows the most realistic depth of image, whilst restricting most of the light scatter from other regions of the cell during scanning. Each scan per channel used bidirectional scanning of each pixel 4 times. This reduced the time taken per scan by around half compared to one-directional scanning. Each channel took

around 8 seconds to scan fully per time point, with the time taken between each photo adjusted for the time taken to scan each image.

2.3-c) Microscopy of crypt samples.

Immunostained crypt samples were imaged by confocal microscopy using a Zeiss LSM510 META microscope. For each crypt, the x63, 1.4 NA oil-immersion objective was used. 0.7x zoom images were taken of the crypt from the base to the top, and a 4x zoom performed on a specified region per crypt. Channels used were 488 nm and emission collected between 495 and 535 nm, and Cy3 excited at 543 nm and emission collected between 555 and 650 nm, Cy5 excited at 640 nm and collected at 670nm. An UV laser was used for Hoescht, which excites at 350nm and is collected at 470nm. A Differential interference contrast (DIC) objective was used to enhance contrast of the unstained channel, collected with the 488nm laser. Specific gains for each channel were taken at around 700 to 800, and the pinhole set to one for all channels for the most optimum depth of image for all channels to relate to each other. Each scan per channel used bidirectional scanning of each pixel 4 times. This reduced the time taken per scan by around half. Each channel took around 8 seconds to scan fully at a 0.7x zoom.

2.3-d) Live cell imaging of crypt cultures.

Cells were cultured on 18mm glass cover slips and transferred to an 18mm POC chamber for live cell imaging of crypts. 18mm glass cover slips were imaged by confocal microscopy using a Zeiss LSM510 META microscope. For each crypt, the x63, 1.4 NA oil-immersion objective was used. 0.7x zoom images were taken of the crypt from the base to the top, and a 4x zoom performed on a specified region per crypt.

Table 6) Excitation and emission of fluorescent probes.

Fluorescent label	Excitation (nm)	Emission (nm)
DAPI	350	-470
Hoescht	346	460
RFP	584	607
GFP	488	507
AlexaFlur 488	495	519
Alexafluor 594	591	618
Lysotracker Red	577	590

2.4) Imaris Software

2.4-a) Puncta number analysis

Microscope images containing scale information (.lsm,) were analysed with the Imaris package (BITPLANE). Within the surpass section of the software, the spot function was used to identify and measure the diameter of fluorescent puncta. A general diameter of an autophagosome was deemed 0.5μm, and this could be used to allow the software locate any regions of the fluorescent image that come close to this measure of fluorescent intensity for the fluorescent channel being analysed. Once Imaris has found regions of the fluorescent image that correspond to this crude diameter measurement, we measured diameters so that each puncta is given its own size. This can be done with relative intensity, which fine-tunes autophagosome sizes due to the intensity of signal where there is strong signal (puncta) to weak signal (no fluorescence/background fluorescence). Typically, regions where spots are found account for around 1% of the total pixels within an image. The numbers for diameter could then be exported and used

for later analysis. The rendered images of the puncta generated from Imaris analysis could be coloured according to diameter on a graded scale with a diameter of 0.1 μm being blue, and anything 1 μm and above being coloured red. This gave the greatest appreciation of the spread of data for autophagosome puncta across all datasets.

2.4-b) Tracking of puncta.

For timelapse fluorescent videos, once spots have been made, an option to track spots over time was used. By selecting autoregressive motion, and choosing 2μm maximum distance of a puncta between channels, a spot could be tracked. By specifying that a spot can move out of frame for 3 frames, tracks could be more clearly followed also. Autoregressive motion took into account the movement of the puncta in the previous and next frames, so this discounted the effect of two spots at the same point in a frame of a timelapse. If Brownian motion was selected, there is was predicted direction of movement, thus more errors could be made. If a spot did not get tracked over the full timelapse by doing this (for example if a puncta jumped a large distance compared to the few frames previously) tracks could be joined after the analysis is finished so that one puncta was tracked. Either vesicle distance (μm) or duration (seconds) were used from this analysis.

2.4-c) Colocalisation

After a spot had been rendered, to check if any other fluorescent signals of a different channel were colocalising with this channel, a filter could be added to the spot function after the spots have been generated (2.4-a). This allows for the software to analyse the fluorescent signals at the region where a spot has been rendered, discounting the fluorescent signal in the rest of the cell. The colocalisation filter was obtained after spot

generation, by selecting the intensity of the second fluorescent channel of interest in the filter section of the final spot analysis. Any rendered spots which had a high level of colocalisation with the second channel, were highlighted by the software. A sliding scale of fluorescence was used in a similar way to generation of spots, but this fluorescence scale was associated with the levels of fluoresence at the point of the fluorescent image where the spot has been generated. The colocalised spots could be made into a separate spot channel, so the user could export numerical data about those co-localising spots within a fluorescent image.

2.4-d) Surfaces

For larger or irregular shaped signals such as nuclei, surfaces were used to render over a fluorescent signal using Imaris. This option is under the surpass menu of the Imaris software, but by choosing the fluorescent channel to analyse, this option rendered a surface onto the fluorescent image, not a spot. A size restriction was chosen, and was dependent on the signal analysed, with larger sized structures needing a larger initial size for the software to search for surfaces. For example, if nuclei within an image were all around 10μm, the user would need to add that to the software so surfaces of that size, of the fluorescent channel they were analysing, could be found. This was used for nuclei rendering, and was not used for generating numerical data on size within the experiments displayed.

2.4-e) Statistics

Analysis of the spread of the data between cells in each starvation condition was performed with a standard deviation across the Imaris outputs for diameter and number across cells. Numbers +/- a mean number within results (eg 1 +/- 0.2) were

indications of the +/- the standard deviation around the mean number. Percentages above 0.75μm were taken as an overall percentage of the numbers of vesicles within each group which had diameters the same as, or above this diameter. Student T-tests were used to check significant differences between starvation conditions, with a 95% confidence used (p=0.05) to determine significance. Graphically, p=0.05 = *, p=0.005 = **, and p=0.0005= ***, with this scoring system displayed above graphs.

Chapter 3:

Development of methods to quantify autophagy using fixed cell and live cell microscopy.

Chapter 3 - Development of methods to quantify autophagy using fixed cell and live cell microscopy.

3.1) Aims

The aims of this chapter are to describe ways in which we can use Imaris software to quantify autophagy through analysis of fluorescent images obtained by microscopy. The main protein of interest is the major structural protein of the autophagosome, LC3, but as we are quantifying vesicles, the methods can be generalised to other autophagy proteins such as WIPI2, and SQSTM1. LC3-II is bound to autophagosome membranes at all points in the pathway up to delivery to lysosomes, and is an accepted tool to monitor autophagy (Wu *et al*, 2006, Klionsky *et al*, 2005). Alternative methods include western blot analysis of LC3 to identify induction of autophagy by analysing the ratio of LC3-I (cytosolic) and LC3-II (membrane-bound) or turnover of SQSTM1/p62 (Mizushima *et al*, 2004, Pankiv *et al*, 2007). Unfortunately, these last two methods cannot be applied to human biopsy because there is insufficient material in the sample. This section describes the use of IMARIS software to represent LC3 puncta as 3D rendered spots. The rendered spots can be then used to give measurements of numbers of autophagosomes present within the cells, their diameters and relative levels of colocalisation with other proteins. The resolution of light in an optical microscope is approximately 0.2-0.25μm, thus resoltuion of separate autophagosomes is possible in the size ranges shown previously (Mizushima *et al*, 2002). If two autophagosomes are directly next to each other at less distance than the resolution limit, they will appear as one structure with optical microscopy (Millar et al, 2004). The overarching aim is to generate digital datasets that are amenable to statistical analysis so that autophagy can be quantified under different conditions and in different tissue samples.

3.2) Analysis of LC3 puncta

LC3 distribution can be tracked by immune staining of endogenous LC3 or by following GFP-LC3 by fluorescence microscopy. Immunostaining for endogenous LC3 is shown in Figure 3.1 A-D, which compares HeLa cells (Fig3.1A), MEF cells (Fig3.1B), Caco2 cells (Fig3.1C) and Vero cells (Fig3.1D). In each case cells were incubated in nutrient media (i), or with HBSS for 4 hours (ii). Regions of interest (ROI) are boxed and shown at high magnification in the quadrant below each image. Similar analysis of CHO cells stably expressing GFP-LC3 is shown in Figure 3.1E, while Figure 3.1F shows Vero cells transduced using an adenovirus expressing GFP-LC3. In each case, the bulk of the LC3 signal was diffuse and located to the cytoplasm with LC3b staining, and both cytoplasmic and nuclear with GFP-LC3 expression when cells were incubated in nutrient media, and punctate LC3 staining, indicating formation of autophagosomes was induced when cells were starved for 4 hours in HBSS. Figure 3.2 shows imaging of separate live Vero cells transduced with GFP-LC3 and either kept in nutrient media containing amino acids (Figure 3.2A), or starved in HBSS for 4 hours (Figure 3.2B). Again, starvation for 4 hours long, induced LC3 puncta indicating increased numbers of autophagosomes, compared to when cells were kept in nutrient media containing amino acids.

3.3) Pixel density measurements of LC3 puncta provide a quantitative analysis of autophagosome formation

Imaris software from BitPlane was used to analyse pixel densities in LC3 puncta. Imaris is a software package that allows the user to create a representative 3D model (hereafter termed a 'render') of a fluorescent image. For live cell experiments of autophagosomes, this render can also be tracked over time. Pixel densities represent

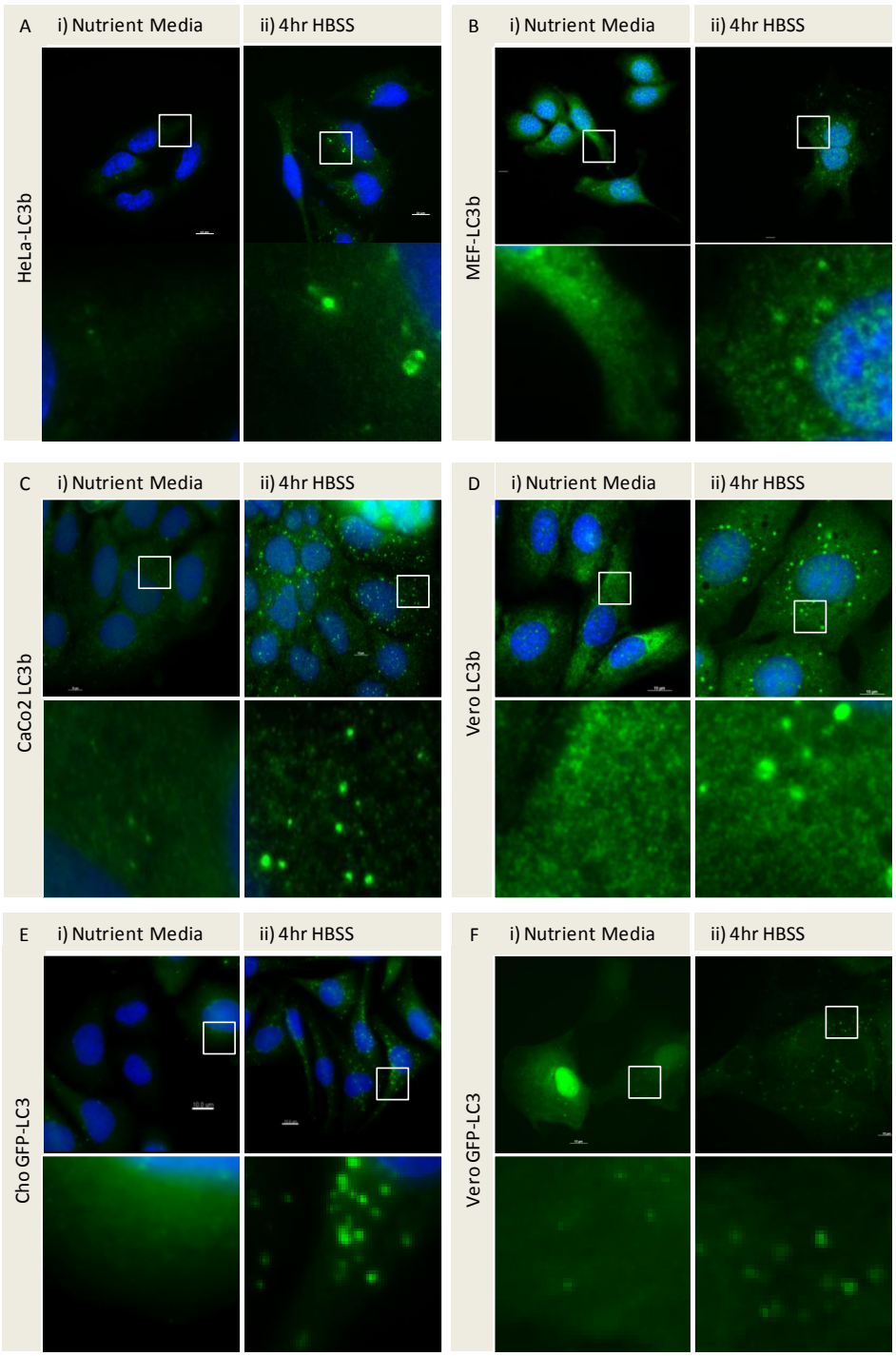

Figure 3.1 - Immunostaining of autophagy protein LC3 in tissue culture cell lines. Cells were incubated in nutrient media (i) or starved for 4 hours in HBSS (ii). Cells were then fixed and permeabilised and incubated with DAPI (Blue) to show nuclei. The top panels show fluorescence images taken at x63, with regions of interest (ROI) indicated by the white box. The lower panels show digital zooms of the ROI. The HeLa cells (A), MEF cells (B), CaCo2 cells (C), and Vero cells (D) were fixed and immunostained for LC3B (green). GFP fluorescence was detected in CHO cells stably expressing GFP-LC3 (E), and Vero cells transduced with an adenovirus expressing mammalian GFP-LC3. All images were taken with a Zeiss Axiovert upright microscope. Scale bars = 10µm.

digital data sets that can be analysed numerically to compare responses between individual cells and between populations of cells analysed in different experiments.

3.3-a) Spot selection using 'Spot Function'.

Figure 3.3 indicates how rendered spots can be generated from fluorescence images of autophagosomes within cells starved for 4 hours. The Figure gives examples of how parameters are set by the user to calculate the correct spot size to aid the software in finding spots in this fluorescent channel. Figure 3.3Ai indicates a fluorescent image of endogenous LC3B staining in Vero cells at 4 hours of starvation, with a zoom showing autophagosomes more closely in Figure 3.3A-ii. In Figure 3B-E fluorescent puncta are analysed using the 'Spot function' in Imaris. The software interface is shown on the left and the annotation of puncta is shown on the right as an x63 image (i), or as a zoom of selected autophagosomes (ii). The annotations are generated after searching for spots using the size parameters set in the left software box. If a size much smaller than that of the autophagosomes is selected, in this case 0.1μm diameter, the Imaris software over estimates the number of puncta (Figure 3.3B-i) with the zoom image in white indicating all signal is shown as a spot, not representing the spots visible in the fluorescent image (3.3Bii). When the spot size for detection is set too large to be an autophagosome, (Figure 3.3C) in this case 6μm , only the largest spots are detected (Figure 3.3C-i), and many puncta are missed, as indicated in the zoom (Figure 3.3C-ii). However, when an intermediate spot size for detection is used (for autophagosomes 0.5 μm (Figure 3.3D) to 0.7μm (Figure 3.3E), digital 'spots' are only visible within the autophagosomes seen within the fluorescent image. The software then allows you to restrict the spot parameters through trial and error to those where fluorescent puncta present within

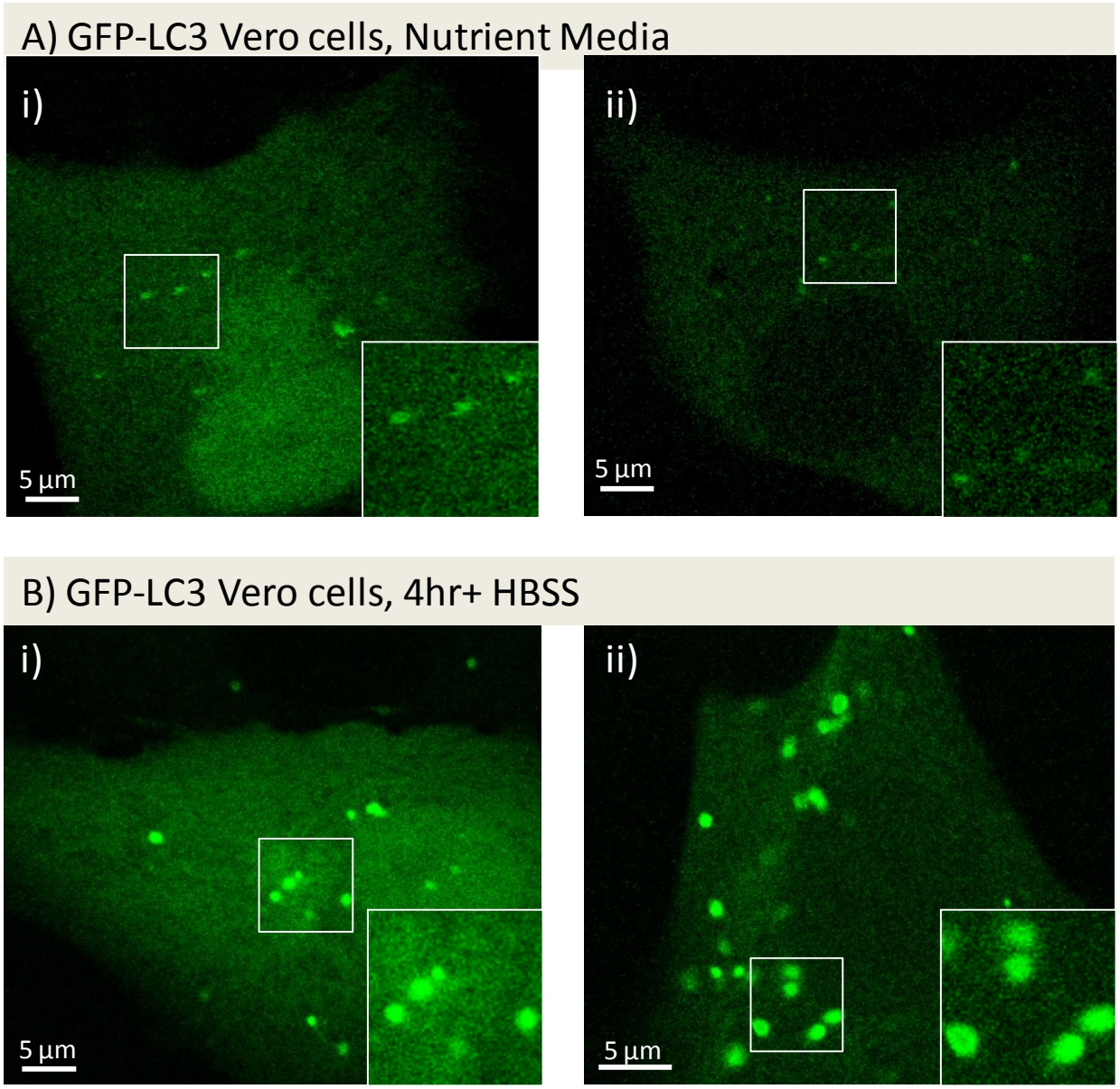

Figure 3.2 - Live cell imaging of Autophagy using Adenoviral transduction of GFP-LC3. Vero cells were transduced with an adenovirus expressing mammalian GFP-LC3, shown in green, and incubated in nutrient media overnight before being incubated in nutrient media (Ai, ii) or starvation media HBSS for 4 hours (Bi, ii). Zooms of ROI's are shown for each image. Images were taken with a Zeiss LSM confocal microscope with a x63 objective. Scale bars=5µm.

the image are identified, and the background signal is blank. Figure 3.4 shows the second method of restricting the Imaris spot analysis to help find a suitable number of rendered spots. The line graph taken from the software package is displayed to the top of every image in Figure 3.4, and represents the intensity of fluorescence in the image.

Peaks further to the right of the line graph are associated with the autophagosomes of strongest intensity, showing as single peaks, whereas the peaks in the far left of the line graph always produce rendered spots which associate inaccurately with background signal of the fluorescent image. Figure 3.4A shows that when the spot detection is restricted to only those in the far right region of the line graph, not all spots seen in the fluorescent image are found. In contrast, Figure 3.4B shows that when you allow more of the intensity to be analysed by Imaris, spots are picked up where the fluorescent signal is not associated with an autophagosome. By choosing a region in-between these two contrasting levels of intensity, spots are visible only where autophagosomes are present in the fluorescent image (Figure 3.4C).

3.3-b) Vesicle rendering using the 'surface border function' to generate different spot sizes.

Once spots have been identified the software can render pixels to provide a surface to the puncta that allows diameters to be calculated. The aim of this process is to set the border between the cluster of pixels that represent the fluorescent puncta and background fluorescence. Figure 3.5A indicates selection of a region of interest, which contains fluorescent puncta. In Figure 3.5B fluorescent puncta are analysed using the 'Render function' in Imaris. The annotation of puncta with white pixels is where borders of the fluorescent puncta are compared to the background signal, and produce rendered puncta, which contain numerical data associated with its corresponding fluorescent image. The rendered spots are shown to the right of each fluorescent image from 3.5Bi-iii, where the final decided upon spot border is shown in 3.5Biii. By using local contrast, the software can differentiate puncta less than 0.3 μm in diameter, green those of about 0.5μm, and red puncta 1μm or more in diameter. To the far right of each row is a higher

magnification of render. Figure 3.5B-i shows that when spot detection is restricted to puncta of high intensity to the right of the line graph, the border between puncta and background is set too high

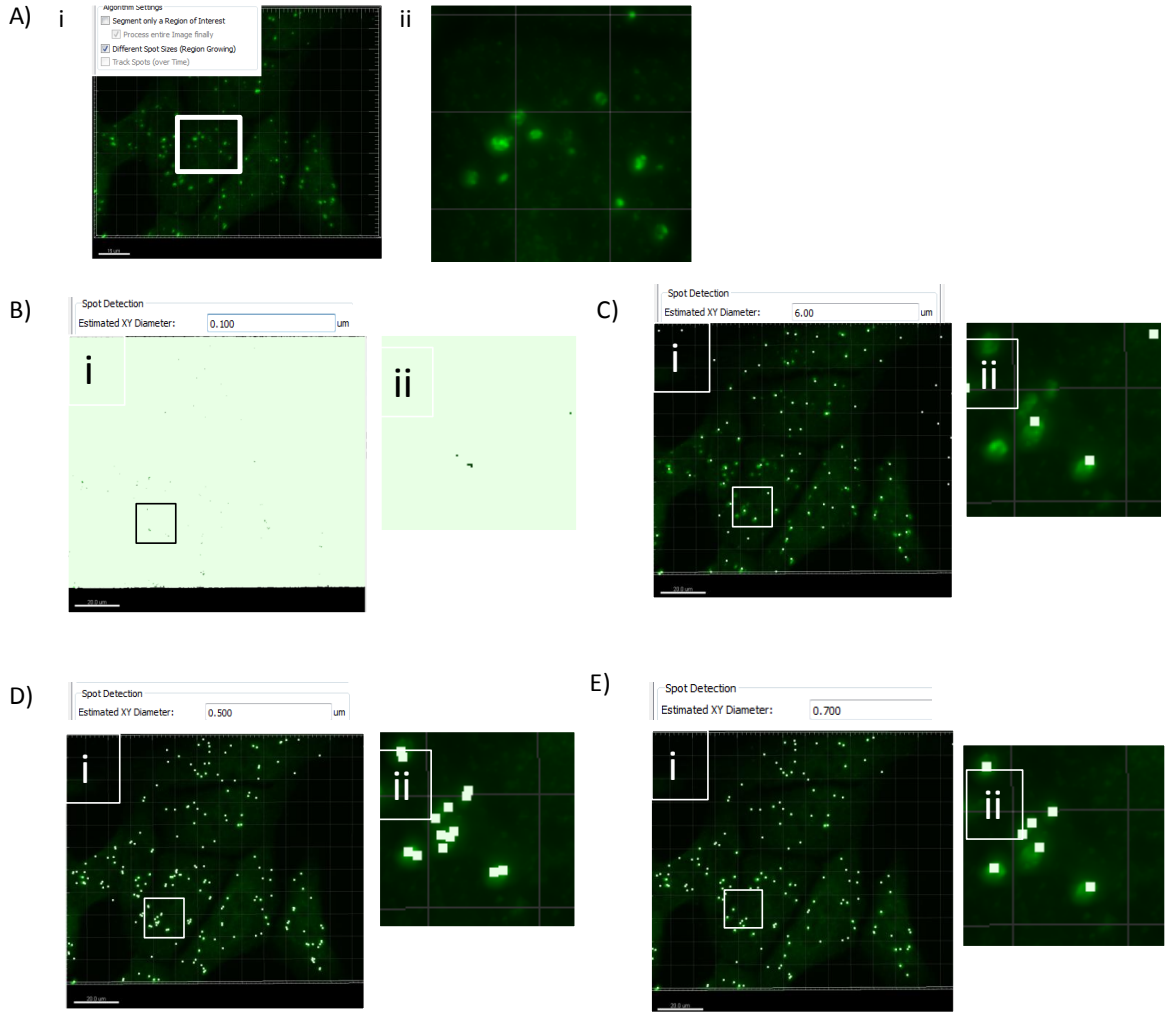

Figure 3.3 - Use of the 'spot selection' function in Imaris to analyse LC3 puncta. Panel A shows the fluorescence signal from endogenous LC3 staining of Vero cells starved in HBSS for 4 hours (Ai)**.** The region of interest is shown at higher magnification in panel Aii. **Panels B-E** show how the same image can be processed in different ways. Each panel shows the Imaris software window on the left, indicating the size of signal the software will search for. The central image (i) shows the signal after the software has attempted to find spots, with a zoom of the same region in each panel shown on the right hand side (ii). **Panel 3B** shows the spot detection set at 0.1µm. **Panel 3C** shows the spot detection set at 6 µm. **Panel 3C** shows the spot detection set at 0.5 µm and **Panel 3D** shows the spot detection set at 0.7 µm.

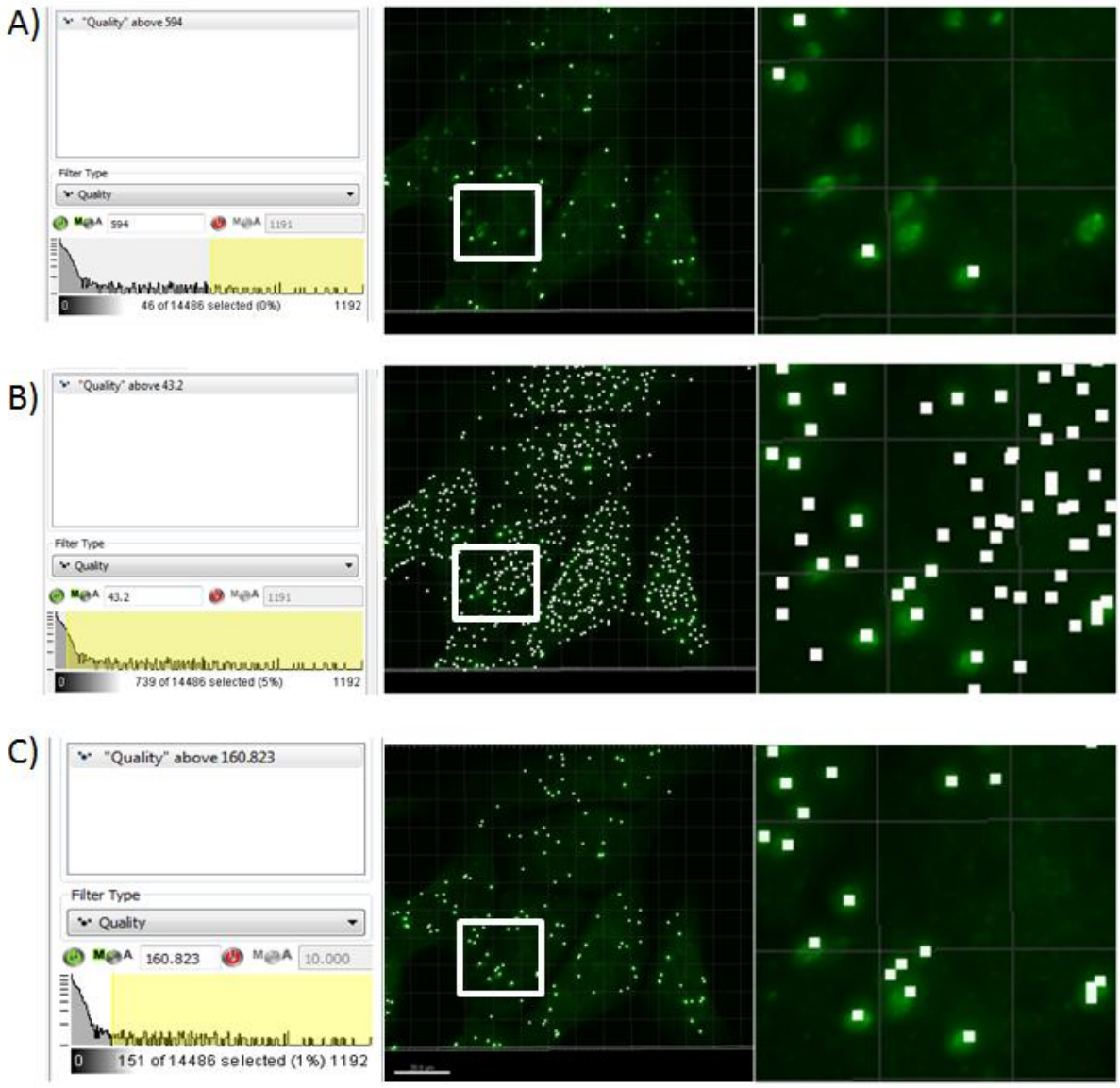

Figure 3.4 - Refining the use of the 'spot selection' function in Imaris to analyse LC3 puncta. The left hand of each panel shows the Imaris software indicating the fluorescence signal as a line graph of the pixel densities detected in the image seen to the right. In **Panel A**, the signal chosen for spot detection is restricted to the right of the line graph. The digital zoom show the spots found in this instance with a white square overlay. In **Panel B** the signal chosen for spot detection extends towards the left of the line graph. **Panel C** shows analysis after an intermediate region of the line graph is used for spot detection.

. Many spots seen in the fluorescent image fail to be identified and the border, identified by white pixels superimposed over the digital fluorescent image (green), which to reach the edge of the puncta. When this information is used to generate a rendered image there are low numbers of small diameter (blue and green) puncta. In contrast, Figure 3.5B-ii shows that when the intensity selection is set too low the white pixel spots extend beyond the perimeter of the puncta (green) and are found within the background fluorescence. All puncta appear large (red) in the rendered image. By choosing a region in-between these two contrasting levels of intensity (Figure 3.5B-iii), spots are located to fluorescent puncta and extend to the perimeter of the puncta. They do not move into the background fluorescence and are only present in the fluorescent image.

3.4) Tracking fluorescent puncta during live cell imaging.

Spot detection and rendering can be applied to analysis of images taken during timelapse microscopy of cells expressing GFP-LC3 to visualise autophagosomes. Again, the user is given options to allow the software to track rendered puncta over time. To begin tracking, autoregressive or Brownian motion can be used to assess the movement of vesicles in the fluorescent image. Brownian motion allows the software to detect random movement, and autoregressive motion allows the software to see movement of spots in a direction, by comparing the spot in relation to spots nearby in previous and later frames of the video. Figure 3.6A compares autoregressive (ii) and Brownian (iii) motion using the same movement restrictions on a live cell video of GFP-LC3 puncta in Vero cells. This shows that the autoregressive motion parameter can keep track of

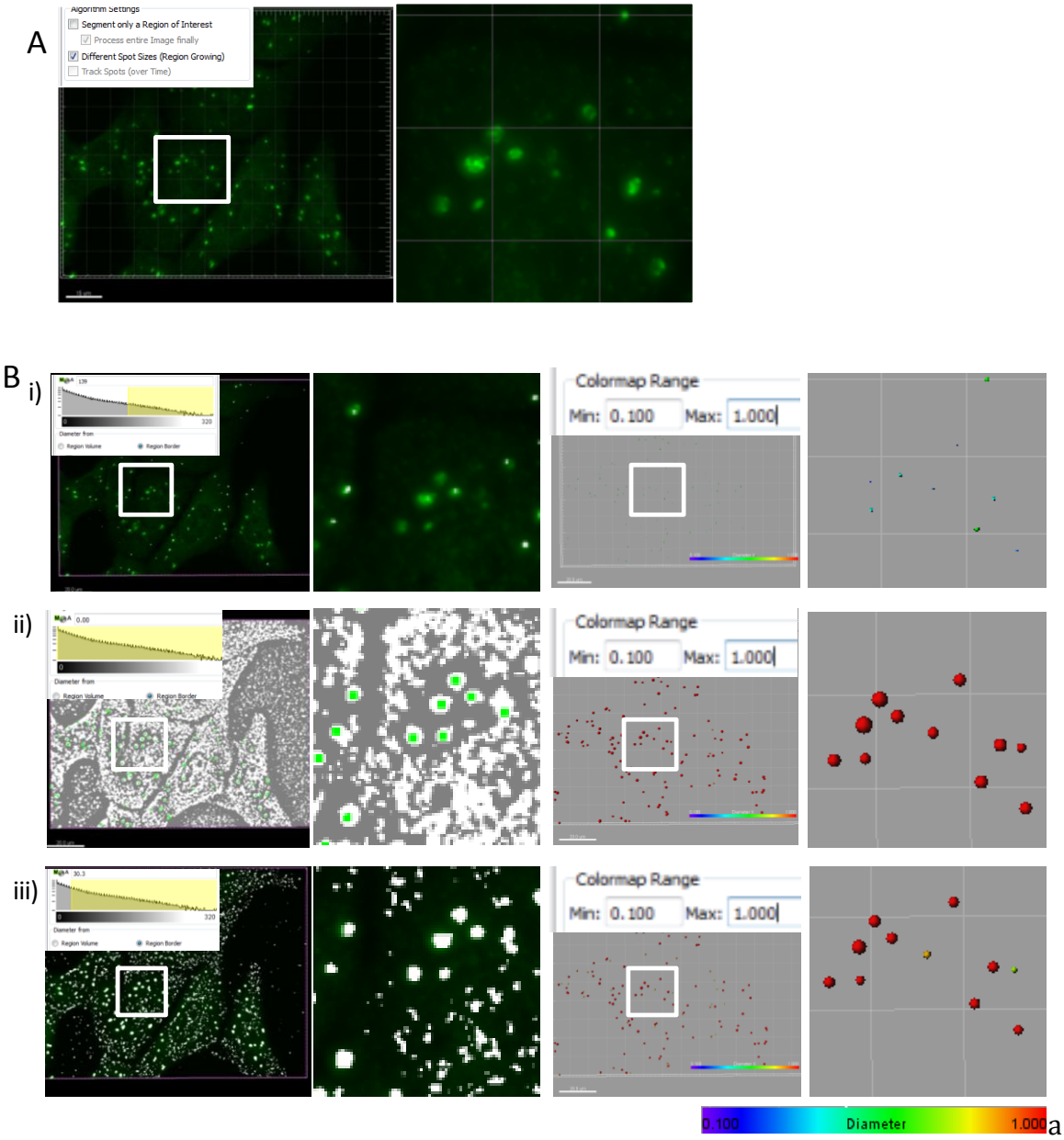

Figure 3.5 - Rendering LC3 puncta by generating appropriate spot borders. Panel A shows a x63 fluorescence image taken from Vero cells starved for 4 hours in HBSS and immunostained for LC3B. The region of interest is presented as a digital zoom on the right. **Panel B** shows how the software is used to set spot borders and the same image is used for each analysis. The software box is shown in the top left of the first image in each series and a digital zoom of a region of interest (white box) is shown in the second image. The third and fourth images show corresponding rendered images. The rendered spots are colour-coded using heat maps so the smallest spots are blue (0.1µm), mid-sized spots (0.5 µm) are labelled green, and larger spots (0.75-1 µm) are labelled yellow, orange and red. **Panel B-i** shows an example where the border is set small and all puncta are blue. In **panel B-ii** the border is set wide and puncta are red regardless of size. **Panel B-iii** shows the rendered spots generated when an intermediate region of the fluorescence intensity graph is used to generate rendered spots.

movement of the vesicles whereas the Brownian motion parameter loses the track after short time. If the track function fails to follow the pathway of movement, the software allows the user to join tracks.

In Figure 3.6B, a track is lost for one vesicle between frame 1(3,6B-i) and 2 (3.6B-ii), but then joined in frame 3.6B-iii to extend the duration of tracking so the track is representative of the vesicles movement. Tracking puncta between frames requires the user to select restrictions on the greatest distance vesicles can move between frames (Figure 3.7). If this were not restricted the software would connect all puncta between frames. In Figure 3.7A, spot distance is set at 0.2μm (Figure 3.7A-i) or 20μm (Figure 3.7A-ii) for tracking puncta, with the lines overlaying the fluorescent image signifying the movement of a vesicle, as predicted with Imaris software. When movement is restricted to 0.2μm, no track is added to the vesicle, indicating that Imaris has not calculated spot movements using this distance. When the distance between frames is made too large at 20μm, aberrant tracks appear at right angles to the direction of travel (arrow heads), thus, movement has been added that is

not from the vesicle present in this region of interest. Figure 3.7A-iii represents a track when the maximum distance is kept at 3μm and tracking continuity is maintained, representing the movement of the vesicle within this region of interest. This number fits in with predicted 3μm/10 second distance travelled calculated previously for movement of autophagosomes via microtubule association (Fass *et al*, 2006).

Figure 3.7B shows how the user can edit the fluorescent track by changing the period of time (gap size) before the software considers that the object has disappeared or before a new track is given to the vesicle. This option allows a vesicle to go out of frame for a number of images in a timelapse and then be recovered. When no gap size selected, the

track can sometimes appear shorter than the actual movement of the vesicle (Figure 3.7B-i), and when the gap size is too large (20 images in succession in a timelapse), too many tracks are seen, because the software is unable to differentiate accurately between spots in the video (Figure 3.7B-ii, arrows). When a maximum gap size is set at 1 frame, the track lasts the lifetime of the vesicle.

3.5) Analysis of protein colocalisation using Imaris software.

After spots have been rendered and tracked with Imaris software, colocalisation analysis can be performed on fluorescent images taken from different fluorescent channels. LIR protein p62 (Chapter 1.5) facilitates the delivery of ubiquitinated proteins to autophagosomes (Pankiv *et al*, 2007, Bjørkøy *et al*, 2009) and an analysis of the degree of co-localization between SQSTM1/p62 and LC3 can be used to see if autophagosomes take up autophagy cargoes. The fluorescent image used in Figure 3.8 A-C is displayed firstly as single channel images of LC3B (A: green 454nm), SQSTM1 (B: red 588nm) and a merge of both (C). All images also contain the nuclear stain DAPI to show the different cells in the image. Rendered fluorescent puncta (as previously described for Figures 3.3-3.5) are shown in Figure 3.8 D-F. The statistical information on the degree of co-localization can be determined by searching for rendered vesicles, which contain fluorescence signals from the other channel the user is interested in. The 'filter option' of Imaris checks the fluorescence intensity of another channel within the rendered puncta it has already found. For example, Figure 3.8, Panels G, H and I show puncta that have been allocated as colocalised (yellow) with the other fluorescent channel. The merged image (I) displays a representative rendered containing yellow colocalised puncta

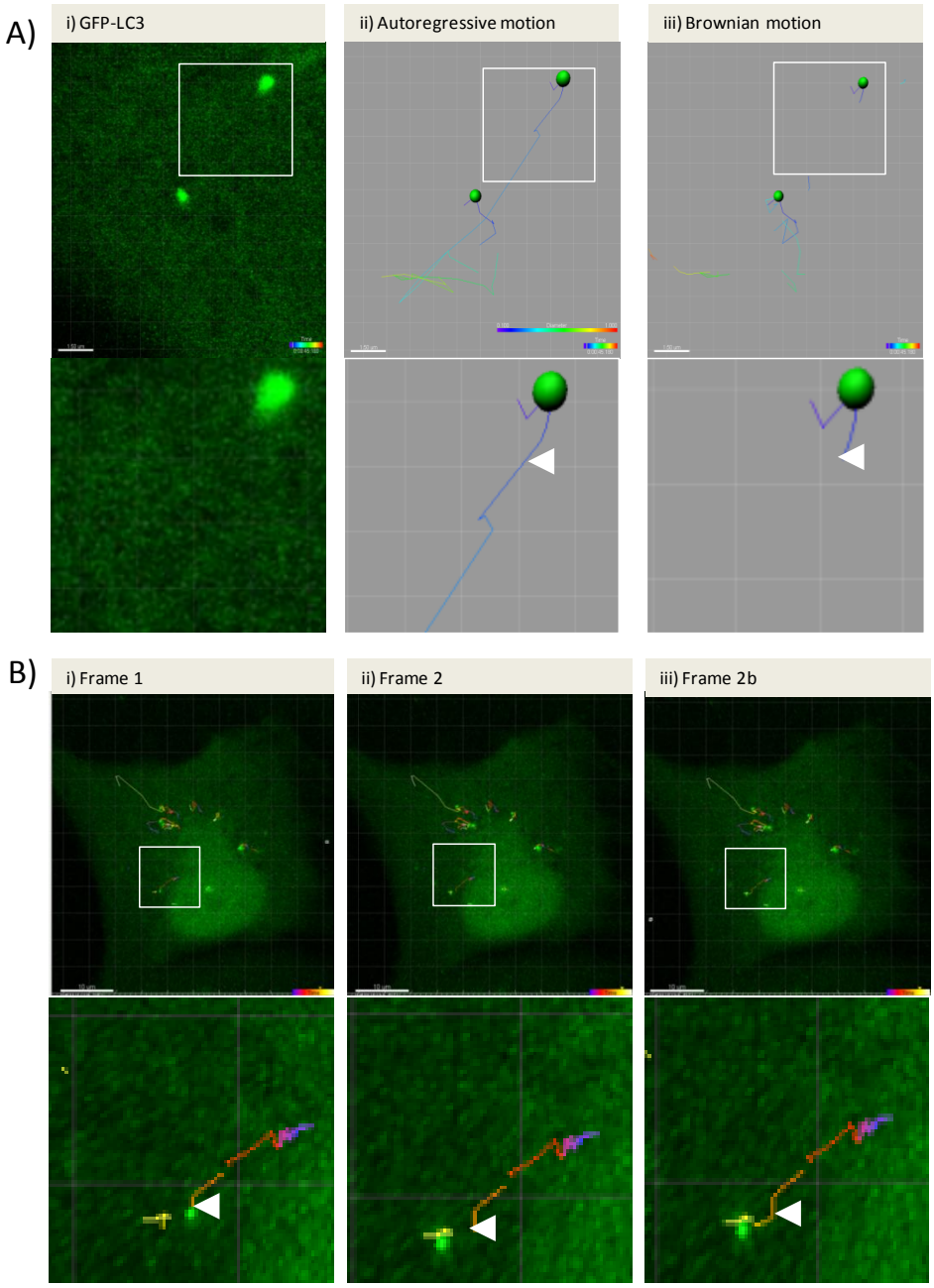

Figure 3.6 - Tracking GFP-puncta during live cell imaging. Vero cells were transduced with GFP-LC3 adenovirus and imaged by live cell imaging confocal microscopy. Time lapse images were collected. **Panel A-i.** Fluorescence signal from GFP puncta at the start of the time lapse with a digital zoom of region of interest shown below. **Panel A-ii** shows the image rendered using Imaris and tracked through the time lapse with autoregressive motion feature. The track is shown by the blue line (arrow head). **Panel A-iii** shows the rendered image tracked through the time lapse with Brownian motion feature. **Panels Bi-iii** track specific GFP puncta with autoregressive motion. The tracks are superimposed over the fluorescence image and colour coded with a heat map so the start of the track is blue and the end red. The tracks in frame 1 (**Bi**) and frame 2 (**Bii**) have been joined in frame 2b (**Biii**).

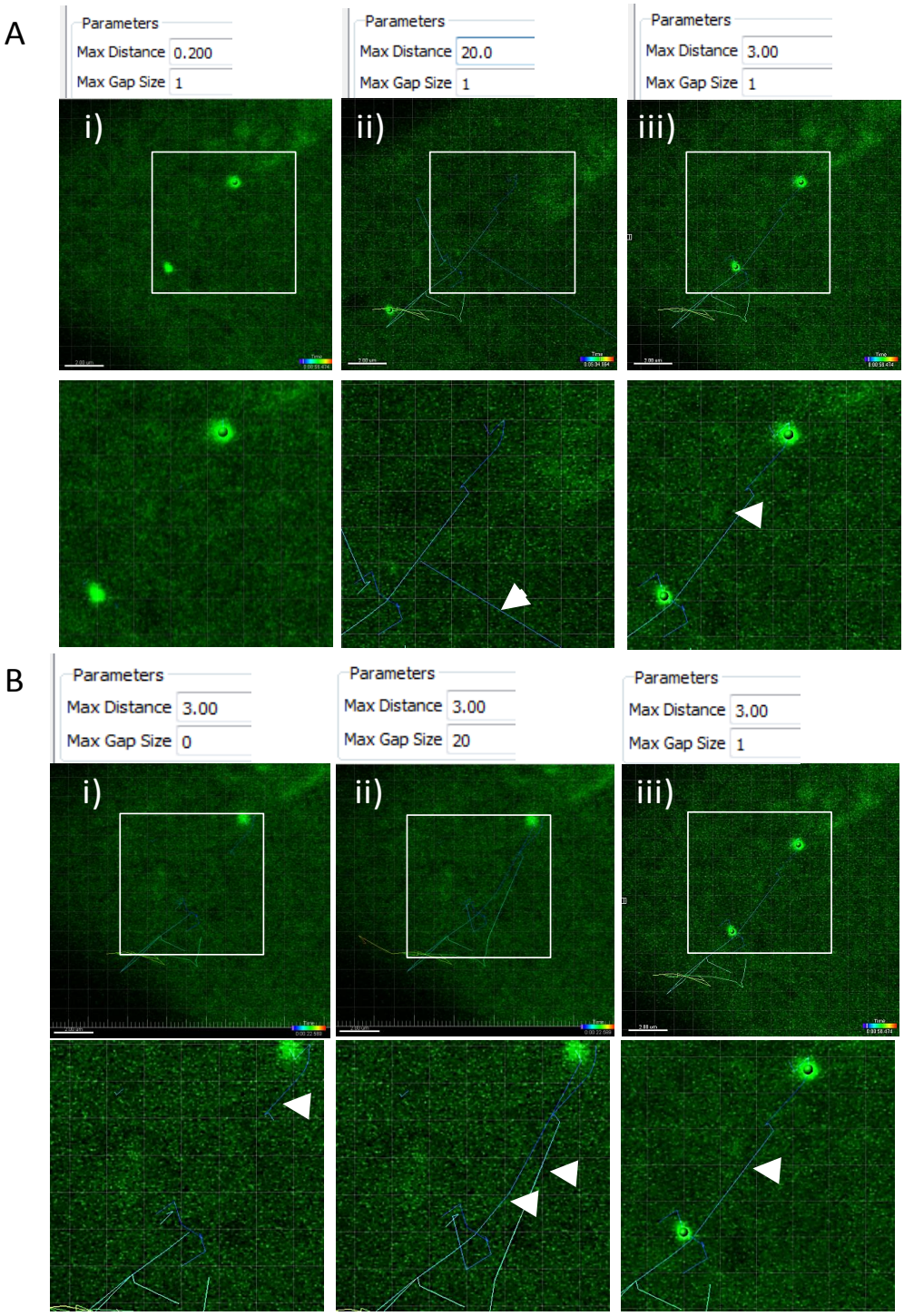

Figure 3.7 - Editing tracks by changing the maximum distances and times tolerated between images in a timelapse video. GFP puncta were imaged in Vero cells transduced with adenovirus expressing GFP-LC3. GFP puncta were tracked through the time lapse series and the fluorescent images, with the lines overlaying the fluorescent image indicating the predicted movement of a puncta tracked by Imaris. The Imaris software box showing the parameters set appears above each image. **Panel A.** Adjusting distance tolerated between frames. **Panel Ai** shows the track distance set at 0.2µm. **Panel Aii** shows the track distance set at 20µm, and Aiii shows the track distance set at 3µm. **Panel B.** Adjusting the time tolerated between frames. **Panel Bi** shows the track when the gap size is 0 frames. **Panel Bii** shows the tracks present

when the gap size is 20 frames, and **Panel 3Biii** shows the tracks present when the gap size is 1 frame. Scale bars = 2µm.

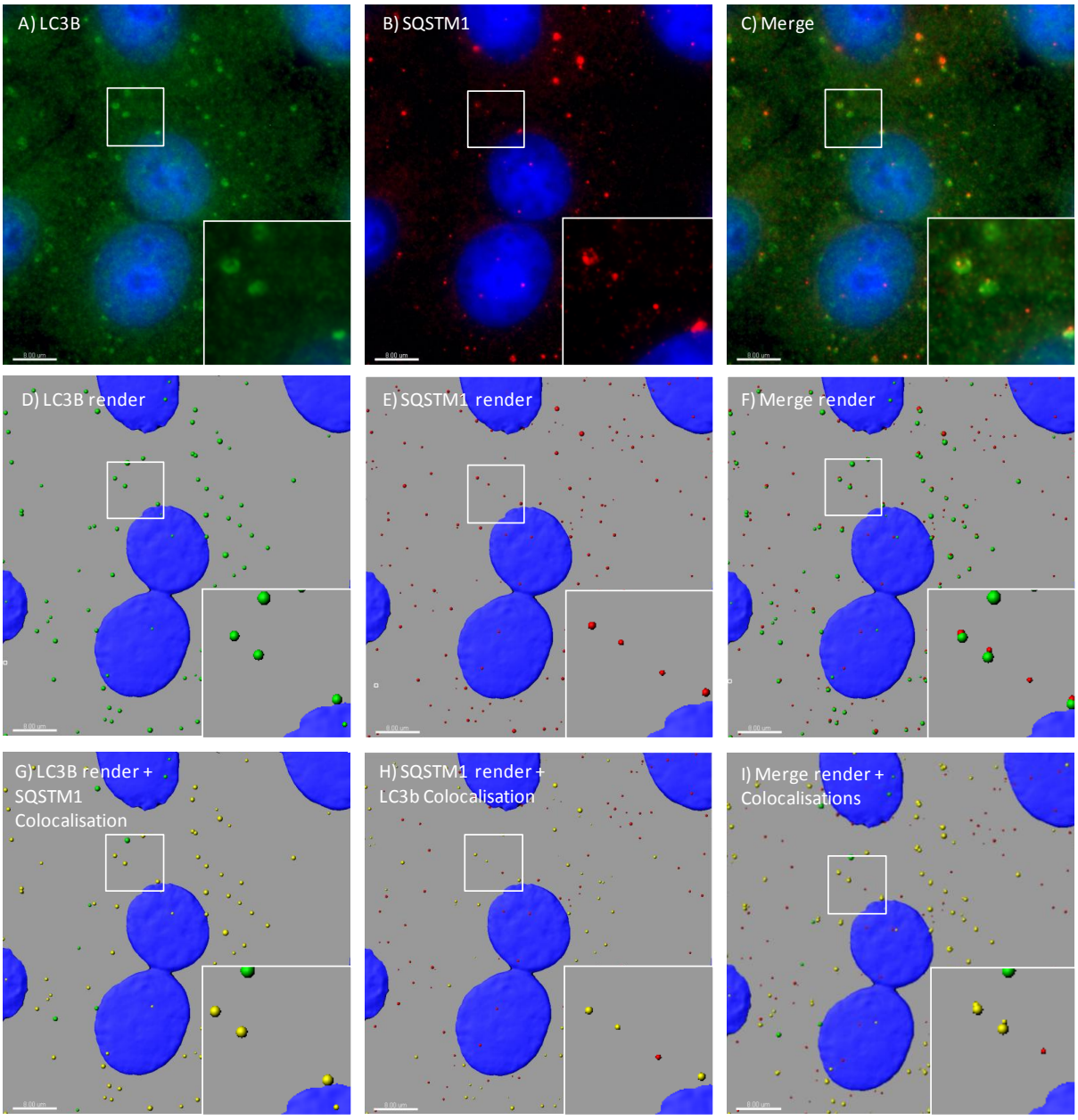

Figure 3.8 - Assessing colocalisation between two fluorescent signals using Imaris. Vero cells starved in HBSS for 4 hours were immunostained for LC3B in green **(A)** and SQSTM1 in red **(B)**, with the merge shown in **C**. Nuclei were also stained with DAPI in blue. **Panels D-F** show corresponding renders of spots generated from fluorescence signals. The renders of corresponding merged images are shown in **panels G-I** with colocalised pixels indicated in yellow after filtering for high levels of fluorescent signal from the reciprocal immuno stain. Scale bars = 8µm.

3.6) Summary

The figures displayed here show the use of the image analysis software, Imaris, to successfully analyse the puncta seen by targeting the autophagy protein LC3B, and associated autophagy markers, within starved cells. We have previously used this to quantify autophagosome number and size in a paper by Berryman *et al* (2012). By assessing many different cell lines we could see that autophagosomes within cells appeared more numerous, and larger across all cell lines when starved for 4 hours compared to nutrient media, regardless of if the cells were immunostained for LC3B, or expressing GFP-LC3. We found that when restricting the software to only search for strong fluorescence, we could find the correct number of autophagosomes present within a fluorescent image. Again with realistically assessing the fluorescent image at all times, and choosing borders around the fluorescent puncta that represent the sizes shown in the fluorescent image, we could generate numerical data on sizes of autophagosomes. The GFP-LC3 signal used to mark autophagosomes in live cell imaging could also be tracked, which will again allow for generation of datasets on distances moved and lifetimes of vesicles seen in time lapse microscopy. The editing shown here to change the distances a spot can move, and allowing for tracks to be joined after they are generated, gives this flexibility to generate a representative dataset. Editing of the spots generated can also mean colocalisation analysis could be performed. The analysis displayed here means that number of autophagosomes interacting with other autophagy signals, here SQSTM1, means that this can be explored further in a more intricate autophagy assessment within cells by starvation or other autophagy inducing conditions.

Chapter 4:

Quantitative analysis of autophagosomes formed during starvation.

Chapter 4 - Quantitative analysis of autophagosomes formed during starvation.

4.1) Aims

The aims of this chapter are to generate digital datasets from LC3 puncta to provide a quantitative analysis of LC3 puncta formed during a starvation time course.

4.2) Use of LC3B as a marker for autophagosomes.

In the mammalian Atg8 family, there are 3 forms of LC3 (LC3A, B and C) which localise to autophagosome membranes during starvation. These are all expressed within mammalian cells (He *et al*, 2003). All forms localise to the autophagosome membrane, after being cleaved at the C terminus (LC3-I), and conjugated with phosphatidylethanolamine (LC3-II). LC3B antibody staining was chosen for this study because is the most widely used for tracking autophagosomes generated during starvation. The use of antibodies directed against LC3B during starvation has been shown to convey the best LC3 I to LC3II conversion by western blot. LC3B also shows increased LC3B puncta after starvation by immunostaining (Klionsky *et al*, 2008). The rat sequence of LC3B was used to generate GFP-LC3 for live cell imaging.

4.3) Live cell analysis of autophagy and autophagosome lifetime

Early research into autophagosome dynamics indicated that vesicles could last around ten minutes. This was found using electron microscopy images of insulin treated mice, and seeing the decrease in autophagosomes over time. The half-life of the drop of vesicles was termed the lifetime of the autophagosomes present (Pfeifer *et al*, 1978). More intricate forms of analysis of autophagosome lifetime have been performed using fluorescent microscopy of GFP tagged LC3. Using GFP-LC3 transgenic mice, where GFP-LC3 is expressed within all cells of the mouse, Mizushima *et al* (2004) observed starvation induced autophagy within cells from the liver, muscles and pancreas.

Pancreas cell-derived autophagosomes increased in size and number during 24 hours of the mouse starving. The work also served to indicate that overexpression of GFP-LC3 did not affect the autophagy signal within cells. Over expressing GFP-LC3 within F9 teratocarcinoma cells still caused the development of autophagosome rings after 2 hours of starvation, even with 10x greater LC3 expression compared to control cells. Thus, even if the expression of GFP-LC3 within cells was greater than the expression of LC3B, it should not have affected the autophagy output visualised in this study. Quantification of autophagy upregulation was performed in this study by visually counting puncta number in a field of view in each mouse organ, with sizes and shapes of autophagosomes described but not quantified.

Jahriess *et al*, 2008, have used live cell imaging of autophagosomes within cell lines to establish a framework for autophagosome dynamics within cells lines. They used mCherry LC3 tagged autophagosomes within flat, thin cells to track movement across time either lifetime, or distances moved of vesicles. The vesicles moved towards lysosomes after being formed randomly, and many colocalised with microtubules, indicating this as a method for transport of these vesicles across cells, with knockdown in microtubule motor protein dynein causing a loss in the organised movement seen in control cells which did not contain this knockout cells.

4.4) Monitoring lysosomes for autophagy research.

Monitoring of lysosomes in relation to autophagosomes can give an idea of the activity of autophagosomes within cells. As the lysosome is the end point for all autophagosomes, where their content is degraded, tools to monitor them can be utilised with autophagosomes. Research by Gannagé *et al* (2009) used two methods to monitor autophagosome/lysosome interactions in cells. lysosomes were tracked with

Lysotracker red, which accumulates within acidic vesicles before fluorescing, and compared this to Lamp1 staining, a lysosome membrane protein(Gannagé *et al* 2009).

4.5) Pixel density analysis of Autophagosome puncta in fixed cells using Imaris.

4.5-a) Pixel density analysis of LC3b puncta within cell lines

Pixel density analysis was used to analyse autophagosomes generated within different cell lines in response to starvation in HBSS. Autophagosomes were identified by immunostaining for endogenous LC3B (Vero, Caco2) or by analysis of GFP-puncta in CHO cells stably expressing GFP-LC3 (CHO LC3 cells). For all cell types, a fluorescent image at x63 is shown, with an Imaris rendering placed below this image. Zooms of regions of interest are shown to the right of each x63 image. Figure 4.1 shows analysis of CHO cells expressing GFP-LC3. The numbers of LC3 puncta were low in cells in nutrient media (11.5 +/- 10) compared to nearly quadruple the number of autophagosomes after 4 hours in HBSS (38 +/- 13.6).

An analysis of the average diameter of LC3 puncta in CHO cells found that the autophagosomes formed in cells in nutrient media appeared small (blue render indicating 0.49 μm +/- 0.08), and that diameters increased following 4 hours in HBSS (0.68 +/- 0.06) The proportion of autophagosomes rendered in red indicating diameters

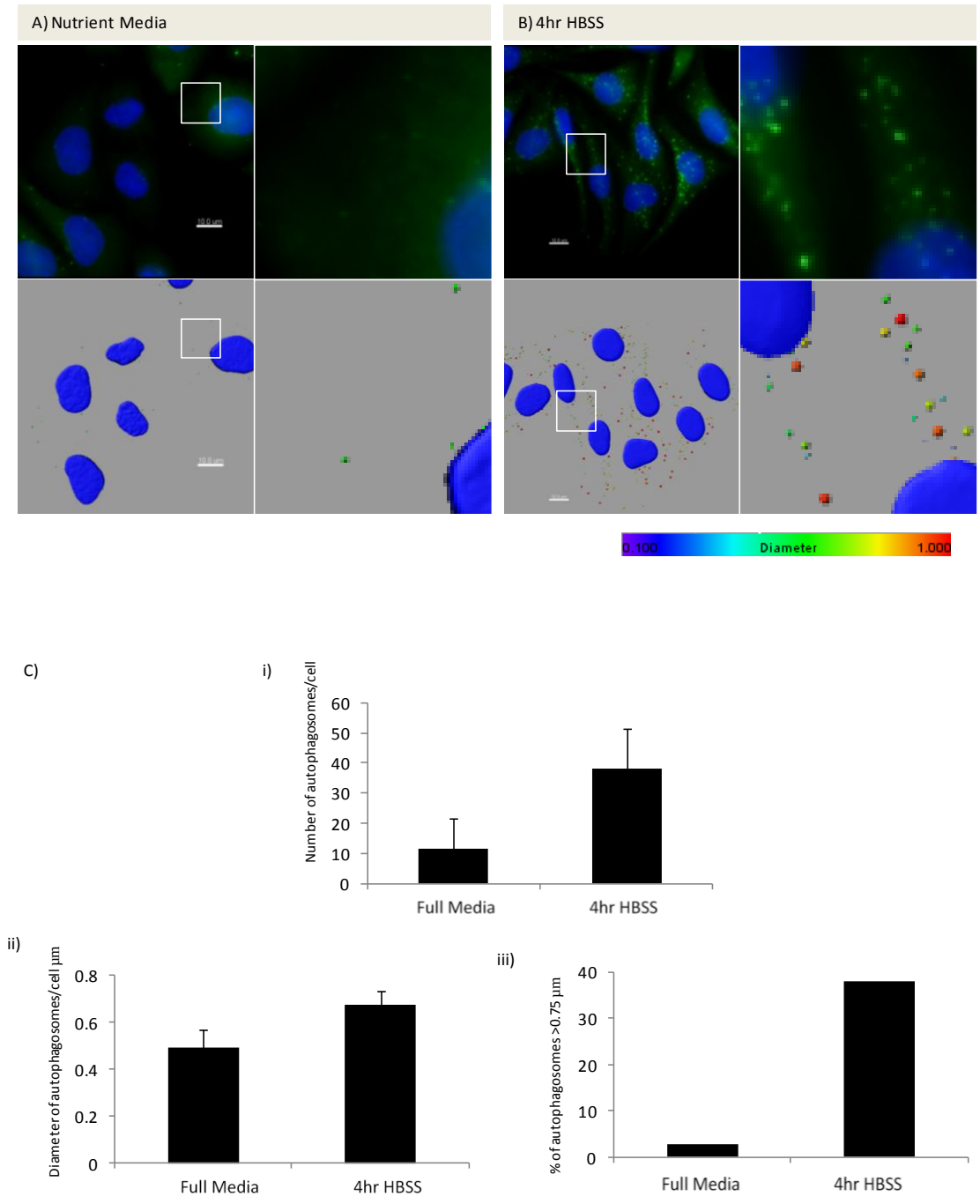

Figure 4.1 - Quantitative analysis of LC3 puncta formed in response to starvation in CHO cells expressing GFP-LC3. CHO cells stably expressing GFP-LC3 were maintained in nutrient media (**A**) or starved in HBSS for 4 hours (**B**). Cells were fixed and permeabilised and incubated with DAPI to show nuclei. The left top panel shows GFP fluorescence imaged using a x63 objective and top right panels show a digital zoom of the region of interest. The lower panels show GFP signal rendered using Imaris software. Rendered vesicles were colour coded using a heat map where small vesicles (0.2µm) are blue, medium sized vesicles (0.5µm) are coloured green, and large vesicles are colour coded yellow, orange or red (0.7-1.0 µm). Rendered puncta were examined from ≥20 cells per time point and plotted with the error bars of standard deviations of standard deviations allowing calculations of mean numbers and diameters of autophagosomes within cells (Panels C and D). Scale bars = 10µm.

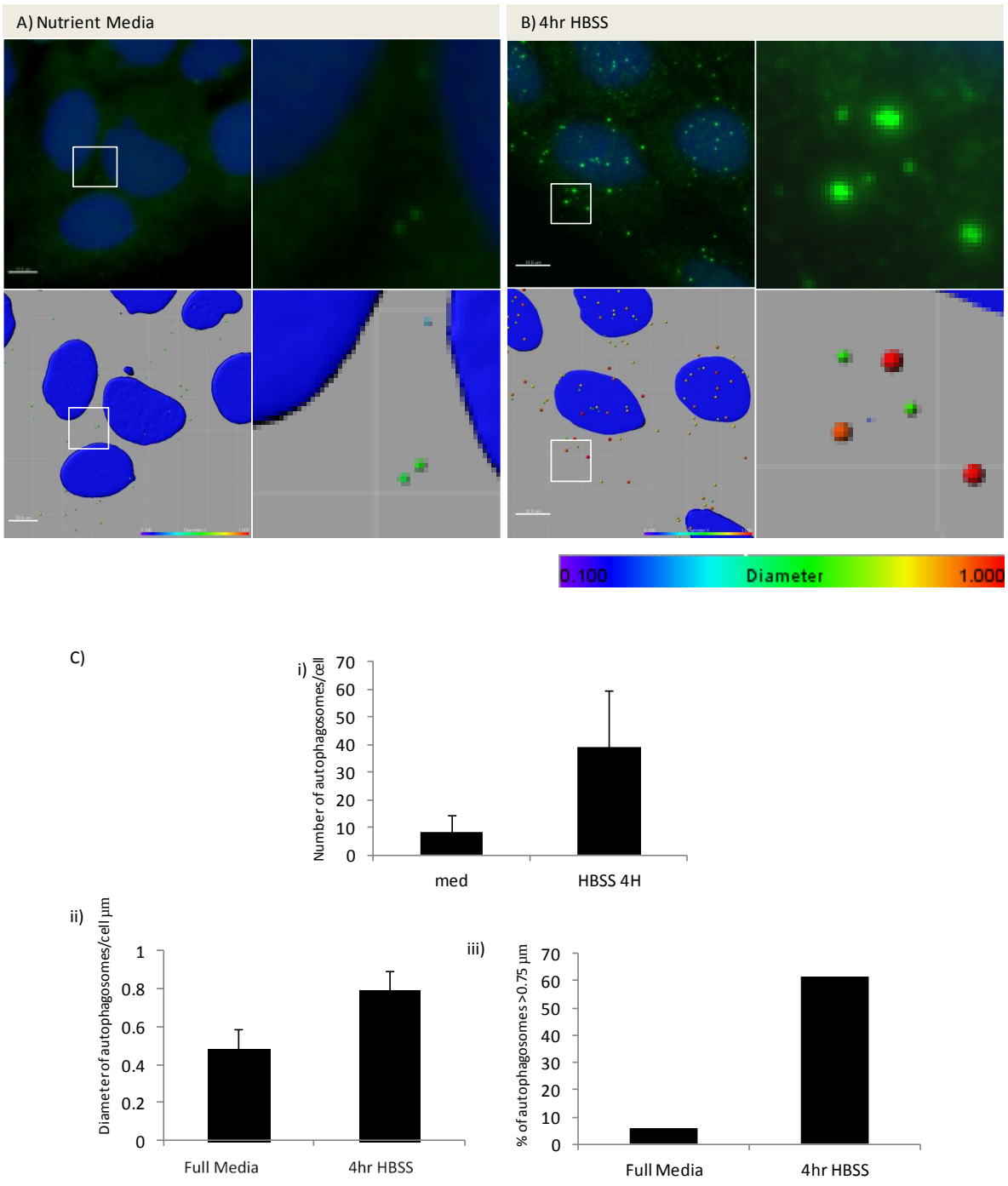

Figure 4.2 - Quantitative analysis of LC3 puncta formed in CaCo2 cells in response to starvation. CaCo2 cells were maintained in nutrient media (**A**) or starved in HBSS for 4 hours (**B**). Cells were fixed and permeabilised and immunostained for endogenous LC3B (green) and incubated with DAPI (blue) to show nuclei. The left top panel shows fluorescence imaged using a x63 objective and top right panels show a digital zoom of the region of interest. The lower panels show fluorescence signal rendered using Imaris software. Rendered vesicles were colour coded using a heat map where small vesicles (0.2µm) are blue, medium sized vesicles (0.5µm) are coloured green, and large vesicles are colour coded yellow, orange or red (0.7-1.0 µm). Rendered puncta were examined from ≥20 cells per time point and plotted with the error bars of standard deviations allowing calculations of mean numbers and diameters of autophagosomes within cells (Panels Ci-iii). Scale bars =10µm.

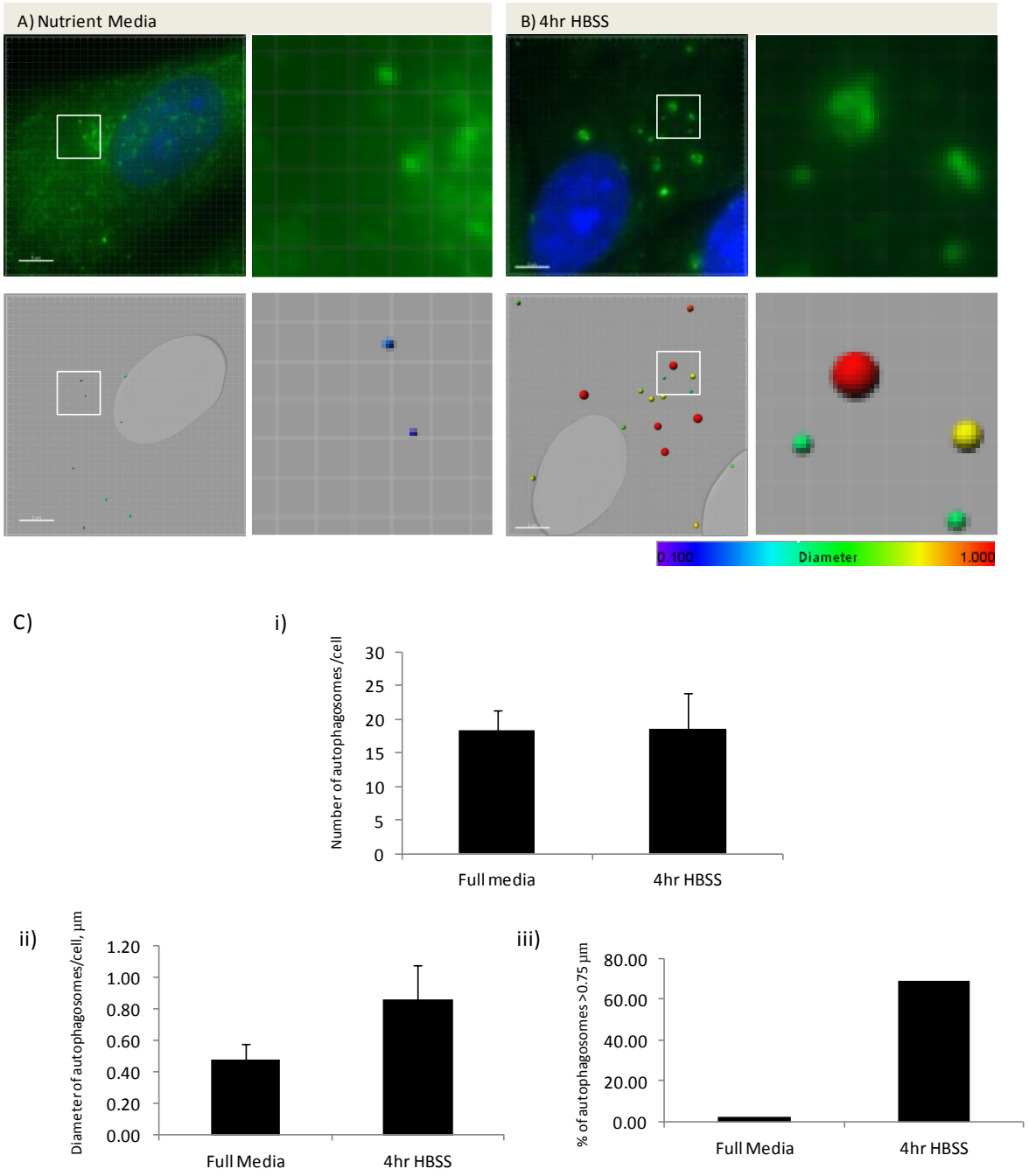

Figure 4.3 - Quantitative analysis of LC3 puncta formed in Vero cells in response to starvation. Vero cells were maintained in nutrient media (**A**) or starved in HBSS for 4 hours (**B**). Cells were fixed and permeabilised and immunostained for endogenous LC3B (green) and incubated with DAPI (blue) to show nuclei. The left top panel shows fluorescence imaged using a x63 objective and top right panels show a digital zoom of the region of interest. The lower panels show fluorescence signal rendered using Imaris software. Rendered vesicles were colour coded using a heat map where small vesicles (0.2µm) are blue, medium sized vesicles (0.5µm) are coloured green, and large vesicles are colour coded yellow, orange or red (0.7-1.0 µm). Rendered puncta were examined from ≥20 cells per time point and plotted with the error bars of standard deviations allowing calculations of mean numbers and diameters of autophagosomes within cells (Panels C i-iii). Scale bars = 5µm.

>0.75 μm, were also compared. Only 2.9% of LC3 puncta were greater than 0.75 μm in cells in nutrient media compared to 38% in cells incubated in HBSS for 4 hours. Figures 4.2 and 4.3 demonstrate similar analysis of Caco2 cells, (Figure 4.2) and Vero cells, (Figure 4.3) immunostained for endogenous LC3B. Average autophagosome numbers and diameters are shown in the bar graphs in C of each Figure. Autophagosome numbers were low in nutrient media (Caco2: 8.5 +/- 6.1, Vero 18.3 +/- 3) but then increased after incubation in HBSS. Autophagosome diameters again increased with starvation as did the percentage of autophagosomes reaching >0.75 μm or greater. This increased from 5.7% in Caco2 cells in nutrient media, to 61.4% after 4 hours in HBSS. For Vero cells, there was also an increase in the number of autophagosomes reaching >0.75μm or greater after 4 hours in HBSS. (75% compared to 2.3% in nutrient media).

4.5-b) Pixel density analysis of puncta containing early autophagosome marker WIPI2.

Early autophagy marker WIPI2 binds PtdIns(3)P and co-localises with DFCP-GFP during autophagosome formation and is a marker for omegasomes (Polson *et al*, 2010). This allows immunostaining for WIPI2 to indicate early autophagosomes. As Figure 4.4 indicates, Imaris analysis of WIPI2 puncta shows low numbers in Vero cells in nutrient media (6.7 +/-0.75 μm) and rendering showed they were of small diameter (0.43μm +/- 0.17). After 4 hours in HBSS, WIPI2 puncta increased in number (12.2+/-5.6) and size (0.72 +/- 0.18) compared to nutrient media. Thus, increases in size and number following starvation could be seen for an early stage autophagy protein.

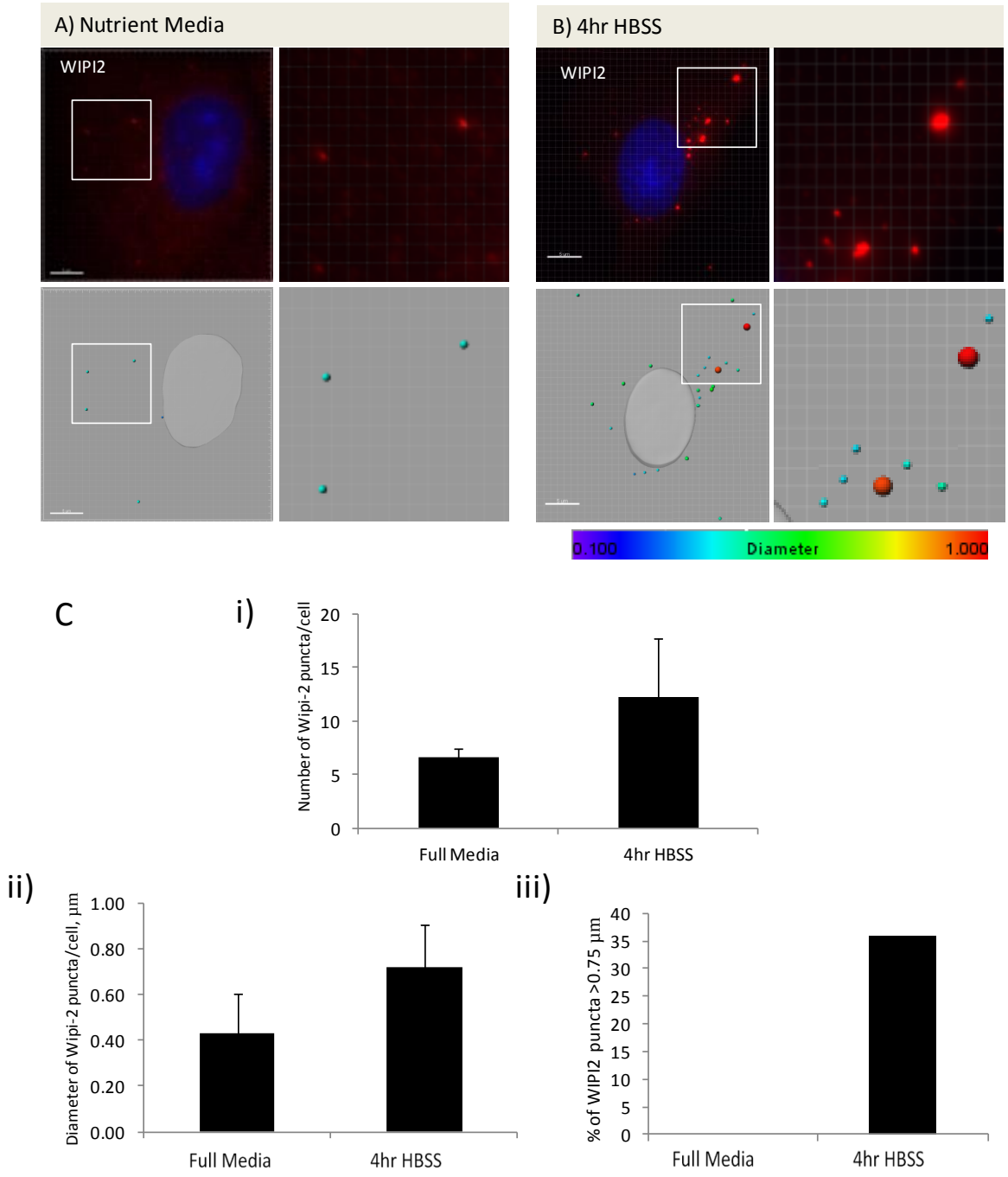

Figure 4.4 - Quantitative analysis of WIPI puncta formed in Vero cells in response to starvation. Vero cells were maintained in nutrient media or starved in HBSS for the indicated times. Cells were fixed and permeabilised and immunostained for endogenous WIPI2 (red) and incubated with DAPI (blue) to show nuclei. **Panel A**. Vero cells were immunostained for WIPI2 (red) and stained with DAPI to show nuclei. The top images show fluorescence signal and the lower images show puncta rendered using Imaris. Rendered vesicles were colour coded so that small vesicles (0.2µm) are blue, medium sized vesicles (0.5µm) are coloured green, and large vesicles are colour coded yellow, orange or red (0.7-1.0 µm). **Panel B** Rendered puncta were examined from ≥20 cells per time point and plotted with the error bars of standard deviations allowing calculations of mean diameters (**B-i)**, numbers of puncta per cell (**B-ii**) and changes in puncta diameter (**B-iii**). Scale bars = 5µm.

4.5-c) A comparison of LC3 puncta detected through immunostaining of endogenous LC3 in fixed cells with GFP-LC3 puncta generated in living cells.

GFP-LC3 will be used in subsequent experiments described in this thesis to characterize autophagosomes in living cells. It was therefore important to show that expression of GFP-LC3 did not induce LC3 puncta alone. The above experiments showed that it was possible to identify autophagosomes in fixed cells by immunostaining for endogenous LC3B, and in live cells by following GFP-LC3. The next experiments carry out a side-by-side comparison of GFP- puncta and LC3 puncta in the same cell type. To do this, Vero cells were transduced using an adenovirus expressing GFP-LC3 (Figure 4.5A), or fixed and then immunostained for endogenous LC3B (Figure 4.5B) . Pixel density analysis of cells incubated in nutrient media, or starved for 4 hours in HBSS, are compared in Figure 4.5. A comparison of data collected from 67 Vero cells shows that the diameters of the autophagosomes in nutrient media do not differ (0.53μm +/- 0.15 in fixed cells compared to 0.56μm +/- 0.16 in live cells), or in cells starved for greater than 3 hours (0.93μm +/- 0.17 in fixed cells compared to 1.0μm +/- 0.36 in live cells) by using the two different forms of analysis.

4.6) Analysis of autophagosomes at different time points during starvation

4.6-a) Analysis of numbers and diameters of LC3 puncta at different time points during starvation.

During analysis of several Imaris-rendered images, it was noted that the larger diameter LC3 puncta (orange-red) were seen in cells starved in HBSS for 4 hours, but were not present in cells incubated in nutrient media. The time course of appearance of large LC3 puncta was therefore determined. Figures 4.6 shows analysis of autophagosome number and diameter in CHO cells expressing GFP-LC3 (Figure 4.6A) and Caco2 cells

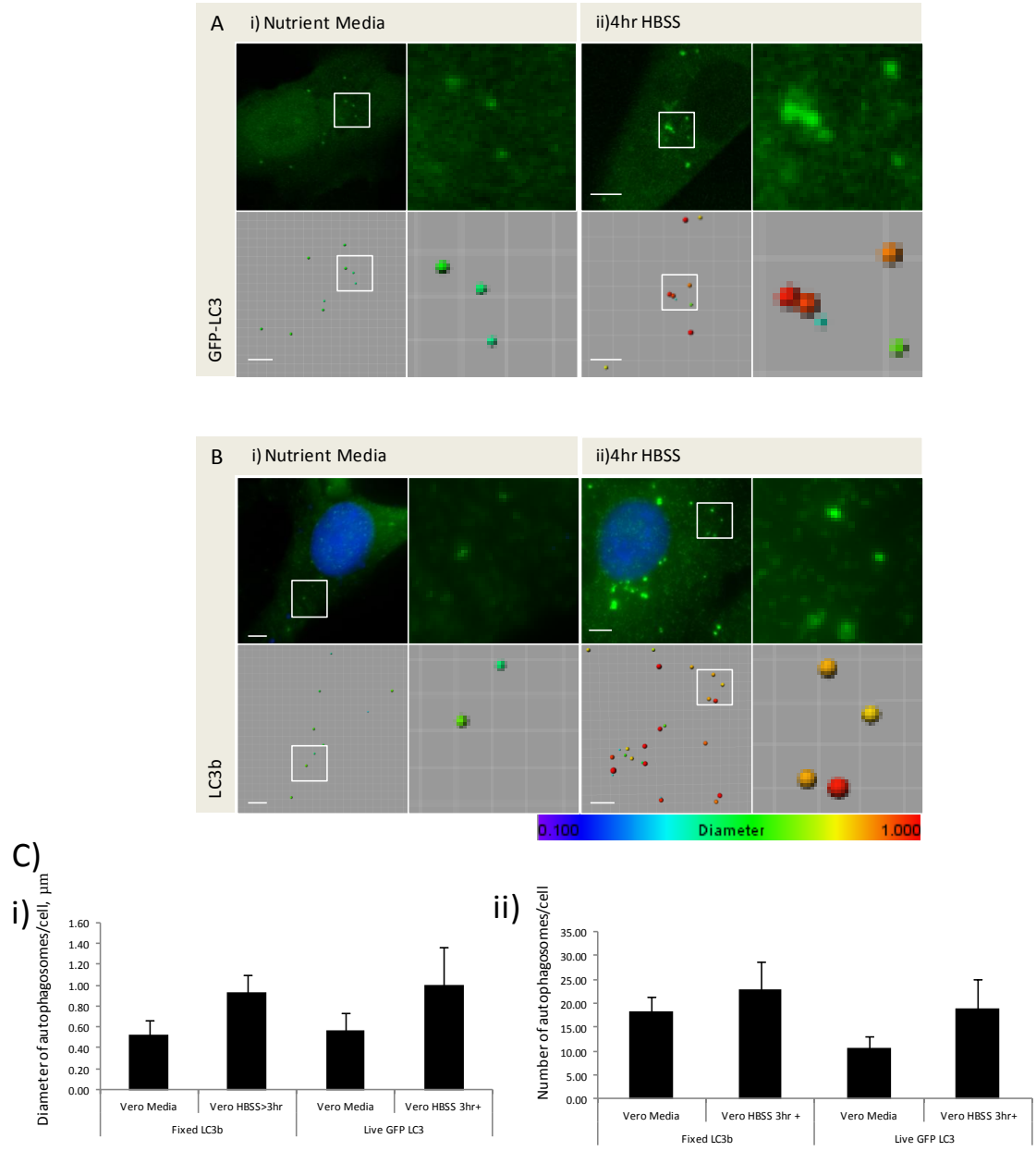

Figure 4.5 - A comparison of LC3 puncta in Vero cells generated by immunostaining for LC3B or Live cell imaging of GFP-LC3. Panel A. Vero cells were transduced with adenovirus expressing GFP-LC3 and maintained in nutrient media **(i)** or starved in HBSS **(ii)** for 4 hours as indicated. The fluorescence signal from GFP-LC3 (green) was captured by live cell imaging. **Panel B.** Vero cells were maintained in nutrient media **(i)** or starved in HBSS **(ii)**. Cells were fixed and immunostained for endogenous LC3B (green) and incubated with DAPI to show nuclei (blue). In each panel, the top left quadrant shows the image of a cell, with a digital zoom of the region of interest in the top right quadrant. Imaris renders are presented below corresponding fluorescence images. Rendered puncta were colour coded so that small vesicles (0.2µm) are blue, medium sized vesicles (0.5µm) are coloured green, and large vesicles are colour coded yellow, orange or red (0.7-1.0 µm). **Panel C**. Rendered puncta were examined from ≥20 cells per time point and plotted with the error bars of standard deviations allowing calculations of mean diameters (**C-i)**, numbers of puncta per cell **(C-ii**) and changes in puncta diameter **(C-iii**). Scale bars = 5µm.

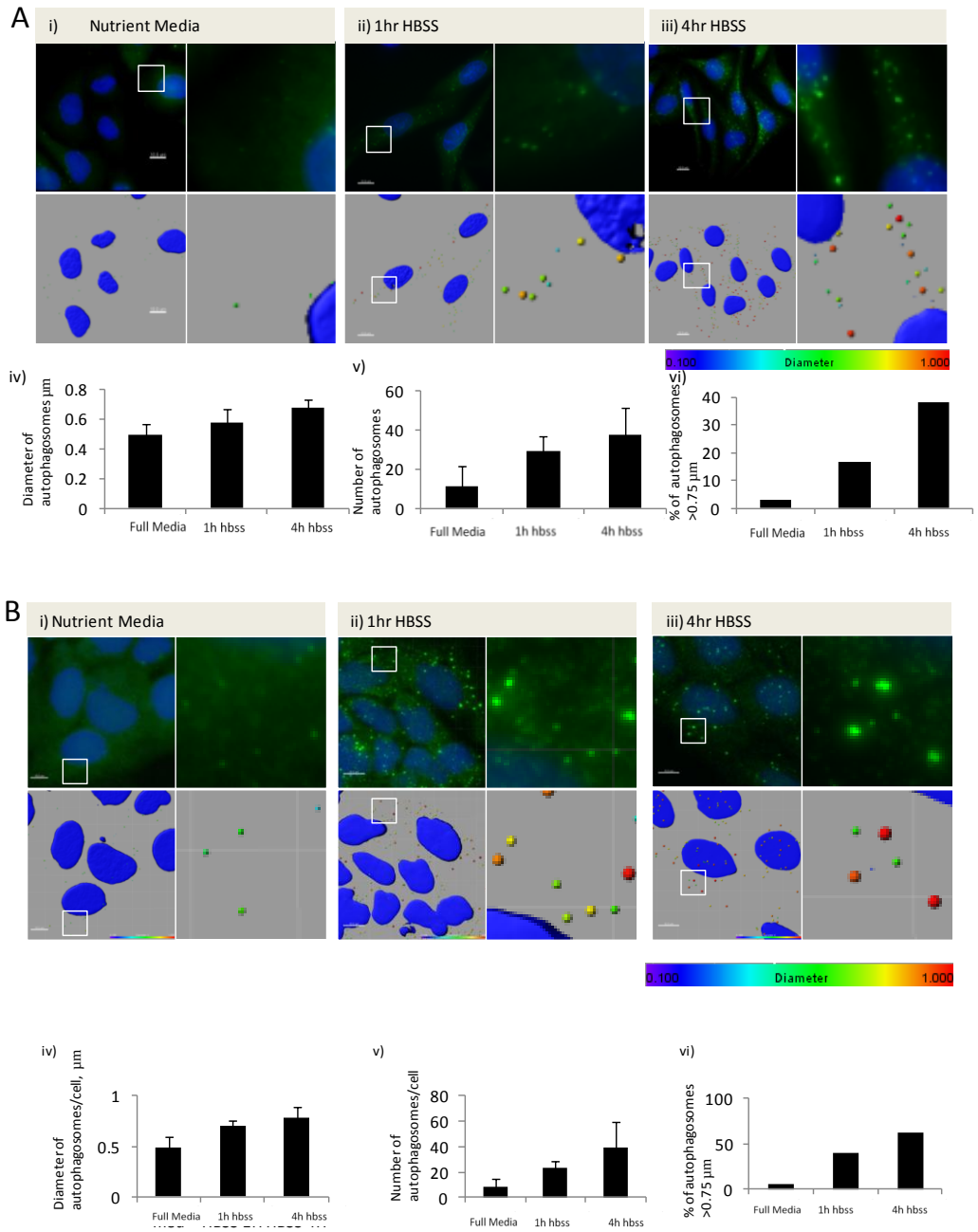

Figure 4.6 - Comparison of LC3 puncta diameters and numbers in CHO cells and CaCo2 cells. Cells were maintained in nutrient media **(i)** or starved in HBSS for one hour **(ii)** or 4 hours **(iii)** as indicated. **Panel A.** CHO cells expressing GFP-LC3 were fixed and analysed for fluorescence signal from GFP (green) and incubated with DAPI to show nuclei (blue). **Panel B.** CaCo2 cells were fixed and immunostained for endogenous LC3B (green) and incubated with DAPI to show nuclei (blue). In each panel, the top left quadrant shows the image of a cell, with a digital zoom of the region of interest in the top right quadrant. Imaris renders are presented below corresponding fluorescence images. Rendered puncta were colour coded so that small vesicles (0.2µm) are blue, medium sized vesicles (0.5µm) are coloured green, and large vesicles are colour coded yellow, orange or red (0.7-1.0 µm). Rendered puncta were examined from ≥20 cells per time point taken, and plotted with the error bars of standard deviations allowing calculations of average diameters of average diameters **(iv)** number of puncta per cell **(v)** and change in diameters during starvation **(vi)**. Scale bars = 10 µm.

(Figure 4.6.B) in nutrient media (A), after 1 hour in HBSS (B) and 4 hours in HBSS (C). The GFP-LC3 signal was rendered and colour coded using a heat map where blue represents puncta less than 0.3 μm, green those of about 0.5μm, and yellow, orange and red puncta 0.75μm or more in diameter. The rendered images indicate that yellow and orange puncta (0.7-0.9μm) were absent from control cells in nutrient media but were first seen following 1 hour in HBSS. The bar graphs in both Figure 1 and 2 show that numbers of LC3 puncta increase with time, as do their average diameters, and proportion of puncta with a diameter greater than 0.75μm.

The experiment was repeated using Vero cells analysed at increasing times between 1-5 hours of starvation with HBSS. Cells were immunostained for endogenous LC3B (Figure 4.7A) and pixel densities present in LC3 puncta were rendered by Imaris software allowing statistical analysis. As seen for CHO and Caco2 cells, large LC3 puncta were absent from early time points and first appeared between 1 and 2 hours. After 4 hours of starvation rendered puncta were mainly orange or red indicating diameters of ≥0.75-1 μm. The size of mature autophagosomes calculated from electron micrographs is around 1μm, so the pixel rendering analysis generating red spheres correlates well with accepted dimension of autophagosomes (Muzishima *et al*, 2002). An analysis of autophagosome numbers showed that Vero cells have higher numbers of LC3 puncta at 1 hour of starvation (Figure 3Bii, 37.2+/- 7.2) compared to 3 hours of starvation (14.7 +/- 3.1). However, the puncta diameter is still small at 1 hour in HBSS (0.54μm +/-0.08) compared to 4 hours of starvation (0.91μm +/-0.12)

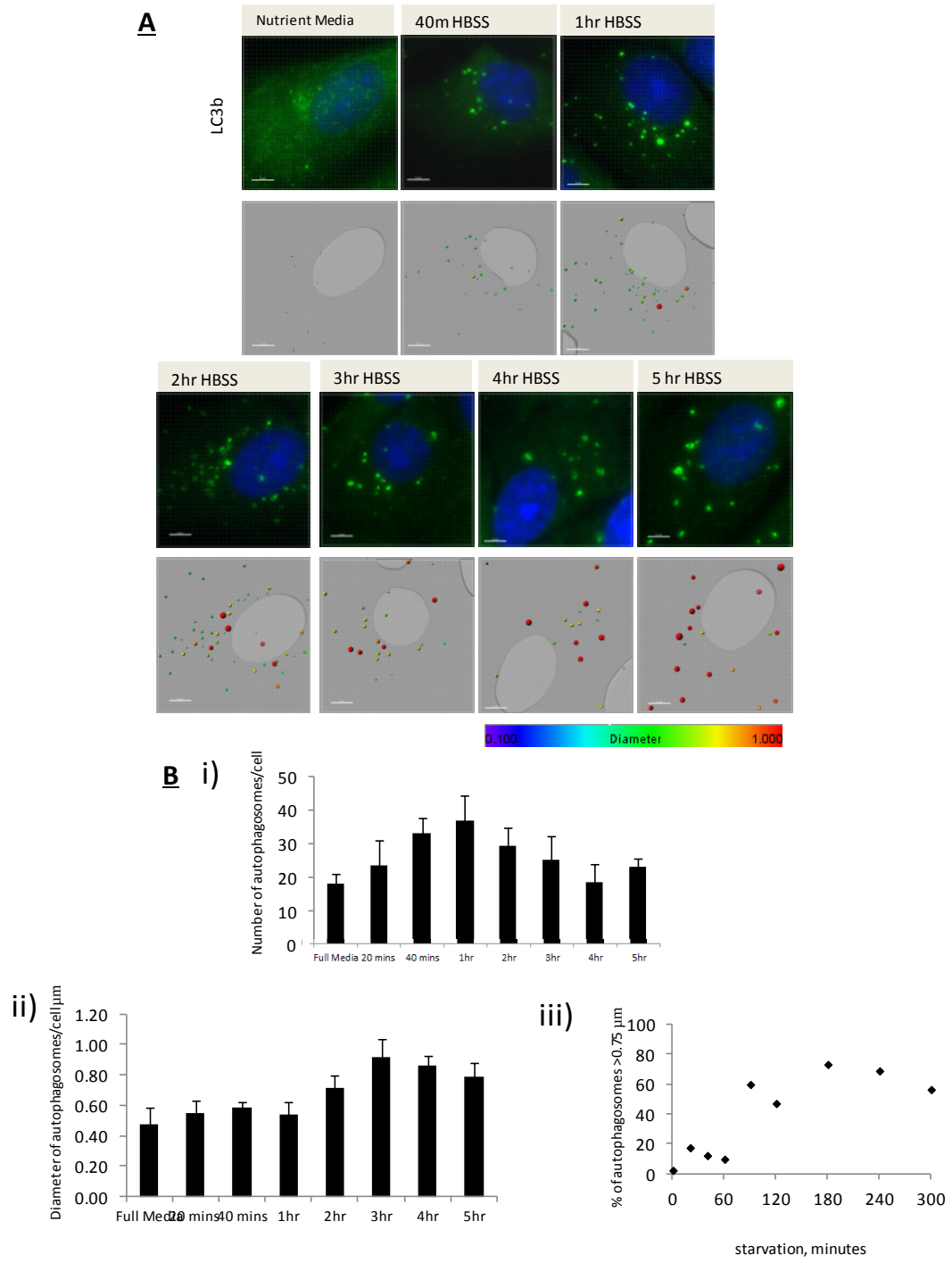

Figure 4.7 - Analysis of LC3 puncta in Vero cells at increasing times after starvation. Vero cells were maintained in nutrient media or starved in HBSS for increasing times as indicated. **Panel A.** Cells were fixed and immunostained for endogenous LC3B (green) and incubated with DAPI to show nuclei (blue). The top images shows the fluorescence image from the cell and Imaris renders are presented below corresponding fluorescence images. Rendered puncta were colour coded so that small vesicles (0.2µm) are blue, medium sized vesicles (0.5µm) are coloured green, and large vesicles are colour coded yellow, orange or red (0.7-1.0 µm). **Panel B.** Rendered puncta were examined from ≥20 cells per time point and plotted with the error bars of standard deviations allowing calculations of average diameters **(i)** number of puncta per cell **(ii)** and change in diameters during starvation **(iii)**. Scale bars = 5µm.

4.6-b) Analysis of numbers and diameters of WIPI and SQSTM1/p62 puncta at different time points during starvation.

Autophagosomes form from the ER and originate from omegasome intermediates, which recruit WIPI2 (Hayashi-Nishino, 2009.Matsunaga, 2010). Figure 4.8A shows examples of Vero cells immuno-stained for endogenous WIPI2 at increasing times after starvation. The numbers and diameters of WIPI2 puncta followed a trend similar to that seen for LC3B staining in Vero cells. The diameters of WIPI puncta were low at early during starvation at 1 hour (0.45μm +/- 0.01) and increased with 3 hours of starvation (0.79μm +/- 0.13). Also, numbers of WIPI2 puncta peaked at 2 hours (19.6 +/- 9.7) and then declined.

Autophagic flux is the movement of cytoplasmic content into autophagosomes and transport to lysosomes for degradation. SQSTM1 binds LC3, and facilitates incorporation of ubiquitinated proteins into autophagosomes (Pankiv *et al*, 2007). Figure 4.9 shows cells double stained for SQSTM1 (red) and LC3 (green) and vesicles containing both green and red signals represent SQSTM delivered to autophagosomes. The fluorescent images have been rendered to show green LC3 and red SQSTM1 rendered vesicles, with colocalised vesicles in yellow. Zooms show regions of interest across all conditions. As Figure 4.9 indicates, Vero cells immunostained for both LC3 and SQSTM1 maintained in nutrient media have lower percentages of SQSTM1 puncta colocalising with LC3 puncta (29%), when compared to after 1 hour HBSS (64.9%) and after 4 hours of HBSS (68.4%).. The sizes of SQSTM1puncta on average do not appear to increase to the same extent as LC3 at later stages of starvation, only reaching 0.57μm compared to their LC3B vesicles (0.75μm) after 4 hours of HBSS during these experiments.

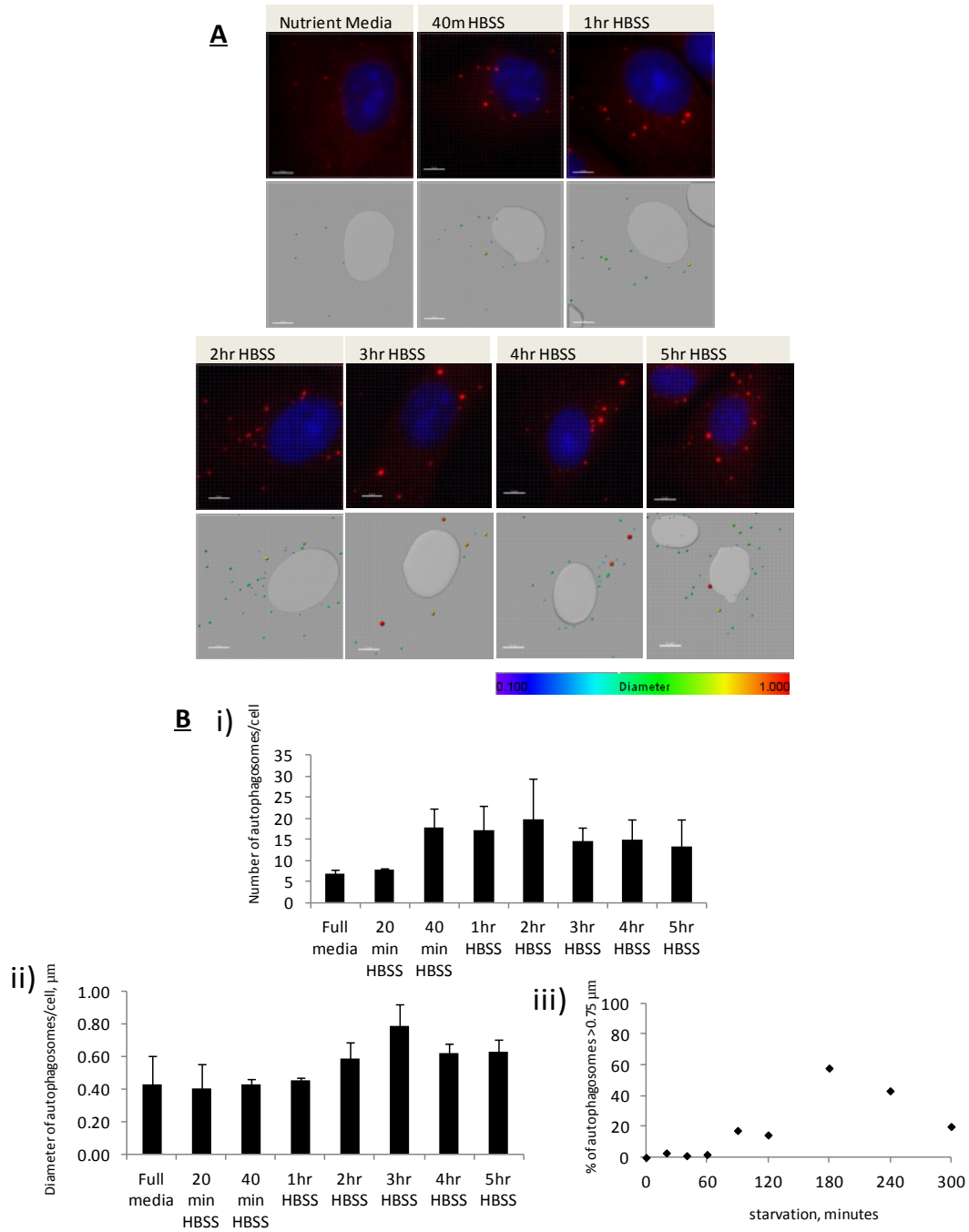

Figure 4.8 - Analysis of WIPI2 puncta in Vero cells at increasing times after starvation. Vero cells were maintained in nutrient media or starved in HBSS for increasing times as indicated. **Panel A.** Cells were fixed and immunostained for endogenous WIPI2 (red) and incubated with DAPI to show nuclei (blue). The top images shows the fluorescence image from the cell and Imaris renders are presented below corresponding fluorescence images. Rendered puncta were colour coded so that small vesicles (0.2µm) are blue, medium sized vesicles (0.5µm) are coloured green, and large vesicles are colour coded yellow, orange or red (0.7-1.0 µm). **Panel B.** Rendered puncta were examined from ≥20 cells per time point and plotted with the error bars of standard deviations allowing calculations of average diameters **(i)** number of puncta per cell **(ii)** and change in diameters during starvation **(iii)**. Scale bars = 5µm

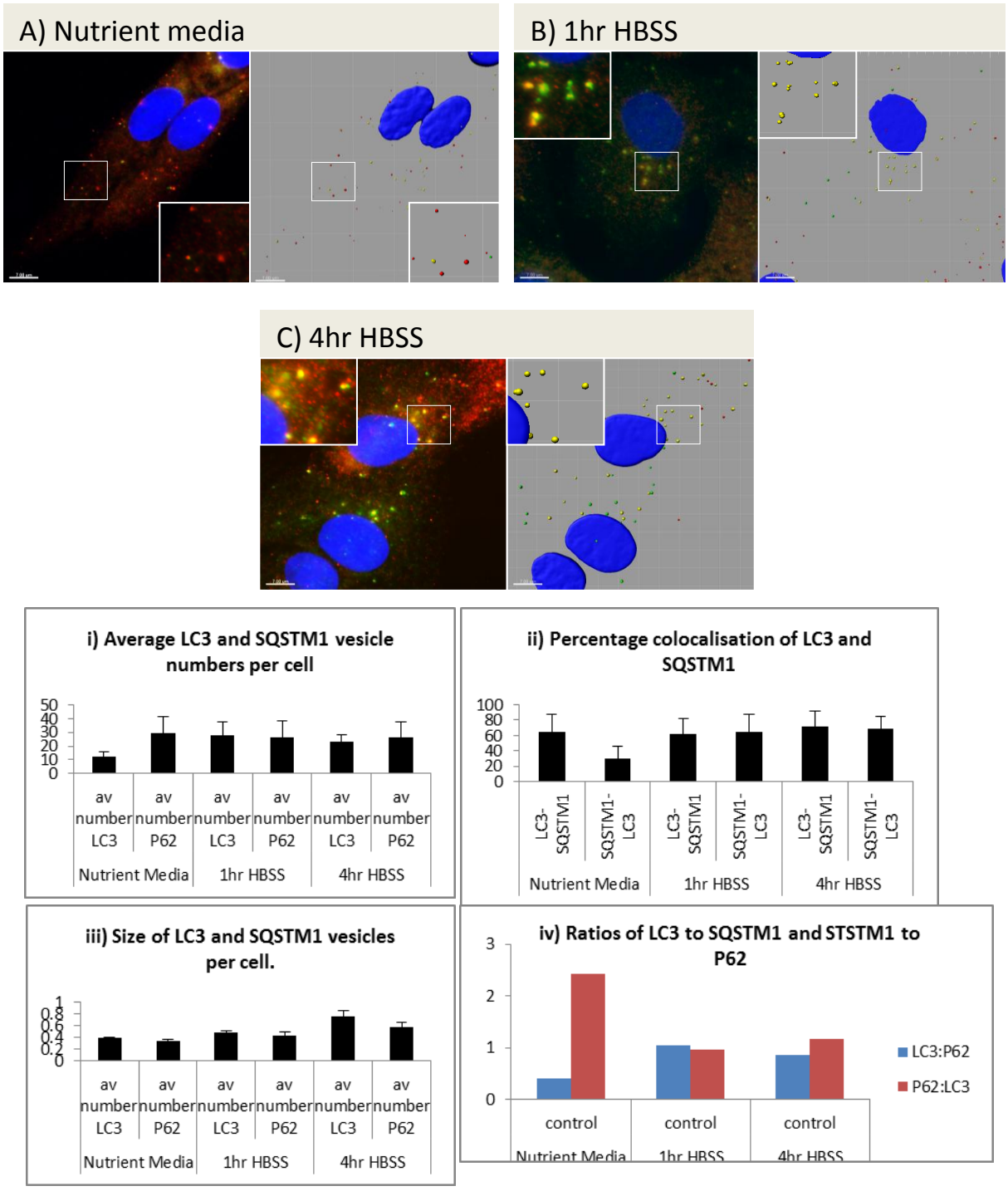

Figure 4.9- Colocalisation of LC3 with SQSTM1 within puncta formed at increasing times of starvation. Vero Cells were incubated in nutrient media **(Panel A),** HBSS for 1 hour **(Panel B**) or HBSS for 4 hours (**Panel C**), fixed and stained for LC3B (Green) and SQSTM1 (Red). Nuclei were stained with DAPI in blue. Fluorescence images are shown to the left with digital zooms of regions of interest. Corresponding rendered images renders are shown to the right. **Panel D.** Rendered puncta were examined from ≥20 cells per time point taken from three starvation time courses and plotted with the error bars of standard deviations allowing calculations of **(i),** the average numbers of puncta per cell; **(ii)** the percentage colocalisation of LC3 and SQSTM1; **(iii)** the diameters of SQSTM1 and LC3B puncta and (iv) the ratios of SQSTM1 puncta to LC3 puncta. Scale bars = 7µm

lysosomes were identified in Vero cells by expressing a fluorescent-tagged lysosome-associated membrane protein (Lamp1-RFP). Figure 4.10 shows the interaction of lysosomes and autophagosomes in cells in nutrient media (Figure 5.5.a), after 1 hour of HBSS (Figure 5.5.b) and 4 hours of HBSS (Figure 5.5.c). Imaris rendering identified LC3 colocalised with LAMP1 as yellow puncta. . The analysis of puncta containing both signals was only performed for instances when LC3 colocalised with LAMP1-RFP. It was not possible to identify LAMP1 puncta because the rendered images showed a reticulum of LAMP positive vesicles and membranes that were difficult to resolve.,

4.6-c) Analysis of the lifetime of LC3 puncta formed at increasing times following starvation.

Mature autophagosomes are reported to be approximately 1μm in diameter (Mizushima *et al*, 2002). The results above showed that LC3 puncta formed in nutrient media, or after 1 hour in HBSS, had diameters less than 0.75μm. This suggested that autophagosomes formed during the first hour of starvation were unable to mature, or that it takes between one and two hours for autophagosomes to reach diameters ≥0.75μm. This was tested directly by comparing time-lapse images of GFP-LC3 puncta taken early or at late times following starvation. GFP-LC3 puncta formed in nutrient media (figs 4.11 A, B) showed blue-green transition within 3 minutes suggesting a diameter of 0.5μm, and remained this size before disappearing. GFP-LC3 puncta formed between 1 and 2 hours after starvation (figs 4.11.C, D) grew rapidly and could reach diameters greater than 0.75μm (orange) within 5 minutes. After 3 hours, vesicles were able to grow to 0.75μm (red) within 5 minutes of forming (figs 4.11E,F). In several cases spherical LC3 puncta generated ring shaped vesicles of ≥1.0μm before changing shape and fading over a period of 8 minutes.

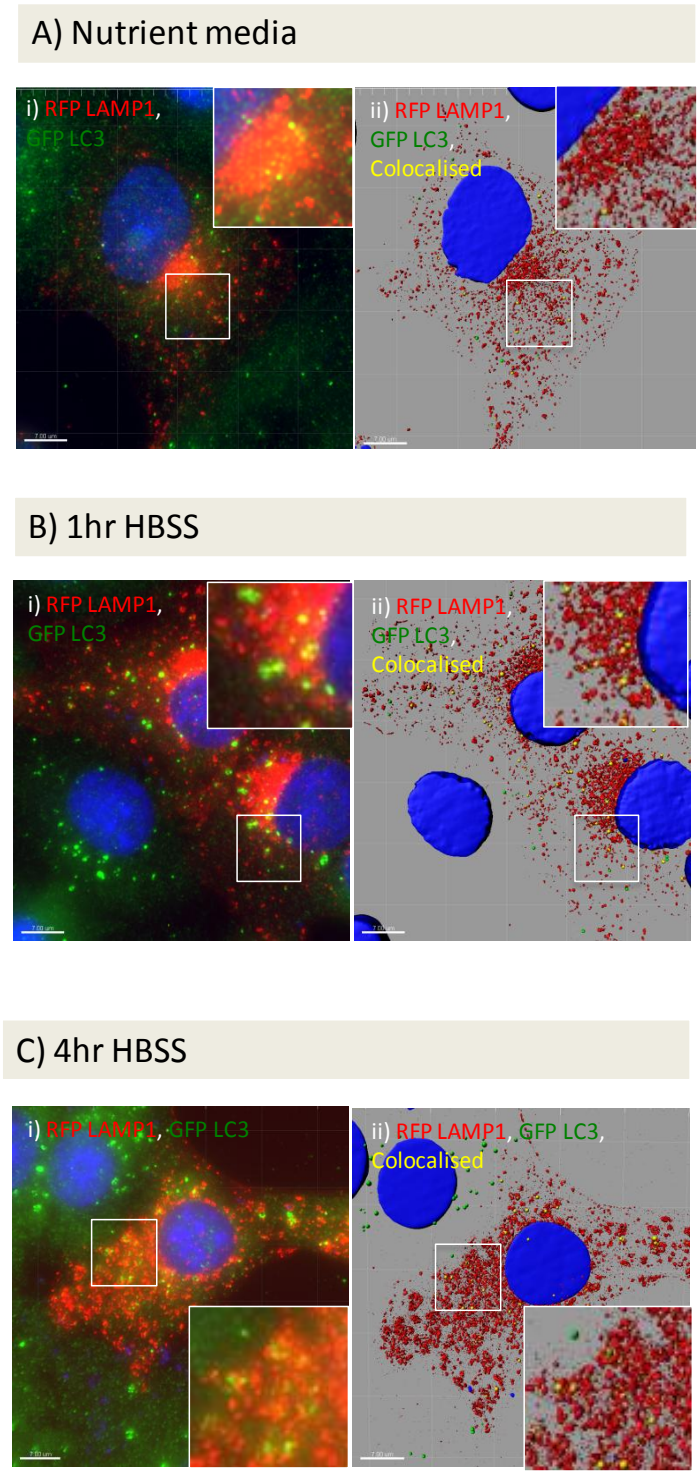

Figure 4.10 - Colocalisation of LC3 and LAMP-1 within puncta formed at increasing times of starvation. Vero cells were transfected with RFP LAMP-1 (Red). incubated in nutrient media **(Panel A),** HBSS for 1 hour **(Panel B**) or HBSS for 4 hours (**Panel C**), fixed and stained for LC3b (Green) Nuclei were stained with DAPI in blue. Fluorescence images are shown to the left with digital zooms of regions of interest. Corresponding rendered images renders are shown to the right. LC3b colocalised with RFP LAMP-1 is shown in yellow. Scale Bars= 7µm.

Autophagosome maturation was further analysed by plotting autophagosome lifetime analysis against the maximum diameter of puncta. An analysis of 190 puncta from 9 different cells maintained in nutrient media (Figure 4.11G, I) showed that the bulk of the vesicles were of low diameter (0.53 μm) and short lived (average: 135 seconds). Analyses of 208 vesicles from 4 different cells, at between 3 and 5 hours of starvation, showed that the puncta formed were of larger diameter and had varied lifetimes (Figure 4.11-G-iii) with some lasting 1500 seconds. Even so, the bulk of the puncta survived less than 500 seconds (8 minutes). Figure 4.12 shows colocalisation analysis of Vero cells expressing GFP-LC3 (green), and incubated with a live cell lysosome marker Lysotracker (red). Videos of green and red puncta in nutrient media (Figure 4.12-A) early (less than 30 minutes) HBSS (Figure 4.12-B) and late (greater than 3 hours) HBSS (Figure 4.12-C). Larger autophagosomes and lysosomes are seen in later starvation. The results on colocalisation with Imaris display that there are interactions of autophagosomes with lysosomes as shown with Imaris renders of yellow spots in all groups. This shows interaction of autophagosomes with lysosomes across all conditions with this live cell technique, parallel to the analysis by fixed cells and LC3B staining in Figure 4.10. Taken together, the data suggest that autophagosomes have similar lifetimes regardless of period of starvation or size of autophagosomes, but autophagosomes generated in nutrient media, or at early times after transfer to HBSS, are unable to reach diameters ≥0.75μm.

A
Nutrient Media
00:30
GFP-LC3
01:00
01:30
02:30
03:30
04:30
05:30
06:30
07:30
08:30
B
Nutrient Media
00:00
GFP-LC3
00:30
00:50
01:20
02:10
02:40
03:30
04:30
05:00
C
1-2hr HBSS
00:00
GFP-LC3
00:30
01:00
02:00
03:00
03:30
05:20
07:10
08:00
10:40

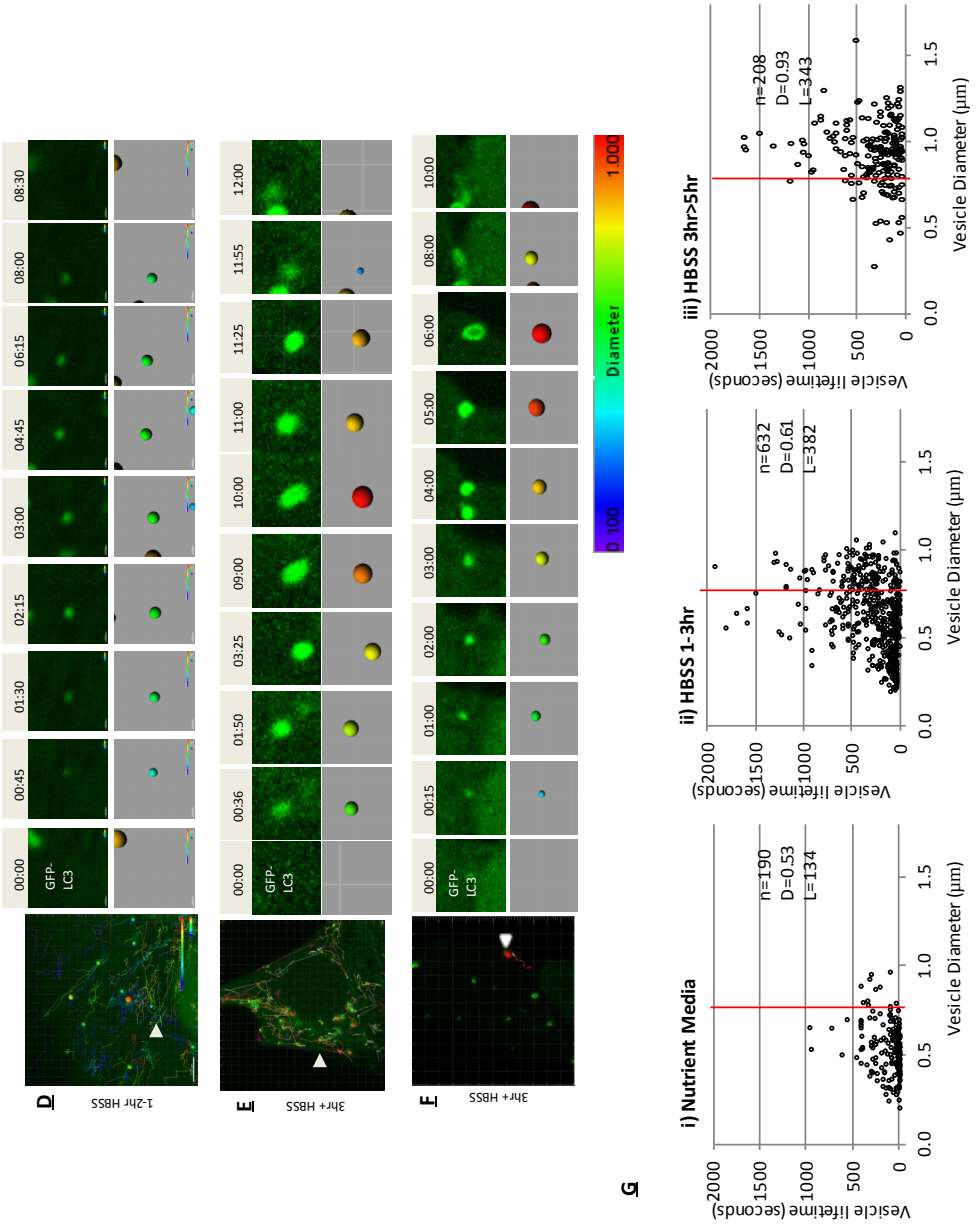

Figure 4.11 - Time lapse imaging of LC3 puncta formed at different times following onset of starvation. Vero cells were transduced with an adenovirus expressing mammalian GFP-LC3. The following day the cells were transferred to HBSS and the time course of GFP-LC3 puncta formation and decay was determined by time lapse imaging. GFP-LC3 puncta were tracked and analysed using Imaris spot and render functions. The left-hand image on each panel identifies the GFP-LC3 puncta of interest and shows its track during the time lapse as determined by Imaris. Individual time lapse images are shown to the right and colour coded rendered images are shown below corresponding fluorescence images. Small puncta (0.2µm) are blue, medium sized puncta (0.5µm) are coloured green, and large puncta are colour coded yellow, orange or red (0.7-1.0 µm). Time points are indicated in minutes. **Panels A and B,** nutrient media; **Panels C and D**, 1-2 hour after transfer to HBSS and **Panels E and F**, 4 hours after transfer to HBSS. **Panel G** Scatter plots show the lifetimes of GFP-LC3 puncta generated under the indicated conditions plotted against maximum vesicle diameter. The vertical bar in each scatter graph represents 0.75□m, which would provide orange spheres in rendered images. **(i)** cells incubated in nutrient media**; (ii)** cells transferred to HBSS from 1-3 hours and **(iii)** cells incubated in nutrient media from 3-5 hours.

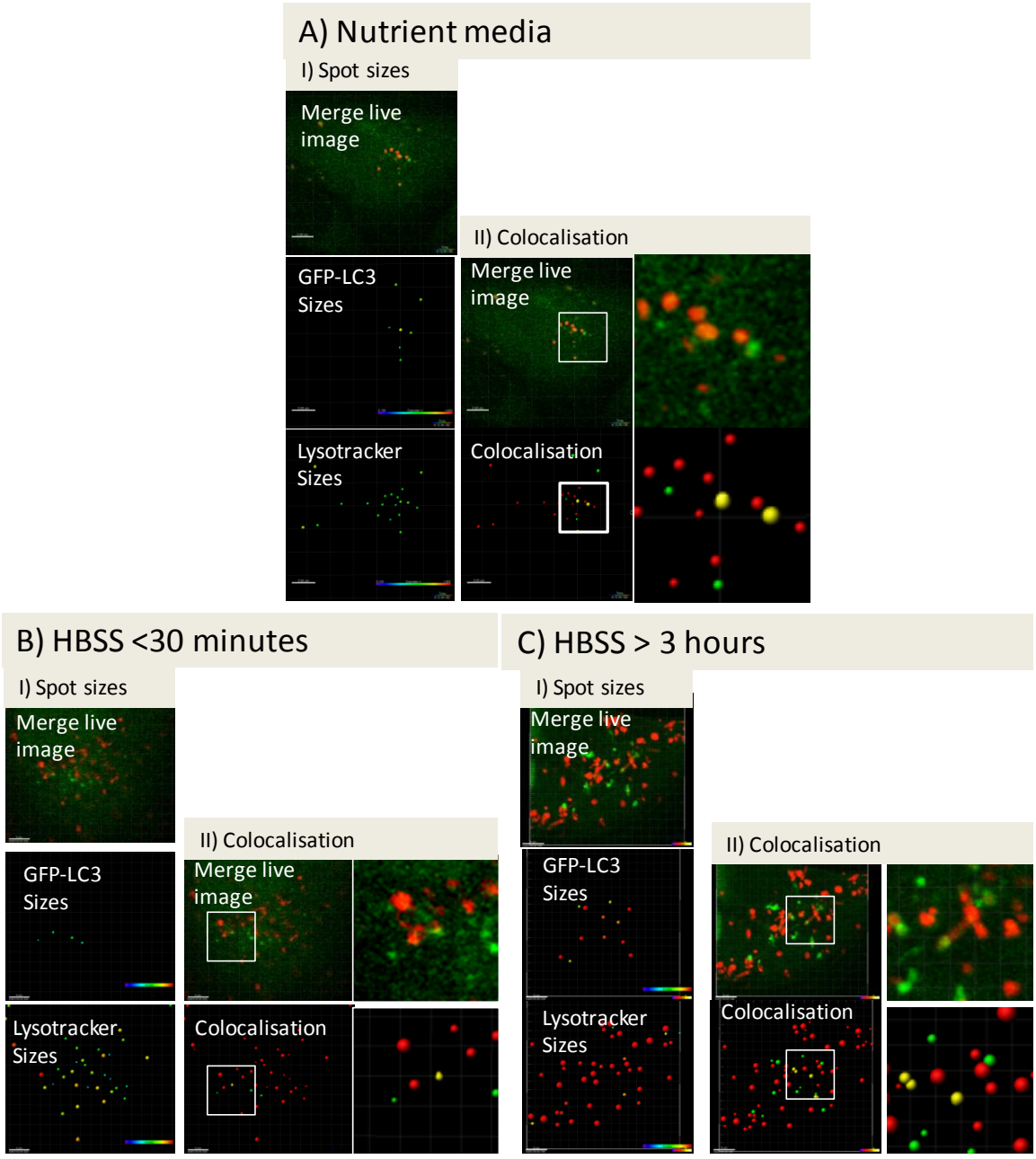

Figure 4.12- Live cell imaging of the interacation of GFP-LC3 puncta with lysosomes labelled with Lysotracker. Vero cells were transduced with GFP-LC3 adenovirus and incubated in the presence of Lysotracker in; (**Panel A**) nutrient media, (**Panel B**) HBSS for less than 30 minutes or (**Panel C**) HBSS for > 3 hours. In each panel merged fluorescent images are presented at the top with GFP-LC3 in green, and Lysotracker in red. The GFP-LC3 and Lysotracker images are rendered separately to give spot sizes **(i)** which are colour coded from blue to red so the smallest autophagosomes are blue (0.1µm), mid-sized autophagosomes (0.5 µm) are labelled green, and large autophagosomes (0.75-1 µm) are labelled yellow, orange and red. In **(ii)** the degree of colocalisation is calculated. The rendered puncta are red when not colocalised, and yellow when colocalised. Images were taken on a Zeiss LSM confocal with an x63 lens. Scale bars = 5µm.

4.7) Summary

To see if autophagosomes formed by starvation change in size or number, we quantified starvation images of LC3 using the Imaris software described in detail in chapter 3. Using 4 hours of HBSS starvation prior to fixation we saw clear changes in autophagosomes shown in the previous chapter. The effect of 4 hours of starvation in CHO-LC3 and Caco2 cells was an increase in both size of autophagosomes, number of autophagosomes, and number of autophagosomes reaching above 0.75µm from nutrient media. There was no statistical difference between numbers of puncta formed in different cell lines but for CHO cells expressing GFP-LC3 and Caco2 cells there was a significant increase in puncta after starvation (p=0.05). Average numbers of puncta increased in Vero cells after starvation but there was a high and varied number of puncta in cells in nutrient media and at a confidence level of 95%, numbers of puncta were not significantly different. A similar analysis of puncta diameter (Figure 4.13) showed that there was no statistical difference between puncta diameters across the three cell lines, but there was a statistical increase in diameter following starvation for 4 hours.

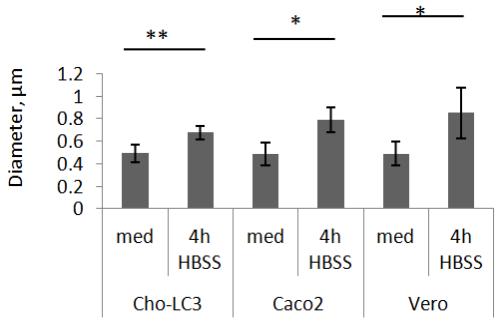

Figure 4.13- Average diameter of autophagosomes across cell lines from nutrient media, to 4 hours of HBSS.

Vero cells followed a similar pattern in size increases, and percentage of autophagosomes above 0.75µm. In comparison to previous work, Mizushima et al

(2004) saw larger autophagosomes after 2 hours of nutrient starvation. We also assessed the number and size of WIPI2 puncta in Vero cell. This early autophagosome marker also cause an increase in sizes of autophagosomes, with autophagosomes >0.75μm only being seen after 4 hours of starvation. By comparing the autophagosomes produced by transducing Vero cells with GFP-LC3, and incubating in nutrient media and 4 hours of HBSS, we saw again that there was an increase in the average sizes of autophagosomes produced.

Tracking of GFP-LC3 puncta with Imaris identified that the vesicles mostly lasted less than 1000 seconds (16.6 minutes) regardless of size or time point of starvation. Jahriess *et al* (2008) also assessed lifetimes of autophagosome puncta within cell lines. They noted the lifetime of vesicles to be around 13 minutes, which fits in with the timeframe of the autophagosomes seen in Vero cell tracking of puncta within this research. By tracking specific vesicles over time, we could see that these autophagosomes are rapidly turning over in this timeframe, and that vesicles appeared to grow to over 1μm with late starvation (>3hours). In nutrient media and across starvation, these all co-localised with Lysotracker when using Imaris software. We concluded that this meant that autophagosomes were not persisting throughout starvation until 4 hours of HBSS, but were constantly being degraded at the lysosomes throughout starvation.

The ability to use Imaris to quantify a visual image of autophagy using LC3B will now be explored to assess autophagy within Isolated GI epithelial organoid cultures.

Chapter 5:

Analysis of autophagy in human biopsy samples and mouse organoid cultures.

Chapter 5 – Analysis of autophagy in human biopsy samples and mouse organoid cultures

---

5.1) Aims.

Autophagy gene Atg16L1, and microbial sensor NOD2, have both been identified as risk alleles for Crohn's disease. The aims of this chapter are to see if it is possible to carry out a quantitative analysis of autophagy in the context of Crohn's disease by studying primary gut epithelial tissue taken from human biopsy, or generated by mouse intestinal organoid culture. If successful this will allow the effects of risk alleles on autophagy to be studied in the context of Crohn's disease by analysing human biopsy material from Crohn's disease patients and/or through studies of intestinal organoids generated from mouse models of Crohn's disease.

5.2) Development of gut organoid cultures.

The epithelium of the intestine regenerates every 4 to 5 days, with cells at the top of villi being shed into the lumen. The epithelial layer is maintained by intestinal stem cells, which produce all the cells within the epithelial wall. The stem cells are located at the base of the crypt in the colon, or at the +4 position above the Paneth cells in the small intestine, and differentiate into enterocytes (absorptive), enteroendocrine (hormone releasing) and goblet (mucous secreting) cells (Reya *et al*, 2005). The microenvironment (or stroma) around each crypt allows regulation of crypt formation.

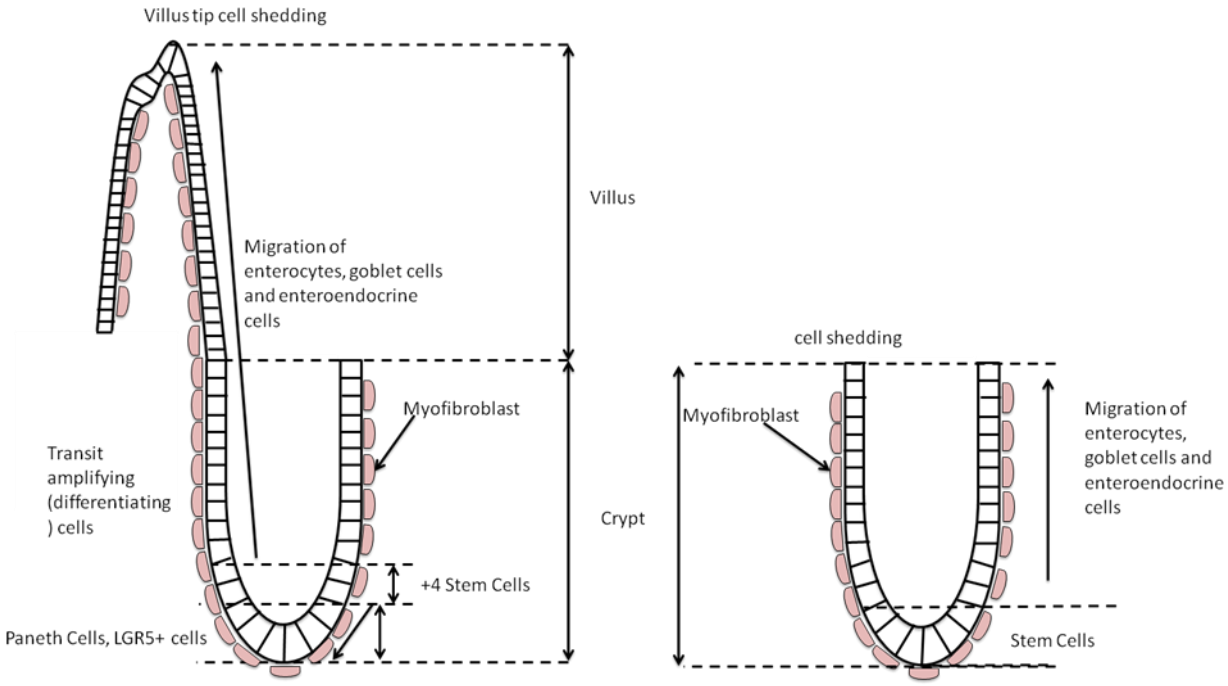

Figure 5.1 - The organisation of the small intestine and colon epithelia. In the small intestine, paneth cells and LGR5+ cells reside at the base of the crypt. The stem cells here, and at the +4 position produce transit amplifying cells which differentiate as they migrate up the crypt. The differentiated cells include enterocytes, goblet cells and enteroendocrine cells. These replace cells lost at the top of the villi, into the lumen of the small intestine. The colon (right) contains LGR5+ stem cells at the base, which produce transit amplifying cells which differentiate as they migrate up the crypt. The differentiated cells include enterocytes, goblet cells and enteroendocrine cells.

The differentiation and movement of cells up the crypt and villus is largely dependent on the Wnt-signalling cascade which is maintained by a Wnt gradient running from the crypt base (high Wnt) to the villus tip (low Wnt). Activation of this pathway is indicated by movement of β -Catenin into the nucleus leading to expression of 'stem cell maintenance' proteins. BMP signalling has been implicated in maintaining stem cell self-renewal by inhibiting the Wnt- β-Catenin signalling pathway (He *et al*, 2004). Inhibitors to BMP signalling such as Noggin are secreted from the myofibroblasts to inhibit this Wnt signalling and maintain a constantly differentiating epithelial layer (Shaker *et al*, 2010). Maintenance of Wnt signalling ex vivo has been shown possible by R-Spondin, which has been shown to enhance β Catenin signalling to the nucleus in stem cells of the

crypt, much like Wnt does typically in all cells expressing the Wnt receptor on their plasma membrane. In crypt stem cells, β-Catenin nuclear localisation causes expression of 'stem cell maintenance' proteins. R-spondin can bind to crypt stem cell specific marker Lgr5, whose expression is controlled by Wnt signalling to the nucleus (Van Der Filer *et al*, 2007). R-spondin is able to activate Wnt-signalling by binding Frizzled receptor on the plasma membrane of stem cells in the crypt, initiating dissociation of the destruction complex within the cell, to allow β-Catenin to localise to the nucleus and initiate gene expression (Sato 2009, de Lau, 2011). Sato *et al* (2009) found that incubation of Lgr5 positive cells from murine small intestines, grown in media containing R-spondin and Bmp inhibitor Noggin, can be used to grow full crypts and maintain crypt organoid cultures. This is all without the stem cell niche present. As R-spondin targets stem cells specifically to initiate β-Catenin signalling, it can be used to maintain this cell population in an ex vivo culture. Another important growth factor in the maintenance of the epithelial layer of the GI tract is Epidermal Growth Factor (EGF). EGF has been shown to induce small intestine epithelial cell proliferation within mice (Malo *et al*, 1982), and Goodlad *et al* (1991) saw that mice fed with EGF had longer crypt lengths than those without EGF.

Sato *et al* (2009) used the above information to formulate a medium to maintain Lgr5 positive stem cells 'in vitro' and from there generate SI organoids. The media contains EGF, R-Spondin and the BMP inhibitor Noggin. Organoids are grown within a 3D matrix termed Matrigel. This contains laminin and collagen IV, and provides structural support for epithelial cultures (Taub *et al*, 1990, Sato *et al*, 2009). The presence of laminin in the Matrigel has been shown to be important in mimicking the normal crypt base environment, which has high levels of laminin α1 and α2. Sato *et al* (2011) , believe that this prevents anoikis, cell death after detachment of cells from their extracellular matrix

(ECM). Sato *et al* (2011) also found that human colon and small intestine organoids can be generated using similar methods.

5.3) Growing 3D cultures of gut organoids.

As described above recent developments in stem cell research show that crypt-villus organoids can be grown in 3D culture from mouse or human intestinal stem cells (Sato *et al* 2009, 2011). Unlike transformed cells the organoids differentiate to make all 4 types of mature cells seen within the gut 'in vivo'. This includes enterocytes, goblet cells, enteroendocrine cells and Paneth cells. These cells are fully polarised with well-defined apical and basolateral surfaces and form tight junctions and are contained within crypt-villus structures with a 3 dimensional architecture similar as seen 'in vivo'. Organoids generated from small aggregates of stem cells and Paneth cells isolated from mouse small intestinal crypts first form spherical cysts. The stem cells divide to produce daughter cells that differentiate producing enterocytes, goblet cells, enteroendocrine cells and Paneth cells while transit amplifying (differentiating goblet, enterocyte and enteroendocrine) cells move to the villus tip, and as seen 'in vivo', undergo apoptosis (Figure 5.1).

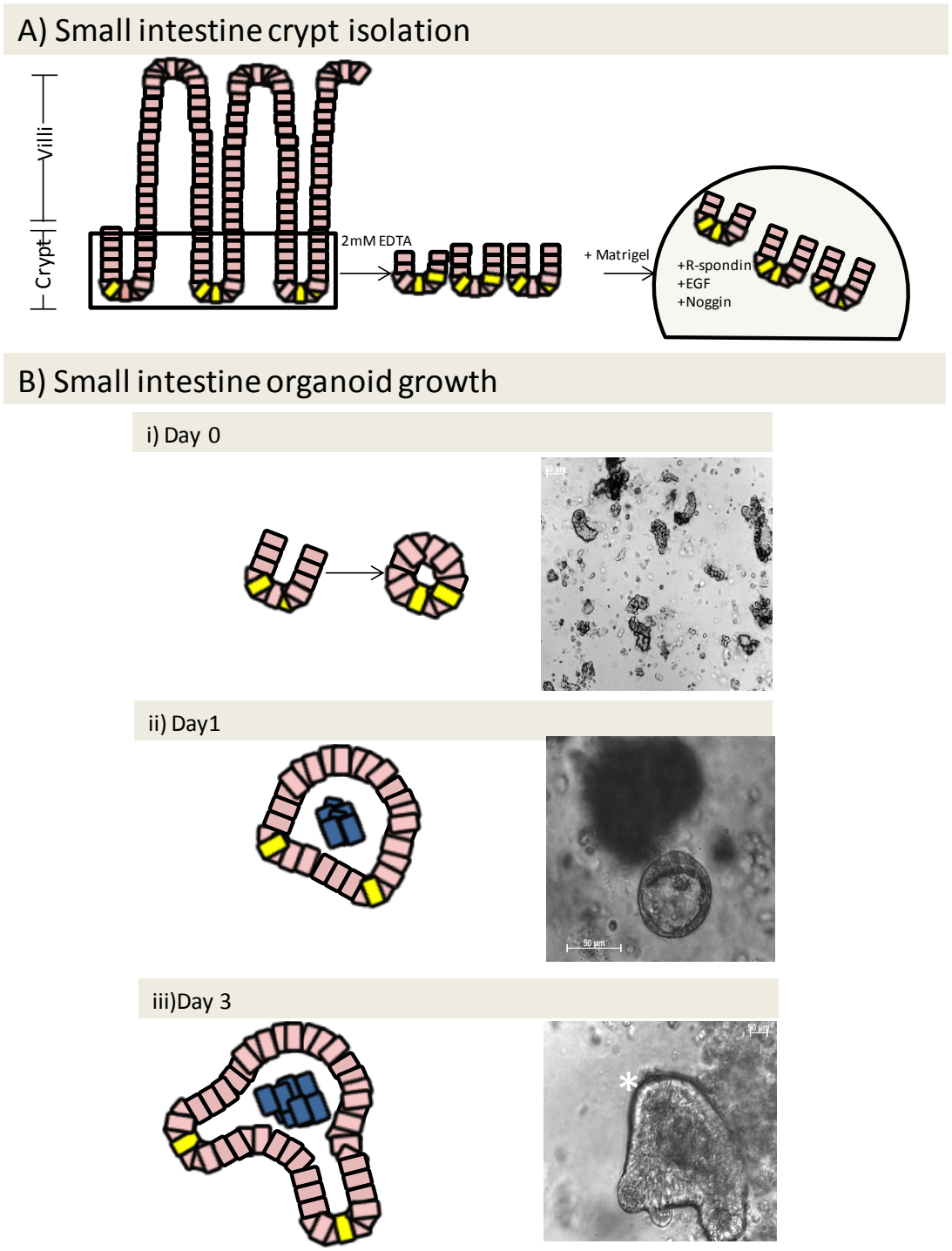

Figure 5.2 - 'In vitro' culture of organoids from mouse small intestine. Panel A. Representative diagrams of small intestine epithelia displaying crypts (base, squared off) and villi (top). Stem cells are shown in yellow in the base of the crypts. **Panel B**. Crypts aggregates are released by washing dissected small intestine in 2 mM EDTA and then filtered to remove broken tissue and larger villi. The crypts are resuspended in Matrigel and incubated in growth factors and form small spherical cysts (day 1). Cysts differentiate into organoids with obvious crypt villus projections after 3 days. Representative phase contrast images are shown next to diagrams. Scale bars = 50 µm.

5.3-a) Organoid culture from mouse intestine.

The production of mouse intestine organoids can be seen in Figure 5.2. Figure 5.2A shows a schematic identifying the methodology for isolation of crypts from the small intestine. The crypts are at the base of each villus, with the stem cells shown in yellow at the base of each crypt. Crypts are isolated from this structure by incubation in 2mM EDTA to chelate calcium followed by manual shaking in PBS. The crypts are then resuspended in Matrigel and cultured with nutrient media containing the stem cell Wnt signalling agonist R-spondin1, EGF and the BMP antagonist Noggin. Figure 5.2B shows a diagram (left hand side) and a brightfield image (right hand side) of the development of small intestine organoids. Crypts released at day 0, just after isolation, are shown in Figure 5.2B-i, with small cysts being made from isolated crypts during this time. Larger cysts appear at day 1 (Figure 5.2B-ii), and organoids containing new crypts, seen as buds, are formed at day 3-post crypt isolation (Figure 5.2B-iii). Stem cells are shown in yellow, and cells shed from the crypts into the lumen of the organoid following apoptosis are shown in blue within the schematic diagrams.

Figure 5.3 shows an organoid culture of crypts taken from mouse colon. The colon epithelium contains crypts but no villi, and the schematic in Figure 5.3A shows that crypts also contain stem cells at their base (in yellow). These can also be isolated with 2mM EDTA, and manual shaking in PBS to release isolated crypts, which are then resuspended in Matrigel containing Rspondin1, EGF, and Noggin. Figure 5.3B shows colon crypts viewed by microscopy. The colon crypts are longer (100μm) than those

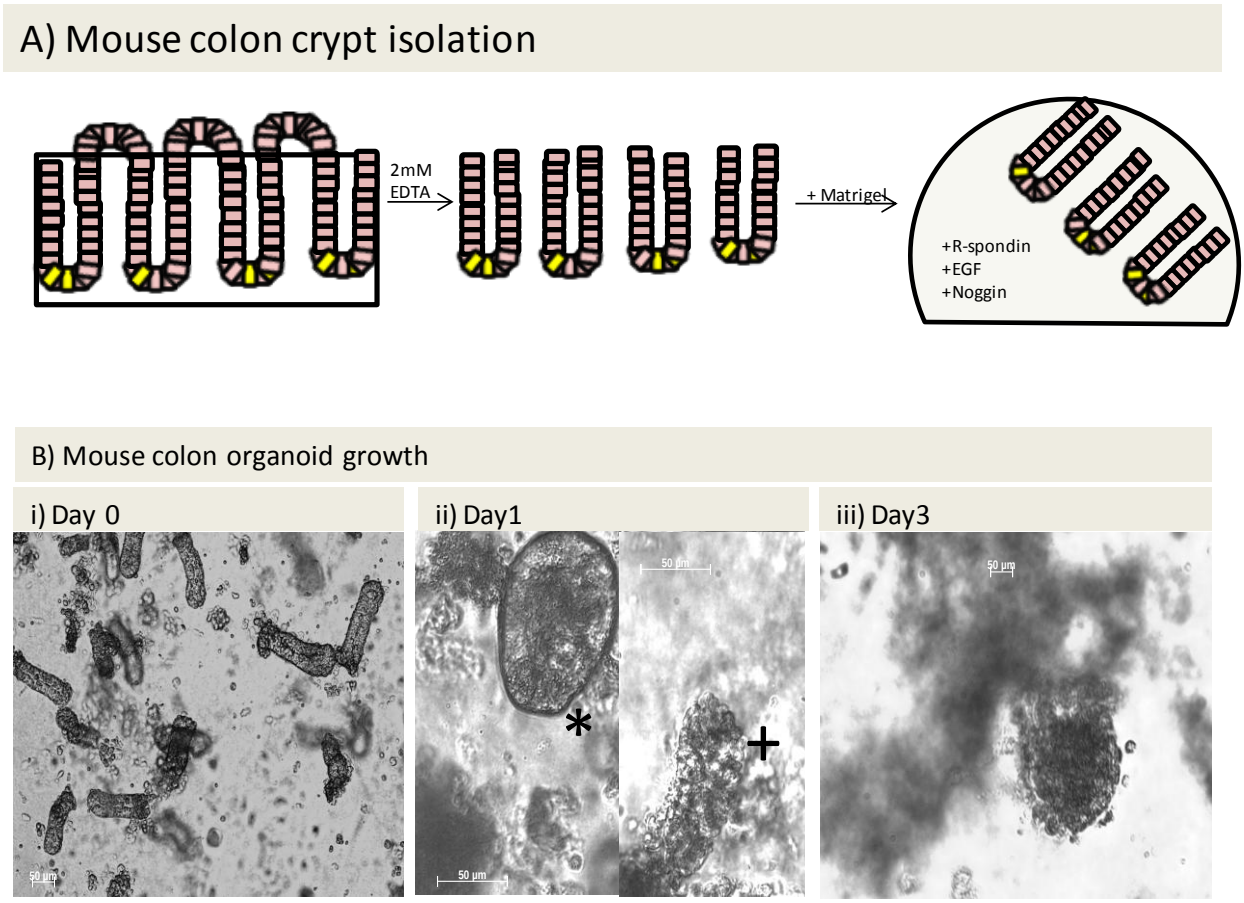

Figure 5.3 - 'In vitro' culture of organoids from mouse colon. Panel A. Representative diagrams of colon epithelia displaying crypts (base, squared off) and villi (top). Stem cells are shown in yellow in the base of the crypts. **Panel B**. Crypts aggregates are released by washing dissected tissue in 4 mM EDTA and then filtered to remove broken tissue and larger villi. The crypts are resuspended in Matrigel and incubated in growth factors and from small spherical cysts (day 1) cysts differentiate into to organoids with obvious crypt villus projections after 3 days. Representative phase contrast images are shown. Scale bars = 50µm.

isolated from small intestine (30-50μm) On day 1, small numbers of spherical cysts were present in the Matrigel, as shown with an '*' in Figure 5.3B-ii. However, most crypts appeared to dissociate, as shown with a '+'in Figure 5.3B-ii. Unlike the small intestinal cysts, the colon cysts did not form buds, indicating formation of new crypts, at day 3. The colon crypts therefore underwent crypt to cyst transition, but failed to divide and differentiate further.

5.3-b) Organoid cultures from human biopsy.

The organoid culture system was applied to human biopsy samples taken from small intestine (Figure 5.4A) and colon (Figure 5.4B). Crypts were isolated using a similar methodology to mouse crypt isolation, using 4mM EDTA instead of 2mM EDTA. It was difficult to identify crypts within cell aggregates isolated from small intestine biopsies however cysts were seen in the Matrigel at day 1 (Figure 5.4A-i) and day 2 (Figure 5.4A-ii) post-isolation. The cysts did not form buds, indicating lack of formation of new crypts. Human colon crypts were isolated from human biopsies and readily seen after isolation (Figure 5.4B-i). These were much longer (500μm-1000μm) than those isolated from mouse (100μm), and formed cysts when grown in human colon crypt culture media containing Wnt3A (Figure 5.4b-ii,) The long crypt structures could be maintained for at least 2 days in organoid media lacking Wnt 3A (Figure 5.4b-iii).

5.4) Analysis of autophagosomes within primary intestinal tissues.

Genes can be introduced into by transfection of plasmids. This can be done chemically, by electroporation, or by using cationic lipids to capture negatively charged DNA and enter the cell by fusing with the plasma membrane. Although transfection has been shown to be possible in primary cultures (Maurisse *et al*, 2010), the efficiency of gene expression is very low. It was therefore important to develop a different method for

delivering GFP-tagged LC3 protein into organoid and crypt cultures. This section describes the use of replication defective viruses for gene delivery into crypt cultures. Replication defective adenoviruses are generated by removing E1 and E3 genes. The E1 genes are essential for replication and the deletion of E3 provides space for insertion of 'trans genes'. Adenoviruses are generated using a 'helper' cell (AD293) that expresses the missing E1 genes.

Kochl *et al* (2006) used GFP-LC3 expressing adenovirus to assess starvation-induced autophagy within primary rat hepatocytes. Autophagosome numbers increased within 2 hours of starvation, demonstrating that viral transduction of primary tissue can be used to study autophagy. This approach was therefore developed for visualisation of autophagy in colon crypt cultures. LC3 puncta were visualised by confocal microscopy and live cell imaging. This form of microscopy uses lasers to scan across the field of view at a point-to-point basis; fluorophores are excited within the sample at a very selective depth of view that eliminates much of the fluorescence above and below the region of interest (Semwogerere *et al*, 2005). Thus, confocal microscopes can be used to take images of cells within 3D structures.

5.4-a) Adenoviral transduction of organoids.

The overall aim of this part of the project was to visualise autophagy in crypts isolated from human or mouse intestine. Figure 5.4A-i and 5.5A-ii show methodologies for testing the effectiveness of adenovirus-mediated transduction of mouse or human small intesine (i) or colon (ii) organoids. Isolation of crypts was performed in the same way as previously described, but adenovirus-expressing GFP-LC3 was added at the point of crypt re-suspension in Matrigel.

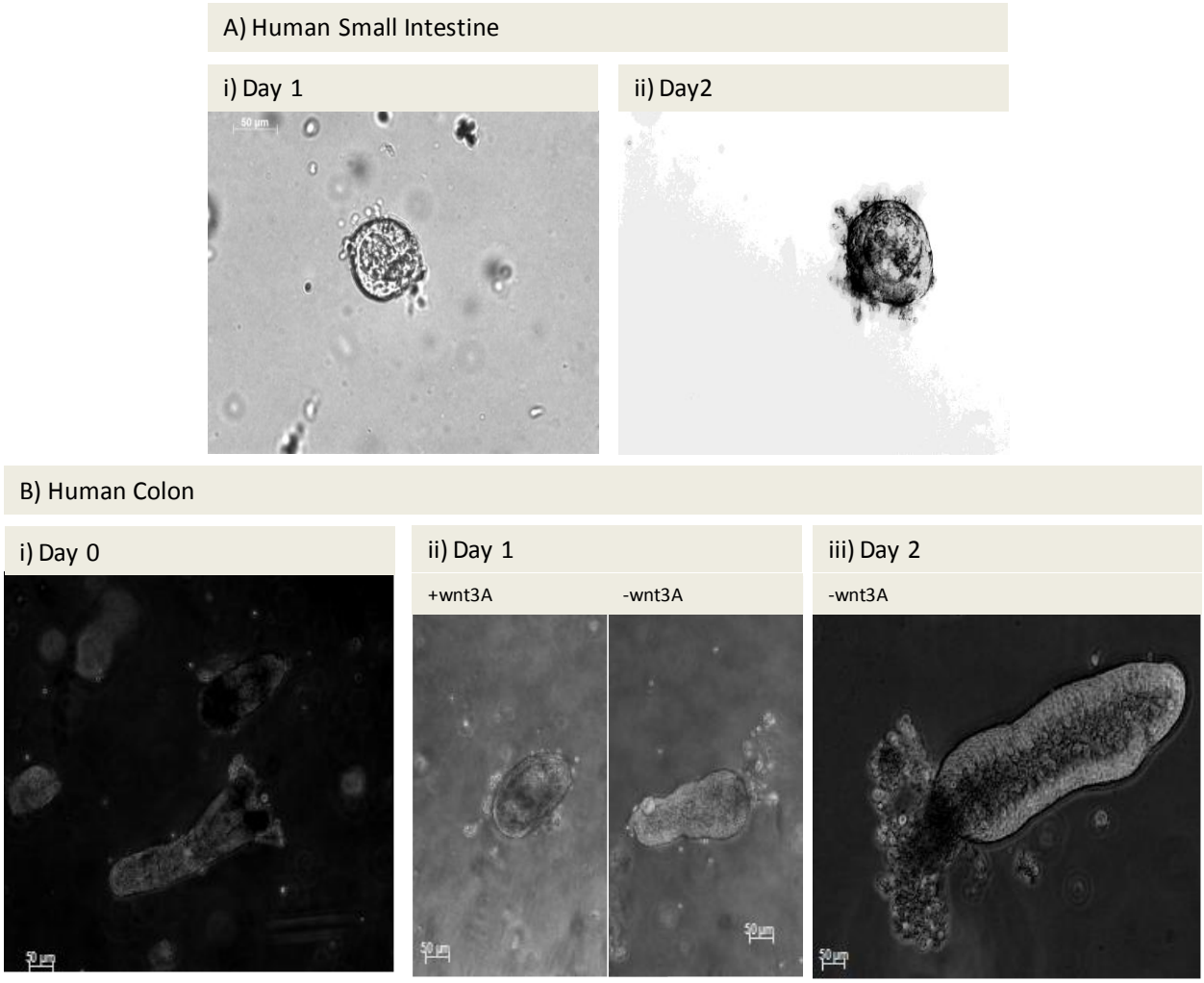

Figure 5.4 - 'In vitro' culture of crypt/organoids from human biopsy. Panel A. Crypts aggregates were released from biopsies by washing in 4 mM EDTA. The crypts were resuspended in Matrigel and incubated in growth factors. Panel A. Brightfield images of material isolated from human small intestine biopsy cultured for one and two days. **Panel B.** Brightfield images of material isolated from human colon biopsy cultured for one and two days in the presence or absence of with Wnt3A as indicated. Scale bars = 50µm.

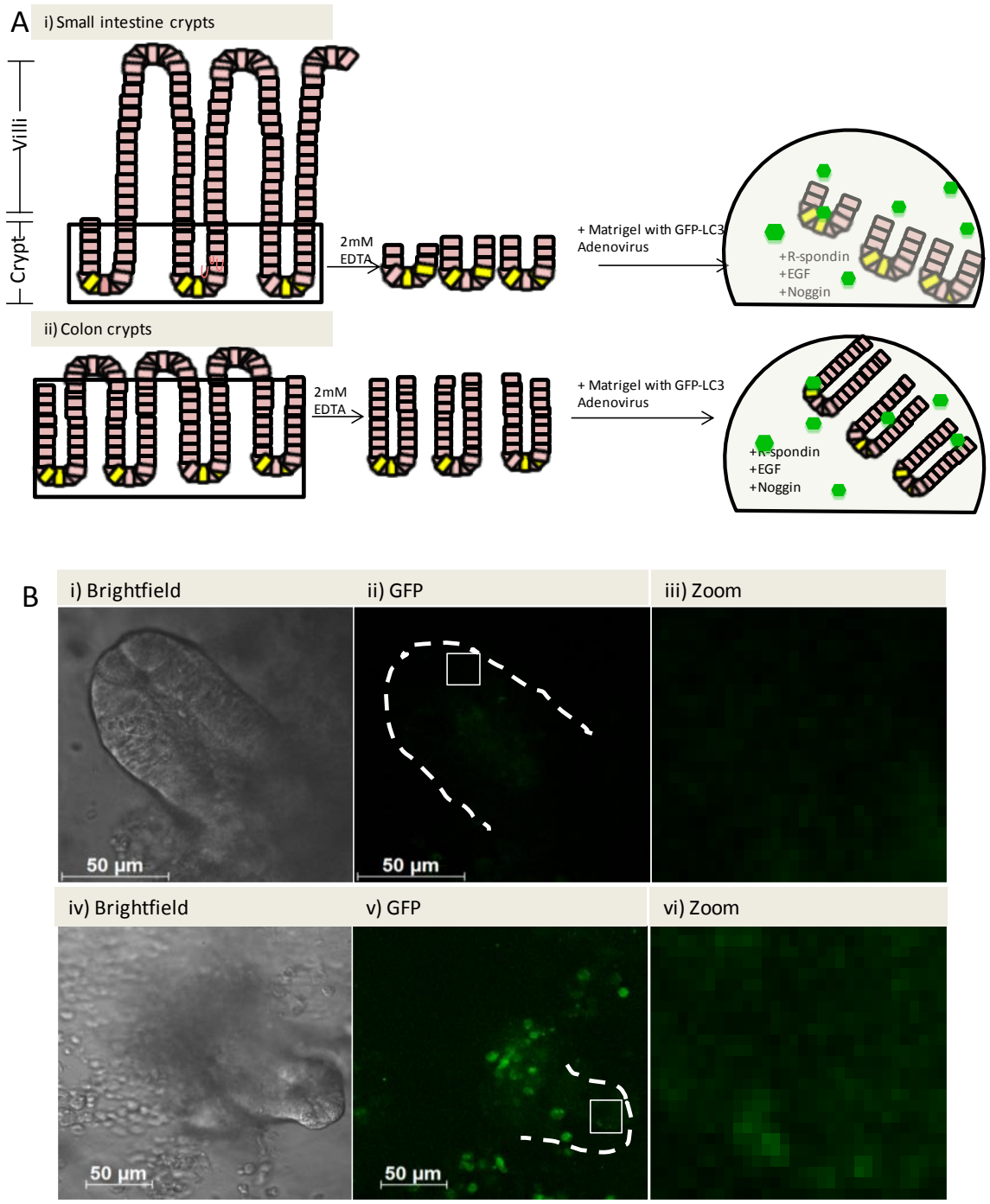

Figure 5.5 - Attempted transduction of mouse crypt cultures with adenovirus expressing GFP-LC3. Panel A. Representative diagrams of small intestine and colon epithelia displaying crypts (base, squared off) and villi (top). Note the villi in colon are much shorter than those seen in small intestine. Stem cells are shown in yellow in the base of the crypts. Crypts aggregates are released by washing biopsy material in 2 mM EDTA. Adenovirus expressing GFP-LC3 is added to crypts cultured in Matrigel. **Panel B.** Two mouse small intestine organoid/crypt cultures are shown as brightfield images (i, iv) and corresponding confocal images of the GFP fluorescence (ii, v). The region of interest in the epithelial layer of the crypts shown is boxed and expanded to the right (iii,vi), with no fluorescence shown. Images were taken with a Zeiss LSM confocal microscope with an x63 objective. Scale bars = 50µm.

Figure 5.5B and C show mouse small intestine crypts at 3 days post isolation and viral transduction. The crypt is shown in brightfield (Figure 5.5B-i), with the GFP channel

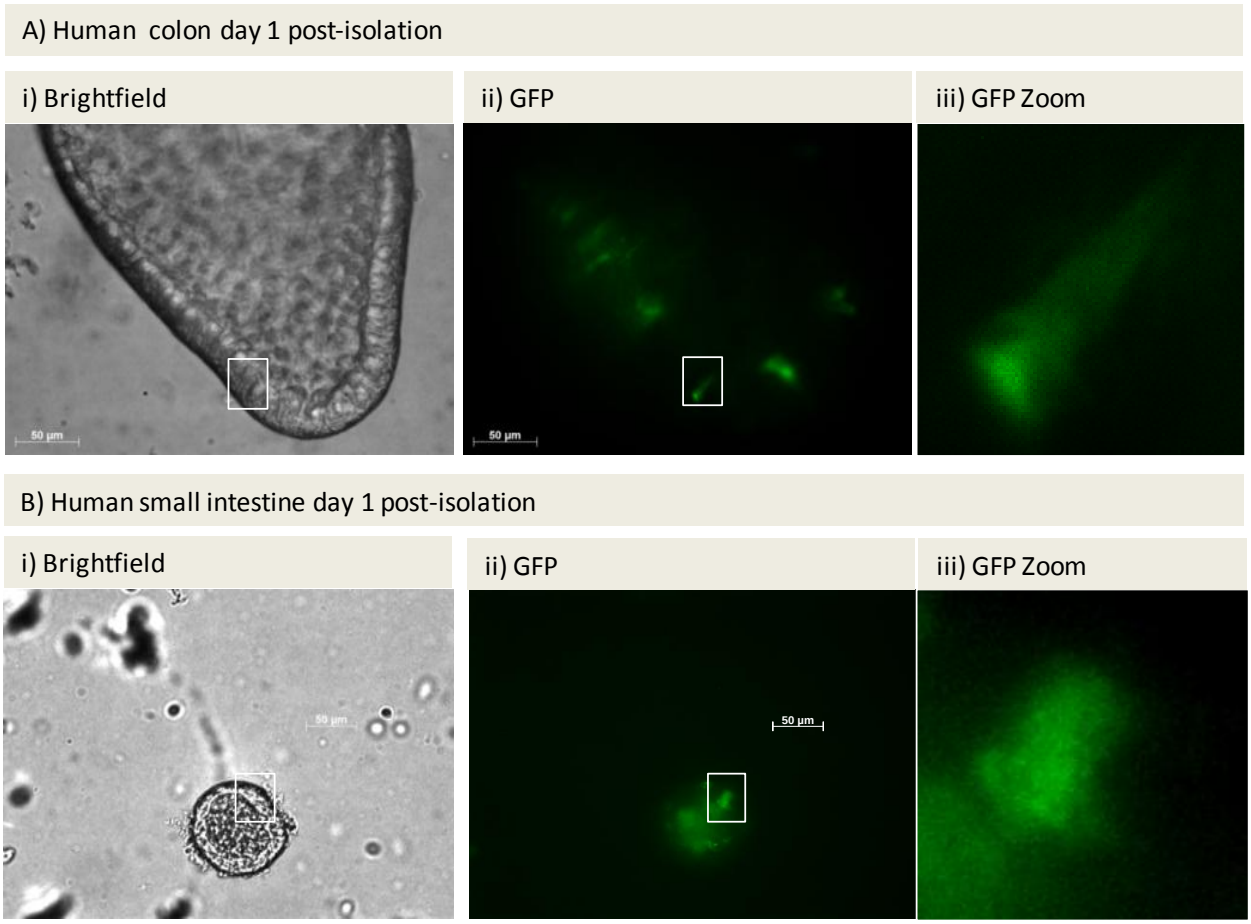

Figure 5.6 -Transduction of human crypt cultures with GFP-LC3 Adenovirus. Crypt aggregates were released by washing biopsy material in 4mM EDTA. Adenovirus expressing GFP-LC3 was added to crypt aggregates cultured in Matrigel. **Panel A.** Human colon crypt culture is shown as brightfield image **(i)** with corresponding confocal images of the GFP fluorescence (**ii**). The region of interest is boxed and expanded to the right (iii). **Panel B.** Human small intestine crypt culture is shown as brightfield image **(i)** with corresponding confocal images of the GFP fluorescence (**ii**). The region of interest is boxed and expanded to the right (iii). Images were taken with a Zeiss inverted brightfield microscope with a x40 objective. Scale bars = 50µm.

Lack of GFP fluorescence in mouse organoids cultured with GFP-LC3 adenovirus is shown in Figure 5.5B-ii,v, and a zoom of the green fluorescence within the epithelial layer of the crypt in Figure 5.5B-iii, vi. After 3 days of growth, GFP signal was absent from the epithelial cells of the crypts shown. However, green cells were seen in the lumen of the crypt and could be seen shedding from the crypt (Figure 5.5 C-ii). These green signals arise from the auto-fluorescence of apoptotic cells and were seen in crypt cultures that had not been transduced with GFP-LC3 adenovirus (not shown).

5.4-b) Adenoviral transduction of crypts cultured from human biopsy.

Figures 5.6A&B show adenovirus transduction of crypts isolated from human colon and small intestinal biopsy following 24 hours of culture within Matrigel. The epithelial layer of the human colon crypt is shown by brightfield microscopy (Figure 5.6A-i) and the GFP-LC3 signal within an area of interest identified by the box is shown at higher magnification in Figure 5.6A-ii and iii. Several cells expressing GFP-LC3 were identified within the epithelial layer. The crypts isolated from small intestine formed cysts (Figure 5.6B-i). The lumen of the cyst showed auto-fluorescence but epithelial cells expressing GFP-LC3 were identified (boxed area). A high magnification of the GFP-LC3 signal is shown in Figure 5.6B-iii.

Human colon crypt cultures were analysed over three days of culture (Figure 5.7A). Green cells were seen along the crypt axis, with this signal persisting throughout 3 days of crypt incubation (Figure 5.7Ai-iii). To test the effectiveness of adenovirus-mediated delivery of GFP-LC3 as a way to study autophagy within these small epithelial cells, the crypt cultures were either incubated in nutrient media (Figure 5.7B-i), HBSS to remove amino acids (Figure 5.7B-ii), or a combination in HBSS and lysosomal inhibitor chloroquine to prevent degradation of LC3 (Figure 5.7B-iii). Crypts were fixed and permeabilised, and viewed using brightfield optics with the fluorescence filters in place to identify epithelial cells expressing GFP-LC3. Regions of interest are boxed and shown at higher magnification in the lower panels. Small puncta were seen within cells in nutrient media (Figure 5.7B-i). The numbers of puncta increased when crypts were treated with HBSS (Figure 5.7B-ii), and showed brighter fluorescence in the presence of chloroquine (fig5.7B-iii).

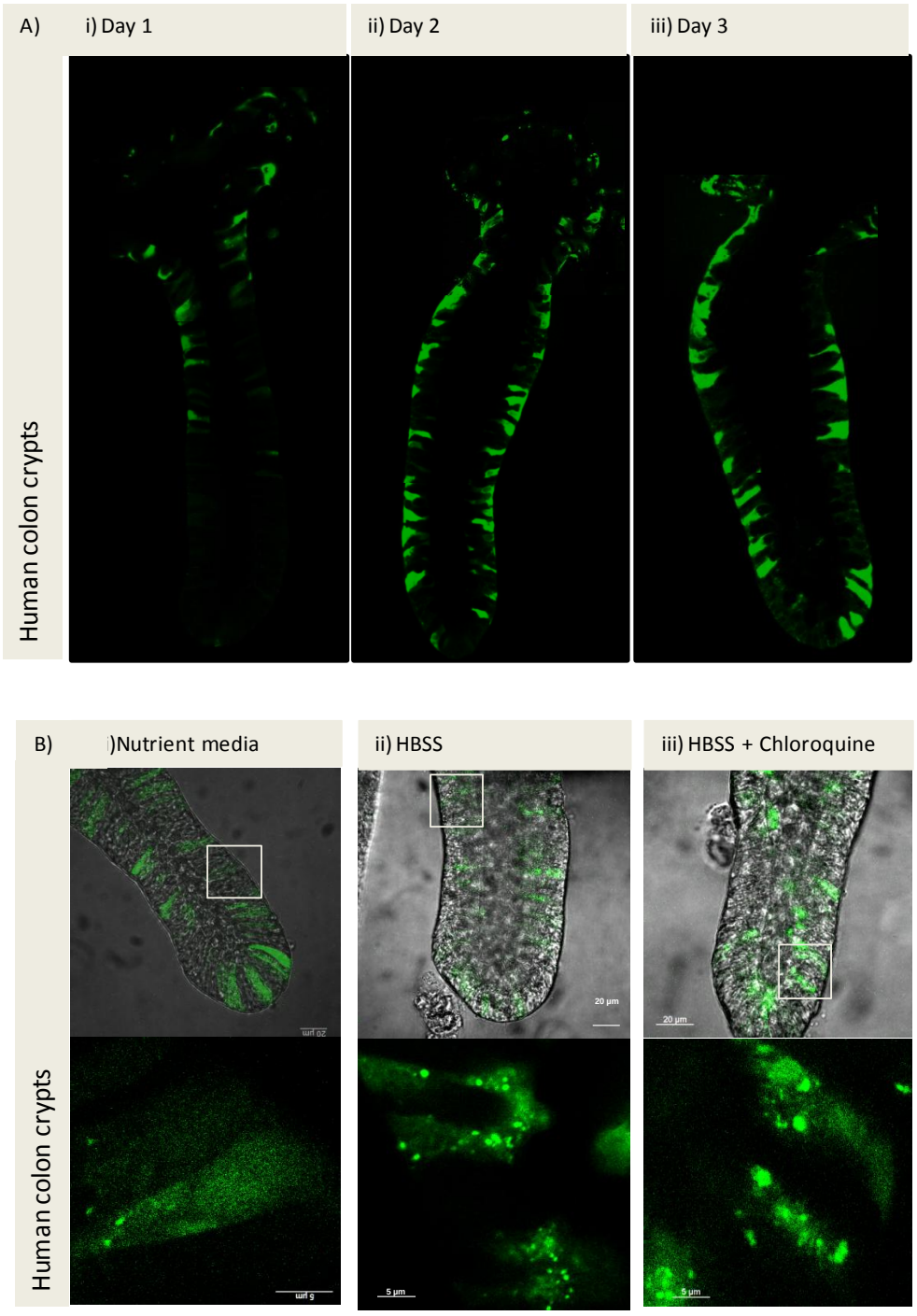

Figure 5.7 - Generation of GFP-LC3 puncta following starvation of human colon crypt cultures transduced with GFP-LC3 Adenovirus. Crypt aggregates were released by washing colon biopsy material in EDTA. Adenovirus expressing GFP-LC3 was added to crypt aggregates cultured in Matrigel for the increasing times. **Panel A.** Confocal microscopy images of the GFP fluorescence in human colon crypts maintained in culture for indicated times **Panel B.** Human colon crypts maintained in culture for three days were incubated in nutrient media **(i),** HBSS for 4 hours **(ii**), or HBSS for 4 hours in the presence of chloroquine **(iii)**. The region of interest is boxed and expanded to show individual epithelial cells (below). Images were taken with a Zeiss LSM confocal microscope with an x63 objective.

5.5) Summary.

Long term culturing of mouse and human mucosa in Laminin-rich Matrigel is a newly defined methodology first displayed by Sato *et al* (2009). Firstly, we show here that mouse small intestine organoids could be grown from crypts isolated from mouse small intestine. Using their methodology colon crypts from mice did not persist or propagate as cysts in the same timeframe after being grown in media containing growth factors. We therefore used mouse small intestine to see if we could express GFP-LC3 signal using an Adenoviral transduction method. This did not appear successful, as no cells within the crypts after formation of organoids appeared to express the GFP signal. New methods using Lentivirus incubation with crypt cells on top of matrigel, have become available and will be used in future experimentation (Onuma et al, 2012). The human crypt culture system favoured the growth of colon crypts above small intestine organoids. The difference here is that the crypts were merely maintained over a lifetime of a few days, compared to the mouse organoids, which made cysts that could form new crypts over 3 days of growth within the Matrigel. However, the colon crypts maintained in Matrigel could successfully be transduced with GFP-LC3 Adenovirus. Overexpression of GFP-LC3 has previously shown no abberant autophagy signals within cells (Tra *et al*, 2011, Muzishima *et al*, 2008). As this fluorescent signal was seen across the whole crypt axis we could therefore use this for later assessment of autophagy activation by starvation, with autophagosomes seen within successfully transduced cells. The ability to use this GFP-LC3 signal will give us the flexibility of assessing autophagy within fixed and live tissue experiments with human colon crypt tissue in the next chapter, by using Imaris analysis of autophagosomes already performed in cell line experimentation in previous results chapters.

Chapter 6:

Quantifying autophagy in primary human colon crypt cultures obtained from biopsy

Chapter 6 – Quantifying autophagy in primary human colon crypt cultures obtained from biopsy

---

6.1) Aims.

GWAS studies have linked mutations in Atg16L1 and NOD2 to susceptibility to Crohn's disease. Travassos *et al* (2010), showed that Atg16L1 binds NOD2 and that activation of NOD2 by muramyl dipeptide (MDP), can induce autophagy suggesting Crohn's disease may result from defects in microbial sensing and autophagy in gut epithelial cells. The aims for this chapter are to combine the methods developed in previous chapters to generate methods to quantify autophagy within human crypt tissue. Autophagy will be assessed following starvation or following incubation with NOD2 ligand MDP to mimic microbial invasion.

6.2) Detection of endogenous autophagy proteins in fixed tissue.

Human colon crypts were cultured in laminin rich Matrigel, fixed and immunostained for autophagy proteins Atg8/LC3, Atg16L1 and SQSTM1 (Figure 6.1). Crypts were maintained in nutrient media, or deprived of amino acids using HBSS to activate autophagy. Crypts were also incubated in HBSS in the presence of chloroquine to activate autophagy but slow degradation of Atg8/LC3 and SQSTM1 in lysosomes. Different antibodies against LC3B were tested in preliminary experiments using colon crypt cultures. LC3B staining proved effective with LC3 antibody from MBL (supplementary Figure 2) but specific staining was not obtained with antibodies from three other sources. The immunofluorescence signal was either absent or gave high background signal at the basal membrane of cells along the crypt. The background staining was due to non-specific binding of primary antibody because the background was absent when secondary antibodies were added alone, or when crypts were

analysed using an IgG1 isotype control, which was formulated to not bind to any known proteins (supplementary Figure 3).

When crypts were analysed with the MBL antibody LC3 puncta were seen in cells maintained in nutrient media and these colocalised with Atg16L1 (Figure 6.1A-i) and SQSTM1 (Figure 6.1B-i) and lysosome marker Lamp1 (Figure 6.1C-i). LC3 puncta were more obvious following starvation in the presence of chloroquine (Figure 6.1A-C-iii) and again Atg8/LC3 colocalised with Atg16L1, SQSTM1 and Lamp1. Having established that autophagy could be activated by removing amino acids from human colon crypts maintained in culture we tested whether the system could be adapted to study autophagy by live cell imaging.

6.3) Detection of GFP-LC3 puncta in crypts transduced with adenovirus.

Crypts were transduced using an adenovirus expressing GFP-LC3 and observed at increasing times by fluorescence microscopy (Figure 6.2). Again, Atg16L1 and SQSTM1 were immunostained in crypts expressing GFP-LC3, and again showed co-localisation between Atg16L1 (Figure 6.2A-i-iii), SQSTM1 (Figure 6.2B-i-iii), and the GFP-LC3 puncta shown within cells. To test the effectiveness of both LC3B and GFP-LC3 being visually the same within crypt cells, we immunostained LC3B in cells expressing GFP-LC3 (Figure 6.2C) and saw localisation of the antibody stain, and GFP-LC3 signal in nutrient media (i) and with chloroquine (ii). Supplementary Figure 1 also shows the interaction of the GFP signal with an anti GFP antibody, indicating this is true GFP fluorescence from the adenovirus expressing GFP-LC3

6.4) Quantitative analysis of autophagosomes in colon crypt cells

6.4-a) Analysis of GFP-LC3 puncta in tissue fixed at increasing times after starvation.

Figure 6.3 shows analysis of colon crypt cells either immunostained against endogenous

A

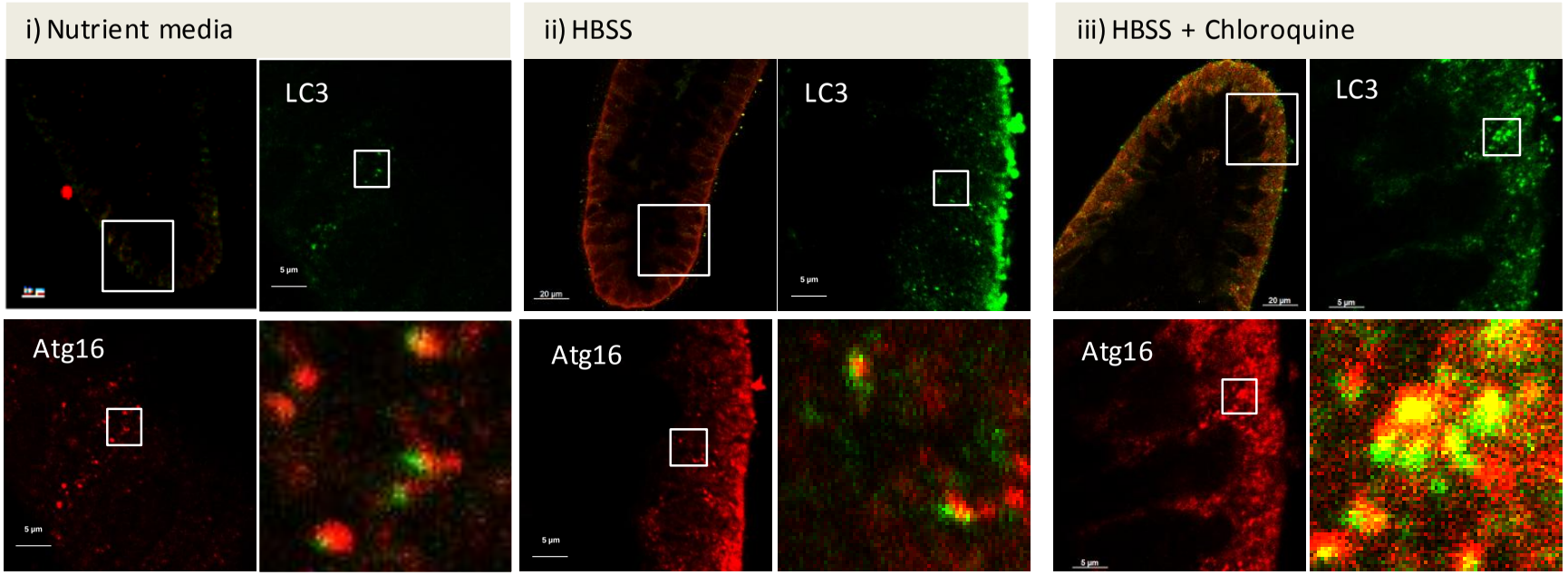
i) Nutrient media
ii) HBSS
iii) HBSS + Chloroquine
LC3
LC3
LC3
Atg16
Atg16
Atg16
5 µm
20 µm

B

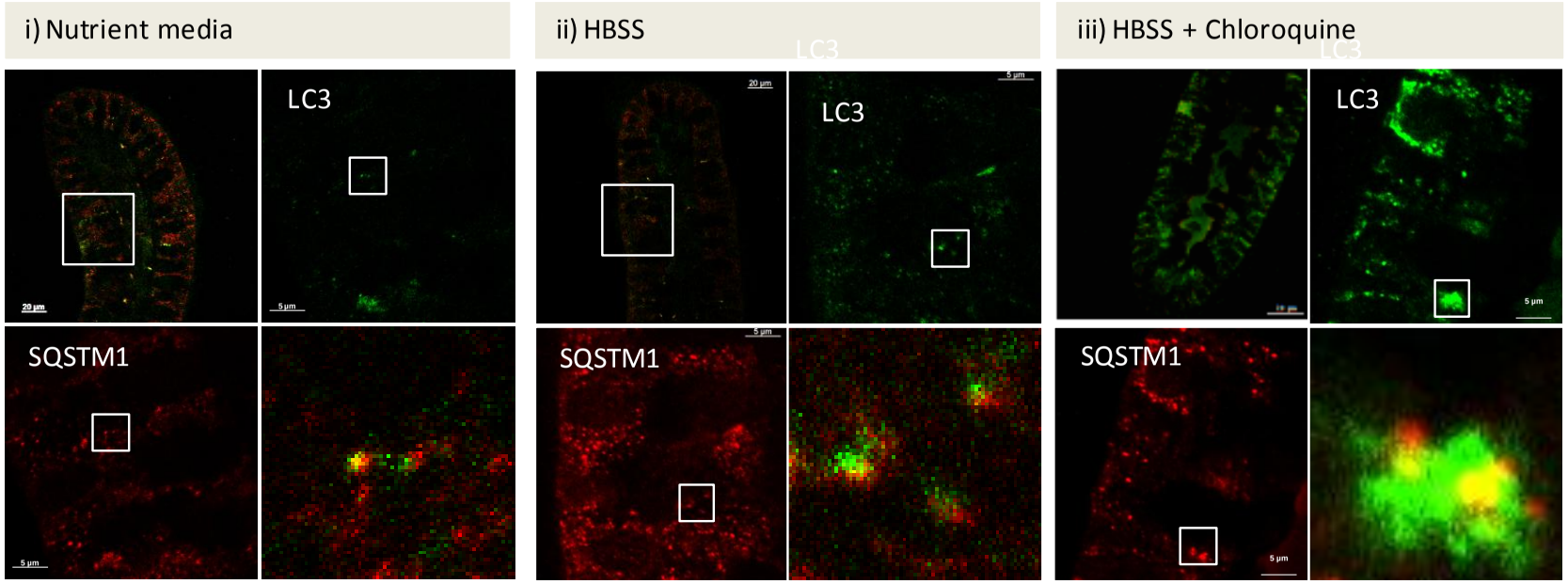
i) Nutrient media
ii) HBSS
iii) HBSS + Chloroquine
LC3
LC3
LC3
SQSTM1
SQSTM1
SQSTM1

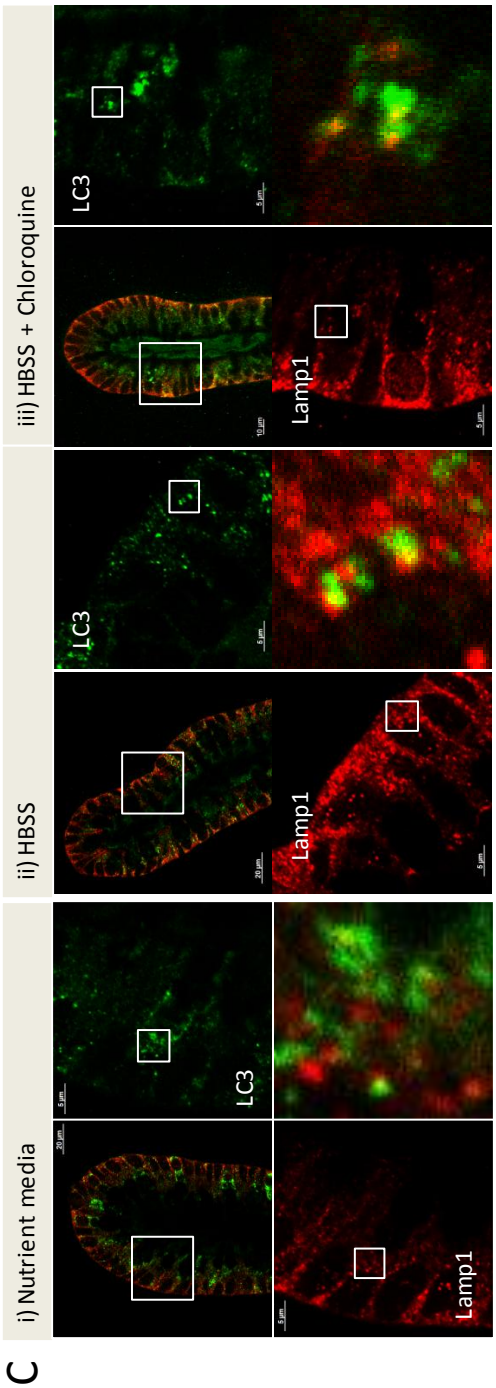

Figure 6.1- Immunofluorescence analysis of endogenous LC3 and other autophagy marker proteins in human colon crypts. Crypt aggregates were released by washing colon biopsy material in EDTA and cultured in Matrigel for one day. Cultures were then incubated in nutrient media **(i)** HBSS for 4 hours **(ii**) or HBSS for 4 hours in the presence of chloroquine **(iii)** as indicated. Crypts were fixed and permeabilised and immunostained for endogenous LC3B (green). **Panel A**, crypts were counterstained for endogenous Atg16L1 (red). **Panel B**, crypts were counterstained for endogenous SQSTM1 (red). **Panel C**, crypts were counterstained for endogenous Lamp1 (red). The top left hand image shows a complete crypt. The white box indicates a region of interest that is magnified to visualise individual LC3 puncta and marker proteins as indicated. A further zoom from this region is shown in the bottom right hand panel of each image, with arrows to mark colocalised puncta. All images were taken with a Zeiss LSM confocal at an x63 objective.

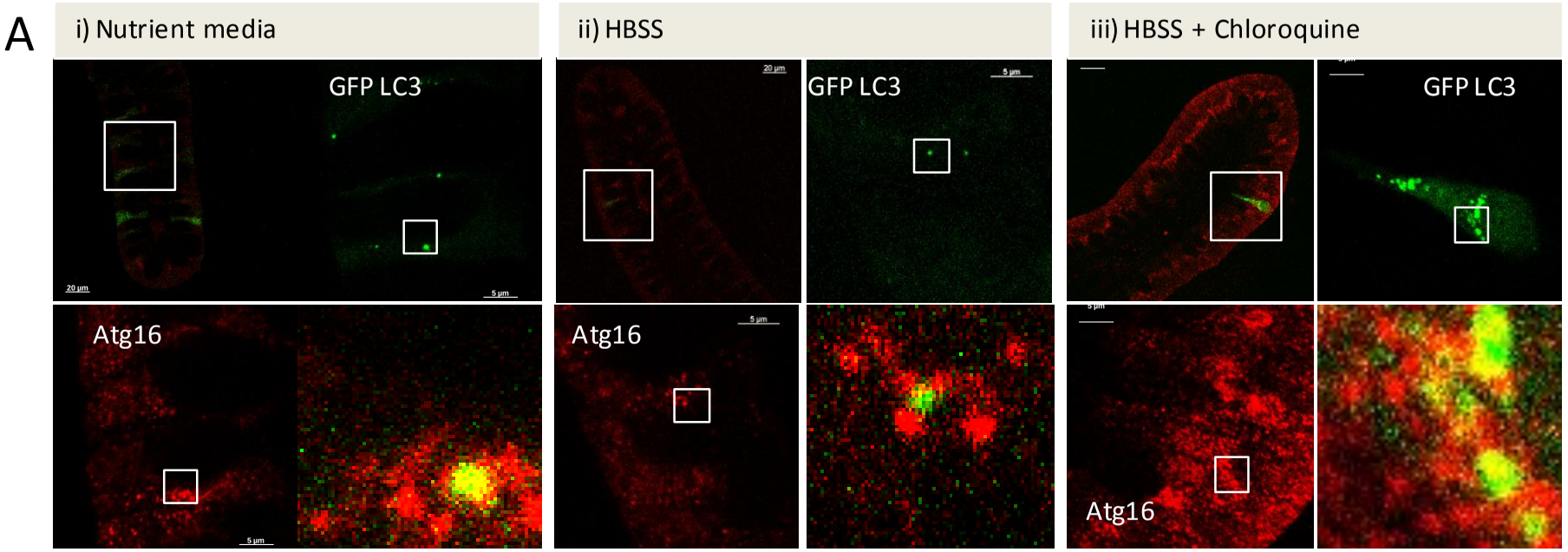
A
i) Nutrient media
ii) HBSS
iii) HBSS + Chloroquine
GFP LC3
GFP LC3
GFP LC3
Atg16
Atg16
Atg16

B

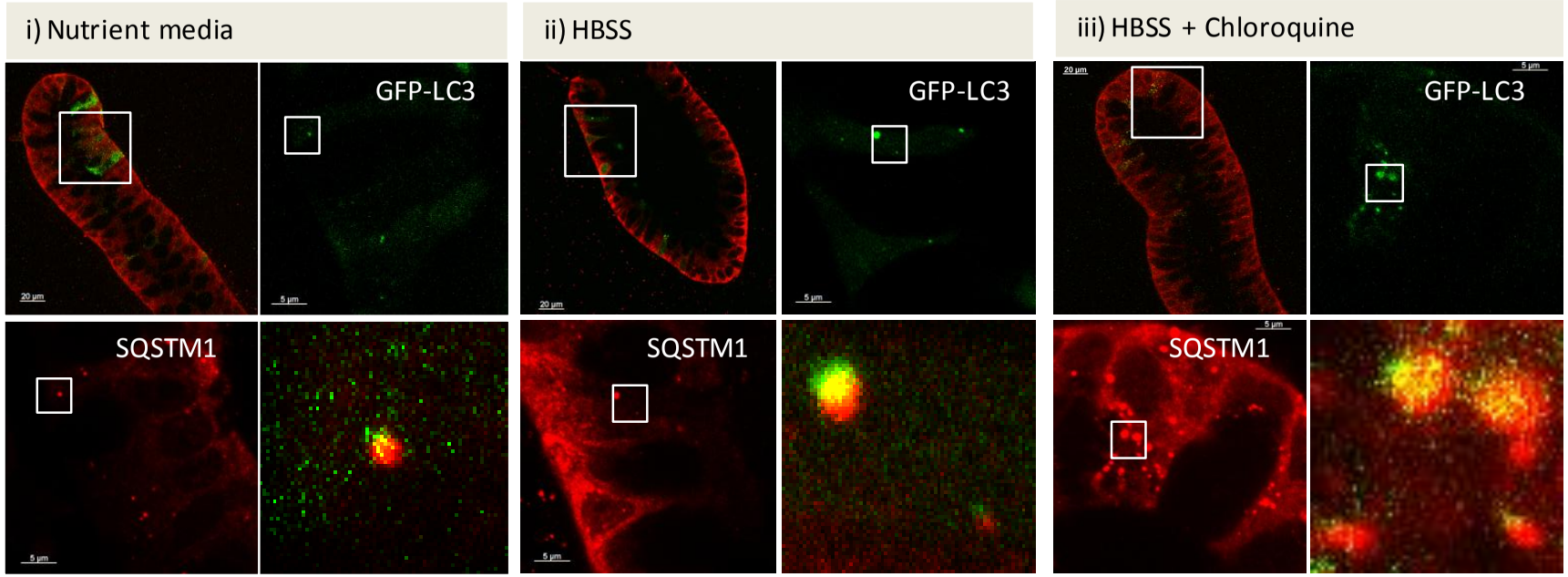
i) Nutrient media
ii) HBSS
iii) HBSS + Chloroquine
GFP-LC3
GFP-LC3
GFP-LC3
SQSTM1
SQSTM1
SQSTM1
20 µm
5 µm
20 µm
5 µm
20 µm
5 µm
5 µm
5 µm
5 µm

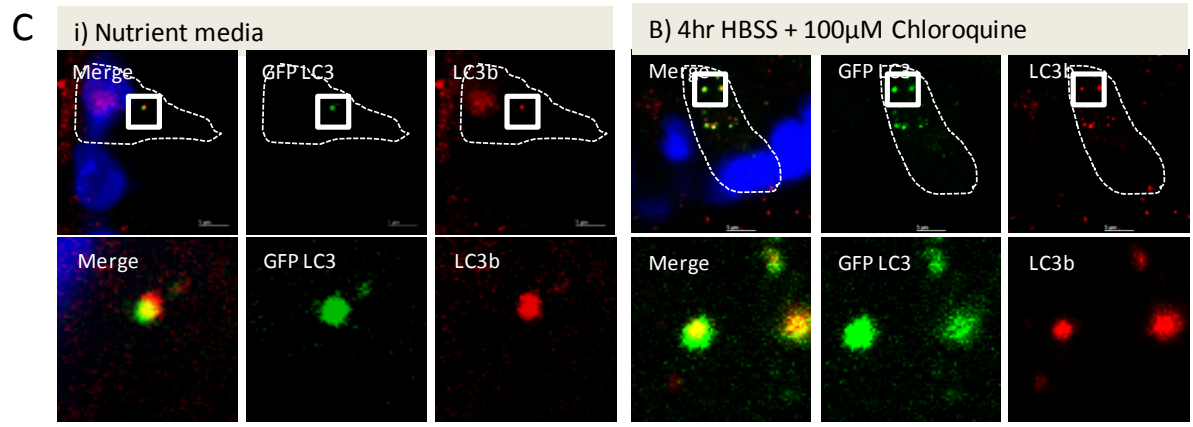

Figure 6.2- Immunofluorescence analysis of autophagy marker proteins in human colon crypts transduced with adenovirus expressing GFP-LC3. Crypt aggregates were released by washing colon biopsy material in EDTA and cultured in Matrigel containing adenovirus expressing GFP-LC3. Cultures were then incubated in nutrient media **(i)** HBSS for 4 hours **(ii**) or HBSS for 4 hours in the presence of chloroquine **(iii)** as indicated. Crypts were fixed and permeabilised and immunostained for endogenous autophagy proteins. **Panel A**, crypts expressing GFP-LC3 (green) were counterstained for endogenous Atg16L1 (red). **Panel B**, crypts expressing GFP-LC3 (green) were counterstained for endogenous SQSTM1 (red). The top left hand image shows a complete crypt. The white box indicates a region of interest that is magnified to visualise individual LC3 puncta and marker proteins as indicated. A further zoom from this region is shown in the bottom right hand panel of each image, with arrows to mark colocalised puncta. **Panel C**, crypts expressing GFP-LC3 (green) were counterstained for endogenous LC3 (red). The dotted line outlines an individual epithelial cell and the box identifies GFP puncta. The lower images show location of endogenous LC3 (right) and merged images (left). All images were taken with a Zeiss LSM confocal at an x63 objective.

LC3B (A), or after transduction with GFP-LC3 expressing adenovirus (B). The images are compared with an identical experiment carried out using Vero cells. Puncta diameters and numbers were analysed before and after incubation in HBSS. Data from 3 replicate experiments are shown in Figure 6.3. the LC3 puncta increased in size and number following starvation. In Vero cells, diameters increased from 0.53µm +/-0.15 to 0.93µm +/- 0.17 in fixed immunostained cells, and from 0.56 +/- µm 0.17 to over 1 µm +/- 0.37 when analysed as GFP-LC3 puncta. The Imaris rendering shows that with HBSS for over 3 hours, most of the vesicles appear yellow or red indicating diameters between 0.7 and 1µm.

Colon crypt cells also showed increases in number and diameters of LC3 puncta following transfer to HBSS. There were on average 2.2 +/-2 autophagosomes per cell in nutrient media when analysed by LC3B immunostaining, and 1.4 +/- 2 per cell in live cells when analysed for GFP-LC3 puncta. In nutrient media, autophagosome diameters were an average of 0.25 μm +/- 0.14 following immunostaining and 0.45 μm +/- 0.1 in cells expressing GFP-LC3. Following transfer to HBSS a proportion of the autophagosomes exhibited larger diameters and appeared as yellow-and red puncta in rendered images (Figure 6.3-Bi-ii). Diameters were calculated to be 0.56 μm +/- 0.12 following immunostaining for LC3B and 0.6 μm +/- 0.05 when analysed in cells expressing GFP-LC3 in nutrient media. Numbers of LC3 puncta in crypt cells increased to 5.8 +/-2.2 puncta after transfer to HBSS and GFP-LC3 puncta increased to 6.4 +/-2.5 puncta. The data indicates that numbers of LC3 puncta increased in diameter and number following incubation in HBSS. Importantly the data obtained from GFP-LC3 puncta correlated well with the analysis of endogenous immunostaining for LC3 (Figure 6.C). Figure 6.3-D compares the properties of autophagosomes in colon crypt cells (i) with Vero (ii) and Caco2 (iii) cells. In all three cells, the vesicles all appear to be similar size, but the crypt cells generate fewer autophagosomes.

number of autophagosomes > 0.75μm also moving from around 0.4 puncta/cell in nutrient media, to 1-2 puncta per cell after HBSS incubation. There was a clear increase in diameter following starvation but this was not affected by the location of the cell along the isolated crypt. Supplementary Figure 4 shows the localisation of the GFP-LC3 signal to both Goblet cells (Muc2 staining) and enteroendocrine cells (chromogrannin A staining), indicating that this transduction is not specific to any cell type.

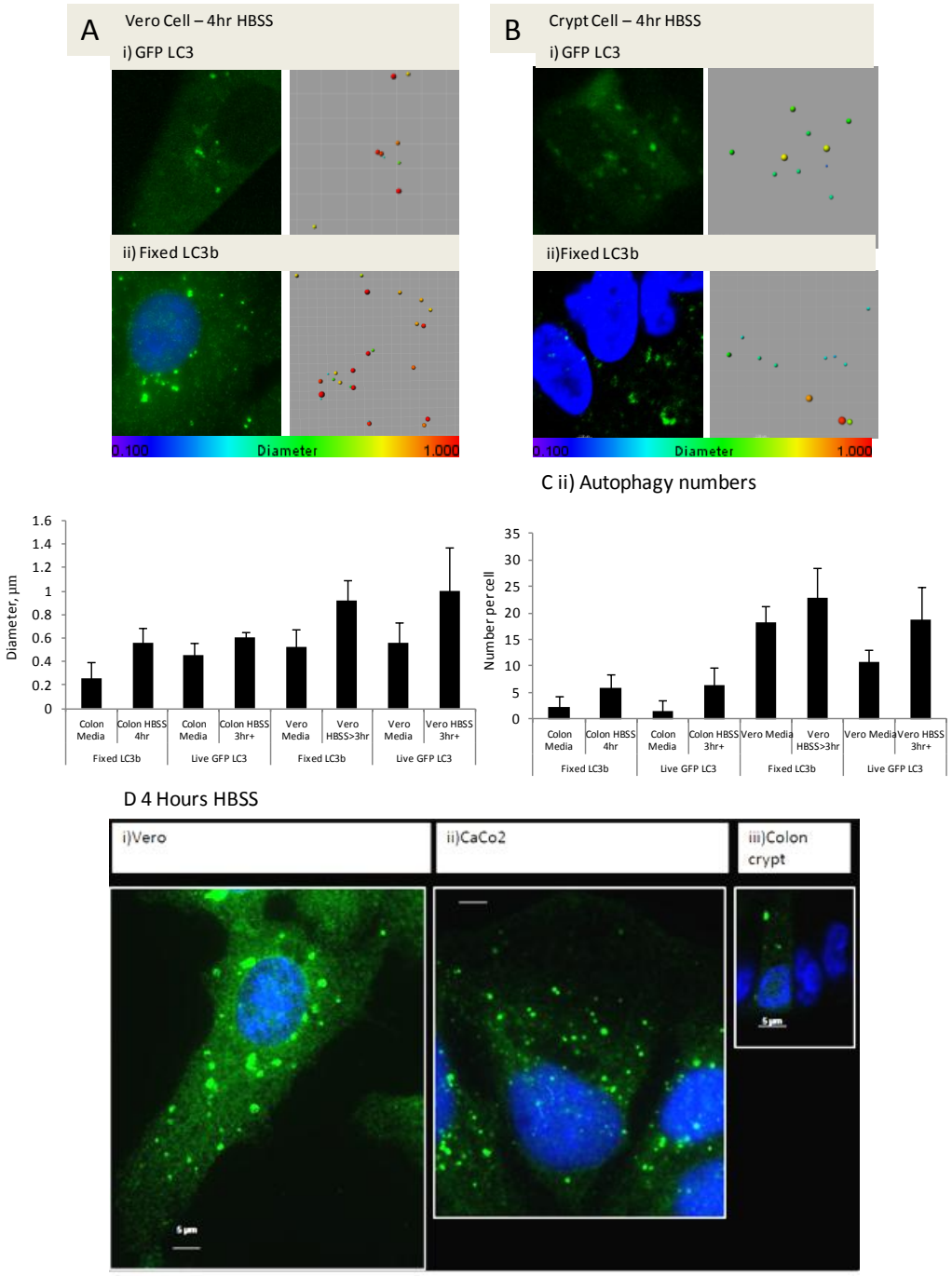

Figure 6.3 - Comparison of Vero cell and Colon crypt cell Imaris quantified endogenous and GFP-LC3 positive autophagosomes. Vero cells **(Panel A)** or colon crypt cells **(Panel B)** were transduced with GFP-LC3 Adenovirus and incubated for 4 hours in HBSS and imaged by live cell microscopy (i) or fixed and stained for LC3B (Green) and DAPI (Blue) after 4 hours of HBSS incubation (ii). The left hand panels show the fluorescent images of representative cells used for Imaris analysis of puncta number per cell and diameter on average at 4 hours of HBSS. The right hand panels show Imaris rendered LC3 puncta. Rendered puncta were colour coded so that small vesicles (0.2µm) are blue, medium sized vesicles (0.5µm) are coloured green, and large vesicles are colour coded yellow, orange or red (0.7-1.0 µm). **Panel C**- The Bar charts show the average diameters (Ci) or numbers of autophagosomes per cell (Cii) in fixed LC3B stained, and live GFP-LC3 expressing Vero and colon crypt cells. Comparisons of Vero (Di), CaCo2 (Dii) and Colon crypt cells (Diii) cells to scale with each other are shown with LC3 in green. Nuclei are stained in blue. All images were taken with a Zeiss LSM confocal at an x63 objective.

6.4-b) Analysis of LC3 puncta in cells at different positions along the crypt axis

Figure 6.4 shows representative images of crypt cells expressing GFP-LC3 at the base, mid region and top of crypts from 3 separate experiments following incubation in control nutrient media (i) or HBSS for 4 hours (ii). Fluorescent images are shown on the left with green GFP-LC3 and blue DAPI (nucleus). Imaris rendered images are presented on the right. The diameters of LC3-puncta were colour coded using a heat map where blue represents puncta less than 0.3μm, green puncta are 0.5μm and red puncta 1.0μm or greater. Bar charts in 6.4-B show average number of autophagosomes per cell at these points along the crypt axis in nutrient media (Figure 6.4B-i), or following 4 hours in HBSS (Figure 6.4B-ii). Graphically, the average diameter of autophagosomes in cells along the crypt axis in nutrient media are shown in Figure 6.4B-iii, with the average diameter of autophagosomes in cells across the crypt axis in crypts incubated for 4 hours in HBSS are shown in Figure 6.4B-iv. The overall numbers of autophagosomes whose diameter are less than or greater than 0.75μm, are shown in Figure 6.4B-v. There were no obvious changes in number of autophagosomes across the crypt axis, as they contain around 2 puncta per cell in nutrient media, and 5 puncta per cell after HBSS starvation. The diameters of autophagosomes were also on average a similar size with the average

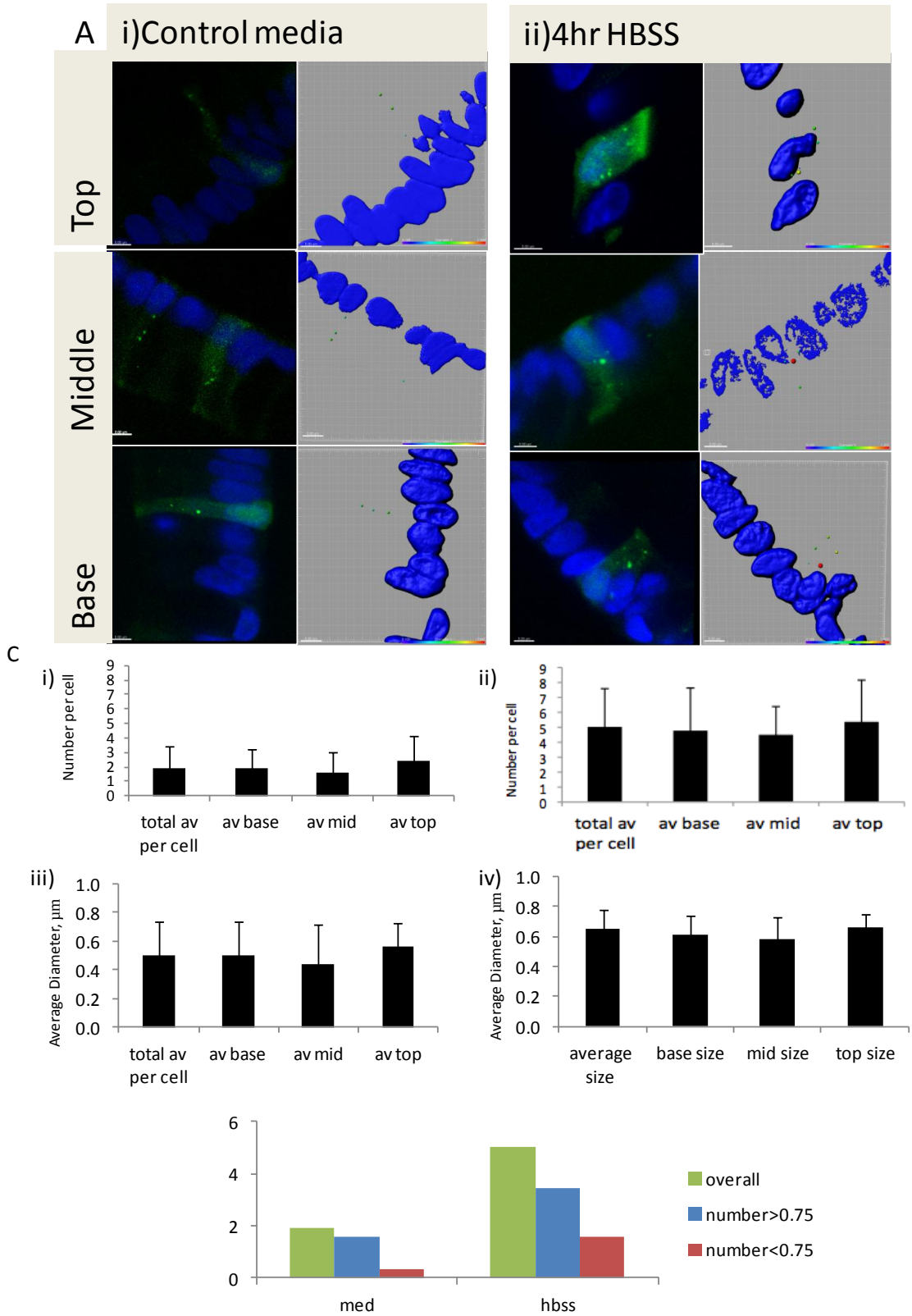

Figure 6.4 - Numbers of GFP-LC3 positive autophagosomes across the crypt axis. Panel A- Representative images of GFP-LC3 expressing colon crypt cells at the base, mid region and top of crypts from 3 separate experiments of incubations in control media (i) and HBSS for 4 hours (ii) are shown as fluorescent images of green GFP-LC3 and blue DAPI to the left of each panel, and Imaris rendering to the right. Rendered puncta were colour coded so that small vesicles (0.2µm) are blue, medium sized vesicles (0.5µm) are coloured green, and large vesicles are colour coded yellow, orange or red (0.7-1.0 µm). Rendered puncta were colour coded so that

small vesicles (0.2μm) are blue, medium sized vesicles (0.5μm) are coloured green, and large vesicles are colour coded yellow, orange or red (0.7-1.0 μm). **Panel B -** Bar charts displaying the average number of autophagosomes per cell at these points along the crypt axis in nutrient media (Bi) or 4 hours of HBSS (Bii). The average diameter of autophagosomes in cells along the crypt axis in nutrient media are shown in Biii, with the average diameter of autophagosomes in cells across the crypt axis in crypts incubated for 4 hours in HBSS are shown in Biv. The overall numbers of autophagosomes whose diameter are < or > 0.75μm are shown in Bv. All images were taken with a Zeiss LSM confocal at an x63 objective.

6.5) Quantitative analysis of autophagosome dynamics in response to starvation in live crypt cultures.

6.5-a) Movement and diameters of GFP-LC3 puncta.

Experiments in chapter 3 and 4 showed that Imaris can track movement of puncta during live cell imaging. The movement of LC3-GFP puncta in crypt cells were compared with LC3-GFP puncta generated in Vero cells (Figure 6.5). A Vero cell in nutrient media (A) contained small (0.5 μm, blue-> green rendered) puncta and a proportion of puncta moved much greater distances than others in the timeframe of the video. When starved for 4 hours (B), the puncta in Vero cells were larger >0.75μm (yellow, orange, red rendered vesicles). The scatter plots in panel D compare vesicle diameter with distance moved. The vesicles were larger following starvation (0.9μm) but there movement is similar to those seen in nutrient media (7μm). Figure 6.5, panel C shows analysis of crypt cells incubated in HBSS for 3 hours. The cell contained vesicles with a range of diameters. The vesicle highlighted as small (i) being able to

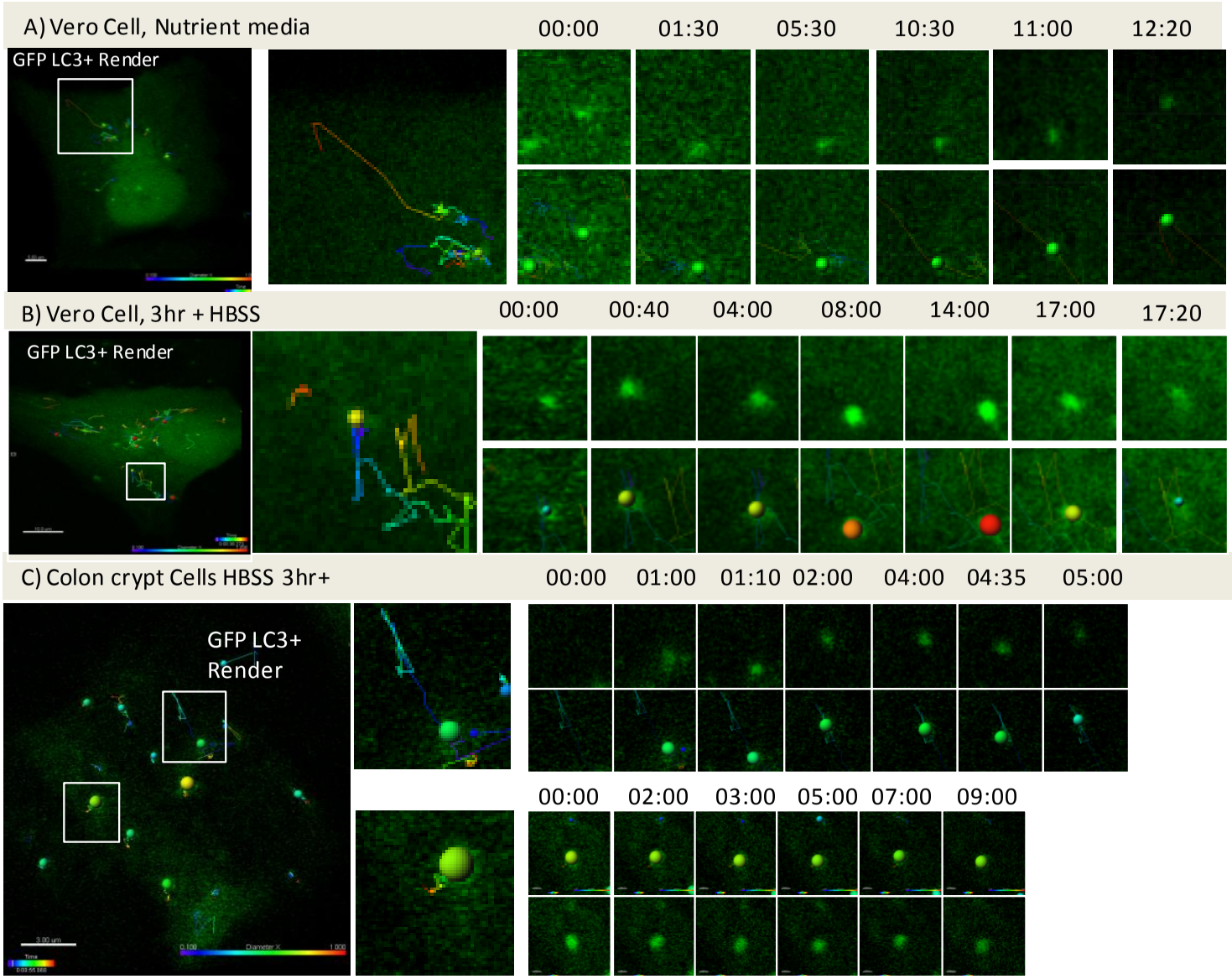
A) Vero Cell, Nutrient media
00:00
01:30
05:30
10:30
11:00
12:20
GFP LC3+ Render
B) Vero Cell, 3hr + HBSS
00:00
00:40
04:00
08:00
14:00
17:00
17:20
GFP LC3+ Render
C) Colon crypt Cells HBSS 3hr+
00:00
01:00
01:10
02:00
04:00
04:35
05:00
GFP LC3+
Render
00:00
02:00
03:00
05:00
07:00
09:00

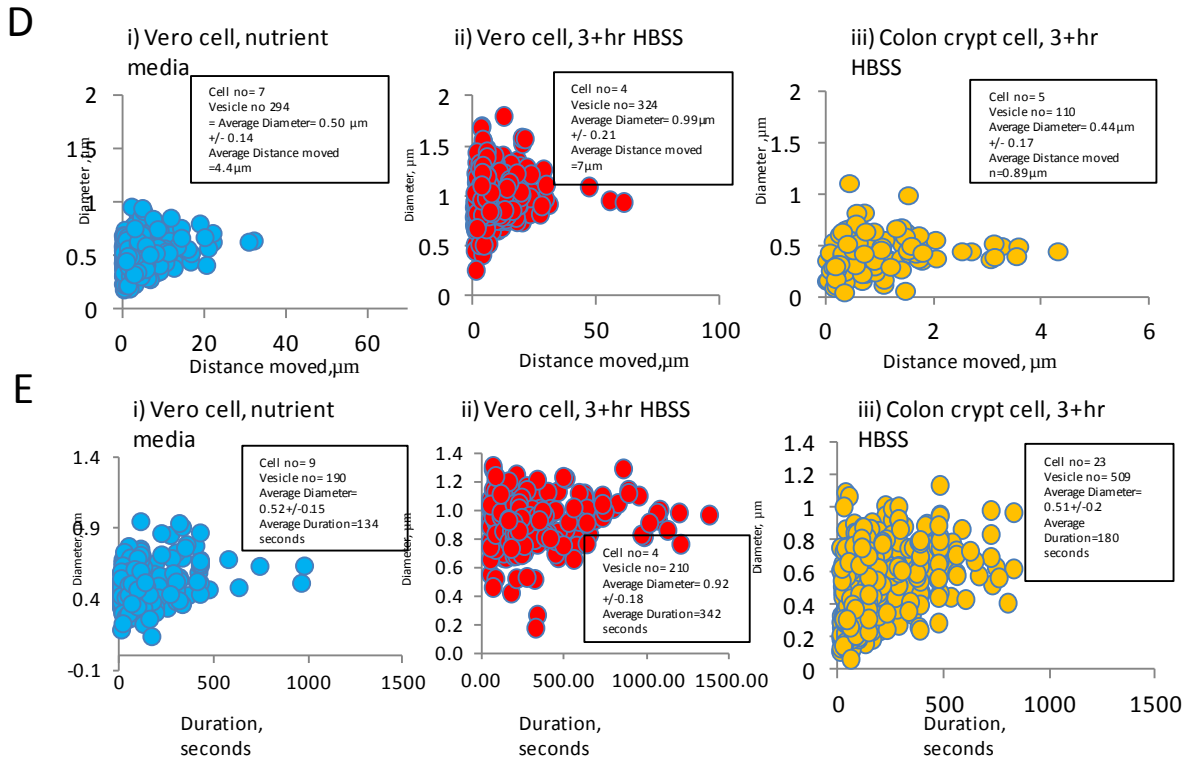

Figure 6.5 - Imaris-tracked movement of autophagosomes in Vero cells and colon crypt cells. Vero cells and colon crypt cells were transduced with an adenovirus expressing mammalian GFP-LC3. The following day the cells were transferred to HBSS and the time course of GFP-LC3 puncta formation and decay was determined by time lapse imaging. GFP-LC3 puncta were tracked and analysed using Imaris spot and render functions. The left-hand image on each panel identifies the GFP-LC3 puncta of interest and shows its track during the time lapse as determined by Imaris. Individual time lapse images are shown to the right and colour coded rendered images are shown below corresponding fluorescence images. Small puncta (0.2µm) are blue, medium sized puncta (0.5µm) are coloured green, and large puncta are colour coded yellow, orange or red (0.7-1.0 µm). Time points are indicated in minutes. **Panel A,** Vero cell, nutrient media ; **Panel C**, Vero cell, 3 hours after transfer to HBSS and **Panel C**, 3 hours after transfer to HBSS. **Panel D,** Scatter plots show the movement of puncta in µm, compared to the maximum vesicle diameter for each timepoint. **Panel E**, Scatter plots displaying duration a vesicle is present within the cell is shown in Vero cells in nutrient media **(Ei)** and Vero cells after 3 hours of HBSS **(Eii)**, and colon crypt cells after 3 hours of HBSS **(Eiii)**. All images were taken with a Zeiss LSM confocal at an x63 objective.

track of over 3μm, whereas the larger vesicle (ii) only moves 0.71μm. The scatter plot (Panel D (iii)) again indicates that where there were mixes of autophagosome sizes, the vesicles of 0.5μm, have the ability to move greater distances within the cell, even so these distances were shorter than seen in Vero cells. This analysis comes from repeats with 4 other different crypt cells from separate experiments (Supplementary Figure 5).

6.5-b) Lifetimes of GFP-LC3 puncta

The lifetimes of GFP-LC3 puncta formed in Vero cell (Figure 6.5E.i, ii) and Colon crypt (Figure 6.5.E iii) were tracked by live cell imaging of cells maintained in nutrient media or following starvation for more than 3 hours. Data from several experiments are presented in the scatter plots in Figure 6.5 panel E. The lifetimes of puncta were the same averaging 500 seconds (approximately 5 minutes). When starved, a small population of puncta showed extended lifetimes of 1000 seconds in both Vero cells and colon crypt cell. Due to the nature of live cell imaging, it was possible to track single cells expressing GFP-LC3 over time of starvation. Figure 6.6A, indicates that the vesicle puncta and size increase in later starvation compared to earlier time points in starvation in two Vero (i) and two Colon crypt cell (ii) long-term starvation experiments. The Imaris rendering of the puncta indicate that the puncta prevalent in early starvation (<1 hour) appear mostly small (green, blue) in both Vero and human colon crypt cells, and increase in number and size in later points of starvation (> 2 hours) to a point where a larger proportion of vesicles can be rendered to be yellow, orange or red (> 0.7μm).

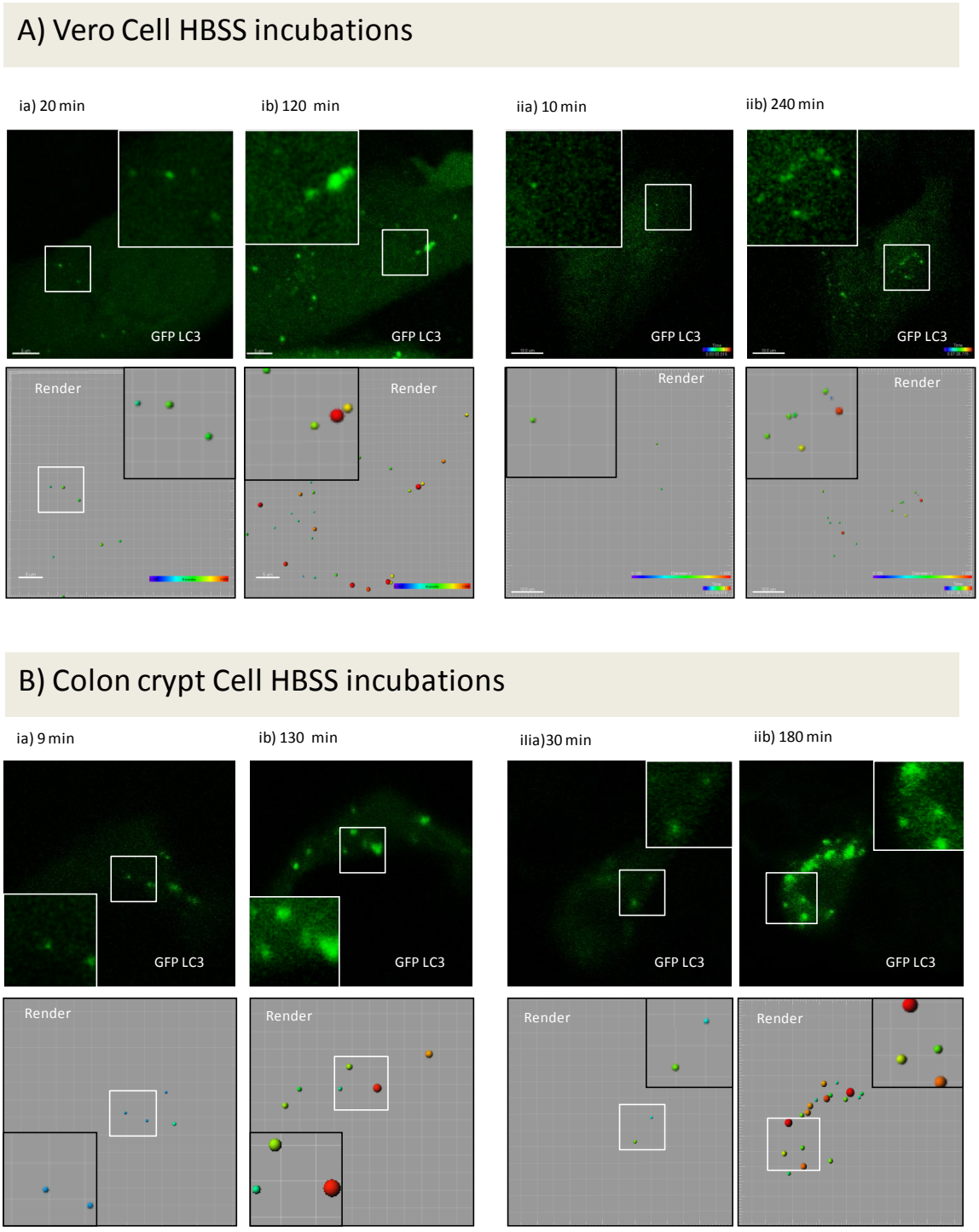

Figure 6.6 - Single cell early vs late HBSS analysis of GFP-LC3 expressed in Vero and Colon crypt cells. Two Vero cells **(Panel A)**, and two colon crypt cells **(Panel B)** from separate experiments expressing GFP-LC3 were incubated in HBSS over a maximum of 4 hours and imaged at early (ia, iia) or late (ib, iib) points in starvation. The top panels show GFP-LC3 expression in green, with Imaris renders of LC3 puncta shown below each fluorescent image. The rendered images of the LC3 puncta are coloured, where Small puncta (0.2µm) are blue, medium sized puncta (0.5µm) are coloured green, and large puncta are colour coded yellow, orange or red (0.7-1.0 µm). All images were taken with a Zeiss LSM confocal at an x63 objective.

6.6) Quantitative analysis of autophagosome induced by Muramyl Dipeptide.

6.6-a) Caco2 cells.

Autophagy can be mediated by Atg16L1, following activation of NOD2 during microbial entry into cells (Travassos *et al*, 2010). NOD2 is activated by MDP. The ability of MDP to activate autophagy was first tested using the Caco2 cell line derived from a human colon tumour (Figure 6.7). Figure 6.7A-i-iv shows LC3 puncta generated after incubation of Caco2 cells with MDP for increasing times. These are compared with puncta generated by incubation in HBSS (panels v-vi). Figure 6.7 panel B shows puncta numbers and diameters assessed in Imaris. MDP added in nutrient media induced formation of LC3 puncta, which grew in numbers with an average of 23 per cell at 16 hours. The diameter of puncta induced by MDP increased slightly with time, but they remained slightly smaller than those observed in cells incubated with HBSS for 4 hours.

6.6-b) Human colon crypt cells.

The ability for MDP to induce autophagy was tested in cells from human colon crypts transduced with adenovirus expressing GFP-LC3 (Figure 6.8). MDP induced formation of GFP-LC3 puncta in all cells expressing GFP-LC3 when incubated for 16 hours. Analysis of GFP puncta in fixed cells observed along the crypt axis indicated that the numbers of puncta increased compared to nutrient media controls from 2.2 +/- 2 to over 7.9 +/- 2.1 puncta after 16 hours of MDP. A proportion of the LC3 puncta reached the larger (0.75um) size.

Live cell analysis of crypt cells incubated in MDP for at least 16 hours again indicated that puncta number (9.5 +/-5.4) increased greatly compared to nutrient media controls

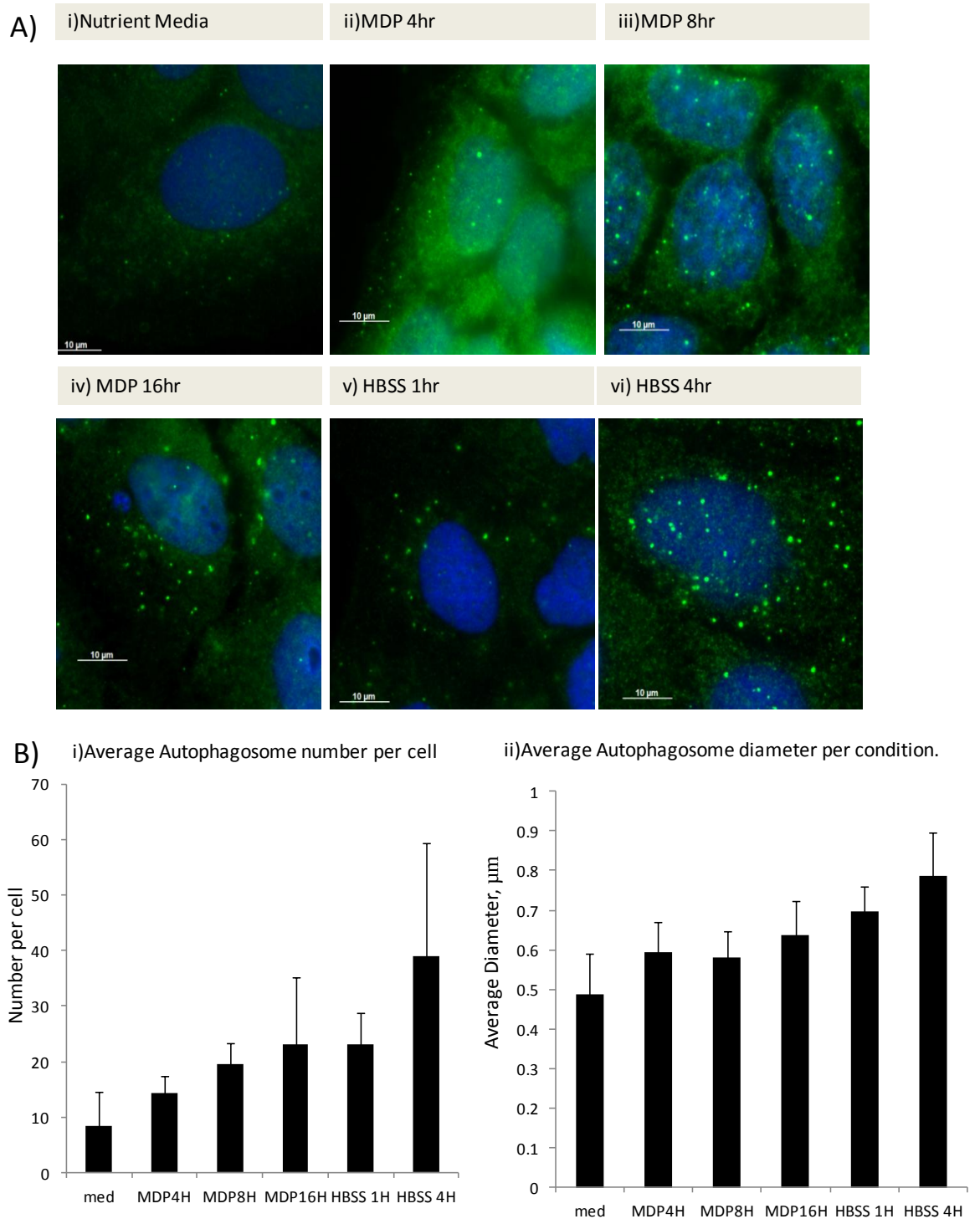

Figure 6.7 - Autophagosome number increases in MDP incubations and starvation in Caco2 cells. Panel A- Caco2 cells were grown and incubated in media (i) MDP for 4 hours (ii) 8 hours (iii) 16 hours (iv) or Hank's Balanced Salt Solution for 1 hour (v) or 4 hours (vi) then fixed in 100% methanol before immuno-staining against endogenous LC3b (Green). Nuclei were stained with DAPI (Blue). **Panel B-** Quantification of autophagosome number (Bi) or autophagosome diameter (Bii) per cell in each condition is also shown. All images were taken with a Zeiss LSM confocal at an x63 objective. Scale bar = 10µm.

(2.2 +/-2). Puncta diameters in nutrient media (0.45 +/-0.13) were smaller than when

cells were incubated with MDP (0.53µm+/-0.24), but the percentage of puncta reaching > 0.75 was increased in MDP compared to nutrient media (Figure 6.8B-i). The Imaris rendering of representative cells from MDP incubations in Figure 6.8b reveals the spectrum of sizes from small (green) to larger (red) puncta but there were no clear differences in autophagosome number along the crypt axis (6.8.b.iv).

When comparing, live GFP-LC3 expressing colon crypt cells, incubated with MDP for 16 hours or HBSS for over 2 hours (Figure 6.9), we saw an increase in autophagosome number (9.5 +/- 5.5) similar to after 2 hours of HBSS in crypt cells (6.3 +/- 2.7) (Figure 7.9.bi). The number of autophagosomes > 0.75 µm are also comparable to HBSS (1.8 for MDP, compared to 1.3 autophagosomes per cell for HBSS>2 hours). There are larger numbers of smaller autophagosomes after MDP incubation (7.7 +/- 4) compared to HBSS incubation (4.9 +/-2) indicating some differences between these two types of autophagy induction techniques.

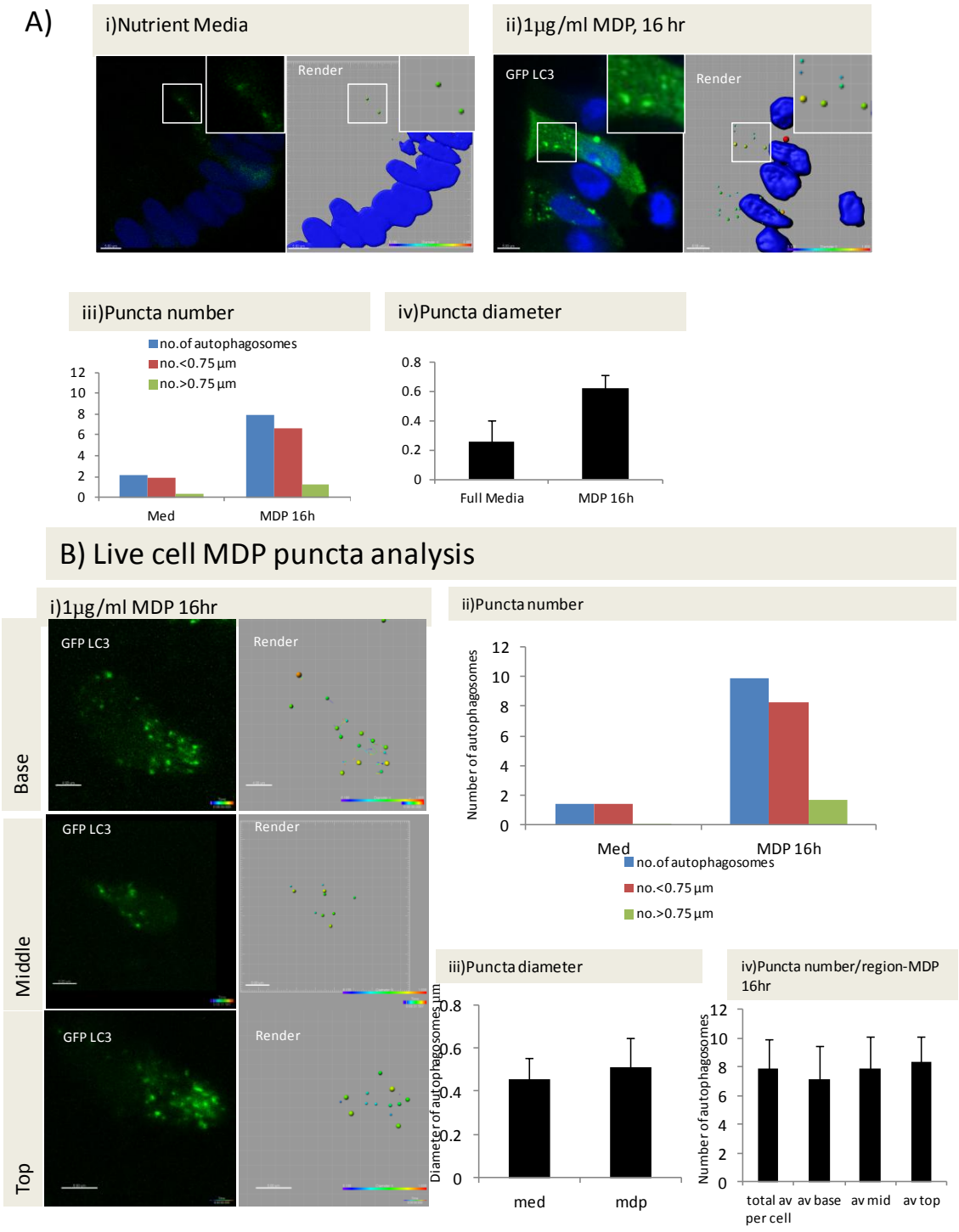

Figure 6.8 - Analysis of MDP Incubated tissue compared to nutrient media using fixed and live cell GFP-LC3 transduced colon crypts. Panel A- Representative images of GFP-LC3 expressing crypt cells in control media (Ai) and 1µg/ml MDP, 16 hr (Aii) are shown as fluorescent images of green GFP-LC3 and blue DAPI to the left of each panel, and Imaris rendering to the right. The rendered images of the LC3 puncta are coloured, where Small puncta (0.2µm) are blue, medium sized puncta (0.5µm) are coloured green, and large puncta are colour coded yellow, orange or red (0.7-1.0 µm). Aiii shows the number of autophagosomes on average in nutrient media, or MDP for 16 hours, with the number of autophagosomes above and below 0.75µm also shown. **Aiv** shows the average diameter of autophagosomes in µm within cells of crypts incubated in nutrient media, or media containing 1 µg/ml MDP. Panel B Shows live cell

analysis of crypts incubated in 1 µg/ml MDP for 16 hours pre-live cell imaging. **Panel B-Bi** shows fluorescent images of cells at this timepoint of MDP incubation at the base, middleand top of representative cells from Imaris analysis of autophagosome size and number. Below each fluorescent image is an Imaris render of LC3 puncta. The rendered images of the LC3 puncta are coloured, where Small puncta (0.2µm) are blue, medium sized puncta (0.5µm) are coloured green, and large puncta are colour coded yellow, orange or red (0.7-1.0 µm). **Bii** shows average puncta number of MDP incubated cells compared to full media, and **Biii** shows the puncta diameters on average. The average puncta number per region compared to the total average is displayed in Figure **Biv**. All images were taken with a Zeiss LSM confocal at an x63 objective.

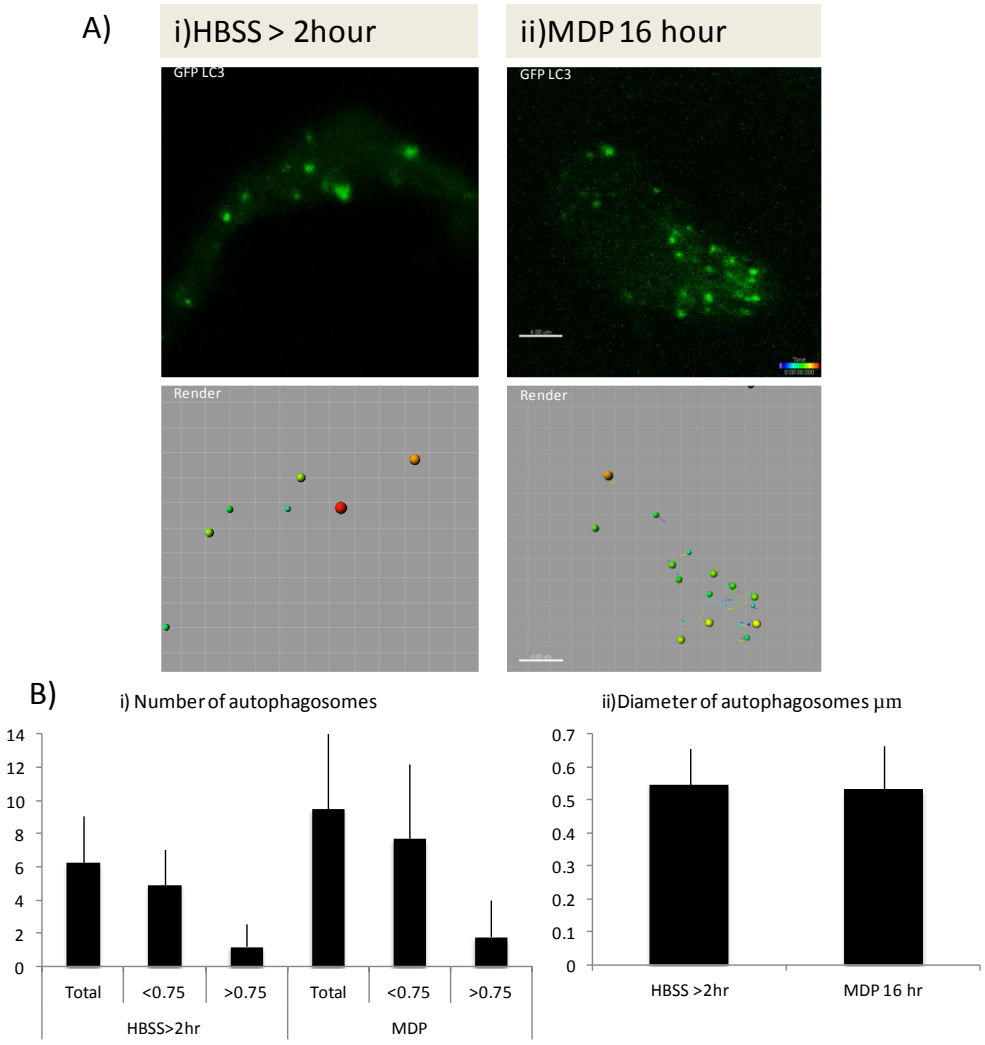

Figure 6.9 - Comparison of GFP-LC3 positive autophagosomes formed during starvation, with those formed after > 2 hours of HBSS. Panel A- Crypt tissue was transduced with GFP-LC3 adenovirus, left for 24 hours before being incubated in HBSS for > 2 hours (Ai) or MDP for 16 hours (Aii) before live cell imaging. To the left of each panel is the live cell fluorescent image, with the right displaying the autophagosome render. The rendered images of the LC3 puncta are coloured, where small puncta (0.2µm) are blue, medium sized puncta (0.5µm) are coloured green, and large puncta are colour coded yellow, orange or red (0.7-1.0 µm). **Panel B**- The bar chart Bi shows the average number of autophagosomes, with this being broken down into +/- 0.75µm. The bar graph Bii shows the average diameters of autophagosomes in µm for both conditions. All images were taken with a Zeiss LSM confocal at an x63 objective.

6.7) Summary

This chapter describes the development of methods to visualise autophagy within colonic epithelial tissue using immunostaining and GFP-LC3 Adenoviral transduction.

As with autophagy visualization in cell culture from previous results chapters, we first analysed LC3B puncta in human colonic crypt tissue as a way of studying autophagy within a fully differentiated tissue. It was possible to culture human colon crypt tissue within Matrigel (see previous chapter) so these were used to detect endogenous LC3B by immunostaining of PFA fixed crypt tissue. In all three conditions (nutrient media, starvation and chloroquine incubation), (Figure 6.1) It was possible to observe co-localisation of Atg16L1 with LC3B puncta by immunostaining, This shows that autophagy was active within this tissue at basal levels, similar to Groulx *et al*(2012) and that recognized autophagy protein Atg16L1 was able to interact with the developing autophagosome across all conditions.

It was also possible to detect endogenous staining for SQSTM1 in crypt tissue. This SQSTM1 signal was greatly increased when lysosome proteolysis was inhibited with chloroquine. There was a degree of colocalisation of LC3B and LAMP-1 antibody signals in all three groups. Both the SQSTM1 and LAMP-1 colocalisaion within colon crypt cells indicated that there was an active flow of autophagosomes to lysosomes within this tissue. We were not able to follow autophagosome formation and turnover by immunostaining. However, these experiments indicated timeframes for starvation over 4 hours as effective in seeing a difference in autophagosome numbers in cells of the colon crypt.

In comparison to Vero cells, tracking autophagosomes within individual colon crypt cells, from early (< 1 hour) to late (> 2 hours) of starvation, showed again that the GFP-LC3 signal, and Imaris rendering of puncta, produced large puncta within crypts cells in a similar way to cell lines thus could be viewed similarly. The differences in size and number of autophagosomes shown here will be useful for future studies in this field.

Atg16L1 and NOD2 have been identified as risk alleles for Crohn's disease. NOD2 is a microbial sensor, which is activated by MDP and activates autophagy through an interaction with Atg16L1. Addition of MDP to cells activated autophagy in colon crypts independently of starvation. MDP generated significantly more puncta (9.5+/-5.4) in crypts compared to nutrient media (2.2+/-2) or following starvation (5.8+/-2.2) (Figure 6.10-a). MDP also induced LC3 puncta in Caco2 cells. This time the numbers were lower (23 +/-12.2) than those induced by starvation (39+/-20.2) (Figure 6.10-b). Interestingly, the average diameter of puncta generated by MDP (0.4μm) in crypt cells was smaller than those observed after 4 hours in HBSS (0.6μm) (Figure 6.10-c). Puncta generated by MDP in Caco2 cells were also smaller (0.9μm vs 0.65μm), but the differences were not statistically significant (Figure 6.10-c). Furthermore, the percentage of vesicles reaching over 0.75μm in diameter fell from the 60% seen following starvation to 24% in the presence of MDP (Figure 6.10-d). The difference in diameter may reflect different mechanisms of activation of autophagy and recruitment of LC3 from the cytoplasm. Starvation induces autophagy through a well-characterised pathway regulated by mTOR. Much less is known about how NOD2 activates autophagy following binding to MDP. The interaction between NOD2 and Atg16L1 is important and this may involve binding to TMEM59. TMEM59 is a transmembrane protein that enters cells by endocytosis. Its cytoplasmic domain contains an Atg16L1-binding motif while the ectodomain can sense bacteria (Staph aureus). Activation of TMEM recruits Atg16L1 to the endosome and results in direct recruitment of LC3 from the cytoplasm to the endosome membrane generating LC3 puncta. These puncta are different from autophagosomes because they are modified endosomes rather than *bona fide* autophagosomes and probably reflect activation of a pathway termed 'LC3 associated phagocytosis' (LAP) (Boada-Romero *et al*, 2013). LAP can be activated by Toll-Like

Receptor 9 (TLR9) ligands and immunoglobulin coated beads and may also be involved in the recruitment of LC3 to salmonella containing vacuoles (Henault *et al*, 2012).

4 hours of HBSS appeared to be enough to induce an autophagic response within the colon crypt tissue, and preliminary live cell imaging experiments showed that it was possible to use the GFP-LC3 signal to track autophagosome formation and movement in living tissue. Imaris was used to assess the autophagy output, measuring size, number and displacement of autophagosomes within media control cells, earlier (less than 2 hours) and late HBSS (2 hours to 4 hours).

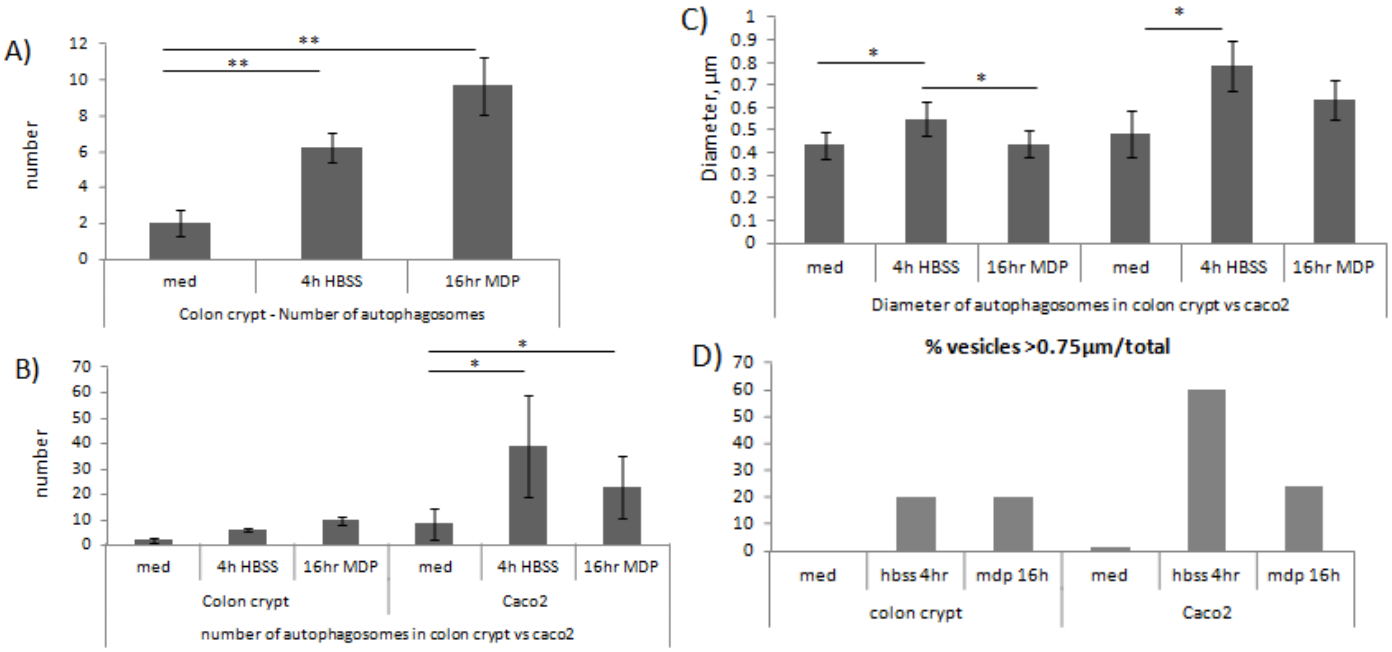

Figure 6.10 - Caco2 and colon crypt cell autophagosome numbers and diameters. Average numbers of autophagosomes in colon crypt cells in nutrient media HBSS or nutrient media containing MDP **(A)**, Numbers of autophagosomes in colon crypt compared to Caco2 cells **(B),** Diameters of autophagosomes in colon crypt cells compared to Caco2 cells **(C),** and Percentages of autophagosomes above 0.75µm in diameter **(D)**.

Imaris analysis of number of autophagosomes was largely the same as fixed data, with 16 hours of MDP incubation producing more autophagosomes than nutrient media incubated cells. Autophagy induction seen by HBSS is said to be operating through different pathway to the non-canonical MDP stimulated autophagy induction via an

Atg16-NOD2 interaction (Travassos *et al*, 2010). The effect of MDP in causing autophagosome formation suggests that this tissue is sensitive to bacteria, and can induce autophagy to aid in bacterial clearance, helping homeostasis of the epithelia to the contents to the lumen of the gut. The autophagy output by MDP, with Atg16L1 localising to invading bacteria, could be explored further sue to the very different methods of autophagy activation, beginning at the Atg16L1 protein and not being controlled by mTOR as is occurring with starvation induced autophagy.

Using this system, we showed that autophagy is an active process occurring within the cells of the colon crypt, and that this method of imaging can effectively track the autophagy status of crypt tissue.

Chapter 7:

Discussion.

7.1) Quantifying autophagosomes within cells.

The first aim of this study was to use imaging software to quantify autophagy by analysing pixel densities in fluorescent images obtained by microscopy. LC3II is the major structural protein of the autophagosome and stays with the autophagosome until fusion with lysosomes. LC3II on the inside of the autophagosome is then degraded and LC3 on the outer membrane is recycled back to the cytosol. These properties of LC3 allow immunostaining for endogenous LC3 and/or live cell imaging of GFP-LC3 to be used to follow autophagosome formation and trafficking in cells. In chapter 3 the possibility of generating digital datasets from fluorescent images of LC3 that were amenable to statistical analysis was explored.

7.1-a) Use of Imaris software to obtain digital data sets.

Imaris is a software module from Bitplane that allows analysis of 3D and 4D microscopy datasets. Imaris software was used to generate digital datasets from fluorescent puncta generated from GFP-LC3 or immunostaining of endogenous LC3 in tissue culture cell lines. Pixel density measurements were optimized using 'Spot', 'Surface Border' and 'Render' functions to produce rendered puncta containing digital datasets. LC3 puncta were then displayed graphically to identify their spatial location within the cell. At the same time the diameters of puncta were represented using a heat map where blue represented puncta of about 0.5μm diameter and red puncta 1.0μm or above. The diameters calculated correlate well with analysis of autophagosomes by electron microscopy showing diameters of 0.5-1.5μm (Muzishima *et al*, 2002).

Autophagosome are reported to be around 0.5-1.5μm in diameter (Mizushima *et al*, 2002). More recent work by Levine *et al*, shows that starvation of MEF cells produced autophagosomes and autophagolysosomes around 1μm in size when analysed by electron microscopy (Mizushima *et al*, 2010), and this agrees with the 0.75-1.0μm calculated by Imaris for cells starved for 4 hours.. Sato *et al* (2007) investigated autophagosome numbers and diameters crudely, by quantifying the area of a cell containing GFP-LC3 dots. This gave an idea of up regulation of autophagy visually, but no specific autophagosome diameter and number data was show
n. The results shown in this thesis, could encourage others to generate quantitative data sets from LC3 puncta so experiments in one laboratory can be compared directly with another. For example, an increase of GFP-LC3 puncta within transgenic mouse tissue after starvation was described by Mizushima *et al* (2004) but not quantified. If digital images of GFP-puncta had been rendered, it would have been possible to compare responses of different tissues.

7.1-b) Quantitative analysis of LC3 puncta produced in response to starvation.

The image analysis was used to see if the formation of LC3 puncta in response to starvation could be expressed quantitatively to describe the average responses of cells to starvation and then use the data to compare different cell lines and conditions. For this analysis a confidence limit of 95% was chosen. Datasets from rendered puncta were collected from three different cells lines to compare ≥20 cells maintained in nutrient media or starved for 4 hours in HBSS. Figures 4.1-4.2 show when cells were starved for 4 hours, LC3 puncta were more numerous.

7.1-c) Quantitative analysis of LC3 puncta observed by live cell imaging.

The spot detection and rendering functions were used to track GFP-LC3 signal during live cell imaging. This allowed collection of datasets describing the distances moved by GFP-LC3 puncta, their diameters and lifetimes. The analysis above showed that LC3 puncta were significantly larger (0.68, 0.78 & 0.85 μm on average) in all three cell lines when analysed 4 hours after starvation compared to nutrient media controls (0.5μm on average for all three cell lines). When the diameters of puncta were calculated from ≥20 cells examined at increasing times after the onset of starvation the percentage puncta with a diameter ≥0.75μm increased to 60% at two hours, and remained at that level for the 4 hours of the time course. One interpretation of the result was that it took 2 hours for an autophagosome to increase in diameter from 0.5μm to ≥0.75μm. Alternatively, autophagosomes formed early during the onset of starvation could be unable to grow to ≥0.75μm. To resolve this the lifetimes and diameters of puncta generated at increasing times after onset of starvation were therefore followed by live cell imaging. The bubble graphs (Figure7.2) shows analysis of between 200 and 600 puncta at different times during a starvation time course. The average lifetimes of puncta generated between 1 and 3 hours were 6.4 minutes and the same as those generated at 4 hours. This lifetime is consistent with early studies of autophagosome dynamics using electron microscopy images of insulin treated mice, to follow the decrease in autophagosomes over time and calculated a half time of vesicles of 10 minutes (Pfeifer *et al*, 1978). Interestingly, the diameters of vesicles formed in cell culture at 4 hours were larger (0.93μm compared to 0.61μm). This suggests that autophagosomes formed late during the onset of starvation were able to increase in diameter to ≥0.75μm.

The analysis was repeated for early autophagosome marker WIPI2 (Atg18) and WIPI2 puncta were also larger if formed later during starvation. WIPI2 binds lipids phosphorylated by vps34 in response to activation of mTOR (Polson *et al*, 2010) and docks to the isolation membrane of the pre-autophagosome and developing omegasome. This suggests that the defect in autophagosome maturation seen at early times of starvation may affect early events in autophagosome formation possibly isolation membrane and omegasome expansion. It may be possible to explore this further by following puncta formed by additional omegasome markers such as DFCP1.

7.2) Possible role for TFEB in autophagosome expansion.

The transcription factor TFEB controls expression of genes with CLEAR regulatory elements that are required for autophagy and the formation of lysosomes (see Figure 1.5). Settembre *et al* (2011) showed that RNAi directed against TFEB, decreases levels of LC3 in cells in nutrient media and following starvation, while over-expression of TFEB increased SQSTM1, WIPI, and LC3b. One possible explanation for the lack of expansion of LC3 puncta seen early during starvation could be that levels of a protein regulated by TFEB, and crucial for autophagosome formation, are low and that there may be a time lag between the onset of starvation and the switching on of its gene by TFEB. The movement of TFEB to the nucleus in response to starvation is regulated by mTORC1 located at the lysosome membrane (Roczniak-Ferguson *et al*, 2012). An efflux of amino acids from the lysosome keeps mTOR active, which in turn inhibits nuclear localisation of TFEB. When cells are starved the flow of amino acids from the lysosome is reduced and TFEB moves to the nucleus to increase expression of genes required for autophagy and delivery of material to lysosomes (Roczniak-Ferguson *et al* 2012). It will therefore be interesting to analyse the movement of TFEB into the nucleus during a

starvation time course and determine the onset of transcription of genes with CLEAR regulatory elements, and see if the time frame correlates with the ability of LC3 to expand in response to starvation.

7.3) Quantifying SQSTM1 puncta during starvation.

Western blot of SQSTM1 can be used to follow autophagic flux because SQSTM1 is degraded by autophagy in response to starvation (Pankiv *et al*, 2007) indicating delivery to lysosomes. An analysis of SQSTM1 showed that cells in nutrient media contained SQSTM1 puncta but the numbers of these puncta did not increase significantly in response to starvation. The SQSTM1 protein binds ubiquitin and contains an LIR domain that binds LC3 to target ubiquitinated proteins for autophagy. An analysis of co-localisation showed that there was an increase in SQSTM1 puncta co-localised with LC3 in response to starvation at both 1 and 4 hours of starvation, and consistent with analysis of LC3 and WIPI2, puncta containing SQSTM1 only showed increased diameter at 4 hours. These results were consistent with delivery of SQSTM1 to autophagosomes in response to starvation, and showed further that SQSTM1 could be delivered to autophagosomes formed early or late during starvation. The small autophagosome diameters seen early during starvation did not therefore result from a lack of delivery of autophagy cargo.

Previous work (Pankiv *et al*, 2007) has used live cell confocal microscopy to visualise a tandem tagged RFP-GFP-SQSTM1. The intact fusion protein is orange but converts to red when delivered to lysosomes because the GFP is pH sensitive. Work on drosophila fat bodies indicate that SQSTM1 immuno-staining could be effective in identifying induction of autophagy with increases in number of SQSTM1 aggregates being associated with starvation of (Pircs *et al*, 2012). Localisation of LC3 negative, SQSTM1

positive puncta seen within our immunostaining during nutrient media compared to starvation, again allows for Imaris analysis of this to indicate autophagy occurring after starvation.

Bjorkoy *et al* (2005) show that SQSTM1 protein aggregates are normally present within cells, and are bound to ubiquitin. The SQSTM1 puncta that are negative for LC3 seen in cells maintained in nutrient media probably represent pools of SQSTM1 attached to aggregated proteins or ubiqutinated organelles. It will be interesting to follow up these observations by live cell imaging to compare the dynamics of single and double (LC3-SQSTM1) positive puncta and their fusion with lysosomes. Jahriess *et al*, 2008, have used live cell imaging of autophagosomes to establish a framework for autophagosome dynamics within cells lines. They observed mCherry LC3 within flat cells to track movement and lifetimes in response to starvation. The vesicles moved towards lysosomes after being formed randomly, and many colocalised with microtubules. A knockdown of dynein caused a loss in organised movement suggesting movement powered by microtubule motor proteins. The tubulin deacetylase HDAC6 (histone deacetlyase 6) binds dynein and ubiquitin. It will be interesting to see if SQSTM1 puncta also contain HDAC6 and if movement of puncta or co-localisation with LC3 is affected by Scriptaid, which inhibits HDAC6.

7.4) Analysis of autophagy in colon crypt cells.

The aims of the last chapters were to carry out a quantitative analysis of autophagy in primary gut epithelial tissue taken from human biopsy, or generated by mouse intestinal organoid culture. If successful this would allow the effects of Crohn's risk alleles to be studied in the context of disease by analysing human biopsy taken from

Crohn's patients and/or through studies of intestinal organoids generated from mouse models of Crohn's disease.

Even though there is great interest in understanding the impact of Crohn's risk alleles on autophagy, there has been only limited work on human tissue. Research by Groulx *et al* (2012) used mucosa from healthy patients to assess the autophagy status of gut tissue. For their research, they used immunofluorescence of cryosectioned adult human biopsy specimens to stain for autophagy proteins SQSTM1 and Beclin1. Using this technique, they were able to indicate that colon crypt cells did produce autophagosomes in both healthy and cancerous patient samples. Each puncta was deemed an autophagosome in the differentiating region of the crypt, the base, whereas the lack of Beclin1 staining at the top regions of the crypt made them doubt the puncta formed by SQSTM1 were autophagosomes. Groulx *et al* (2012), also used human intestinal epithelial crypt (HIEC) cells as a cell culture system for activating autophagy. Other work into autophagy activation of gut epithelial cells has used Caco2 or HCT116, human colon epithelial cell lines to assess autophagy activation (Kathiria *et al*, 2012).

7.4-a) Adenovirus transduction of organoid and crypt cultures.

The work in this thesis concentrated on exploiting the long-term culture of mouse and human intestinal organoids in laminin-rich Matrigel. Organoids represent a new method of stem cell culture, which was first described by Sato *et al* in 2009. The first experiments showed that it was possible to use these methods to grow mouse small intestine organoids from crypts isolated from mouse small intestine. The mouse organoids were then used as a source of primary tissue to pilot the use of adenovirus vectors to express GFP-LC3. Unfortunately, it was not possible to detect expression of GFP in the cultures. This may be because the cultures lack the adenovirus receptor. Clevers *et al* have reported transduction of isolated mouse small intestine and gastric

organoid cultures recently. Here, they used mouse stem cell retrovirus (MSCV) to introduce transgenes and manipulate gene expression of organoid cultures (Koo *et al*, 2012). It is possible that the MSCV vector can be used to introduce GFP-LC3 into mouse organoid cultures.

Experiments using human crypt cultures were more successful. The human crypt cultures were maintained over 3 days within the Matrigel and could successfully be transduced with GFP-LC3 adenovirus. It was possible to transduce cells across the whole crypt axis allowing an analysis of autophagy in different cell types in different positions in the crypt. It was, however, possible that over-expression of GFP-LC3 in crypt tissue may affect endogenous autophagy pathways. The properties of endogenous autophagosomes in human crypt tissue were therefore analysed by standard immuostaining before and after starvation and compared with GFP-LC3 puncta. The results showed that crypt tissue generated endogenous LC3 puncta in response to starvation and these puncta co-localised with endogenous Atg16L1 and SQSTM1. Crypt tissue transduced with GFP-LC3 generated GFP puncta following starvation and these also co-localised with endogenous Atg16L1 and SQSTM1. A quantitative analysis of puncta showed that numbers and diameters of endogenous and GFP-LC3 puncta were the same. Taken together the results provide strong evidence that GFP-LC3 delivered by adenovirus transduction does not perturb autophagy in crypt tissue and that this method can be used to follow autophagosome formation in primary human tissue.

7.4-b) Analysis of GFP-LC3 puncta in crypt cells following starvation.

The next experiments compared the formation of LC3 puncta between primary crypt tissue, Vero cells and the Caco2 cells that are commonly used as a tissue culture model for gut. Endogenous LC3 puncta and GFP-LC3 puncta increased in all three cell types in

response to starvation but the numbers of puncta generated in crypt cells (5.8 +/- 2.2) were much lower than in tissue culture cell lines (25-30). The LC3 puncta generated in crypts in nutrient media were also smaller (0.25 +/- 0.14m) compared to Caco2 cells (0.45 +/- 0.13 μm) but they did expand three-fold following starvation to 0.6μm diameter. One reason for the relatively low numbers of autophagosomes in crypt cells may be because the crypt cells are small and lack the space to accommodate more. Vero cells, Caco2 cells and colon crypt cells are shown at the same magnification (Figure 7.3) and it is clear that tissue culture cells are much larger (at least 6x larger) than crypt cells, but the density of LC3 puncta are similar.

The lifetimes, movement and diameters of puncta generated 3 hours after onset of starvation in crypt cells were followed by live cell imaging. The bubble graph (Figure 7.4) compares puncta lifetime or puncta movement (y axis) with puncta diameter (x axis). The average lifetime were 3 minutes, and had a similar range of lifetimes calculated for Vero cells, but there was no correlation between lifetime and diameter. The ranges of autophagosome durations within cells can be shown in supplementary Figure 7. Most (~90%) of the puncta moved very short distances (less than 2μm). The remaining (~10%) moved longer distances (2-5μm) and the most motile puncta were around 0.5μm in diameter.

This could be attributed to the small size of the cells, where vesicles being formed may be more mobile compared to mature vesicles whose function has been fulfilled and have less room to move. This could be investigated further by quantifying the dynamics of lysosomes within these colon crypt cells, to understand if these are less dynamic than the autophagosomes and lysosomes seen in cell lines in previous research by Jahriess *et al* (2008).

7.4-c) Quantitative estimation of autophagic capacity.

Taken together the results allowed a calculation of autophagic capacity for crypt cells. For example, if LC3 puncta have a lifetime of 10 minutes this means that 6 puncta are generated every hour for each puncta observed. For crypt cells to maintain 6 puncta they have to produce around 36 puncta every hour. For the tissue culture cells the capacity is much higher and to maintain 40 puncta they must generate around 240 LC3 puncta each hour if autophagosomes are constantly being formed.

7.5) Future work.

The next phase of this work will be to use the methods developed in this thesis to provide quantitative assays for autophagy in gut epithelial tissue taken from patients that express Atg16L1 and NOD2 risk alleles in for Crohn's disease. By using samples from patients with and without Crohn's disease, this methodology will be used to determine if patients with the Atg16L1 T300A point mutation, or truncations in NOD2, generate more or less LC3 puncta in response to starvation or and/or MDP, which has been shown to be possible in this work on technique development of a newly defined method of epithelial tissue culturing. The work reported above has shown that human colon crypt cells incubated with MDP have on average 10 LC3 puncta. A statistically significant decrease (or increase) of one puncta per cell would represent a 10% change in autophagy capacity that may be relevant in the contexts of microbial sensing and pathogen control in the gut mucosa.

It will also be possible to use these methods to assess the effects of Crohn's disease risk alleles in mouse models where the endogenous Atg16l1 has been replaced by mutated genes. It was not possible to transduce organoids with the adenovirus and the experiments will require development of the MSCV retroviral vector reported by Koo *et al* (2012) to transduce stem cells in mouse organoids.

Appendix

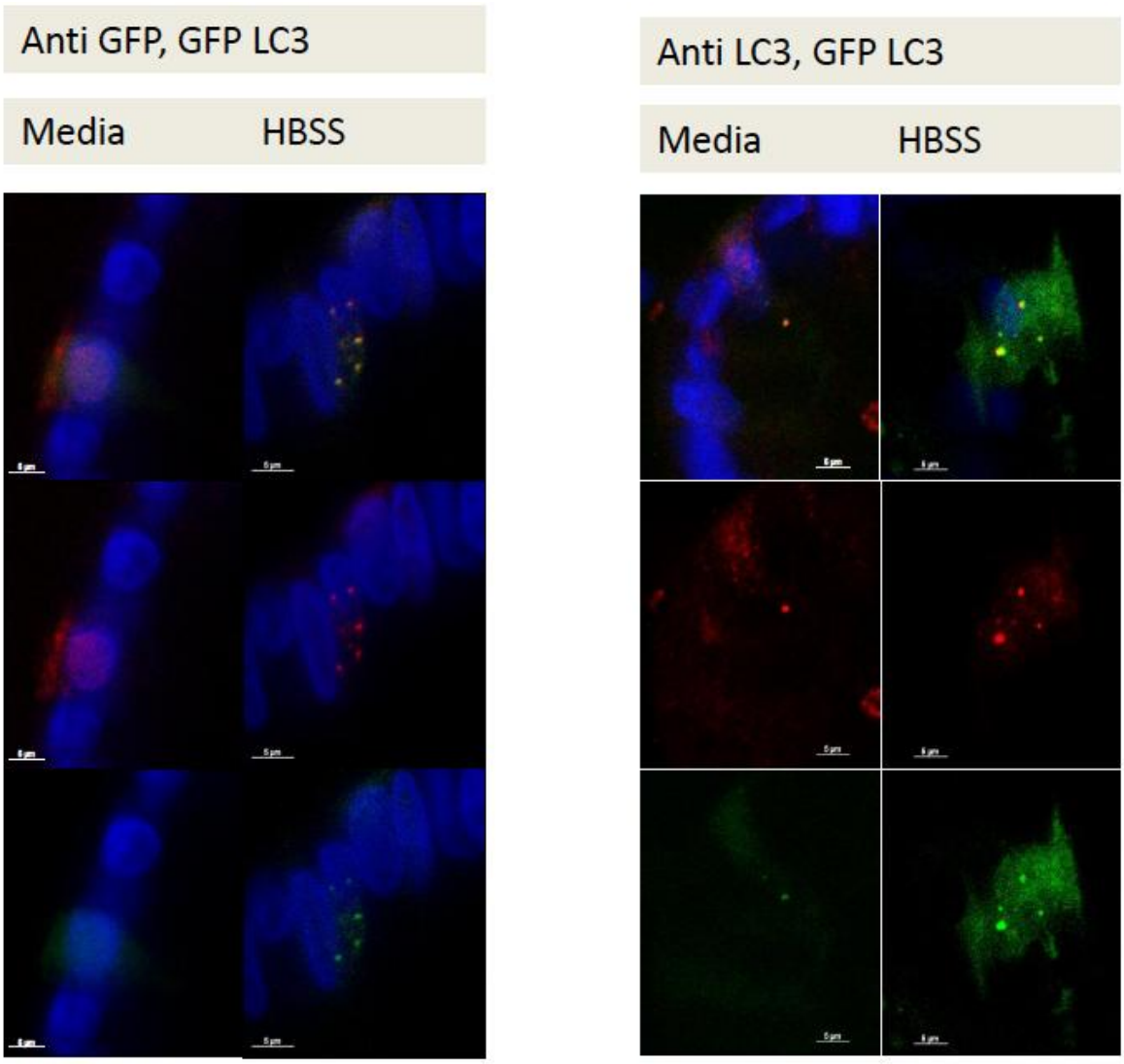

Supplementary Figure 1 – Colocalisation of anti LC3B , anti GFP and GFP-LC3

Colon crypt tissue was isolated and incubated in Matrigel containing GFP-LC3 Adenovirus. After 1 day crypts were incubated in nutrient media, or HBSS. A) Shows immunostaining using an anti GFP antibody (red) and the GFP-LC3 expression (green) in media (i) and HBSS (ii). Panel B shows crypts immunostained for LC3B (red), and transduced with GFP-LC3 (green) in media (i) and HBSS (ii). Nuclei were stained with Hoescht.

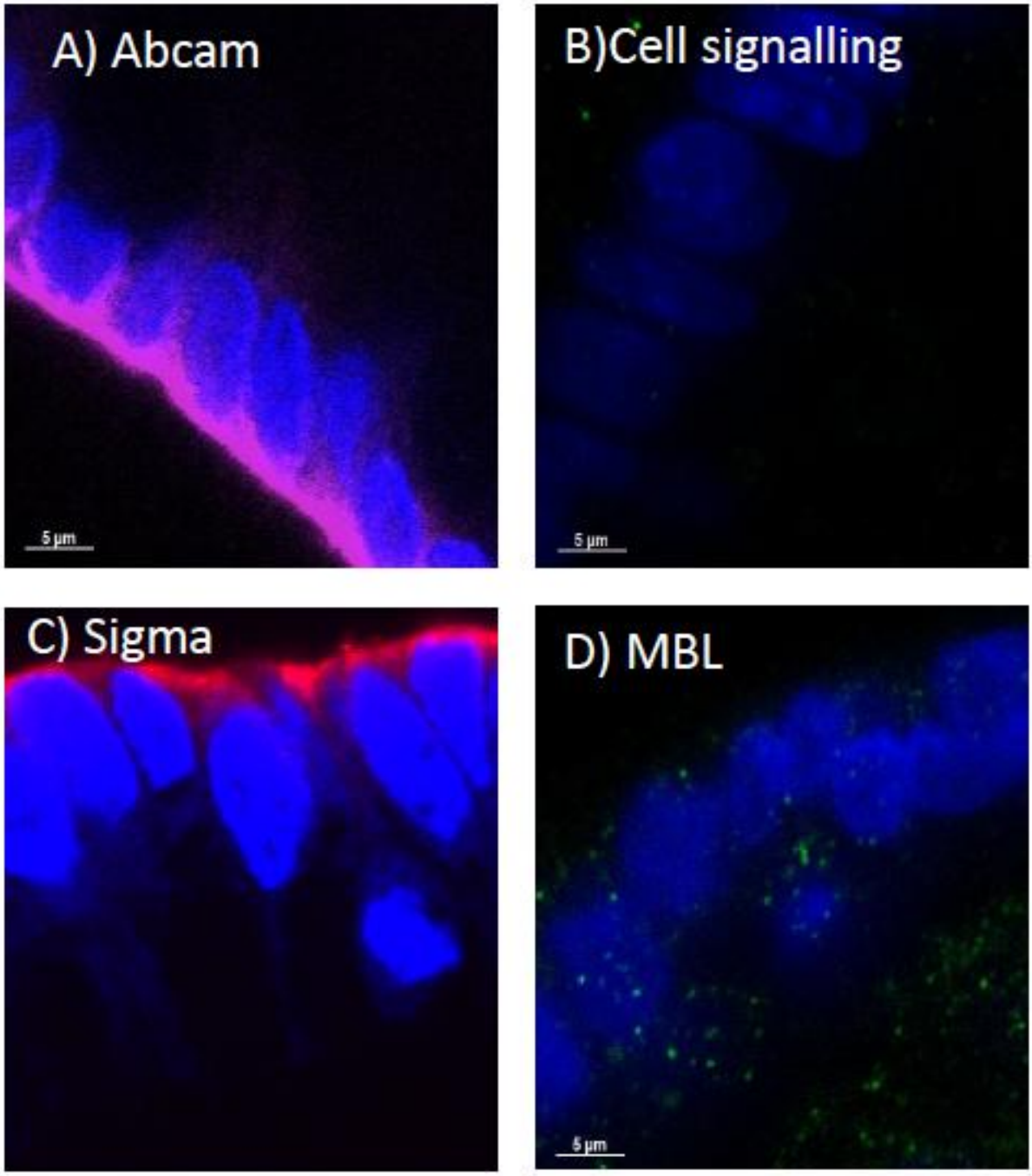

Supplementary Figure 2. –Staining of LC3B antibodies in human colon crypt cells.

Colon crypt tissue was starved in HBSS, fixed and immunostained against LC3B with an Abcam Antibody (A), a call signalling antibody (B), a Sigma antibody (C), and an MBL antibody (D) Nuclei were stained with Hoescht.

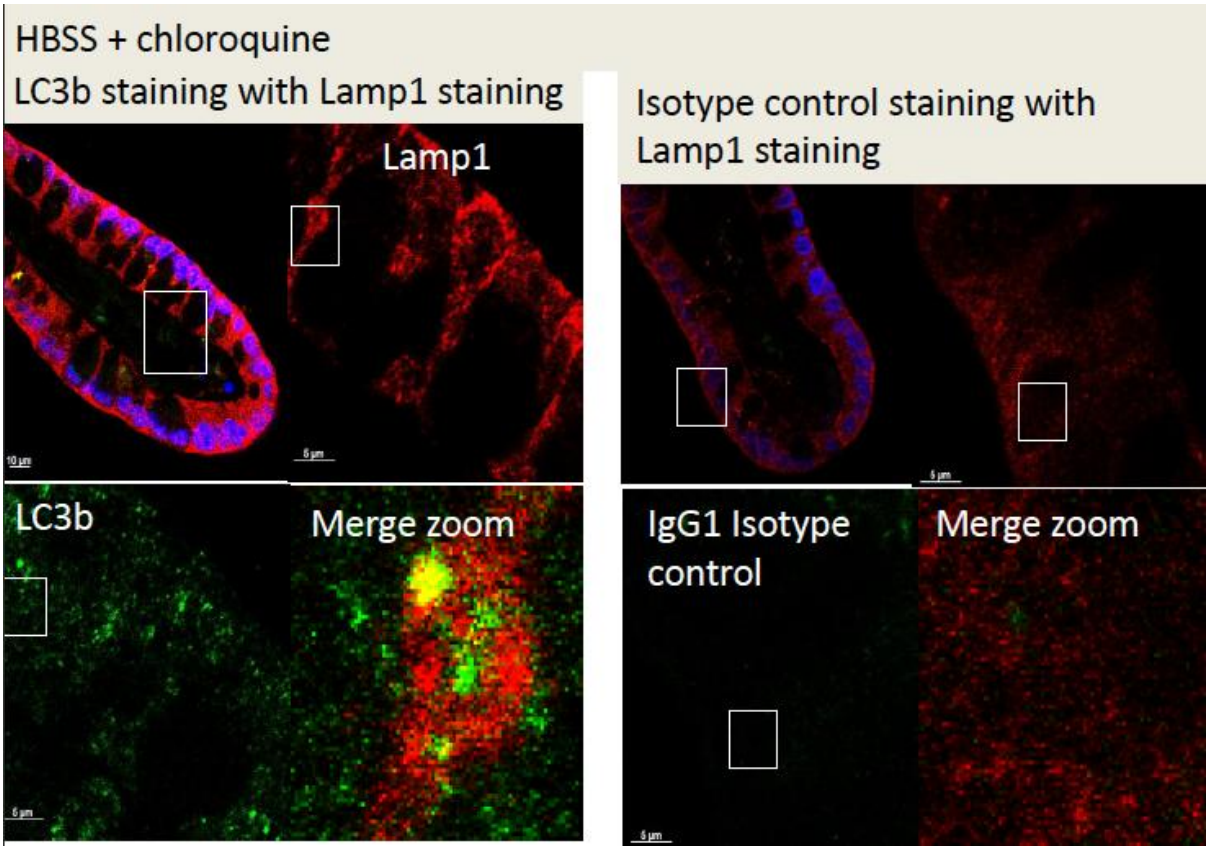

Supplementary Figure 3. – Isotype control staining compared to LC3B staining in human colon crypt cells. Isotype control experiment proved the MBL antibody was true staining. Panel A shows MBL LC3B staining in green, localising with LAMP-1 staining in red. The Isotype control in B shows no staining within cells of the crypt with the Isotype control (green), thus, no localisation with LAMP-1 staining in red.

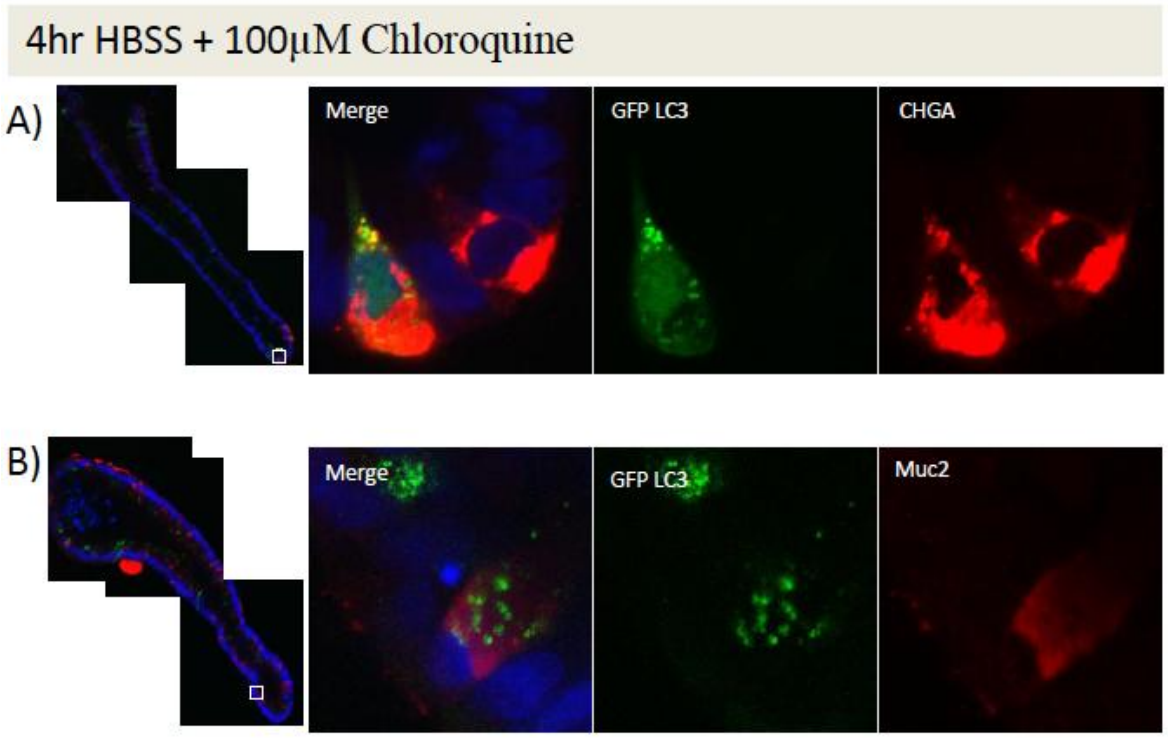

Supplementary Figure 4 – Expression of GFP-LC3 within differentiated cells in human colon crypts. Staining against enteroendocrine cells (A) and Goblet cells (B) was performed after incubation in HBSS+ 100µM chloroquine. Staining for Enteroendocrine cells with Cromogrannin a, and goblet cells with Muc2, are both in Red. GFP-LC3 is shown in green. Nuclei were stained with Hoescht.

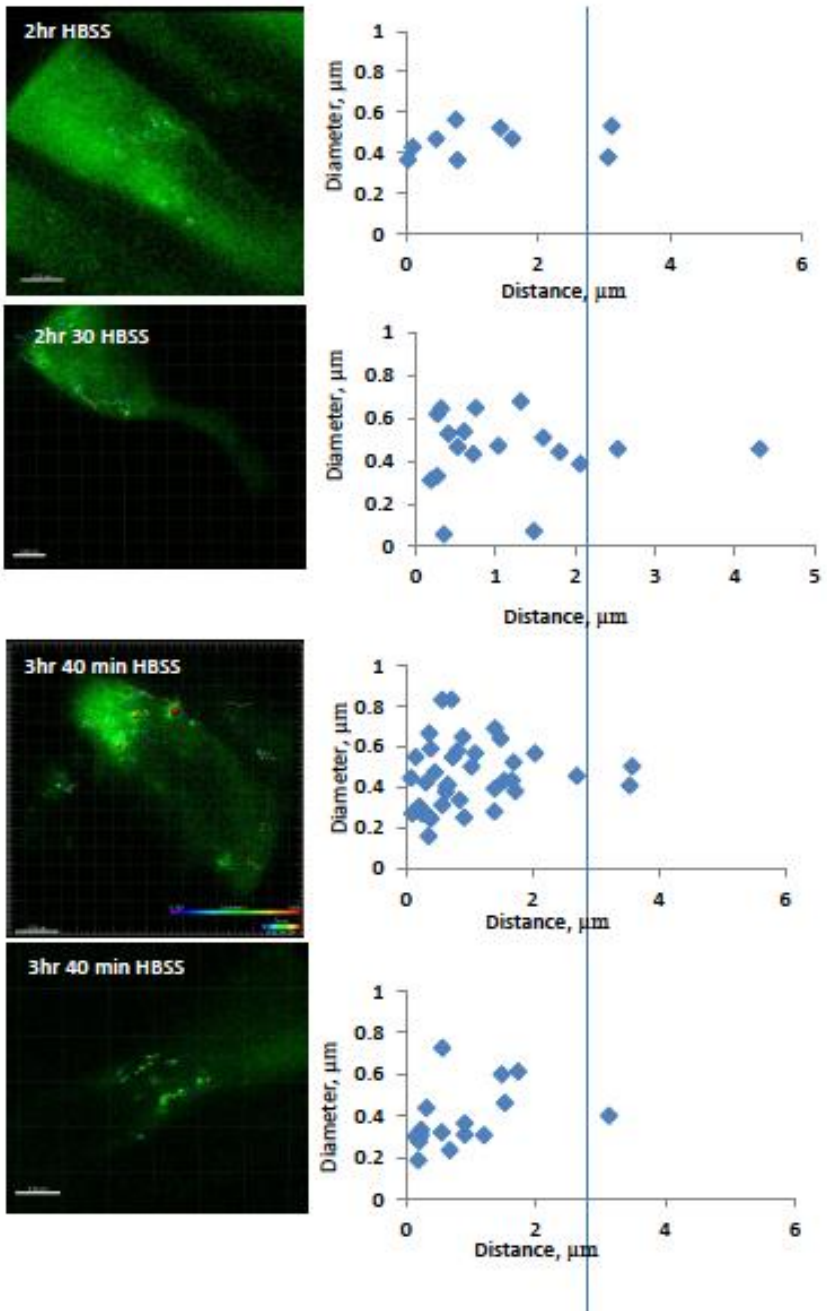

Supplementary Figure 5 – distance moved of autophagosomes within different crypt cells.

4 Crypt cells from separate experiments expressing GFP-LC3 (green) were imaged by confocal timelapse microscopy, and the Imaris tracked vesicles were plotted for diameter (µm) against distance moved (µm) the blue line indicates movement above 3µm

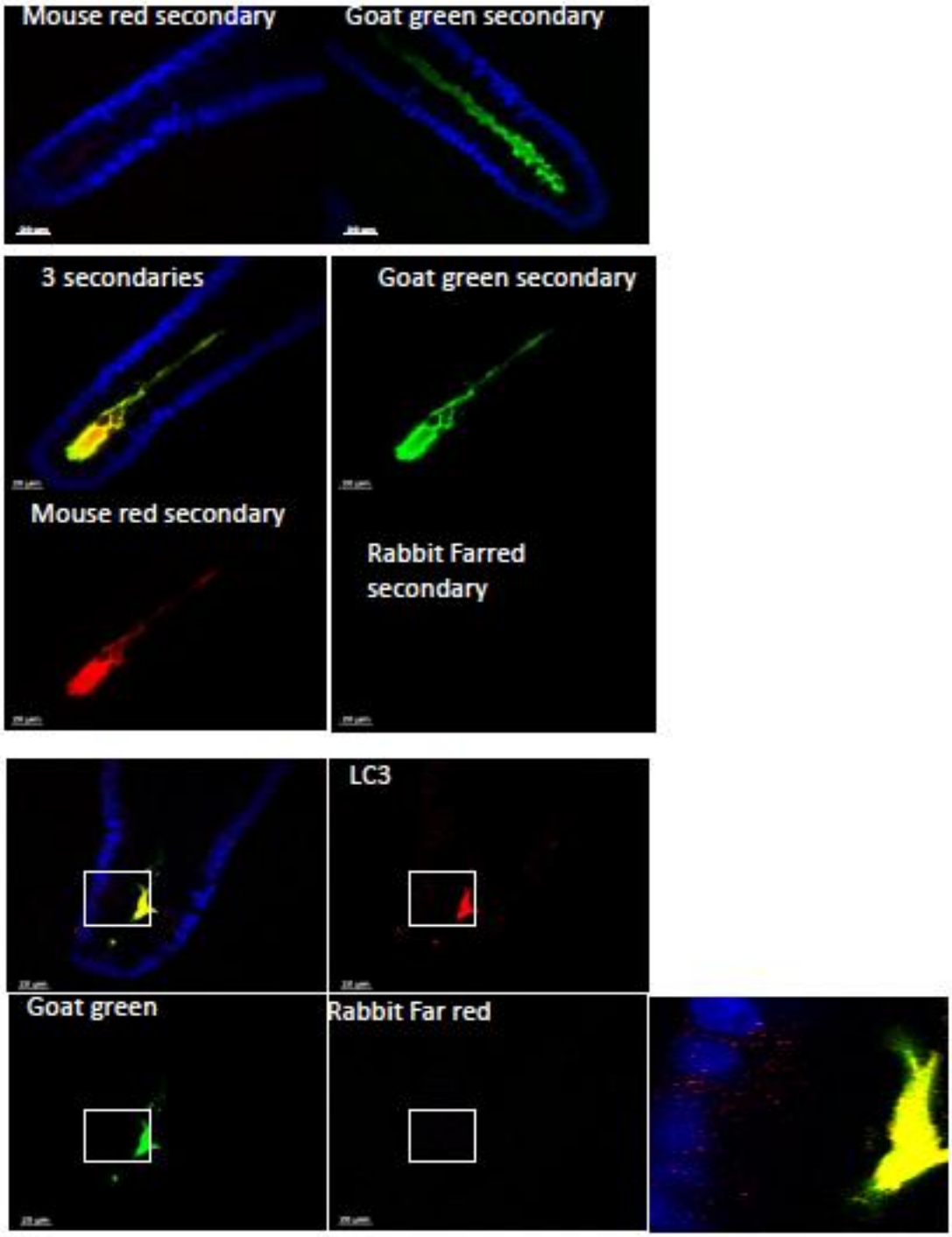

Supplementary Figure 6 – Secondary control staining of human colon crypt cells.

Staining for secondary antibodies alone (a-anti mouse red secondary, b-anti goat green secondary) or together (C) along anti rabbit far red were shown. LC3B staining (red) and Rabbit far red, show no overlap of the rabbit secondary antibody with the LC3B staining.

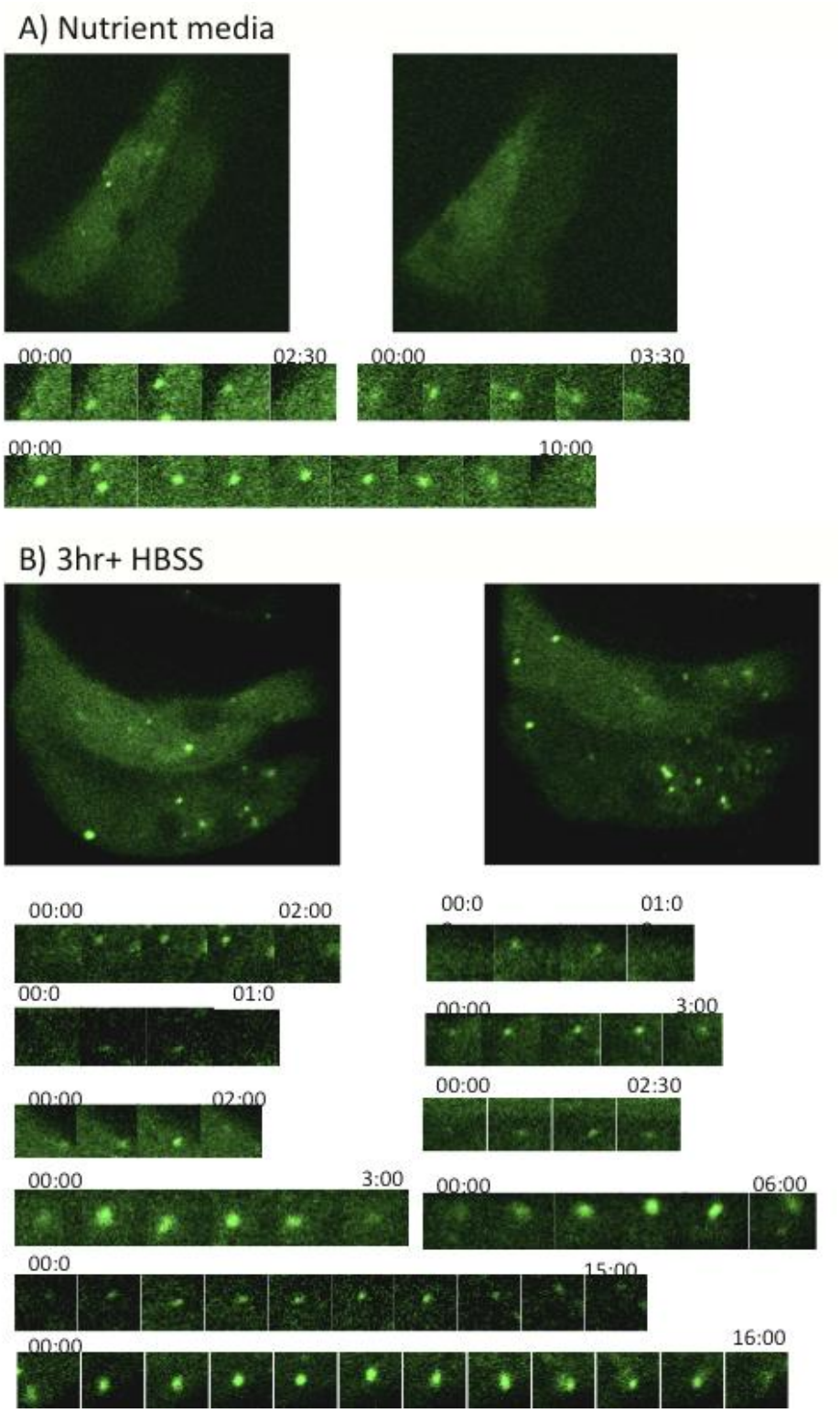

Supplementary Figure 7 – Ranges of lifetimes of autophagosomes. Colon crypt cells expressing GFP-LC3 in nutrient media (a) of HBSS for over 3 hours (B) were imaged over time and vesicles forming and degrading over time are shown in panels below each full cell image with the first image when the vesicle is first visible, and the last when it is no longer visible. 00:00 = minutes:seconds. Images were taken on a Zeiss confocal with an x63 objective.

Acknowledgements

I would firstly like to acknowledge the guidance of my supervisor Tom Wileman, and for allowing me to be involved with many different projects within his lab alongside mine. I feel like I became a much more accomplished scientist due to the different challenges I have been given. I would also like to thank everyone else in the laboratory, past and present. Special thanks to Rebecca Roberts and Eleanor Cottam, who both enjoy a coffee break, and a good discussion about autophagosomes via email now they have moved elsewhere. The crypt isolation techniques from the Williams lab allowed for me to gain images of crypt tissue and utilize the Imaris software from the Wileman lab within my own project also. I would like to thank Paul Thomas for the bio imaging assistance at the University of East Anglia, and Paul Verkade and colleagues for the assistance with microscopy at the University of Bristol.

References

Axe E, Walker S, Manifava M, Chandra P, Roderick H, Habermann A, Griffiths G, Ktistakis N. (2008). *Autophagosome formation from membrane compartments enriched in phosphatidylinositol 3-phosphate and dynamically connected to the endoplasmic reticulum.* J Cell Biol. 182(4):685-701.

Bampton ET, Goemans CG, Niranjan D, Mizushima N, Tolkovsky AM. (2005). *The dynamics of autophagy visualized in live cells: from autophagosome formation to fusion with endo/lysosomes.* Autophagy. 1(1):23-36.

Bar-Peled L, Schweitzer LD, Zoncu R, Sabatini DM.(2012). *Ragulator is a GEF for the rag GTPases that signal amino acid levels to mTORC1.* 150(6):1196-1208.

Baumgart DC, Carding SR. (2007). *Inflammatory bowel disease: cause and immunobiology.*Lancet. 369(9573):1627-40.

Berryman S, Brooks E, Burman A, Hawes P, Roberts R, Netherton C, Monaghan P, Whelband M, Cottam E, Elazar Z, Jackson T, Wileman T. (2012). *Foot-and-mouth disease virus induces autophagosomes during cell entry via a class III phosphatidylinositol 3-kinase-independent pathway.* J Virol. 86(23):12940-12953.

Birmingham CL, Smith AC, Bakowski MA, Yoshimori T, Brumell JH (2006). *Autophagy controls Salmonella infection in response to damage to the Salmonella-containing vacuole*. J Biol Chem. 281. 11374-11383.

Bjørkøy G, Lamark T, Brech A, Outzen H, Perander M, Overvatn A, Stenmark H, Johansen T. (2005)*p62/SQSTM1 forms protein aggregates degraded by autophagy and has a protective effect on huntingtin-induced cell death.* J Cell Biol. 171(4):603-614.

Bjørkøy G, Lamark T, Pankiv S, Øvervatn A, Brech A, Johansen T (2009). Monitoring autophagic degradation of p62/SQSTM1.Methods Enzymol. 452:

181-97.

Boada-Romero E, Letek M, Fleischer A, Pallauf K, Ramón-Barros C, Pimentel-Muiños F.(2013). *TMEM59 defines a novel ATG16L1-binding motif that promotes local activation of LC3.* Immunity. 37(6):986-997.

Cadwell K, Liu J, Brown SL, Miyoshi H, Loh J, Lennerz J, Kishi C, Kc W, Carrero JA, Hunt S, Stone C, Brunt E, Xavier R, Sleckman B, Li E, Mizushima N, Stappenbeck T, Virgin H. (2009). *A key role for autophagy and the autophagy gene Atg16l1 in mouse and human intestinal Paneth cells.* Nature 456, 259-263.

Cadwell, K. Patel. K, Maloney. S, Liu.T, Ng, A. Storer, C. Head, R. Xavier, R. Stappenbeck, T, Virgin, H. (2010) . *Virus-plus-susceptibility gene interaction determines Crohn's disease gene Atg16L1 phenotypes in intestine*. Cell. 141. 1135–1145.

Cemma M, Kim P, Brumell J. (2011).*The* ubiquitin-*binding adaptor proteins p62/SQSTM1 and NDP52 are recruited independently to* bacteria-*associated microdomains to target Salmonella to the autophagy pathway.*Autophagy. 7(3):341-5.

Cherra S, Kulich S, Uechi G, Balasubramani M, Mountzouris J, Day B, Chu C. (2010) *Regulation of the autophagy protein LC3 by phosphorylation.* J Cell Biol. 190(4):533-9.

Congcong H **,** Klionsky, D. (2009). *Regulation Mechanisms and Signaling Pathways of Autophagy.* Annual Review of Genetics 43:67-93**.**

Cooney R, Baker J, Brain O, Danis B, Pichulik T, Allan P, Ferguson D, Campbell B, Jewell D, Simmons A. (2010*). NOD2 stimulation induces autophagy in dendritic cells influencing* bacteria*l handling and antigen presentation.* Nat Med.16(1):90-7**.**

de Lau W, Barker N, Low T, Koo B, Li V, Teunissen H, Kujala P, Haegebarth A, Peters P, van de Wetering M, Stange D, van Es J, Guardavaccaro D, Schasfoort , Mohri Y, Nishimori K, Mohammed S, Heck A, Clevers H.(2011)*. Lgr5 homologues associate with Wnt receptors and mediate R-spondin signalling*. Nature. 476(7360):293-7**.**

Dupont N, Jiang S, Pilli M, Ornatowski W, Bhattacharya D, Deretic V. (2011). *Autophagy-based unconventional secretory pathway for extracellular delivery of IL-1β.* EMBO J. 30(23):4701-11

Fass E, Shvets E, Degani I, Hirschberg K, Elazar Z. (2006) *Microtubules support production of starvation-induced autophagosomes but not their targeting and fusion with lysosomes.* J Biol Chem. 281(47):36303-36316

Friedmann T, Xu L, Wolff J, Yee J, Miyanohara A. (1989). *Retrovirus vector-mediated gene transfer into hepatocytes.* Mol Biol Med. 6(2):117-125.

Fujita N, Itoh T, Omori H, Fukuda M, Noda T, Yoshimori T. (2008*). The Atg16L complex specifies the site of LC3 lipidation for membrane biogenesis in autophagy.* Mol Biol Cell. 19(5):2092-100.

Fujita N, Hayashi-Nishino M, Fukumoto H, Omori H, Yamamoto A, Noda T, Yoshimori T (2008). *An Atg4B mutant hampers the lipidation of LC3 paralogues and causes defects in autophagosome closure.* Mol Biol Cell 19. 4651-9.

Fujita N, Saitoh T, Kageyama S, Akira S, Noda T, Yoshimori T.(2009). *Differential involvement of Atg16L1 in Crohn disease and canonical autophagy: analysis of the organization of the Atg16L1 complex in fibroblasts.*J Biol Chem. 20;284(47):32602-9.

Gannagé M, Dormann D, Albrecht R, Dengjel J, Torossi T, Rämer P, Lee M, Strowig T, Arrey F, Conenello G, Pypaert M, Andersen J, García-Sastre A, Münz C. (2009). *Matrix protein 2 of influenza A virus blocks autophagosome fusion with lysosomes.* Cell Host Microbe. 6(4):367-380.

Gingras AC, Kennedy S, O'Leary M, Sonenberg N, Hay N, (1998) *.4E-BP1, a repressor of mRNA translation, is phosphorylated and inactivated by the Akt(PKB) signaling pathway.*Genes Dev. 12(4):502-13.

Girardin SE, Travassos L, Hervé M, Blanot D, Boneca I, Philpott D, Sansonetti P, Mengin-Lecreulx D. (2003). *Peptidoglycan molecular requirements allowing detection by* NOD*1 and* NOD*2.* J Biol Chem. 278(43):41702-41708.

Goodlad R, Raja K, Peters T, Wright N. (1991). *Effects of urogastrone-epidermal growth factor on intestinal brush border enzymes and mitotic activity.* Gut. 32(9): 994-998.

Groulx J, Khalfaoui T, Benoit YD, Bernatchez G, Carrier J, Basora N, Beaulieu J. (2012) *Autophagy is active in normal colon mucosa.* Autophagy. 8(6):893-902.

Gutierrez O, Pipaon C, Inohara N, Fontalba A, Ogura Y, Prosper F, Nunez G, Fernandez-Luna JL (2002). *Induction of* NOD*2 in myelomonocytic and intestinal epithelial cells via nuclear factor-kappa B activation*. J Biol Chem 277. 41701-41705**.**

Halme L, Paavola-Sakki P, Turunen U, Lappalainen M, Färkkilä M, Kontula M (2006) *Family and twin studies in inflammatory bowel disease*. World J Gastroenterol.12 3668-3672**.**

Hampe J, Franke A, Rosenstiel P, Till A, Teuber M, Huse K, Albrecht M, Mayr G, De La Vega FM, Briggs J, Günther S, Prescott NJ, Onnie CM, Häsler R, Sipos B, Fölsch UR, Lengauer T, Platzer M, Mathew CG, Krawczak M, Schreiber S. (2007). *A genome-wide association scan of nonsynonymous SNPs identifies a susceptibility variant for Crohn disease in* Atg*16L1.* Nat Genet 39. 207-211.

Hanada T, Noda N, Satomi Y, Ichimura Y, Fujioka Y, Takao T, Inagaki F, Ohsumi Y.(2007). *The Atg12-5 conjugate has a novel E3-like activity for protein lipidation in autophagy.* J Biol Chem. 282(52):37298-302.

Hayashi-Nishino M, Fujita N, Noda T, Yamaguchi A, Yoshimori T, Yamamoto A. (2009). *A subdomain of the endoplasmic reticulum forms a cradle for autophagosome formation.* Nat Cell Biol. 11(12):1433-1437.

He H, Dang Y, Dai F, Guo Z, Wu J, She X, Pei Y, Chen Y, Ling W, Wu C, Zhao S, Liu JO, Yu L. (2003). *Post-translational modifications of three members of the human MAP1LC3 family and detection of a novel type of modification for MAP1*LC3B. J Biol Chem. 278(31):29278-29287.

Heitman J, Movva N, Hall M. (1991). *Targets for cell cycle arrest by the immunosuppressant rapamycin in yeast*. Science. 253:905–9.

Henault J, Martinez J, Riggs JM, Tian J, Mehta P, Clarke L, Sasai M, Latz E, Brinkmann M, Iwasaki A, Coyle A, Kolbeck R, Green DR, Sanjuan MA. (2012). *Noncanonical autophagy is required for type I interferon secretion in response to DNA-immune complexes.* Immunity. 37(6):986-97.

Hsu P, Kang S, Rameseder J, Zhang Y, Ottina K, Lim D, Peterson T, Choi Y, Gray N, Yaffe M.Marto J, Sabatini D. (2011). *The mTOR-regulated Phosphoproteome Reveals a Mechanism of mTORC1-mediated Inhibition of Growth Factor Signaling*. Science 332:1317-1322.

Hugot J, Chamaillard M, Zouali H, Lesage S, Cézard JP, Belaiche J, Almer S, Tysk C, O'Morain CA, Gassull M, Binder V, Finkel Y, Cortot A, Modigliani R, Laurent-Puig P, Gower-Rousseau C, Macry J, Colombel JF, Sahbatou M, Thomas G. (2001). *Association of NOD2 leucine-rich repeat variants with susceptibility to Crohn's disease*. Nature. 411(6837):599-603.

Itakura E, Mizushima N. (2010). *Characterization of autophagosome formation site by a hierarchical analysis of mammalian Atg proteins*. Autophagy. 6(6):764-76.

Jahreiss L, Menzies F, Rubinsztein DC.(2008) *The itinerary of autophagosomes: from peripheral formation to kiss-and-run fusion with lysosomes.* Traffic. 9(4):574-587.

Jung, H, Seyn-Hyun. R, Cao, J, Otto, N.M., Ki, D.H. (2010*) mTOR regulation of autophagy* FEBS Letters 584:1287-1295.

Kabeya Y, Mizushima N, Yamamoto A, Oshitani-Okamoto S, Ohsumi Y, Yoshimori T. (2003). *LC3, GABARAP and GATE16 localize to autophagosomal membrane depending on form-II formation.* J Cell Sci. 117(Pt 13):2805-12.

Kathiria A, Butcher LD, Feagins L, Souza R, Boland C, Theiss A. (2012). *Prohibitin 1 modulates mitochondrial stressrelated autophagy in human colonic epithelial cell s.* PLoS One. 7(2):e31231.

Kim J, Kundu M, Viollet B, Guan K. (2011) *AMPK and mTOR Regulate Autophagy Through Direct Phosphorylation of ULK1.* Nat Cell Biol 13:132-141.

Kirkin V, Lamark T, Sou Y, Bjørkøy G, Nunn JL, Bruun JA, Shvets E, McEwan DG, Clausen TH, Wild P, Bilusic I, Theurillat J, Øvervatn A, Ishii T, Elazar Z, Komatsu M, Dikic I, Johansen T. (2009). *A role for NBR1 in autophagosomal degradation of* ubiquitin*ated substrates.* Mol. Cell. 33(4):505-16.

Klionsky D. Cueva R, Yaver, D. (1992). *AminopeptidaseI of Saccharomyces cervisiae is localised to the vacuole independent of the secretory pathway.* J Cell Biol. 119(2): 287–299.

Klionsky D. (2005). *The Molecular Machinery of Autophagy; Unanswered Questions*. J Cell Sci 118:7 – 18.

Klionsky D, Abeliovich H, Agostinis P, Agrawal D, Aliev G, Askew DS, Baba M, Baehrecke EH, Bahr BA, Ballabio A, *et al*. (2008). *Guidelines for the use and interpretation of assays for monitoring autophagy in higher eukaryotes.* Autophagy. ;4(2):151-75.

Knorr R, Dimova R, Lipowsky R. (2012). *Curvature of double membrane organelles generated by changes in membrane size and composition.* PLoS One. 7(3):e32753.

Köchl R, Hu X, Chan E, Tooze S. (2006) *Microtubules facilitate autophagosome formation and fusion of autophagosomes with endosomes.* Traffic. 7(2):129-145.

Koo B, Stange D, Sato T, Karthaus W, Farin H, Huch M, van Es J, Clevers H. (2011), *Controlled gene expression in primary Lgr5 organoid cultures.*Nat Methods. 9(1):81-83.

Koo B, Spit M, Jordens I, Low T, Stange D, van de Wetering M, van Es JH, Mohammed S, Heck A, Maurice M, Clevers H. (2012). *Tumour suppressor RNF43 is a stem-cell E3 ligase that induces endocytosis of Wnt receptors.* Nature. 488(7413):665-669.

Korolchuk V, Saiki S, Lichtenberg M, Siddiqi F, Roberts E, Imarisio S, Jahreiss L, Sarkar S, Futter M, Menzies F, O'Kane CJ, Deretic V, Rubinsztein D. (2011). *lysosomal positioning coordinates cellular nutrient responses.* Nat Cell Biol 13(4):453-60.

Koyama-Honda I, Itakura E, Fujiwara T, Mizushima N.(2013*). Temporal analysis of recruitment of mammalian ATG proteins to the autophagosome formation site.* Autophagy; 9:1491–1499.

Kuballa P, Huett A, Rioux J, Daly M, Xavier R.(2008). *Impaired autophagy of an intracellular pathogen induced by a Crohn's disease associated* Atg*16L1 variant.* PLoS One. 2008;3(10):e3391.

Lam G, Cemma M, Muise A, Higgins D, Brumell J.(2013). *Host and* bacteria*l factors that regulate LC3 recruitment to Listeria monocytogenes during the early stages of macrophage infection.* Autophagy.12;9(7).

Levine B. (2005). *Eating oneself and uninvited guests: autophagy-related pathways in cellular defence.* Cell 120(2): 159-62.

Li M, Hou Y, Wang J, Chen X, Shao Z, Yin X.(2011). *Kinetics comparisons of mammalian Atg4 homologues indicate selective preferences toward diverse Atg8 substrates.*J Biol Chem. 286(9):7327-38.

Loftus E, Silverstein M, Sandborn W, Tremaine W, Harmsen W, Zinsmeister A.(1998) *Crohn's disease in Olmsted County, Minnesota, 1940-1993: incidence, prevalence, and survival.* Gastroenterol. 114(6):1161-1168.

Loftus E. (2004) *Clinical epidemiology of inflammatory bowel disease: incidence, prevalence, and environmental influences.* Gastroenterol*.* 126.1504-1517.

Long X, Lin Y, Ortiz-Vega S, Yonezawa K, Avruch J. (2005) *Rheb binds and regulates the mTOR kinase.* Curr Biol 15(8):702-13.

Maier H, Cottam E, Stevenson-Leggett P, Wilkinson J, Harte C, Wileman T, Britton P. (2013). *Visualizing the autophagy pathway in avian cells and its application to studying infectious bronchitis virus.* Autophagy. 9:496 - 509;

Malo C, Ménard D. (1982). *Influence of epidermal growth factor on the development of suckling mouse intestinal mucosa.* Gastroenterol. 83(1):28-35.

Mari M, Griffith J, Rieter E, Krishnappa L, Klionsky D, Reggiori F. (2010). *An Atg9-containing compartment that functions in the early steps of autophagosome biogenesis.* J Cell Biol. 2010 190(6):1005-22.

Mariño G, Salvador-Montoliu N, Fueyo A, Knecht E, Mizushima N, López-Otín C. (2007). Tissue-specific autophagy alterations and increased tumorigenesis in mice deficient in Atg4C/autophagin-3. J Biol Chem. 282(25):18573-83.

Massey D, Bredin, F, Parkes M. (2008). *Use of sirolimus (rapamycin) to treat refractory Crohn's disease* Gut 57.1294-1296.

Matsunaga K, Morita E, Saitoh T, Akira S, Ktistakis NT, Izumi T, Noda T, Yoshimori T. (2010) *Autophagy requires endoplasmic reticulum targeting of the PI3-kinase complex via Atg14L.* J Cell Biol. 190(4):511-521.

Maurisse R, De Semir D, Emamekhoo H, Bedayat B, Abdolmohammadi A, Parsi H, Gruenert DC. (2010). *Comparative transfection of DNA into primary and transformed mammalian cells from different lineages.* BMC Biotechnol. 10:9.

Messer J, Murphy S, Logsdon M, Lodolce J, Grimm W, Bartulis S, Vogel TP, Burn M, Boone DL. (2013) *The Crohn's disease: associated* Atg*16L1 variant and Salmonella invasion.* BMJ Open. 3(6).

Millar N, White I. (2004). *Microscopy* [online].

Mizushima N, Noda T, Yoshimori T, Tanaka Y, Ishii T, George M .(1998). *A protein conjugation system essential for autophagy*. Nature 395. 395-398.

Mizushima N, Kuma A. (2008). *Autophagosomes in GFP-LC3 Transgenic Mice.* Methods Mol Biol. 445:119-124.

Martina J, Chen Y, Gucek M, Puertollano R. (2012).*MTORC1 functions as a transcriptional regulator of autophagy by preventing nuclear transport of TFEB.* Autophagy. 8(6):903-14

Matsushita M, Suzuki N, Obara K, Fujioka Y, Ohsumi Y, Inagaki F. (2005). *Structure of Atg5.Atg16, a complex essential for autophagy.* J Biol Chem. 282(9):6763-6772.

Mizushima N, Ohsumi Y, Yoshimori T. (2002). *Autophagosome formation in mammalian cells.* Cell Struct Funct. 27(6):421-429.

Mizushima N, Kuma A, Kobayashi Y, Yamamoto A, Matsubae M, Takao T, Natsume T, Ohsumi Y, Yoshimori T.(2003). *Mouse Apg16L, a novel WD-repeat protein, targets to the autophagic isolation membrane with the Apg12-Apg5 conjugate.*J Cell Sci. 1;116(Pt 9):1679-1688.

Mizushima N. (2004). *Methods for monitoring autophagy*. Int J Biochem Cell Biol. 36(12):2491-2502.

Mizushima N, Yamamoto A, Matsui M, Yoshimori T, Ohsumi Y. (2004). *In vivo analysis of autophagy in response to nutrient starvation using transgenic mice expressing a fluorescent autophagosome marker.* Mol Biol Cell. 15(3):1101-1111.

Mizushima N, Yoshimori T, Levine B. (2010). *Methods in mammalian autophagy research*. Cell. 140(3):313-326.

Molejon M, Ropolo A, Re A, Boggio V, Vaccaro MI. (2013). *The VMP1-Beclin 1 interaction regulates autophagy induction.* Sci Rep.;3:1055.

Moreau K, Ravikumar B, Renna M, Puri C, Rubinsztein DC. (2011). *Autophagosome precursor maturation requires homotypic fusion.* Cell. 146(2):303-17.

Mowat A.(2003). *Anatomical basis of tolerance and immunity to intestinal antigens.* Nat Rev Immunol. 3(4):331-41.

Noda T, Ohsumi Y.(1998).*Tor, a phosphatidylinositol kinase homologue, controls autophagy in yeast.* J Biol Chem. 273(7):3963-6.

Noda T, Fujita N, Yoshimori T.(2009). *The late stages of autophagy: how does the end begin?* Cell Death Differ. 16(7):984-90.

Pankiv S, Clausen T, Lamark T, Brech A, Bruun J, Outzen H, Øvervatn A, Bjørkøy G, Johansen T.(2007). *p62/SQSTM1 binds directly to Atg8/LC3 to facilitate degradation of* ubiquitin*ated protein aggregates by autophagy.*J Biol Chem. 282(33):24131-24145.

Ogura Y, Bonen D, Inohara N, Nicolae D, Chen F, Ramos R, Britton H, Moran T, Karaliuskas R, Duerr R, Achkar J, Brant S, Bayless T, Kirschner B, Hanauer S, Nuñez G, Cho J. (2001). *A frameshift mutation in NOD2 associated with susceptibility to Crohn's disease.* Nature. 411(6837):603-606.

Onuma K, Ochiai M, Orihashi K, Takahashi M, Imai T, Nakagama H, Hippo Y. (2012). *Genetic reconstitution of tumorigenesis in primary intestinal cells.* Proc Natl Acad Sci U S A. 110(27):11127-32.

Orsi A, Razi M, Dooley H, Robinson D, Weston A, Collinson L, Tooze S.(2012). *Dynamic and transient interactions of Atg9 with autophagosomes, but not membrane integration, are required for autophagy.* Mol Biol Cell. 23(10):1860-73.

Pankiv S, Clausen T, Lamark T, Brech A, Bruun JA, Outzen H, Øvervatn A, Bjørkøy G, Johansen T. (2007).*p62/SQSTM1 binds directly to Atg8/LC3 to facilitate degradation of* ubiquitin*ated protein aggregates by autophagy.* J Biol Chem.17;282(33):24131-45.

Park S, Ha S, Coleman M, Meshkibaf S, Kim S. (2013). *p62/ SQSTM1 enhances NOD2 mediated signaling and cytokine production through stabilizing NOD2 oligomerization.* PLoS One. 8(2): e57138.

Paz Y, Elazar Z, Fass D. (2000). *Structure of GATE-16, membrane transport modulator and mammalian ortholog of autophagocytosis factor Aut7p.* J Biol Chem. 275(33):25445-50.

Peterson R, Schreiber S. (1998). *Translation control: onnecting mitogens and the ribosome*. Curr. Biol. 8 (7): 248-50.

Pickart C, Eddins M. (2004). *Ubiquitin: structures, functions, mechanisms.* Biochim Biophys Acta 1695(1-3):55-72.

Pfeifer U. (1978). *Inhibition by insulin of the formation of autophagic vacuoles in rat liver. A morphometric approach to the kinetics of intracellular degradation by autophagy.* J Cell Biol. 78(1):152-167.

Philpott D (2009). NOD*1 and* NOD*2 direct autophagy by recruiting* Atg*16L1 to the plasma membrane at the site of* bacteria*l entry.* Nat Immunol.11. 55-62.

Pircs K, Nagy P, Varga A, Venkei Z, Erdi B, Hegedus K, Juhasz G. (2012). *Advantages and limitations of different p62-based assays for estimating autophagic activity in Drosophila.* PLoS One. 7(8):e44214.

Polson H, de Lartigue J, Rigden D, Reedijk M, Urbé S, Clague M, Tooze S. (2010). *Mammalian Atg18 (WIPI2) localizes to omegasome-anchored phagophores and positively regulates LC3 lipidation.* Autophagy. 6(4):506-522.

Proikas-Cezanne T, Robenek H. (2011). *Freeze-fracture replica immunolabelling reveals human WIPI-1 and WIPI-2 as membrane proteins of autophagosomes.* J Cell Mol Med. 15(9):2007-2010.

Puri C, Renna M, Bento C, Moreau K, Rubinsztein DC. (2014). *ATG16L1 meets ATG9 in recycling endosomes: Additional roles for the plasma membrane and endocytosis in autophagosome biogenesis.* Autophagy. 10(1):182-184.

Raju D, Hussey S, Ang M, Terebiznik MR, Sibony M, Galindo-Mata E, Gupta V, Blanke SR, Delgado A, Romero-Gallo J, Ramjeet M, Mascarenhas H, Peek R, Correa P, Streutker C, Hold G, Kunstmann E, Yoshimori T, Silverberg M, Girardin S, Philpott D, El Omar E, Jones N. (2012). *Vacuolating cytotoxin and variants in Atg16L1 that disrupt autophagy promote Helicobacter pylori infection in humans.* Gastroenterol. 142(5)L 1160-1171.

Ravikumar B, Moreau K, Jahreiss L, Puri C, Rubinsztein D. (2010). *Plasma membrane contributes to the formation of pre-autophagosomal structures.* Nat Cell Biol.12(8):747-57.

Razi M, Tooze S. (2009). Correlative light and electron microscopy. Methods Enzymol. 452:261-275.

Reya T, Clevers H (2005). *Wnt signalling in stem cells and cancer.* Nature 434. 843-850.

Roccio M, Bos J, Zwartkruis F. (2006). *Regulation of the small GTPase Rheb by amino acids.* Oncogene 25:657-664.

Roczniak-Ferguson A, Petit C, Froehlich F, Qian S, Ky J, Angarola B, Walther T, Ferguson S. (2012). *The transcription factor TFEB links mTORC1 signaling to transcriptional control of lysosome homeostasis.* Sci Signal. 5(228) . ra42.

Romanov J, Walczak M, Ibiricu I, Schüchner S, Ogris E, Kraft C, Martens S. (2012). *Mechanism and functions of membrane binding by the Atg5-Atg12/Atg16 complex during autophagosome formation.* EMBO J. 31(22):4304-4317.

Rong Y, McPhee C, Deng S, Huang L, Chen L, Liu M, Tracy K, Baehrecke E, Yu L, Lenardo M.(2011).*Spinster is required for autophagic lysosome reformation and mTOR reactivation following starvation.* Proc Natl Acad Sci U S A. 108(19):7826-31.

Ropolo A, Grasso D, Pardo R, Sacchetti ML, Archange C, Lo Re A, Seux M, Nowak J, Gonzalez CD, Iovanna J, Vaccaro M. (2007). *The pancreatitis-induced vacuole membrane protein 1 triggers autophagy in mammalian cells..* J Biol Chem.;282(51):37124-33.

Russell R, Tian Y, Yuan H, Park H, Chang Y, Kim J, Kim H, Neufeld TP, Dillin A, Guan K. (2013). *ULK1 induces autophagy by phosphorylating Beclin-1 and activating VPS34 lipid kinase.* Nat Cell Biol. 15(7):741-50.

Sancak Y, Peterson T, Shaul Y, Lindquist R, Thoreen C, Bar-Peled L, Sabatini D. (2008). *The Rag GTPases bind raptor and mediate amino acid signalling to mTORC1.* Science 320(5882):1496-501.

Sancak Y, Bar-Peled L, Zoncu R, Markhard A, Nada S, Sabatini D. (2010). *Ragulator-Rag complex targets mTORC1 to the lysosomal surface and is necessary for its activation by amino acids.* Cell 141 (2):290-303.

Sancho E, Batlle E, Clevers H. (2003). *Live and let die in the intestinal epithelium*. Curr Opin Cell Biol. 15(6):763-770.

Sarbassov D, Ali S, Kim D, Guertin D, Latek R, Erdjument-Bromage H, Tempst P, Sabatini D (2004). *Rictor, a novel binding partner of mTOR, defines a rapamycin-insensitive and raptor-independent pathway that regulates the cytoskeleton*. Curr Biol 14:1296-302.

Sardiello M, Ballabio A. (2009). *lysosomal enhancement: a CLEAR answer to cellular degradative needs.* Cell Cycle. 8(24):4021-40212.

Sato T, Vries R, Snippert H, van de Wetering M, Barker N, Stange D, van Es J, Abo A, Kujala P, Peters P, Clevers H.(2009). *Single Lgr5 stem cells build crypt-villus structures in vitro without a mesenchymal niche.* Nature. 459(7244):262-265.

Sato T, Stange D, Ferrante M, Vries R, Van Es J, Van den Brink S, Van Houdt W, Pronk A, Van Gorp J, Siersema P, Clevers H. (2011). *Long-term expansion of epithelial organoids from human colon, adenoma, adenocarcinoma, and Barrett's epithelium.* Gastroenterol. 141(5):1762-1772.

Scherz-Shouval R, Sagiv Y, Shorer H, Elazar Z. (2003). *The COOH terminus of GATE-16, an intra-Golgi transport modulator, is cleaved by the human cysteine protease HsApg4A*.J Biol Chem. 2003 Apr 18;278(16):14053-8.

Settembre C, Di Malta C, Polito V, Garcia Arencibia M, Vetrini F, Erdin S, Erdin SU, Huynh T, Medina D, Colella P, Sardiello M, Rubinsztein DC, Ballabio A. (2011). *TFEB links autophagy to lysosomal biogenesis.* Science. 332(6036):1429-1433.

Shaker A, Rubin D. (2010). Intestinal stem cells and epithelial-mesenchymal interactions in the crypt and stem cell niche. Transl Res. 156(3):180-187.

Shigemitsu K, Tsujishita Y, Hara K, Nanahoshi M, Avruch J, Yonezawa K. (1999). *Regulation of translational effectors by amino acid and mammalian target of rapamycin signaling pathways. Possible involvement of autophagy in cultured hepatoma cells.* J Biol Chem 274(2):1058-65.

Shpilka T, Weidberg H, Pietrokovski S, Elazar Z.(2011). *Atg8: an autophagy-related ubiquitin-like protein family.* Genome Biol;12(7):226.

Tanida I, Sou Y, Ezaki J, Minematsu-Ikeguchi N, Ueno T, Kominami E.(2004). *HsAtg4B/autophagin1 cleaves the carboxyl termini of three human Atg8 homologues and delipidates microtubule-associated protein light chain 3- and GABAA receptor associated protein- phospholipid conjugates*. J Biol Chem. 279(35):36268-76.

Thoreen C, Sabatini D. (2009). *rapamycin inhibits mTORC1, but not completely.* Autophagy 5:725-6.

Thoreen C, Kang S, Chang J, Liu Q, Zhang J, Gao Y, Reichling L, Sim T, Sabatini D, Gray N. (2009). *An ATP-competitive mammalian target of rapamycin inhibitor reveals rapamycin-resistant functions of mTORC1.* J Biol Chem 284(12):8023-32.

Thumm M, Egner R, Koch B, Schlumpberger M, Straub M, Veenhuis M, Wolf D. (1994). *Isolation of autophagocytosis mutants of Saccharomyces cerevisiae.* FEBS Lett. 349(2):275-280.

Thurston T, Ryzhakov G, Bloor S, von Muhlinen N, Randow F. (2009). *The TBK1 adaptor and autophagy receptor NDP52 restricts the proliferation of ubiquitin-coated bacteria.* Nat Immunol. 10:1215-1221.

Tokunaga C, Yoshino K, Yonezawa K. (2004). *Mtor integrates amino acid- and energy sensing pathways.* Biochem Biophys Res Commun. 313(2):443-446.

Travassos LH, Carneiro LA, Ramjeet M, Hussey S, Kim YG, Magalhães JG, Yuan L, Soares F, Chea E, Le Bourhis L, Boneca IG, Allaoui A, Jones NL, Nuñez G, Girardin SE. (2009). NOD*1 and* NOD*2 direct autophagy by recruiting* Atg*16L1 to the plasma membrane at the site of* bacteria*l entry.* Nat Immunol.11. 55-62.

Taub M, Wang Y, Szczesny TM, Kleinman HK. (1990) *Epidermal growth factor or transforming growth factor alpha is required for kidney tubulogenesis in matrigel cultures in serum-free medium.* Proc Natl Acad Sci U S A. 87(10):4002-4006.

Tra T, Gong L, Kao LP, Li XL, Grandela C, Devenish RJ, Wolvetang E, Prescott M. (2011). *Autophagy in human embryonic stem cells.* PLoS One. 6(11).

Uehara A, Fujimoto Y, Fusake K, Takada H. (2007). *Various human epithelial cells express functional Toll-like receptors NOD1 and NOD2 to produce anti-microbial peptides, but not proinflammatory cytokines.* Mol Immunol. 44(12): 3100-3111.

Ungar D, Hughson F.(2003). *SNARE protein structure and function*. Annu Rev Cell Dev Biol.19:493-517.

Van der Flier L, Sabates-Bellver J, Oving I, Haegebarth A, De Palo M, Anti M, Van Gijn M, Suijkerbuijk S, Van de Wetering M, Marra G, Clevers H.(2007). *The Intestinal Wnt/TCF Signature.* Gastroenterology. 132(2):628-32.

Weidberg H, Shvets E, Shpilka T, Shimron F, Shinder V, Elazar Z. (2010). *LC3 and GATE-16/GABARAP subfamilies are both essential yet act differently in autophagosome biogenesis.*EMBO J.;29(11):1792-802.

Weidberg H, Shpilka T, Shvets E, Abada A, Shimron F, Elazar Z.(2011). *LC3 and GATE-16 N termini mediate membrane fusion processes required for autophagosome biogenesis.* Dev Cell. 20(4):444-54.

Wilkinson, K. (2005). *The discovery of ubiquitin-dependent proteolysis*. Proc Natl Acad Sci USA. 102(43):15280-2.

Wu J, Dang Y, Su W, Liu C, Ma H, Shan Y, Pei Y, Wan B, Guo J, Yu L. (2006). *Molecular cloning and characterization of rat LC3A and* LC3B--*two novel markers of autophagosome.* Biochem Biophys Res Commun. 339(1):437-442.

Xie Z, Klionsky D. (2007). *Autophagosome Formation: Core Machinery and Adaptations.* Nature Cell Biol. 9; 1102 –1108

Xie Z, Nair U, Geng J, Szefler M, Rothman E, Klionsky D. (2007). *Indirect estimation of the area density of Atg8 on the phagophore.* Autophagy. 5(2):217-20.

Yamamoto H, Kakuta S, Watanabe T, Kitamura A, Sekito T, Kondo-Kakuta C, Ichikawa R, Kinjo M, Ohsumi Y. (2012). *Atg9 vesicles are an important membrane source during early steps of autophagosome formation.* J Cell Biol. 198(2):219-33.

Yip C, Murata K, Walz T, Sabatini D, Kang S. (2010). *Structure of the human mTOR complex I and its implications for rapamycin inhibition.* Mol. Cell 38:768-774.

Yoshikawa Y, Ogawa M, Hain T, Yoshida M, Fukumatsu M, Kim M, Mimuro H, Nakagawa I, Yanagawa T, Ishii T, Kakizuka A, Sztul E, Chakraborty T, Sasakawa C.(2009). *Listeria monocytogenes ActA-mediated escape from autophagic recognition.*Nat Cell Biol. 11(10):1233-40.

Young A, Chan E, Hu X, Köchl R, Crawshaw S, High S, Hailey D, Lippincott-Schwartz J, Tooze S.(2006). *Starvation and ULK1-dependent cycling of mammalian Atg9 between the TGN and endosomes.* J Cell Sci. 2006 119(Pt 18):3888-900.

Yu L, McPhee C, Zheng L, Mardones GA, Rong Y, Peng J, Mi N, Zhao Y, Liu Z, Wan F, Hailey D, Oorschot V, Klumperman J, Baehrecke E, Lenardo M. (2010). *Termination of autophagy and reformation of lysosomes regulated by mTOR.* Nature. 456: 942-946.

Zheng X, Kinsella T. (2011). *Impact of autophagy on chemotherapy and radiotherapy mediated tumor cytotoxicity: "to live or not to live".* Front. Oncol. 3;1:30

Zheng YT, Shahnazari S, Brech A (2009). *The adaptor protein p62/SQSTM1 targets invading* bacteria *to the autophagy pathway.* J immunol 183. 5909-5916.

Zoncu R, Bar-Peled L, Efeyan A, Wang S, Sancak Y, Sabatini D. (2011). *mTORC1 senses lysosomal amino acids through an inside-out mechanism that requires the vacuolar H(+)-ATPase.* Science 334 (6056): 678-683 Nature. 465(7300):942-946.